The Simulated Performance of AGATA Following Relativistic Coulomb Excitation at GSI

Daniel Bloor

Thesis submitted for the degree of Doctor of Philosophy

University of York

Department of Physics

September 2013

Abstract

In preparation for the AGATA campaign at GSI, a set of simulation tools to be utilised with the AGATA simulation code has been developed, enabling the response of the proposed AGATA geometries for use at GSI to be simulated following a relativistic Coulomb excitation reaction. The γ-ray tracking algorithms, crucial to the performance of AGATA, have previously been untested in a relativistic environment with high levels of background, and as a result has been evaluated in a variety of simulated conditions with varying levels of background.

To assess the performance of the γ-ray tracking algorithms, the γ-ray spectra of the RISING array from a recent PreSPEC experiment (Experiment S377 in May 2011) has been compared with a simulation, in order to determine the simulation input that provided a similar spectral response. The optimum simulation input was then used to evaluate the performance of the AGATA geometries and the γ-ray tracking under the same conditions.

Simulations have highlighted that tracking is possible for unshielded detectors in the experimental conditions at GSI, providing that the atomic background multiplicity can be kept below a certain threshold. The inclusion of the extreme levels of atomic background in the simulations completely saturates the γ-rays of interest, suggesting that the use of shielding needs to be further investigated. Assuming that shielding or analysis techniques are to be used experimentally, the atomic background was removed from the simulations leaving only the high energy background component, and the consecutive performance of the AGATA geometries were investigated and compared with RISING. Under such conditions, the AGATA geometries gave up to a factor of $\sim$2 improvement in terms of the peak-to-total ratio compared to the RISING array.

Contents

Abstract **ii**

List of Figures **vii**

List of Tables **xiii**

Acknowledgements **xv**

Declaration **xvi**

1 Introduction **1**

1.1 Thesis Overview 2

2 γ-ray Detection and Theory **6**

2.1 Gamma Decay 6

2.2 γ-ray Interaction Mechanisms 9

2.2.1 Photoelectric Absorption 10

2.2.2 Compton Scattering 11

2.2.3 Pair Production 11

2.3 Semiconductor Detectors 12

2.4 Outline of γ-ray Spectroscopy 16

2.5 γ-ray Spectroscopy at GSI 19

2.5.1 Atomic Background 21

2.6 The Advanced GAmma Tracking Array 25

2.6.1 Design of AGATA and Crystal Characteristics 25

2.6.2 γ-ray Tracking 28

3 The GSI Accelerator Facility **33**

3.1 Reaction Mechanisms 33

3.1.1 Projectile Fragmentation 34
3.1.2 Relativistic Coulomb Excitation 36
3.2 Primary Beam Production 37
3.3 Heavy Ion Selection with the FRagment Separator (FRS) 38
3.3.1 $B\rho$-ΔE-$B\rho$ Method 38
3.3.2 FRS Particle Identification Detectors 40
3.4 RISING Cluster Array 40
3.5 LYCCA Detector Array 43
3.5.1 Double-sided Silicon-Strip Detectors 44
3.5.2 Large-area Fast Plastic Scintillator 44
3.5.3 Caesium Iodide Detectors 46
3.6 Existing Simulation Tools 46
3.6.1 MOCADI 47
3.6.2 LISE++ 49
3.6.3 LYCCA Simulation Package 49

4 Development of Simulation Tools for Relativistic Reaction Processes at GSI 51

4.1 Detector Geometries 52
4.1.1 Simulated LYCCA-0 Geometry 52
4.1.2 Simulated RISING Geometry 53
4.1.3 Simulated AGATA Geometries 54
4.2 Event Generation 59
4.2.1 MOCADI 59
4.2.2 GammaWare 59
4.2.3 DWEIKO 59
4.2.4 ABKG 63
4.2.5 High Energy Background 65
4.2.6 Creation of the Input Events File 66
4.3 AGATA Simulation Code 69
4.4 Event Reconstruction and Processing 70
4.4.1 Detector Resolutions 70
4.4.2 Recoil Direction 72
4.4.3 Recoil Velocity 73

4.4.4 Rest Mass . . . 75
4.4.5 Simulated LYCCA-0 Spectra . . . 76

5 Simulations for AGATA at INFN 80
5.1 The Effect of Position Smearing on the γ-ray Tracking . . . 80

6 Simulations for AGATA at GSI (Expt. S377) 89
6.1 Experiment S377 Setup . . . 89
6.2 Experimental Spectra . . . 90
6.2.1 Experiment Particle Gate Conditions . . . 90
6.2.2 ^{36}Ar: Experimental Spectra . . . 95
6.2.3 ^{33}Ar: Experimental Spectra . . . 95
6.3 RISING Simulations . . . 97
6.3.1 Atomic Background Considerations . . . 97
6.3.2 ^{33}Ar: Determination of the Branching Ratio . . . 102
6.3.3 Determination of the High Energy Background Multiplicity . . 105
6.3.4 Simulation Particle Gate Conditions . . . 111
6.3.5 ^{36}Ar: Simulation and Experiment Comparison . . . 111
6.3.6 ^{33}Ar: Simulation and Experiment Comparison . . . 111
6.4 AGATA Simulations . . . 114
6.4.1 Effect of the Background on the $\gamma-$ray Tracking . . . 114
6.4.1.1 γ-rays of Interest (No Background) . . . 115
6.4.1.2 Atomic Background+High Energy Background+γ-rays of Interest . . . 118
6.4.1.3 High Energy Background+γ-rays of Interest . . . 122
6.4.2 Effect of the Timing Resolution on the Peak Shape . . . 125
6.4.3 Tracking Settings Considerations . . . 130
6.4.3.1 Energy Threshold . . . 130
6.4.3.2 Packing & Smearing . . . 134
6.4.4 Comparison Between the RISING and AGATA Simulations . . 136

7 Discussion and Conclusions 139
7.1 Evaluation of the AGATA Simulations . . . 140
7.1.1 Tracking Performance . . . 140
7.1.2 Effect of the Timing Resolution on the Peak Shape . . . 144

7.1.3 Improvements of AGATA over RISING 146
7.2 Future Work 147
7.2.1 AGATA and Pb Shielding 147
7.2.2 AGATA and Miniball 149
7.2.3 Simulation Upgrades 151
7.3 Concluding Remarks 151

References **153**

List of Figures

1.1 Photograph of the AGATA Demonstrator. 2
1.2 Sensitivity of the full AGATA array compared to previous arrays. . . 3

2.1 Schematic of the γ-ray interaction mechanisms within a detector. . . 9
2.2 Dependence of the main γ-ray interaction mechanisms on the atomic number of the absorbing material and the incident photon energy. . . 10
2.3 Schematic of the energy band structure in doped semiconductors. . . 13
2.4 Key features of a γ-ray spectrum. 16
2.5 Gammasphere γ-ray spectra showing the effect of Compton suppression shields. 18
2.6 Contributions to the energy resolution in the GSI environment. . . . 21
2.7 ABKG simulation containing target x-rays. 23
2.8 ABKG simulation containing Radiative Electron Capture. 23
2.9 ABKG simulation containing Primary Bremsstrahlung. 24
2.10 ABKG simulation containing Secondary Electron Bremsstrahlung. . . 24
2.11 The various geometries considered for the full AGATA array. 26
2.12 Drawing of the AGATA crystals and the segmentation positions. . . . 27
2.13 Mechanical drawing of the AGATA detector segmentation scheme. . . 27

3.1 Schematic of the GSI accelerator facility. 34
3.2 Schematic of the projectile fragmentation process. 35
3.3 Simulated Z vs. A/Q FRS identification plot. 35
3.4 Schematic of the Coulomb excitation process. 36
3.5 Schematic of the FRS. 38
3.6 Schematic of the RISING detector array. 41
3.7 Schematic of the LYCCA-0 detector array. 43
3.8 Schematic of the LYCCA detector chamber mainframe. 45

3.9 Images and drawings of the LYCCA-0 DSSSDs. 45
3.10 Photograph of the LYCCA-0 Fast Plastic Scintillator. 46
3.11 Image and drawing of a LYCCA-0 CsI detector module. 47

4.1 Flow chart of the simulation process. 52
4.2 VRML image of the LYCCA-0 detector array. 53
4.3 VRML images of the RISING detector array. 54
4.4 Simulated photopeak efficiency as a function of the target-to-array distance for the AGATA 5ATC+5ADC geometry. 55
4.5 Simulated photopeak efficiency as a function of the γ-ray detection angle for the AGATA 5ATC+5ADC geometry. 55
4.6 Simulated energy resolution as a function of the target-to-array distance for the AGATA 5ATC+5ADC geometry. 56
4.7 VRML image of the simulated AGATA 5ATC+5ADC geometry. . . . 56
4.8 Simulated photopeak efficiency as a function of the target-to-array distance for the AGATA 10ATC+5ADC geometry. 57
4.9 Simulated photopeak efficiency as a function of the γ-ray detection angle for the AGATA 10ATC+5ADC geometry. 57
4.10 Simulated energy resolution as a function of the target-to-array distance for the AGATA 10ATC+5ADC geometry. 58
4.11 VRML image of the simulated AGATA 10ATC+5ADC geometry. . . 58
4.12 Technical drawing of the S2 focal plane. 60
4.13 Technical drawing of the S4 focal plane. 61
4.14 Level schemes of the ^{36}Ar and ^{33}Ar nuclei showing the states populated during experiment S377. 62
4.15 $W(\theta_{lab})$ distribution obtained from the DWEIKO code. 63
4.16 Average γ-ray interaction positions in the RISING crystals for a simulation containing ^{36}Ar γ-rays and no background components. 64
4.17 Energy vs. θ distribution produced from the ABKG code. 64
4.18 Simulated ^{36}Ar RISING spectrum for an input events file containing high energy background. 66
4.19 OGLIX image of the simulated RISING+LYCCA-0 detector setup and particle trajectories. 71
4.20 Schematic of the LYCCA-0 TOF setup. 74

4.21 Comparison between the simulated measured and corrected β values from an ^{36}Ar simulation. 75
4.22 Simulated ^{36}Ar mass distribution. 76
4.23 Simulated LYCCA-0 spectrum showing the ΔE vs. E correlation. . . 78
4.24 Simulated LYCCA-0 spectrum showing the TOF vs. the total kinetic energy correlation. 78
4.25 Simulated LYCCA-0 spectrum showing the hit pattern of the beam at the target DSSSD. 79
4.26 LYCCA-0 spectrum showing the hit pattern of the beam at the wall DSSSDs. 79

5.1 Experimental ^{60}Co spectra measured with 2ATCs. 81
5.2 Comparison between the tracked experimental and simulated ^{60}Co spectra. 82
5.3 Plot of the position and energy smearing functions used by the OFT code. 83
5.4 Normalised experimental and simulated ^{60}Co core spectra. 84
5.5 VRML image of the simulation setup for the ^{60}Co source experiment. 85
5.6 P/T as a function of the scaling factor in the position smearing function. 86
5.7 Comparison between the experimental and optimised simulated ^{60}Co spectra. 86
5.8 Example of a Quiver plot. 87
5.9 Simulation results from packing γ-ray interactions at the centre of the AGATA detector segments. 88

6.1 Experimental spectra showing the Z vs. A/Q particle gate. 90
6.2 Experimental spectra showing the ΔE_{DSSSD} vs. $E_{DSSSD+CsI}$ particle gate. 91
6.3 Experimental spectra showing the ΔE_{wall} vs. ΔE_{target} particle gate. . 91
6.4 Experimental spectra showing the $\beta_{LYCCA-0}$ vs. β_{FRS} particle gate. . 92
6.5 Experimental spectra showing the $\beta_{LYCCA-0}$ vs. E_{CsI} particle gate . . 92
6.6 Experimental spectrum showing the time vs. energy matrix of the target DSSSD. 93
6.7 Experimental spectrum showing the time vs. energy matrix of the RISING array. 93

6.8 Timing spectrum of the RISING array for the ^{36}Ar setting. 94
6.9 Experimental ^{36}Ar RISING spectrum containing singles and addback events. 95
6.10 Experimental ^{36}Ar RISING spectrum containing singles events. 96
6.11 Experimental ^{36}Ar RISING spectrum containing addback events. . . . 96
6.12 Experimental ^{33}Ar RISING spectrum containing singles and addback events. 97
6.13 Experimental ^{33}Ar RISING spectrum containing singles events. 98
6.14 Experimental ^{33}Ar RISING spectrum containing addback events. . . . 98
6.15 Response of the RISING array without absorbers for simulations containing atomic background. 100
6.16 Response of the RISING array with absorbers for simulations containing atomic background. 101
6.17 Simulated absolute efficiency curve of the RISING array. 103
6.18 Experimental ^{33}Ar RISING outer rings spectrum containing singles and addback events. 103
6.19 Experimental ^{33}Ar RISING inner ring spectrum containing singles and addback events. 104
6.20 Fit of the ^{33}Ar RISING inner ring spectrum. 104
6.21 Fit of the experimental ^{36}Ar RISING spectra. 107
6.22 Fit of the experimental ^{33}Ar RISING spectra. 108
6.23 Determination of the high energy background multiplicity per simulated event. 110
6.24 Comparison between the simulated and experimental ^{36}Ar RISING spectra. 112
6.25 Final comparison between the simulated and experimental ^{36}Ar RISING spectra. 112
6.26 Final comparison between the simulated and experimental ^{33}Ar RISING spectra. 113
6.27 Comparison between the simulated and experimental ^{33}Ar RISING inner ring spectra. 114
6.28 Simulated raw and tracked ^{36}Ar AGATA spectra resulting from an input events file containing γ-rays of interest. 116

6.29 Simulated raw and tracked ^{33}Ar AGATA spectra resulting from an input events file containing γ-rays of interest. 117
6.30 Tracked AGATA spectra for simulations containing only atomic background. 120
6.31 Tracked AGATA spectra for simulations containing atomic background, γ-rays of interest and high energy background. 121
6.32 Simulated raw and tracked ^{36}Ar AGATA spectra resulting from an input events file containing high energy background and γ-rays of interest. 123
6.33 Simulated raw and tracked ^{33}Ar AGATA 5ATC+5ADC spectra resulting from an input events file containing high energy background and γ-rays of interest. 124
6.34 Simulated ^{33}Ar AGATA 5ATC+5ADC spectra and β distributions as the timing resolution of the scintillators are incremented from 25 ps to 75 ps. 127
6.35 Simulated ^{33}Ar AGATA 5ATC+5ADC spectra and β distributions as the timing resolution of the scintillators are incremented from 100 ps to 150 ps. 128
6.36 Tracked ^{36}Ar and ^{33}Ar AGATA spectra with an energy threshold of 100 keV applied to the packed interaction points. 131
6.37 Tracked ^{36}Ar and ^{33}Ar AGATA spectra with an energy threshold of 200 keV applied to the packed interaction points. 132
6.38 Tracked ^{36}Ar and ^{33}Ar AGATA spectra with an energy threshold of 300 keV applied to the packed interaction points. 133
6.39 Tracked AGATA spectra with packing and smearing disabled. 135
6.40 Comparison between the simulated RISING spectrum and tracked AGATA spectra for the ^{36}Ar setting. 137
6.41 Comparison between the simulated RISING spectrum and tracked AGATA spectra for the ^{33}Ar setting. 138

7.1 Extracted P/T and $\epsilon_{photopeak}$ values for the different simulated conditions for both fragment settings. 141
7.2 P/T and $\epsilon_{photopeak}$ values as a function of the atomic background multiplicity. 143

7.3 Effect of the timing resolution on the peak shape. 145
7.4 Comparison between the experimental ^{36}Ar and ^{33}Ar RISING spectra and the simulated tracked AGATA 5ATC+5ADC and 10ATC+5ADC spectra. 148
7.5 Simulated efficiency and P/T values of the 10ATC+5ADC, 5ATC+5ADC and 5ADC AGATA geometries with the inclusion of lead shielding. . 149
7.6 Current AGATA geometry at GSI. 152

List of Tables

2.1 Key properties of intrinsic silicon and germanium. 15
2.2 Simulated performance of the full AGATA array. 25
2.3 Comparison between the forward and backward tracking algorithms. . 29
2.4 OFT simulation results with the tracking of single hit interactions enabled. 30
2.5 Simulated efficiency and P/T values of the full AGATA array. 32

3.1 Ring positions and estimated performance of the RISING array. . . . 42
3.2 Summary of the MOCADI output. 48

4.1 Example of the production of the simulated high energy background. 65
4.2 Format of the input events file for the AGATA code. 67
4.3 Summary of the format of the list-mode output file produced by the AGATA code. 69
4.4 Summary of the detector resolutions included in the simulations. . . . 72

6.1 Summary of the FWHM, P/T and energy resolution values extracted from the experimental ^{36}Ar RISING spectra 109
6.2 Summary of the FWHM, P/T and energy resolution values extracted from the experimental ^{33}Ar RISING spectra. 109
6.3 P/T and $\epsilon_{photopeak}$ values extracted from the raw and tracked AGATA spectra for simulations containing no background. 118
6.4 P/T and $\epsilon_{photopeak}$ values extracted from the tracked AGATA spectra for simulations containing atomic background, γ-rays of interest and high energy background. 122
6.5 P/T and $\epsilon_{photopeak}$ values extracted from the raw and tracked AGATA spectra for simulations containing γ-rays of interest and high energy background. 125

6.6 FWHM values of the tracked ^{33}Ar peaks and β distributions for timing resolutions in the range 25-150 ps. 129
6.7 P/T and $\epsilon_{photopeak}$ values extracted from the tracked ^{33}Ar AGATA spectra with an energy threshold of 100 keV applied to the packed interaction points. 131
6.8 P/T and $\epsilon_{photopeak}$ values extracted from the tracked ^{33}Ar AGATA spectra with an energy threshold of 200 keV applied to the packed interaction points. 132
6.9 P/T and $\epsilon_{photopeak}$ values extracted from the tracked ^{33}Ar AGATA spectra with an energy threshold of 300 keV applied to the packed interaction points. 133
6.10 P/T and $\epsilon_{photopeak}$ values extracted from the tracked AGATA spectra with packing and smearing disabled. 135

7.1 Ratios between the P/T of the tracked AGATA spectra and the RISING spectra. 146

Acknowledgements

I would like to give a huge thanks to both my supervisors, Prof. Bob Wadsworth and Prof. Mike Bentley, for giving me the fantastic opportunity to study and further my interest in the fascinating field of nuclear physics. I have greatly appreciated their excellent guidance, encouragement and advice over the duration of my Ph.D. I owe an enormous thanks to Dr. Pankaj Joshi for his help with all aspects of my research, and for his company during overseas experiments. I am extremely grateful to the STFC for funding my Ph.D and to the University of York for all the opportunities I have had over the last few years.

I would like to extend my gratitude to all collaborators and researchers I have met during overseas experiments, conferences and workshops. Particularly, I would like to thank Andreas Wendt and Peter Reiter from the University of Cologne for providing me with the experiment S377 spectra.

It has been a pleasure working with all my fellow postgrads and academics at York, and I'd need to list the whole nuclear physics group to thank everyone who has helped me during some stage of my research! Particularly, I would like to thank all whom I shared an office with for the majority of my Ph.D: Lianne, Harith, Tim, Carine and Jack. I also owe a big thanks to Adam for proof reading my thesis.

I would like to thank all my friends at home for keeping me sane: Lee, Stunt Man, Tom, Math, the Bedwas crew, the Swansea crew, the music crew and a big 'shaka' to my surf butties - King and the Raging Potato!

I owe a massive thanks to my family for their continuous love, support and encouragement in all aspects of life: Mam, Dad, Brother Jon, Non, Lloyd, Nan, Sel and June. Nan and Sel - knowing how proud you were of my work kept me motivated right until the end. I would also like to give a huge thanks to my family in-law for all their love and support: Di, Sean, Cal, Pip, Lidj, Kait, Charles, Shirley, Doris and Fred.

Finally, I give all my love and a monumental thanks to my fiancé Kerry for her love, patience, and every kind of support since 2006. There are no words to express how grateful I am. On the 27th of January 2013, our little girl Evie Summer entered the world, which has been the most amazing experience of my life. I would also like to mention my dogs, Twiglet and Bryn, who joined our family during the beginning of my Ph.D who always keep me highly entertained. Diolch o galon!

Declaration

This thesis has been submitted for the degree of Doctor of Philosophy, in accordance with the regulations of the University of York. The work contained herein has not been previously submitted for any other degree or qualification. I declare that the work presented in this thesis, except where otherwise stated, is my own research under the supervision of Prof. R. Wadsworth and Prof. M. Bentley.

Signed:

Daniel Bloor

September 2013

Dedicated to Selwyn Thomas Bloor (1935-2013), Patricia Mary Bloor (1937-2013) and June Margaret Born (1939-2013).

Chapter 1

Introduction

The Advanced GAmma Tracking Array (AGATA) is a next generation 4π γ-ray spectrometer built as a major improvement to existing 4π arrays such as Euroball [1], Miniball [2] and Gammasphere [3]. The AGATA spectrometer, combined with the new generation of Radioactive Ion Beam (RIB) facilities, will allow for advances and insights into the nuclear structure of exotic nuclei. The full AGATA array will consist of 180 highly segmented High Purity Germanium (HPGe) crystals operated in position sensitive mode, and the success of the spectrometer will largely rely on the performance of the γ-ray tracking codes and Pulse Shape Analysis (PSA).

AGATA is to be utilised at a variety of European laboratories for use with different beams and ancillary detectors. The first AGATA campaign was held at INFN Laboratory Nazionali di Legnaro (LNL) where developments led to the construction of the AGATA 'Demonstrator', consisting of 5 x AGATA triple clusters (see figure 1.1). During 2012, AGATA was shipped to the GSI laboratory in Germany for its second physics campaign to take advantage of the relativistic beams provided by the FRagment Separator (FRS) (see chapter 3).

The GRETA [4] γ-ray tracking array, which is the US equivalent of AGATA, will consist of 120 individual detectors compared to the 180 of the full AGATA array. The initial phase of the GRETA array, known as GRETINA [5], is the equivalent of the AGATA demonstrator that operated at LNL. GRETINA was initially hosted at Michigan State University (MSU) where it completed its first physics campaign, and is currently being shipped to Argonne National Laboratory for use with the Caribou RIB source.

Figure 1.2 illustrates the improved sensitivity of the full AGATA array, compared

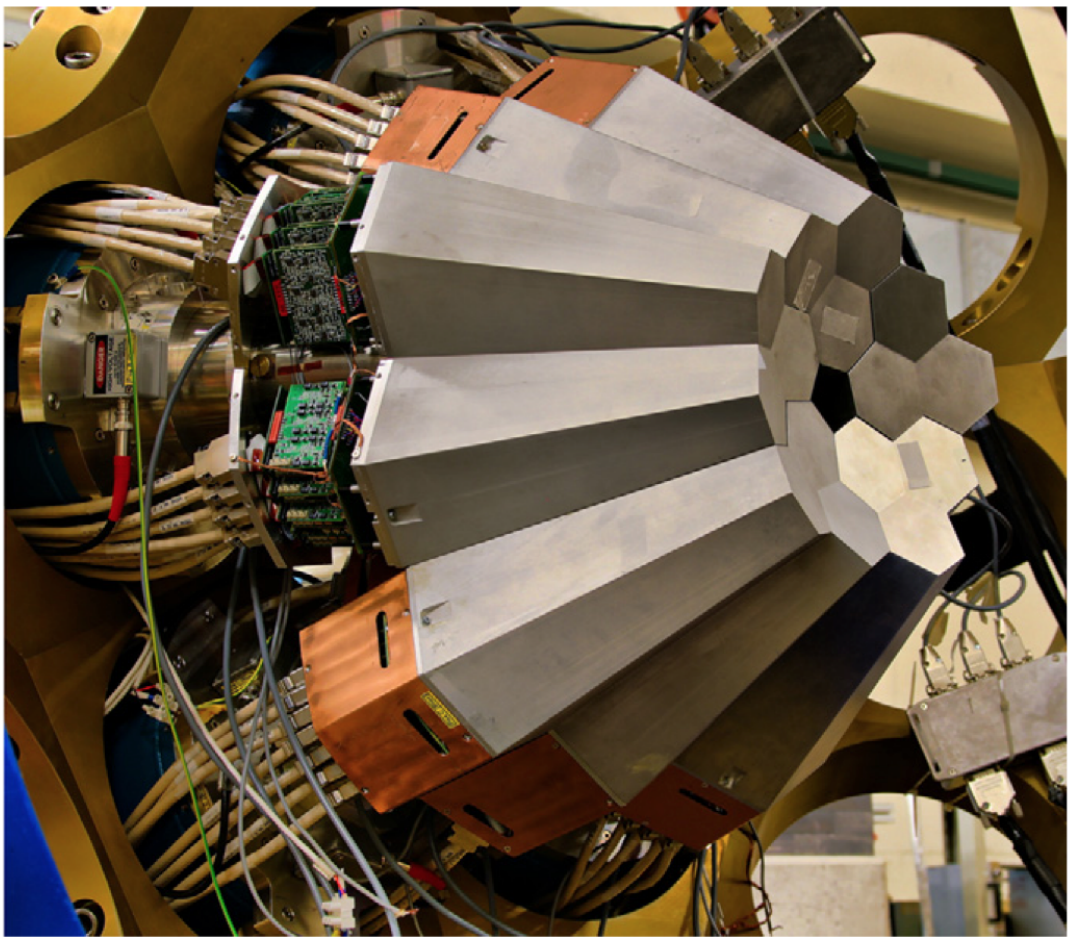

Figure 1.1: A photograph of the AGATA Demonstrator at LNL consisting of 5 triple clusters. Figure taken from reference [6].

with existing arrays, in the ability of detecting the weakest signals from exotic nuclear events. The techniques and developments leading to the construction of AGATA will have a wide range of applications in fields such as medical imaging, astrophysics, nuclear safeguards and radioactive waste monitoring, and the array will be the next platform for nuclear structure studies combined with new Radioactive Ion Beam (RIB) facilities [7].

1.1 Thesis Overview

Following a successful physics campaign at LNL, the AGATA detectors have been shipped to GSI during 2012 for an experimental campaign. The AGATA detectors will be combined with the initial test phase of the Lund-York-Cologne-CAlorimeter [8] (known as LYCCA-0) to take advantage of the available RIBs provided by the

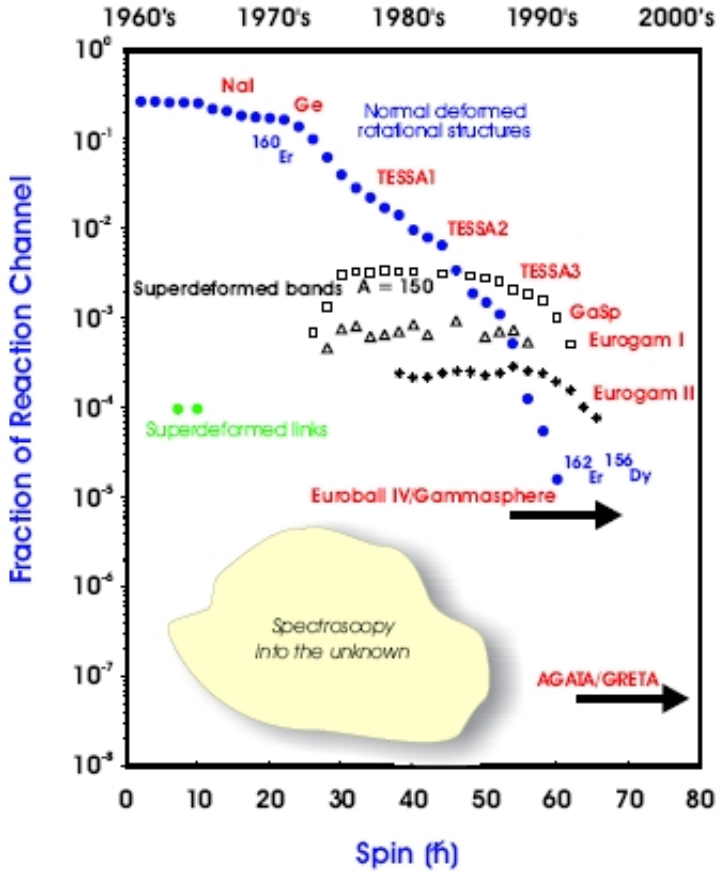

Figure 1.2: The sensitivity of the various spectrometers at detecting a percentage of the reaction channel as a function of spin. The full AGATA array will be able to detect the weakest of exotic nuclear events and will be enhanced up to a factor of 1000 compared to its predecessors. Figure taken from reference [7].

FRagment Separator (FRS) facility (see chapter 3). The primary goal of this thesis is to develop simulation tools to enable an investigation to be carried out on the spectral response of the AGATA array at GSI, in combination with LYCCA-0 as an ancillary detector. An existing simulation package [9] is currently available to simulate the response of AGATA and the spatial profile of the RIBs at GSI, however, many key components are not considered by this package, such as the high levels of background present in the relativistic environment, and the ability to track the heavy ions leaving the reaction target using LYCCA-0. The reconstruction of the simulated events in the previously existing package is performed without γ-ray tracking and is instead performed with an 'addback' technique (see section 3.4). Expanding on the work of reference [10], the key objectives of this thesis were to:

1. Develop a method of external event generation for relativistic Coulomb excitation and secondary fragmentation reaction processes for use as an input to the AGATA detector response code [11].

2. Implement LYCCA-0 as an ancillary detector within the AGATA code to allow for heavy ion tracking following the secondary target.

3. Investigate the spectral response of AGATA and the performance of the Orsay Forward Tracking (OFT) and Mars Gamma Tracking (MGT) codes in a relativistic environment.

In order to achieve the goals listed above, a recent relativistic Coulomb excitation PreSPEC experiment (experiment S377 in May 2011) was simulated, where the RISING [12] array was used in conjunction with LYCCA-0. The aim of the experiment was to determine the $B\left(E2; \frac{3}{2}^{+} \rightarrow \frac{1}{2}^{+}_{g.s}\right)$ and $B\left(E2; \frac{5}{2}^{+} \rightarrow \frac{1}{2}^{+}_{g.s}\right)$ values for the decay of the 1359 keV and 1798 keV states in ^{33}Ar. However, in this thesis a key goal was to investigate the spectral response of the RISING array. Once a satisfactory comparison between the simulated and experimental RISING spectra was achieved, the RISING array was replaced by the 5 x AGATA Triple Cluster (ATC) + 5 x AGATA Double Cluster (ADC), and the 10ATC+5ADC AGATA geometries in the simulations, in order to compare the performance of both configurations with the RISING results under the exact same conditions.

Chapter 2 gives an overview of γ-ray detection and the basic theory needed to provide an understanding of the operation and characteristics of the AGATA detectors, and the relevant interaction mechanisms crucial to the operation of the γ-ray tracking algorithms. An overview of the γ-ray tracking technique is also provided. Chapter 3 outlines the setup at the GSI facility to provide knowledge on how the various components of the simulations correspond to their experimental counterparts. The existing simulation tools used to simulate components of the setup at GSI are discussed, and how these are used in the current work. Chapter 4 discusses the development of the simulation tools and the various stages of the simulation process, beginning with the event generation of relativistic reaction processes through to the event processing/reconstruction stage. Chapter 5 presents simulation work relating to the AGATA at LNL campaign, where an investigation was performed on the effect of position smearing on the γ-ray tracking. Chapter 6 discusses the

experiment S377 spectra and a comparison with the RISING simulations. The response of AGATA is then investigated under the same conditions as determined from the RISING simulations, and the performance of both the OFT and MGT tracking codes are investigated in a variety of simulated conditions. The effect of the timing resolution of the plastic scintillators on the peak shape is also investigated. Finally, the performance of AGATA at GSI and conclusions of the investigations are discussed in Chapter 7, in addition to an outlook on the future work relevant to this research.

Chapter 2

γ-ray Detection and Theory

This chapter provides an overview of γ-decay theory, followed by an overview of the interaction mechanisms in which γ-rays interact with matter and how semiconductor detectors are used to provide a spectroscopic response to the ionised radiation. The design and characteristics of the AGATA array are discussed and an overview of the γ-ray tracking technique is provided.

2.1 Gamma Decay

γ-rays are electromagnetic radiation that are emitted following the decay of a nucleus from an initial quantum state to another, resulting from a radioactive decay (α or β) or nuclear reaction that left the nucleus in an excited state. Following the emission of a γ-ray from an initial state, i, to a final state, f, in a nucleus at rest with mass, M_0, the nucleus recoils with a momentum equal and opposite to the γ-ray with the kinetic energy of the recoiling nucleus given as [13]:

$$T_R = \frac{E_\gamma^2}{2M_0c^2}. \tag{2.1}$$

From conservation of energy, the energy difference between the initial and final states can be expressed as:

$$\Delta E = E_\gamma + T_R. \tag{2.2}$$

The recoil term is generally negligible compared to the uncertainty in which energies can be measured experimentally, and the γ-ray energy can therefore be assumed as:

$$E_\gamma = \Delta E = E_i - E_f. \tag{2.3}$$

An emitted γ-ray carries away angular momentum, $\vec{L}$, such that the transition from a state with angular momentum, $\vec{J}_i$, to a state with angular momentum, $\vec{J}_f$, results in the relation $\vec{J}_f = \vec{L} + \vec{J}_i$. The allowed values of angular momentum carried away by the photon is given as:

$$|J_i - J_f| \leq L \leq J_i + J_f, L \neq 0. \tag{2.4}$$

The value of L determines the multipolarity of the γ-radiation and parity selection rules state whether the transition is of electromagnetic (E) or magnetic (M) type:

$$\pi(ML) = (-1)^{L+1}, \tag{2.5}$$

$$\pi(EL) = (-1)^{L}. \tag{2.6}$$

Following a transition, if parity remains unchanged between states ($\pi_i = \pi_f$), the radiation must be M1, E2, M3, E4, and if parity changes ($\pi_i \neq \pi_f$), the radiation must be E1, M2, E3, M4. The angular momentum values, J_i and J_f, often permit the emission of several multipoles, each with different probabilities. Typically, the lowest permitted multipole dominates [13].

The decay rate, λ, between nuclear states depends on the matrix element of the multipole operator:

$$m_{fi}(\sigma L) = \int \psi_f^* \, m(\sigma L) \, \psi_i \, dv. \tag{2.7}$$

The purpose of the multipole operator, $m(\sigma L)$, is to change the nuclear state from ψ_i to ψ_f, whilst creating a photon of the appropriate energy, parity and multipole order [13]; σ represents the type of radiation (either E or M) and L represents the multipolarity (e.g. $L = 2$ is quadrupole). By evaluating the theory of electromagnetic radiated power from multipoles, an expression for the decay rate, i.e. the probability per unit time for photon emission, is obtained:

$$\lambda(\sigma L) = \frac{2(L+1)}{\epsilon_0 \hbar L[(2L+1)!!]^2} \left(\frac{\omega}{c}\right)^{2L+1} B(\sigma L). \tag{2.8}$$

The quantity, $B(\sigma L)$, is called the reduced transition probability and is related to the matrix element of the multipole operator as follows:

$$B(\sigma L) = |m_{fi}(\sigma L)|^2. \tag{2.9}$$

The reduced transition probability is a quantity that can be measured experimentally and gives direct information on the wavefunctions of the initial and final nuclear states.

Equation 2.8 can be expressed in reduced forms [14]:

$$\lambda(E1) = 1.587 \times 10^{15} E_\gamma^3 \, B(E1) \tag{2.10}$$

$$\lambda(E2) = 1.223 \times 10^{9} E_\gamma^5 \, B(E2) \tag{2.11}$$

$$\lambda(E3) = 5.698 \times 10^{2} E_\gamma^7 \, B(E3) \tag{2.12}$$

$$\lambda(M1) = 1.779 \times 10^{13} E_\gamma^3 \, B(M1) \tag{2.13}$$

$$\lambda(M2) = 1.371 \times 10^{7} E_\gamma^5 \, B(M2) \tag{2.14}$$

$$\lambda(M3) = 6.387 \times 10^{0} E_\gamma^7 \, B(M3), \tag{2.15}$$

where λ is the transition rate in units of s^{-1}. The units of E_γ are MeV, the units of B(EL) are $e^2 fm^{2L}$, and the units of B(ML) are $\mu_N^2 fm^{2L-2}$.

The $B(\sigma L)\downarrow$ and $B(\sigma L)\uparrow$ values for the de-excitation and excitation of a nuclear state are related as follows:

$$B(\sigma L)\downarrow = \frac{2J_i + 1}{2J_f + 1} \, B(\sigma L)\uparrow, \tag{2.16}$$

where J_i is the lower state and J_f is the higher state.

Simple estimates of the reduced transition probability can be obtained by evaluating the single-particle Weisskopf estimates. Assuming that the transition is the result of a single proton changing between shell-model states, the following simplified expressions for the single particle $B(\sigma L)_{sp}$ values are obtained [14]:

$$B(E1)_{sp} = 0.06446 \, A^{\frac{2}{3}} \tag{2.17}$$

$$B(E2)_{sp} = 0.05940 \, A^{\frac{4}{3}} \tag{2.18}$$

$$B(E3)_{sp} = 0.05940 \, A^{2} \tag{2.19}$$

$$B(M1)_{sp} = 1.7905 \tag{2.20}$$

$$B(M2)_{sp} = 1.6501 \, A^{\frac{2}{3}} \tag{2.21}$$

$$B(M3)_{sp} = 1.6501 \, A^{\frac{4}{3}} \tag{2.22}$$

where A is the mass number. The units of B(EL) are $e^2 fm^{2L}$ and the units of B(ML) are $\mu_N^2 fm^{2L-2}$. Experimentally measured transition rates can then be compared to the Weisskopf estimates to provide insight on the collective nature of a transition, which in turn can provide information on the single particle structure of the states involved.

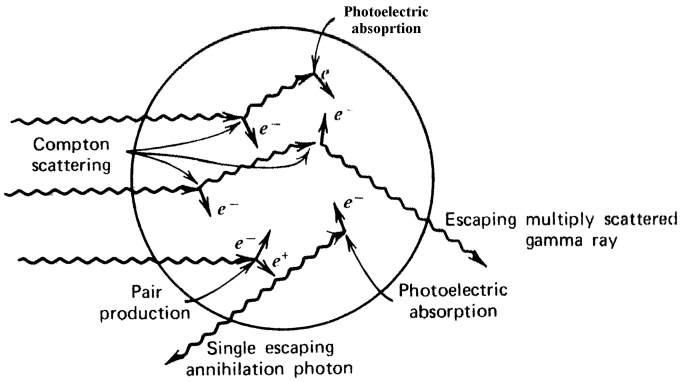

Figure 2.1: The schematics of the three interaction processes within an intermediate sized γ-ray detector, such as for example an individual AGATA crystal. See text below for details of the interaction mechanisms. Figure taken from reference [15].

2.2 γ-ray Interaction Mechanisms

As photons are massless and charge free, the interaction of γ-rays with matter occurs via the transfer of energy from an incident γ-ray to atomic electrons in an absorbing material through scattering or absorption. Radiation detectors such as semiconductor detectors and scintillators detect the ionisation produced via the mechanisms discussed below. The three main γ-ray interaction mechanisms important for radiation detection in the energy region 1 keV to 10 MeV are: photoelectric absorption, Compton scattering and pair production. Figure 2.1 displays a drawing of an intermediate sized γ-ray detector and the schematics of the three interaction mechanisms. For a beam of collimated mono-energetic photons, the attenuation of the beam may be expressed as:

$$I(x) = I_0\, exp(-\mu\, x), \tag{2.23}$$

where I_0 is the incident beam intensity, x is the thickness of the absorber, and μ is the linear attenuation coefficient. The linear attenuation coefficient represents the probability that a fraction of the incident beam of photons is scattered or absorbed per unit length of the absorber by one of the interaction mechanisms listed above. The total linear attenuation is given by the sum of the attenuation coefficients due to each individual interaction mechanism:

$$\mu_{total} = \mu_{photoelectric} + \mu_{Compton} + \mu_{pair}. \tag{2.24}$$

Figure 2.2 illustrates how each interaction mechanism depends on the energy of

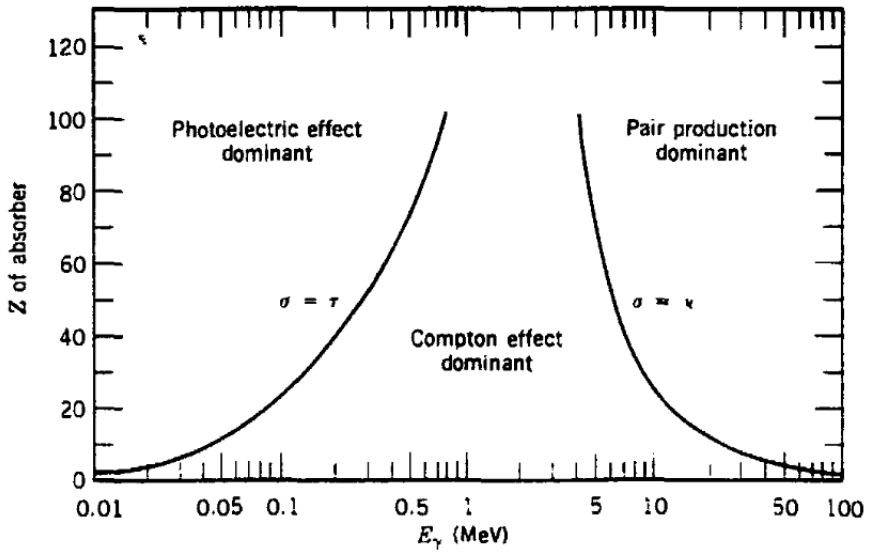

Figure 2.2: The dependence on the atomic number, Z, of the absorbing material and the incident photon energy, E_γ, of the three main γ-ray interaction mechanisms. Figure taken from reference [13].

the incident γ-ray and also on the atomic number of the absorber medium.

2.2.1 Photoelectric Absorption

Photoelectric absorption is the mechanism where a photon is absorbed by an atomic electron; the electron (or photoelectron) is then ejected from the atom. The process is most likely to occur on tightly bound K-shell electrons. Following the emission of a photoelectron, the absorber atom is left ionised; a free electron is then captured by the vacancy in the ionised atom resulting in the emission of x-rays. The kinetic energy of the photoelectron can be expressed as the difference between the initial photon energy and the binding energy of the photoelectron in its original shell:

$$E_e = E_\gamma - B_e, \tag{2.25}$$

where E_γ is equal to hv, h is Planck's constant and v is the frequency of the photon. The effect is usually dominant for low energy photons, typically $\sim$100 keV. The probability of the photoelectric effect is roughly proportional to Z^4 or Z^5 of the absorber atom [15]. The Z dependence makes high Z materials such as lead favourable for γ-ray shielding. In germanium ($Z = 32$), photoelectric absorption is the dominant interaction mechanism for energies up to $\sim$0.2 MeV (see figure 2.2).

2.2.2 Compton Scattering

The Compton scattering process occurs when an incident photon is deflected through an angle θ as it interacts with a loosely bound atomic electron in the absorbing material, resulting in a less energetic photon and a scattered electron, known as a recoil electron. The recoil electron carries away the energy lost by the photon. Applying energy and momentum conservation, the following expression can be obtained for the energy of the scattered photon in terms of the incident photon [15]:

$$E'_{\gamma} = \frac{E_{\gamma}}{1 + \frac{E_{\gamma}}{m_0 c^2}(1 - cos\,\theta)}. \tag{2.26}$$

The kinetic energy of the recoil electron is given as [15]:

$$E_{e^-} = hv \left(\frac{(hv/m_0c^2)(1 - cos\,\theta)}{1 + (hv/m_0c^2)(1 - cos\,\theta)} \right). \tag{2.27}$$

The energy transferred to the recoil electron varies from $\sim$0 at $\theta \cong 0$ to a large portion of the original γ-ray energy at $\theta = \pi$. In the latter case, the γ-ray is backscattered towards its original direction and the recoil electron recoils along the direction of the incident γ-ray; this results in the Compton edge which is often visible for intense γ-rays in a γ-ray spectrum. The cross section of Compton scattering increases linearly with Z and is the dominant interaction mechanism in germanium between $\sim$0.2 MeV and $\sim$8 MeV (see figure 2.2).

The differential cross section of scattered γ-rays can be predicted by the Klein-Nishina equation [15]:

$$\frac{d\sigma}{d\Omega} = Z r_0^2 \left(\frac{1}{1 + \alpha(1 - cos\,\theta)} \right)^2 \left(\frac{1 + cos^2\,\theta}{2} \right) \left(1 + \frac{\alpha^2 (1 - cos\,\theta)^2}{(1 + cos^2\,\theta)[1 + \alpha(1 - cos\,\theta)]} \right) \tag{2.28}$$

where $\alpha = hv/m_0c^2$ and r_0 is the classical electron radius of r_0=2.82 fm. For high energy incident γ-rays (2 MeV-10 MeV), the distribution favours forward scattering.

Rayleigh scattering can also occur, which is the mechanism where a photon scatters off an atom without any transfer in energy, although the incidence direction is modified. The Rayleigh scattering mechanism can be considered negligible at relatively high energies of x-rays and γ-rays [16].

2.2.3 Pair Production

The pair production mechanism is energetically possible and restricted to when the energy of the incident γ-ray is at least twice the rest mass of an electron ($2m_0c^2$),

i.e. 1.022 MeV or above. An incoming γ-ray is absorbed in the Coulomb field of a nucleus and is replaced by an electron-positron pair. Any additional kinetic energy above the 1.022 MeV supplied by the incident γ-ray is shared amongst the electron and positron. As the positron slows down in the absorbing medium, the positron annihilates with an electron and two annihilation photons of energy 511 keV are emitted. The probability of pair production increases roughly with Z^2 of the absorber medium and is the dominant interaction mechanism in germanium above $\sim$8 MeV (see figure 2.2).

2.3 Semiconductor Detectors

Semiconductor materials, such as germanium, are favourable as γ-ray detectors as they provide superior energy resolution compared to scintillator detectors such as NaI(Tl). This is due to the low average energy required to generate an electron-hole pair (2.96 eV in germanium), resulting in a large number of charge carriers generated per incident photon. The cross section for photoelectric absorption is proportional to Z^4, making germanium ($Z = 32$) an ideal candidate for high resolution γ-spectroscopy.

Crystalline semiconductor materials exhibit an energy band structure that defines allowed energy levels for the electrons to reside. The energy band structure arises from the overlap of electron wavefunctions due to the periodic arrangement of atoms in a crystal [16]. The properties of the energy band structure give rise to the electrical characteristics of the material.

The valence band, which is the lowest band, consists of the outer shell electrons that are bound to lattice atoms within a crystal. The conduction band, which is the highest band, consists of unbound electrons that are free to migrate throughout a crystal which contributes to the conductivity of the material. The gap between each band, known as the forbidden gap or bandgap, is a region where there are no available energy levels. The width of the gap determines whether the material is an insulator ($\sim$5eV or more) or semiconductor ($\sim$1eV).

When a valence electron is excited to the conduction band, a hole is left in the valence band; the combination is known as an electron-hole pair. At room temperature, electron-hole pairs are generated in germanium as electrons are excited to the conduction band due to thermal energy, leaving holes in the valence band. Neigh-

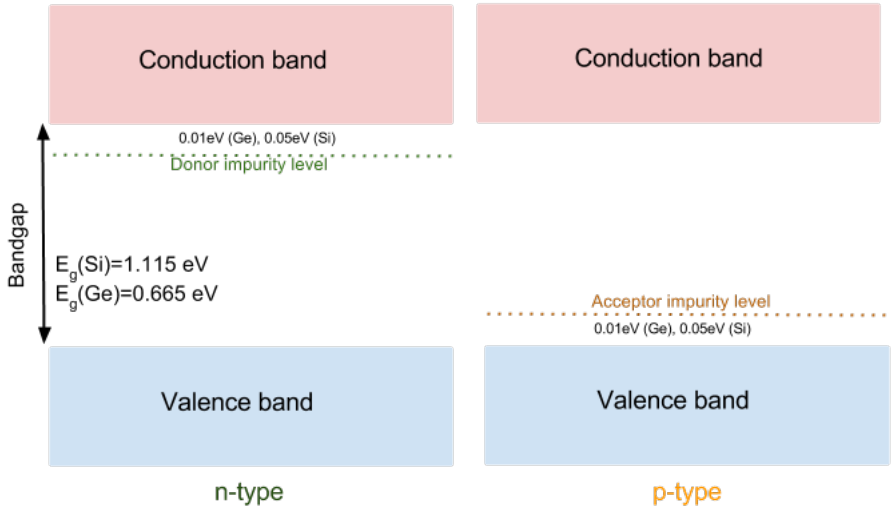

Figure 2.3: A schematic drawing of the energy band structure for n-type and p-type semiconductors.

bouring electrons in the valence band can then fill the holes, leaving holes in their original position. An electric current is therefore observed due to the movement of free electrons in the conduction band, and also the movement of holes within the valence band, which act as positive charge carriers. As a consequence, semiconductor detectors are often operated as a reversed bias diode in order to remove free charge carriers. One limitation to germanium is that cooling is required to reduce the leakage current resulting from thermal electrons. As charged radiation passes through a semiconductor detector, many electron-hole pairs are generated along the path of the incident particle. In the presence of an external electric field, the electrons and holes migrate in opposite directions parallel to the direction of the electric field, which are collected on electrical contacts where the electric signal can then be read out.

In a pure (intrinsic) semiconductor, the number of electrons in the conduction band is equal to the number of vacant holes in the valence band. Naturally, a small concentration of impurity atoms will be present in a semiconducting material, or intentionally added during the fabrication process; a process known as doping. There are two types of doped semiconductor (also known as extrinsic semiconductor): n-type and p-type, and the energy band structure for each type is displayed in figure 2.3.

The operation of a semiconductor detector is based on the characteristics of a semiconductor junction, known as an np junction, which is formed when n-type and p-type semiconductor material are brought together in good thermodynamic contact. In such a configuration, an initial diffusion of electrons across the junction towards the p-type material occurs where they combine with holes, leaving immobile positive charges behind as ionised donor impurities. Similarly, an initial diffusion of holes across the junction towards the n-type material occurs, leaving behind acceptor sites that will gain an extra electron resulting in immobile negative charge/ionised acceptor impurities. The resulting effect is a gain in net positive charge on the n side of the junction and a net negative charge on the p side of the junction, forming an electric field. The electric field eventually stops the net diffusion across the junction, forming a region of immobile charge carriers, known as the depletion region. The depletion region extends into both the n and p sides of the junction and any electron-hole pairs generated within the region are swept out by the electric field. The best operating characteristics for radiation detection is achieved by applying a reverse-bias voltage to the junction. This has the effect of enlarging the depletion width, thus increasing the sensitive volume for radiation detection, and the higher voltage provides more efficient charge collection. The thickness of the depletion region is given as [15]:

$$d = \left(\frac{2\epsilon V}{eN}\right)^{\frac{1}{2}}, \tag{2.29}$$

where ϵ is the dielectric constant, V is the reverse bias voltage, and N is the net impurity concentration. Using equation 2.29, for a net impurity concentration of 10^{10} atoms/cm^3, a depletion depth of 10 mm is obtained when a reverse bias of 1000 V is applied to the detector. The maximum voltage is limited by the resistivity of the detector; for a given voltage it is possible to further increase the depth of the depletion region by lowering the net impurity concentration. The AGATA crystals are constructed of n-type high purity germanium (HPGe) with an impurity concentration specified to be between 0.4 and 1.8×10^{10}atoms/cm^3 [6]. The net impurity concentration determines the electrical conductivity of the detector. For larger net impurity concentrations, the conductivity increases as the resistivity decreases. For low impurity concentrations of 10^{10} atoms/cm^3 or less, the need to cool the detectors without the presence of an applied voltage is removed. Some of the key properties of intrinsic silicon and germanium are highlighted in table 2.1.

	Si	Ge
Atomic Number	14	32
Atomic Weight	28.09	72.60
Density [g cm^{-3}]	2.33	5.32
Atoms/cm^3	4.96×10^{22}	4.41×10^{22}
Forbidden Energy Gap (300K) [eV]	1.115	0.665
Forbidden Energy Gap (0K) [eV]	1.165	0.746
Intrinsic Carrier Density (300K) [cm^{-3}]	1.5×10^{10}	2.4×10^{13}
Intrinsic Resistivity (300K) [Ω cm]	2.3×10^{5}	47
Electron Mobility (300K) [cm^2/Vs]	1350	3900
Electron Mobility (77K) [cm^2/Vs]	2.1×10^{4}	3.6×10^{4}
Hole Mobility (300K) [cm^2/Vs]	480	1900
Hole Mobility (77K) [cm^2/Vs]	1.1×10^{4}	4.4×10^{4}
Energy per electron-hole pair (300K) [eV]	3.62	-
Energy per electron-hole pair (77K) [eV]	3.76	2.96

Table 2.1: A table displaying some of the key properties of intrinsic silicon and germanium semiconductor materials. Table adapted from reference [15].

2.4 Outline of γ-ray Spectroscopy

γ-ray spectroscopy is one of the most effective ways of studying the structure of excited nuclear states. For example, the study of a γ-ray spectrum shows the energies and intensities of the transitions between the various nuclear states for a given nucleus, and coincidence measurements can give insight into the possible arrangement of the excited states [13]. Figure 2.4 displays a typical γ-ray spectrum labelled with the important features of the spectrum.

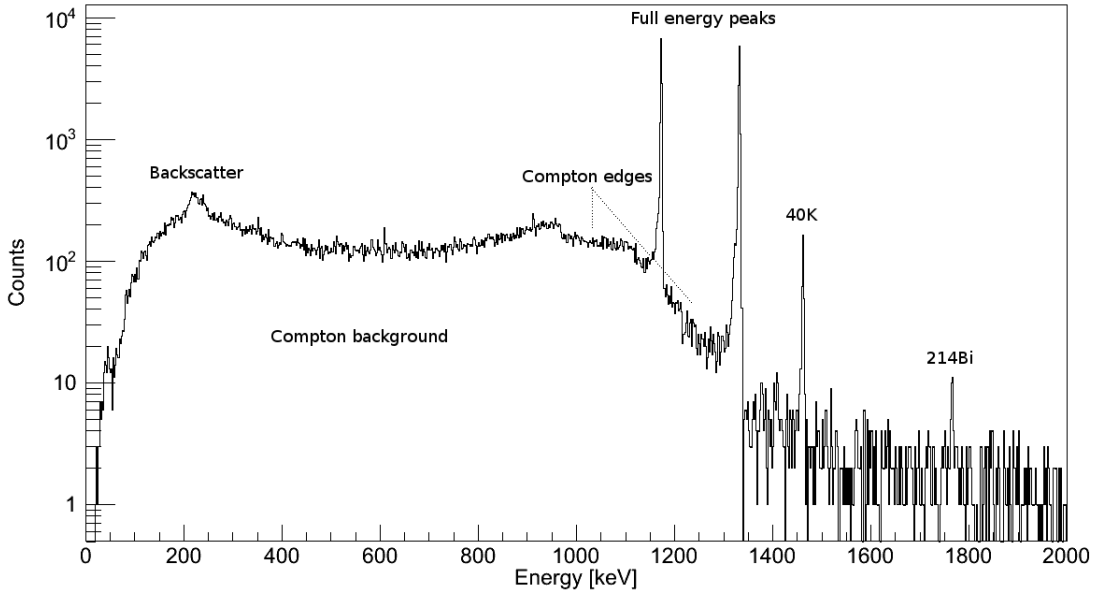

Figure 2.4: A ^{60}Co γ-ray spectrum recorded with 2ATCs. The features labelled on the spectrum correspond to the interaction processes discussed in section 2.2. The Compton background is present due to γ-rays partially depositing their energy and then scattering out of the detector volume. The full energy peaks can be seen at 1173.2 keV and 1332.5 keV. The backscatter peak occurs when photons are scattered through the largest possible scattering angle ($\theta \simeq \pi$) in material surrounding the detector, which are then absorbed in the detector. The Compton edges are present due to the maximum transfer of energy from the incident photon to the recoil electron. The backscatter peak and Compton edge can be determined from equation 2.26; for the 1332.5 keV peak, the backscatter peak occurs at $\sim$214 keV and the Compton edge at $\sim$1118 keV. Photopeaks are also visible at 1460 keV (^{40}K) and 1765 keV (^{214}Bi) resulting from natural background radiation.

Energy resolution is an important quantity in γ-spectroscopy and reflects the

ability of a detector to measure the energy of an incident γ-ray. A delta-function peak is desired, however, in reality the energy peak will have a finite width due to contributions from various factors. The energy resolution can either be expressed as the full width at half maximum height (FWHM) of the peak, or as a fraction:

$$\frac{FWHM}{H_0} = R, \tag{2.30}$$

where H_0 is the peak centroid. A NaI(Tl) detector typically has a resolution of $\sim$8/9% for γ-rays of 1 MeV, whereas germanium detectors have resolutions of the order of 0.2% [16]. Due to the excellent energy resolution of germanium, they are especially preferred in high γ-multiplicity experiments since to resolve an energy peak, it is required that they are separated by an energy greater than their FWHM.

The full-energy peaks in a γ-ray spectrum can be approximated as a Gaussian shape with width, σ. Such a distribution centred around an energy, E, can be written:

$$f(x) = A\, exp[\frac{-(x-E)^2}{2\sigma^2}], \tag{2.31}$$

where A is a normalisation constant, σ is the width parameter (also the standard deviation of the distribution), and E is the mean energy. It can be shown that the FWHM is related to σ by the following relation [16]:

$$FWHM = 2.35\,\sigma. \tag{2.32}$$

A number of external factors can affect the overall energy resolution of a detector, such as noise and drifts in the electronics, and fluctuations in the ionisation process as γ-rays interact with the detector [16]. Assuming that all the additional sources of error contributing to the energy resolution are independent and are of Gaussian form, the total resolution of a detector is written:

$$(FWHM_{tot})^2 = (FWHM_{det})^2 + (FWHM_{elect})^2 + \ldots \tag{2.33}$$

In the GSI environment, one of the main contributions to the energy resolution is the effect of Doppler broadening (see section 2.5).

Other important quantities in γ-spectroscopy are the efficiency of the detector, and the peak-to-total ratio (P/T). Generally there are two types of efficiency that are commonly used in γ-spectroscopy; *absolute* efficiency and *intrinsic* efficiency [16]. The absolute efficiency is defined as the fraction of events emitted from a source that

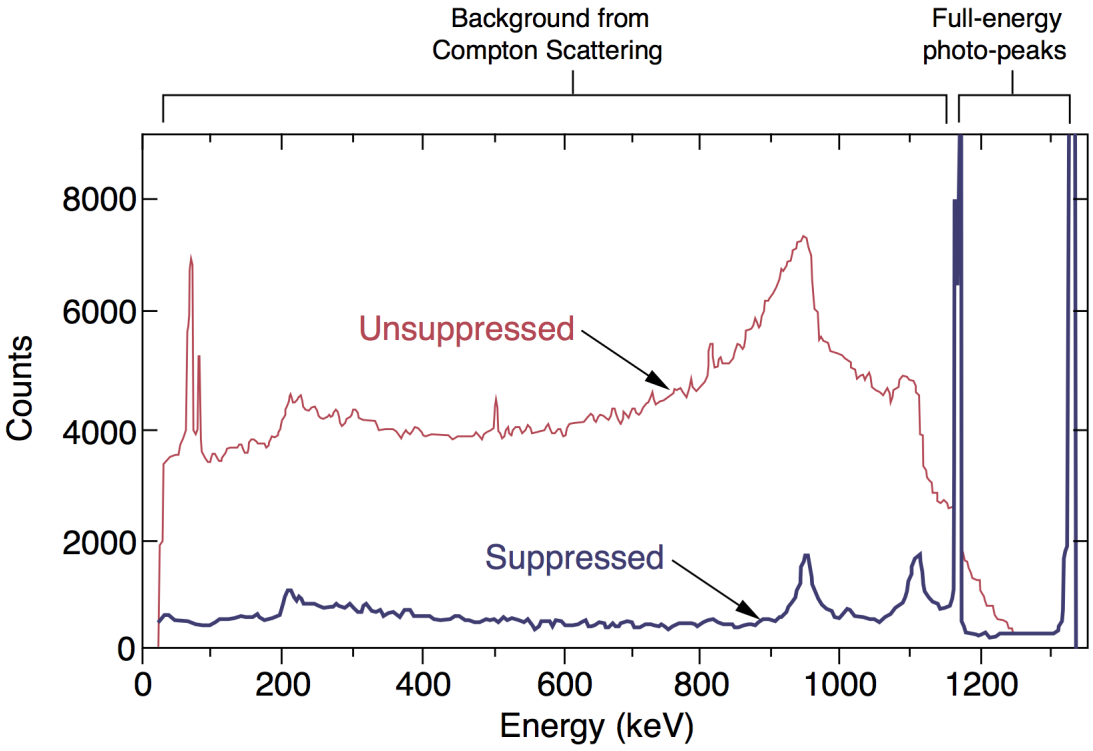

Figure 2.5: A ^{60}Co spectrum recorded with the Gammasphere array showing the effect of the suppression shields. Figure taken from reference [17].

is registered by the detector, and is written:

$$\epsilon_{abs} = \frac{events\ registered}{events\ emitted\ by\ source}. \tag{2.34}$$

The second type of efficiency is the intrinsic efficiency which represents the fraction of events that hit the detector which are then registered, and is written:

$$\epsilon_{int} = \frac{events\ registered}{events\ impinging\ on\ detector}. \tag{2.35}$$

The P/T ratio is an important measure as it represents the ratio between the total counts in a photopeak to the total counts in a γ-ray spectrum. The P/T value can be used to quantify the performance of the γ-ray tracking algorithms.

The P/T ratio can be increased by surrounding γ-ray detectors with Bismuth Germanate (BGO) scintillation detectors, known as a Compton suppression shields. Existing arrays such as Gammasphere [3] utilise the suppression shield technique to enhance the P/T ratio. For Gammasphere, the P/T ratio for 1.3 MeV γ-rays increases from 25% to 60% when suppression shields are used [17]. The spectral response of Gammasphere utilising suppression shields can be seen in figure 2.5.

Any γ-rays that are scattered out of the detector and detected in the surrounding BGO detector cause a veto signal to be sent to the data acquisition system (DAQ),

removing the event from the spectrum and reducing the Compton background. The advantage of this technique is that the background is greatly reduced since a large portion of the γ-rays that do not deposit their full energy in the detector volume are removed from the spectrum. As the shields cover a large portion of the germanium crystals, the total solid angle coverage of the detectors for a large array like Gammasphere is limited to $\sim$50% giving a 10% maximal efficiency for the detection of γ-rays of energy 1.3 MeV [7]. The full AGATA array, however, will consist solely of germanium with a solid angle coverage of 82%, yielding a much higher efficiency compared to existing 4π arrays. By utilising the γ-ray tracking technique, the need for Compton suppression becomes unnecessary, resulting in a greater efficiency whilst maintaining spectral response [6]. The full AGATA array will not be 100% efficient since pentagonal holes are left free on either side of the shell to allow for beam entry and exit ports. Additionally, there is a small spacing ($\sim$0.5 mm) between the flat surfaces of each crystal within an ATC.

Following a nuclear reaction, an excited product nucleus can recoil out of a thin reaction target causing γ-rays to be emitted mid flight. For non-relativistic recoil velocities, the emitted γ-rays will be Doppler shifted by an amount:

$$\frac{E_{\gamma}^{'}}{E_0} = (1 + \beta \, cos \, \theta) \, , \tag{2.36}$$

where $E_{\gamma}^{'}$ is the shifted energy in the laboratory frame, E_0 is the original energy in the rest frame and β is the velocity of the projectile. If uncorrected for, the energy peaks will become broadened, as well as shifted. Equation 2.36 is dependent on the projectile velocity, β, and more importantly the angle, θ, between the emitted γ-ray and the projectile. The AGATA array will consist of highly segmented crystals and the first interaction point of a γ-ray within a segment will be more accurately known than in existing arrays.

2.5 γ-ray Spectroscopy at GSI

At the GSI laboratory (see chapter 3), heavy ions following relativistic reaction processes can leave the reaction target with velocities $\beta \geq 0.4$ and with energies typically >100 MeV/u. Performing high resolution in-flight γ-spectroscopy in these conditions can be extremely challenging. In these conditions, large Doppler shift and Doppler broadening effects occur, in addition to unwanted nuclear reactions

and background resulting from atomic processes. Due to the Lorentz boost effect, the largest contribution to the efficiency is at extreme forward angles, however, this is where the Doppler shift effect is maximum. At small values of θ, the shifted energy can reach $\sim$1.7 times that of the rest frame energy for projectile velocities of $\beta = 0.47$. This effect, in addition to the energy resolution resulting from the Doppler broadening contributions is illustrated in figure 2.6. It is essential to track the heavy ions prior to and following the reaction target with the highest possible accuracy in order to determine the origin of the emitted γ-rays and to correct for these effects. The relativistic Doppler shift is defined as:

$$\frac{E_{\gamma}^{'}}{E_0} = \frac{\sqrt{1-\beta^2}}{(1-\beta\, cos\,\theta)}, \tag{2.37}$$

where $E_{\gamma}^{'}$ is the observed shifted γ-ray energy in the laboratory frame, E_0 is the γ-ray energy in the rest frame, and θ is the angle between the projectile and the detected γ-ray in the laboratory frame. The velocity of the projectile is defined:

$$\beta = \sqrt{1 - \frac{m_0^2 c^4}{(E_k + m_0 c^2)^2}}, \tag{2.38}$$

where E_k is the total kinetic energy of the projectile in the laboratory frame and m_0 is the rest mass of the projectile.

The quantities $E_{\gamma}^{'}$, β and θ must be accurately measured in order to correct and reduce the Doppler shift and Doppler broadening effects. The uncertainty in the determination of these quantities contributes to the Doppler broadening which affects the energy resolution, as illustrated in figure 2.6. The Doppler broadening resulting from the opening angle of a detector is defined as [12]:

$$\frac{\Delta E_0}{E_0} = \frac{\beta\, sin\,\theta_{\gamma}}{1-\beta\, cos\,\theta_{\gamma}}\,\Delta\theta_{\gamma}, \tag{2.39}$$

where the opening angle of a RISING crystal is estimated to be $\Delta\theta_{\gamma} = 2.9^{\circ}$ at a detection angle of θ_{γ}=15°.

Thick reaction targets ($\sim$4000 mg/cm^2) are often used at the final focal plane of the FRS where a projectile may decay within the target itself. This results in an uncertainty in the velocity, $\Delta\beta$. This mainly affects short-lived states with lifetimes of the order $\sim$ps [12]. The Doppler broadening due to the uncertainty in β is defined as [12]:

$$\frac{\Delta E_0}{E_0} = \frac{\beta - cos\,\theta_{\gamma}}{(1-\beta^2)(1-\beta\, cos\,\theta_{\gamma})}\,\Delta\beta. \tag{2.40}$$

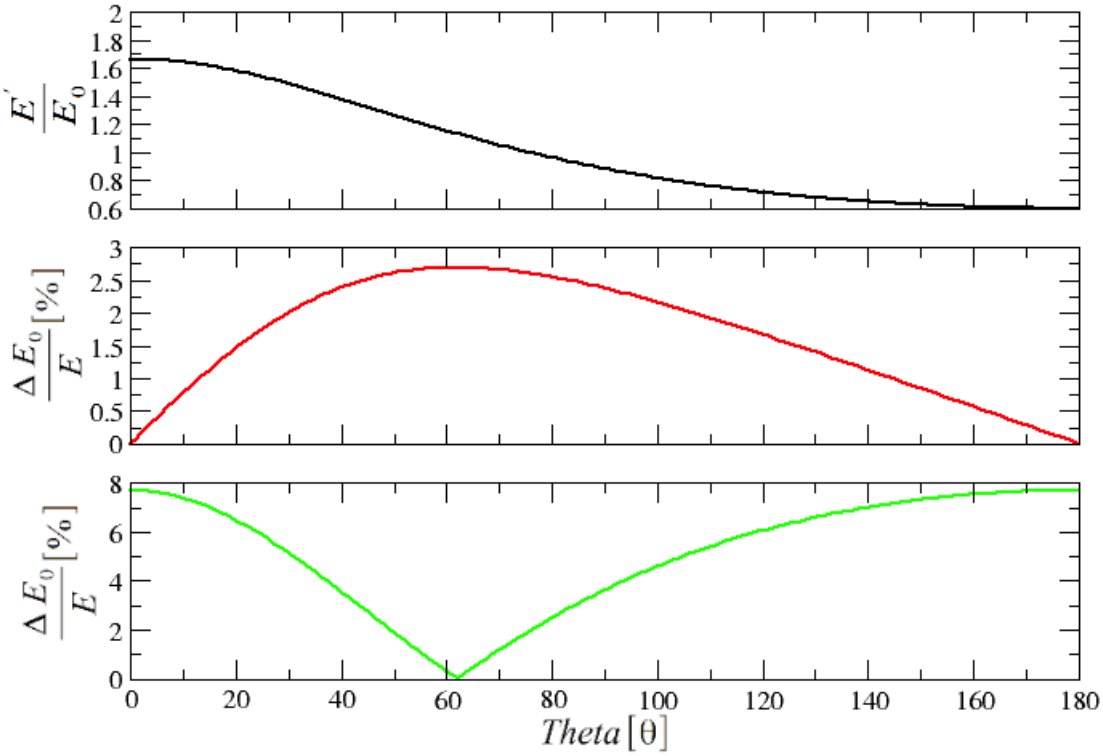

Figure 2.6: The top panel shows the shift of the observed γ-ray in the laboratory frame relative to the energy of the γ-ray in the rest frame as a function of θ_γ, which is the angle between the projectile and detected γ-ray in the laboratory frame. The middle panel shows the energy resolution due to the opening angle of a RISING crystal as a function of θ_γ for a value of $\Delta\theta$=2.9°, and the bottom panel shows the energy resolution due to the target thickness as a function of θ_γ for a value of $\Delta\beta = 6\%$. The projectile velocity in each case is β=0.47.

2.5.1 Atomic Background

Nuclear reactions involving relativistic heavy ions results in a background arising from atomic processes, generally with cross sections thousands of times greater than the reaction channel of interest. The origin and properties of the background is well understood (see references [18],[19] and [20]) and the four main processes contributing to the background are summarised below:

1. Emission of K and L x-rays from ionised target atoms: the process is charge dependent and the angular distribution of the emitted x-rays is isotropic. An energy vs. theta matrix in the laboratory frame resulting from an ^{36}Ar ABKG simulation (see subsection 4.2.4) containing target x-rays can be seen in figure 2.7. For the ^{36}Ar setting, the x-rays are discrete lines ranging between 67-80 keV

2. Radiative Electron Capture (REC): target electrons are captured into the projectile K and/or L shells. The process is charge dependent and the angular distribution has a dependence on $\sim sin^2\theta_\gamma$, where θ_γ is the angle between the emitted photon and the beam in the laboratory frame. An energy vs. theta matrix in the laboratory frame resulting from an ^{36}Ar ABKG simulation (see subsection 4.2.4) containing REC can be seen in figure 2.8. For the ^{36}Ar setting, the energy of the emitted x-rays ranges between ∼50-135 keV.

3. Primary Bremsstrahlung (PB): target electrons are scattered from the projectile nuclei. The angular distribution for PB has a dependence on $\sim sin^2\theta_\gamma(1-\beta\, cos\,\theta_\gamma)$ and the cross section has a dependence on $Z_p^2 Z_t$. An energy vs. theta matrix in the laboratory frame resulting from an ^{36}Ar ABKG simulation (see subsection 4.2.4) containing PB can be seen in figure 2.9. For the ^{36}Ar setting, PB results in a continuous energy distribution reaching up to ∼90 keV.

4. Secondary Electron Bremsstrahlung (SEB): energetic secondary electrons (hundreds of keV) following PB re-scatter with the target and/or surrounding matter. The angular distribution for SEB is isotropic and the cross section has a dependence on $Z_p^2 Z_t^2$. An energy vs. theta matrix in the laboratory frame resulting from an ^{36}Ar ABKG simulation (see subsection 4.2.4) containing SEB can be seen in figure 2.10. For the ^{36}Ar setting, SEB results in a continuous energy distribution reaching up to ∼320 keV.

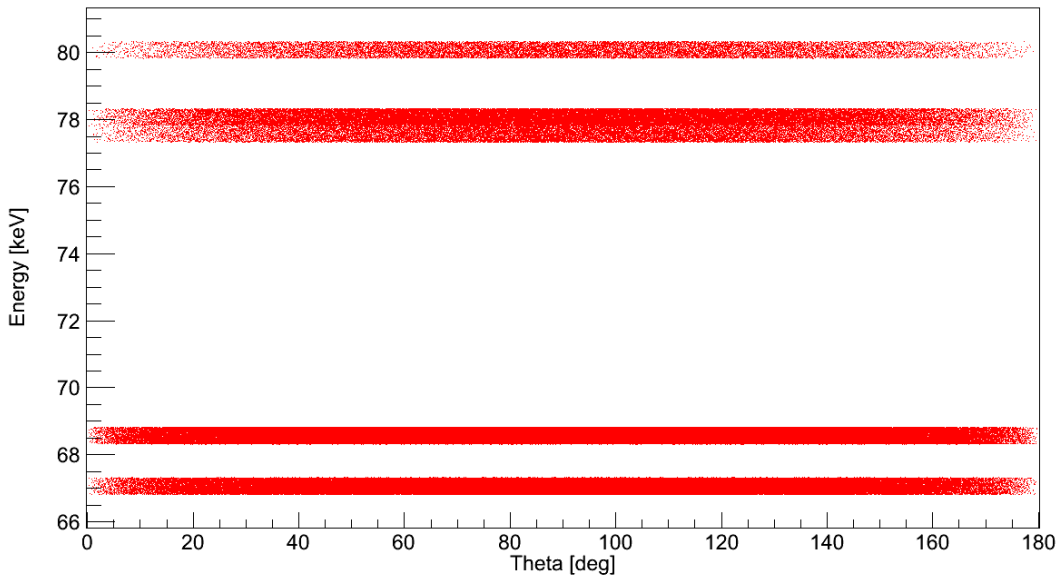

Figure 2.7: The energy vs. theta distribution (laboratory frame) resulting from an ABKG simulation (see subsection 4.2.4) containing target x-rays for the ^{36}Ar setting (experiment S377).

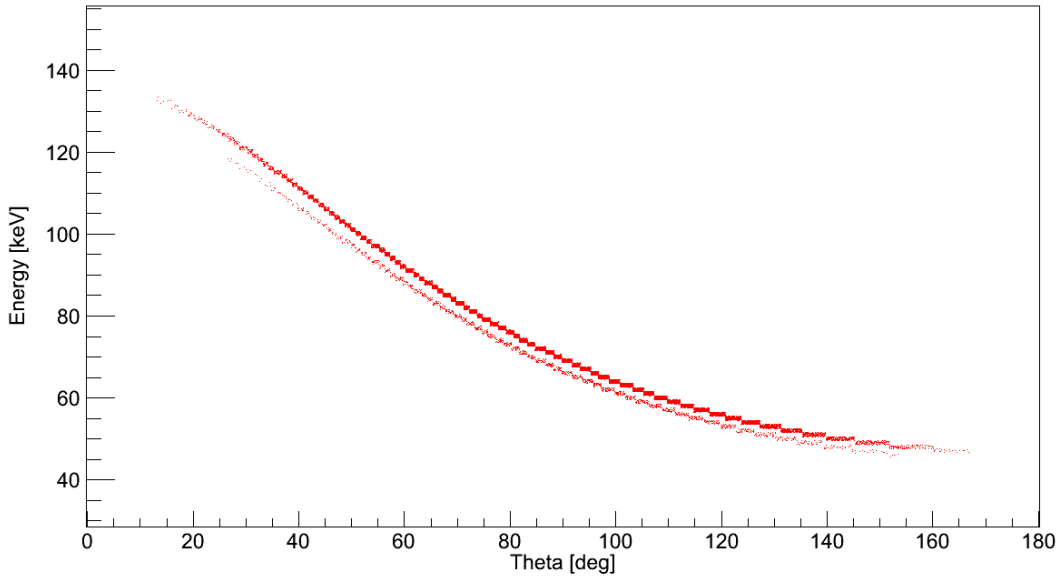

Figure 2.8: The energy vs. theta distribution (laboratory frame) resulting from an ABKG simulation (see subsection 4.2.4) containing REC for the ^{36}Ar setting (experiment S377).

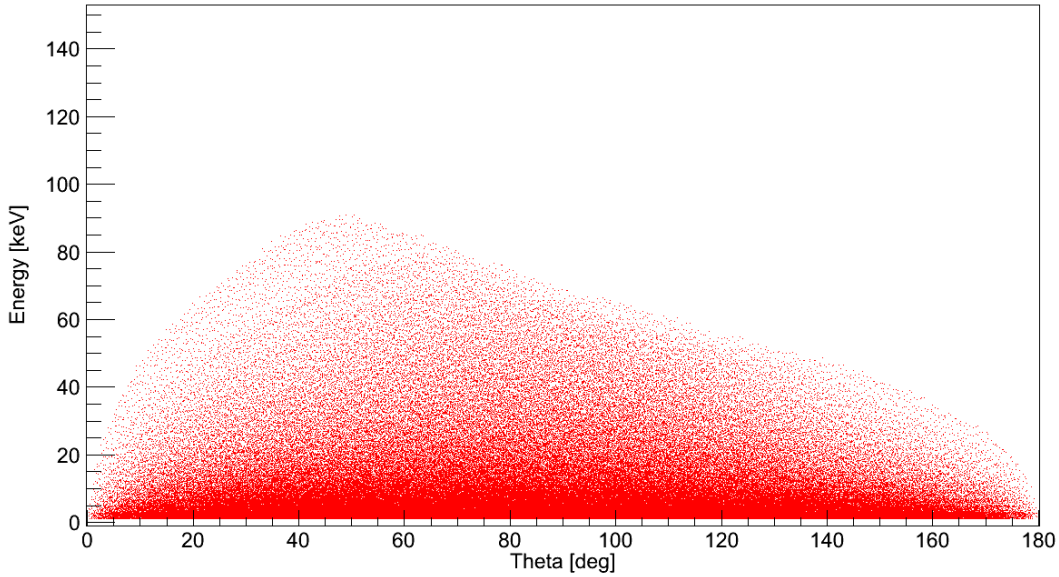

Figure 2.9: The energy vs. theta distribution (laboratory frame) resulting from an ABKG simulation (see subsection 4.2.4) containing PB for the ^{36}Ar setting (experiment S377).

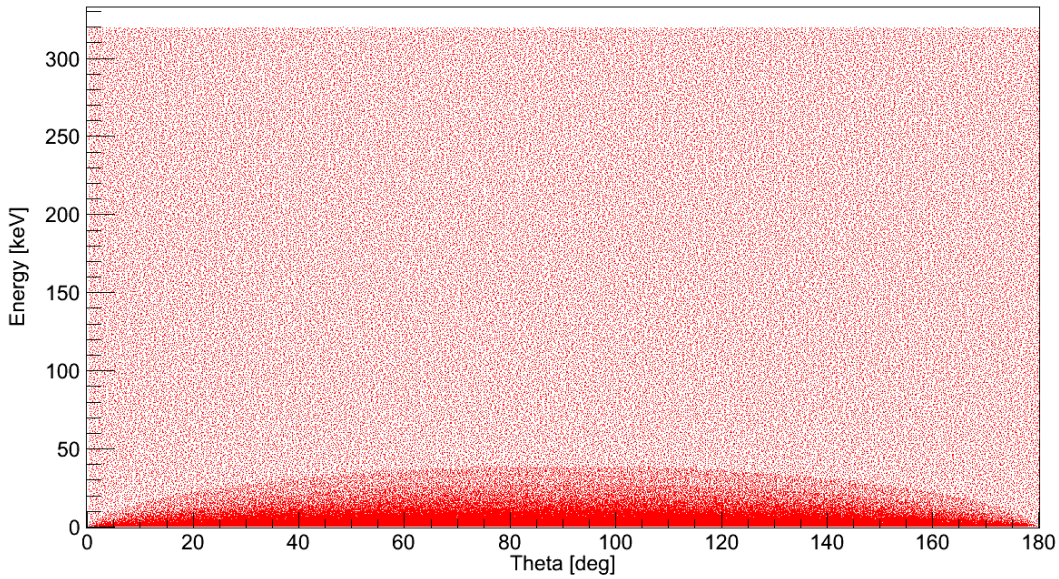

Figure 2.10: The energy vs. theta distribution (laboratory frame) resulting from an ABKG simulation (see subsection 4.2.4) containing SEB for the ^{36}Ar setting (experiment S377).

	$M_\gamma = 1$	$M_\gamma = 30$
Photopeak Efficiency [%]	43	28
P/T [%]	59	43

Table 2.2: The simulated performance of the 180 crystal geometry that covers a solid angle of 82%. The data represents a stationary source emitting 1 MeV γ-rays at different multiplicities (M_γ), placed at the centre of the array. The data were processed with the MGT tracking code. Data taken from reference [22].

2.6 The Advanced GAmma Tracking Array

2.6.1 Design of AGATA and Crystal Characteristics

Advancements in γ-spectroscopy can be achieved by removing the Compton suppression shields as used in current spectrometers, and building a 4π array composed solely from germanium. In order to maximize the solid angle coverage from the detectors, the concept of a pure spherical shell of germanium detectors was proposed. After testing different geometry configurations using Geant4 [21], and considerations such as the space required to include additional ancillary detectors in the setup, the optimised geometry of the full array was chosen based on the tiling of a sphere with 180 hexagons and 12 pentagons, where the 180 hexagons are grouped into 60 identical triple clusters. The performance of the optimised geometry is tabulated in table 2.2. Figure 2.11 illustrates the possible geometry configurations that were considered for the full AGATA array.

Each triple cluster consists of three germanium crystals, labelled: A/red, B/green and C/blue. The colour scheme of the crystals can be seen in figures 2.11 and 2.12. Each crystal is electronically segmented into 6 x 6 azimuthal and longitudinal independent segments and is tapered into three slightly different asymmetric hexagonal shapes at the front face of each crystal with a tapering angle of 8°. Figure 2.12 illustrates a drawing of the three asymmetric crystal geometries, which also shows the colour code for the crystals within the AGATA labelling convention.

Longitudinally the crystals are segmented into rings of 8, 13, 15, 18, 18 and 18 mm (beginning at the front face). Each crystal has a length of 90±1 mm and a rear diameter of $80^{+0.7}_{-0.1}$ mm. The longitudinal and azimuthal segmentation scheme and labelling convention can be seen in figure 2.13. Each crystal is encapsulated

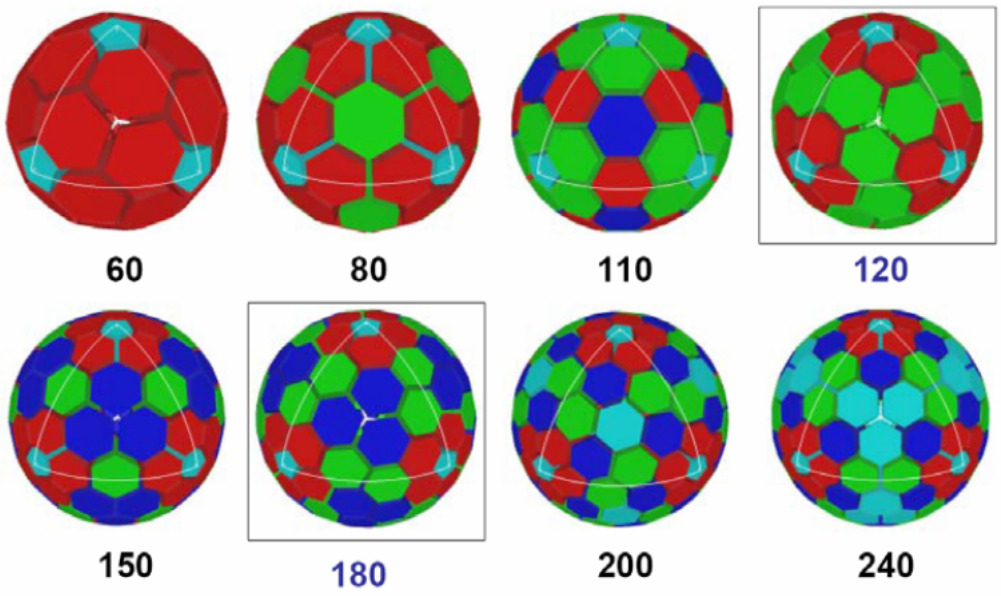

Figure 2.11: The various geometry configurations considered for the AGATA array. The two main configurations tested are enclosed in squares. The optimum tiling for the AGATA array consisted of 180 germanium crystals. The full GRETA [23] array will consist of 120 crystals with 4 crystals per cryostat. Figure taken from reference [7].

in a 0.8 mm thick aluminium casing and each triple cluster is housed by a cryostat which cools the germanium crystals to 90 K. The full germanium shell will be 9 cm thick, consisting of 363 kg of active germanium. The inner radius of the shell will be 22.5 cm, allowing sufficient space to mount additional ancillary detectors. The full array will have a solid angle coverage of 82%, leaving minimal dead spaces within the shell and thus providing high detection efficiency. The AGATA crystals are closed-ended coaxial shaped and the 36 fold electronic segmentation is obtained through separation of the outer contacts into six slices and six orthogonal sectors. The 36 segments share the inner core contact and therefore an AGATA crystal generates 36+1 signals (111 signals per ATC). The central hole of the crystal is isolated with ceramic material and has a diameter of 10 mm that extends to 13 mm from the front end. The outer p^+ contacts are produced through boron implantation and a Lithium diffusion technique is used to produce the n^+ contacts [24]. The boron implanted contact results in a dead layer of 0.3 μm and the Lithium diffusion process results in a dead layer of 0.6 mm.

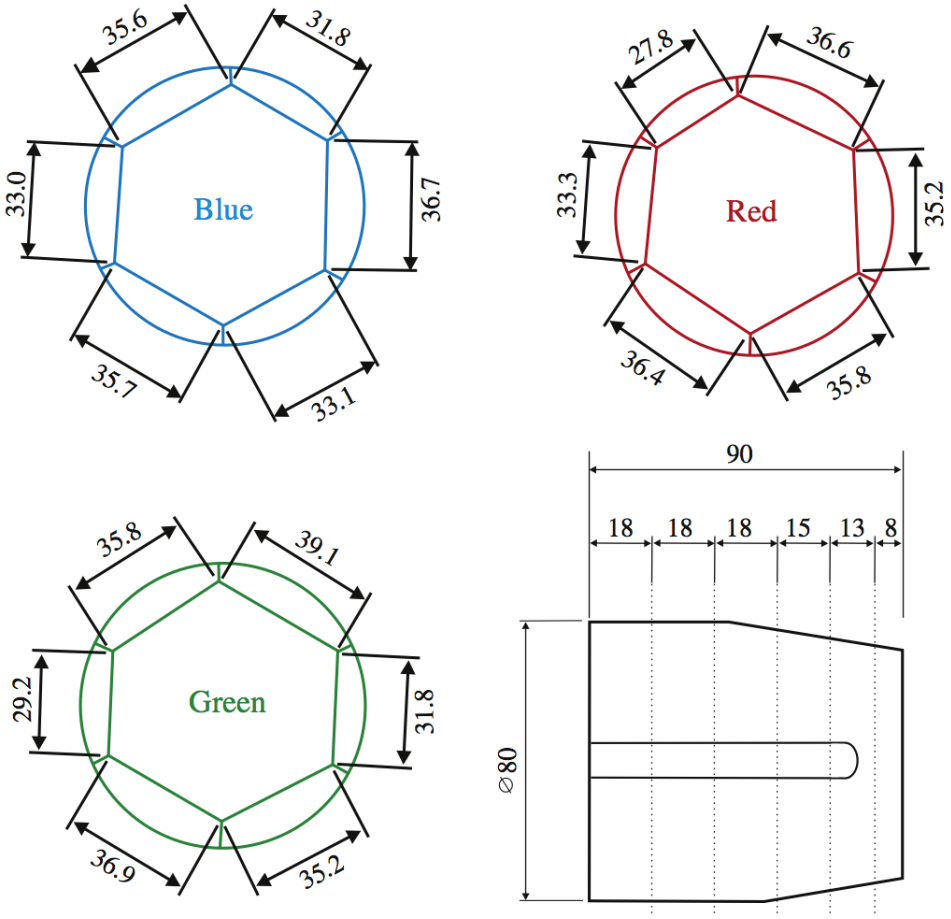

Figure 2.12: A drawing of the AGATA crystal geometries that form one triple cluster and a side view of a detector showing the position of the segmentation (bottom right). All dimensions are in mm. Figure taken from reference [6].

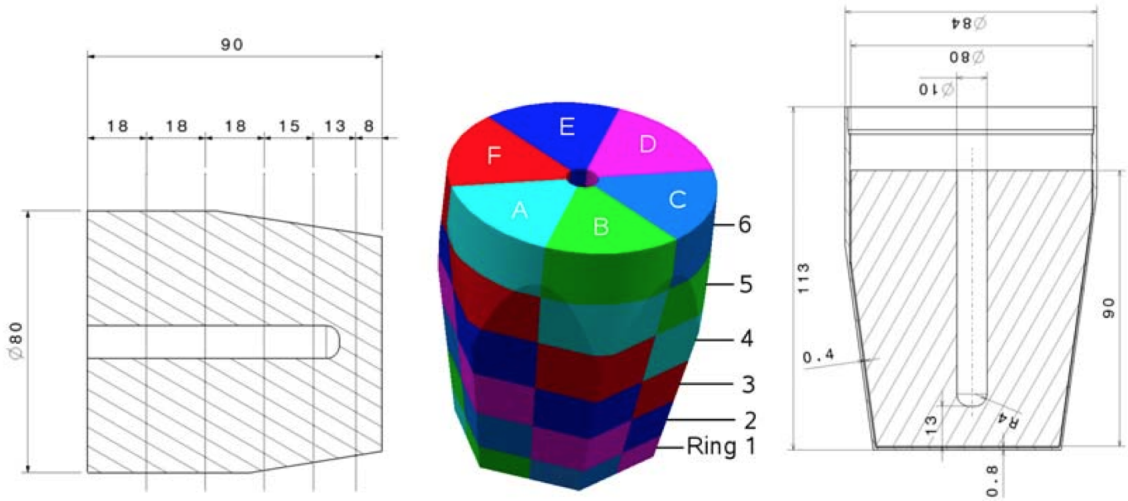

Figure 2.13: A mechanical drawing showing the azimuthal and longitudinal segmentation scheme and encapsulation for a crystal. All dimensions are in mm. Figure taken from reference [7].

2.6.2 γ-ray Tracking

The overall success of the spectrometer will be largely dependent on the performance of the Pulse Shape Analysis (PSA) and γ-ray tracking algorithms. The primary goal of the PSA is to identify the 3D positions and energy of each individual interaction point through detailed analysis of the detected waveforms.

After an AGATA crystal has passed the performance requirements and is accepted by the collaboration, a basis of waveforms from the detector response to γ-radiation is required. A basis is a database of the signal shapes produced by interactions throughout the volume of an AGATA crystal. Ideally, a basis would contain the measured detector response for each crystal, however, due to the amount of time required to characterise a detector, the full characterisation of a crystal can instead be calculated by solving the Poisson equation for the geometry of the detectors, and the boundaries of the electric field for a detector can be determined. Currently, two codes are used to calculate the basis for the AGATA detectors: a code named *Multi Geometry Simulation* (MGS) [25] and a code named *Java AGATA Signal Simulation* (JASS) [26]. Experimental pulse shapes can then be compared with the calculated basis to determine the energy and position of an interaction point.

With the determined energy and position of the interaction points, a tracking algorithm can be applied to reconstruct the scattered paths of the γ-rays. Investigations have been performed to test the performance of different types of algorithms such as back tracking and forward tracking. The back tracking algorithms begin by identifying the final photoelectric interaction point, based on the assumption that the photoelectric interaction occurs between an energy of $\sim$100 keV to 250 keV [27]. The forward tracking code is based on a different logic and begins by assigning the interaction points to clusters in (θ,ϕ) space. The forward tracking algorithm has been found to provide a better P/T ratio and photopeak efficiency than the back tracking algorithm for a range of γ-ray multiplicities [27] (see table 2.3). The tracking codes utilised in this thesis (Orsay Forward Tracking (OFT) [28] and Mars Gamma Tracking (MGT) [29]) are both based on forward tracking.

Two important parameters within the tracking codes are *packing* and *smearing*. Since there are difficulties with the PSA algorithms in the ability to identify two nearby interaction points, interactions separated less than a defined distance

	Forward Tracking		Back Tracking	
M_γ	Photopeak Efficiency [%]	P/T [%]	Photopeak Efficiency [%]	P/T [%]
1	53.6	75.2	36.7	67.4
15	42.2	63.1	27.3	53.7
30	35.8	56.8	23.4	46.9

Table 2.3: A comparison between the performance of the forward and backward tracking algorithms to cascades of 1.332 MeV γ-rays emitted at the centre of the full array for different γ-ray multiplicities, M_γ. Data taken from reference [27].

(d_{res}=5 mm by default) are packed together. Additionally, the positions of the interactions provided by the PSA have an associated uncertainty and this is accounted for in the tracking codes through smearing of the interaction points. For the OFT, the smearing is applied through sampling an energy-dependent Gaussian distribution with σ=1 mm by default.

The treatment of single hit interactions can affect the photopeak efficiency and P/T. When not included, the efficiency loss is very large at low energies as this will disregard many photoelectric absorption interactions. When single interactions are included, the P/T worsens at intermediate to high energies as there will be more counts in the lower energy region contributing to the total counts in the spectrum. Often, the tabulated performance figures between the MGT and OFT differ due to the treatment of single hit interactions; even though the OFT searches for single interaction points, it fails to reconstruct any single interaction photopeak events for γ-rays of 1.332 MeV, however, the OFT is capable of reconstructing single interaction photopeak events for γ-rays of 0.1 MeV (see table 2.4). As a result of the OFT being unable to reconstruct single interaction photopeak events for γ-rays of 1.332 MeV, the processing of single interactions is often disabled in the code which results in a higher P/T compared to the same data tracked with the MGT.

For a single hit interaction to be processed by the OFT, the interaction point must be isolated such that the nearest interaction point is $\geq$4 cm away. Additionally, the following quantity must be larger than the set threshold [27]:

- The probability of the incident photon reaching the determined interaction position in the detector volume $\times$ the probability of a photoelectric interaction.

Table 2.4 highlights two different cases where single γ-ray cascades of energies

	0.1 MeV	1.332 MeV
# of incident photons	3000	3000
# of photopeak events	3000	2109
# of single interaction photopeak events	2860	114
# of reconstructed photopeaks	2826	1583
# of reconstructed single interaction photopeaks	2763	0

Table 2.4: A table showing the simulation results from the OFT for two different cases where single γ-ray cascades of energies 0.1 MeV and 1.332 MeV were emitted at the centre of the full AGATA array with the processing of single hit interactions enabled. Data taken from reference [27].

0.1 MeV and 1.332 MeV were emitted at the centre of the full AGATA array. The table highlights how the number of reconstructed single hit interactions varies in each case.

The forward and back tracking algorithms are discussed in detail in [27] and [4]. The forward tracking begins by assigning angular coordinates (θ,ϕ) to all of the interaction points and the algorithm calculates the distance between the interaction points. The points are then clustered with respect to their relative angular distance governed by a threshold, α. For an initial interaction point, i, the next interaction point, j, is added to the same cluster as the first when the following condition is satisfied [27]:

$$|cos^{-1}\left(sin\theta_j \sin\theta_i cos(\phi_j - \phi_i) + cos\theta_i cos\theta_j\right)| \leq \alpha. \tag{2.41}$$

The same method is repeated for the remaining interaction points and any interaction points satisfying the condition above will be added to the cluster. In the case where [27]:

$$|cos^{-1}\left(sin\theta_j \sin\theta_i cos(\phi_j - \phi_i) + cos\theta_i cos\theta_j\right)| \geq \alpha, \tag{2.42}$$

the interaction point is assigned to a single interaction cluster. The clusterisation is then repeated for different values of α (by default, α=0.15-1.0 rad in increments of 0.1 rad). Following the completion of the clusterisation stage, n clusters are obtained containing between 1 to 6 interaction points in each. The energies of the interaction points within a cluster are then summed to give the energy, E_{tot}, of the incident γ-ray.

The next step is to calculate the figure of merit for each individual cluster. The figure of merit is a quantity used to determine the closeness of the scattered energies determined from equations 2.43 and 2.44 [27]. Beginning at the source location, the first interaction of a sequence is assigned i, and the second interaction as j. The scattered energy after i can be written:

$$E_{s,e} = E_{tot} - e(i), \tag{2.43}$$

and the incident energy prior to the scatter is denoted $E_t = E_{tot}$. The scattered energy can also be calculated from the Compton scattering equation:

$$E_{s,p} = \frac{E_t}{1 + \frac{E_t}{m_e c^2}(1 - cos\,\theta_p)}. \tag{2.44}$$

In equation 2.44, the value of $\cos\theta_p$ is determined from the source location and the interaction points i and j. The two methods of calculating the scattered energy are then compared and quantified by the following expression:

$$F_E = exp[-2\frac{(E_{s,p} - E_{s,e})^2}{\sigma_e^2}], \tag{2.45}$$

where F_E is the figure of merit and σ_e is the position uncertainty of the interaction points. For clusters containing two interaction points, the following statistics are used to quantify the optimum scattering path:

$$F_{s\to i\to j} = P(E_t)_{Comp} P(r_{s\to i}) P(E_{s,e})_{Photo} P(r_{i\to j}) F_E \tag{2.46}$$

$$F_{s\to i\to j} = P(E_t)_{Comp} P(r_{s\to i}) P(E_{s,e})_{Comp} P(r_{i\to j}) F_E, \tag{2.47}$$

where $P(E_t)_{Comp}$ is the probability for the incident photon to Compton scatter, $P(r_{s\to i})$ is the probability for the photon to travel the distance between the source position and interaction point i, $P(E_{s,e})_{Photo}$ is the probability for the scattered photon to undergo photoelectric absorption, $P(E_{s,e})_{Comp}$ is the probability for the scattered photon to undergo a Compton scatter, and $P(r_{i\to j})$ is the probability for the photon to travel the distance between interaction points i and j. Equations 2.45, 2.46 and 2.47 are applied to clusters containing two interaction points, however, for clusters containing more interaction points slightly different expressions are used (see reference [27] for further details).

Following the evaluation of all possible scattering paths within a cluster containing two interaction points, the sequence which maximises the total figure of merit, given as:

$$F_{tot} = (F_{s\to i\to j})^{1/(2j-1)}, \tag{2.48}$$

Algorithm	Efficiency (%)	P/T (%)
MGT	28(43)	49(58)
OFT	24(37)	54(68)

Table 2.5: The simulated efficiency and P/T for 1 MeV photons emitted at the centre of the full AGATA array for γ-ray multiplicities of M_γ=30 (and M_γ=1). Data taken from reference [7].

is taken as the correct sequence for the cluster.

The remaining clusters are then sorted into decreasing order in terms of the figure of merit and bad clusters are rejected. Single interaction clusters, if any, are processed at the end of the OFT tracking procedure. The tracking procedure above details the OFT [27].

To summarise the performance of the MGT and OFT tracking codes, table 2.5 shows the calculated efficiency and P/T of the tracking codes to 1 MeV photons emitted at the centre of the full AGATA array.

Additional tracking algorithms have been developed within the AGATA collaboration; one with a clustering technique based on Fuzzy C-Means [30] and another with a clustering method known as deterministic annealing (DAF) [31]. Neither are discussed in the scope of this thesis as the OFT and MGT are the key codes adopted by the collaboration.

The performance of the γ-ray tracking algorithms are previously untested under the experimental conditions at GSI. One of the key objectives in this thesis is to determine the performance of the two tracking codes, OFT and MGT, and the resulting spectral response of AGATA (see chapter 6).

Chapter 3

The GSI Accelerator Facility

The following chapter provides an overview of the facilities at GSI Helmholtzzentrum für Schwerionenforschung GmbH [32] (GSI) followed by an overview of the existing simulation tools that are often used to simulate the passage of the ions through the FRS and following the secondary target. At GSI, secondary Radioactive Ion Beams (RIBs), produced from fragmentation of the primary beam, are focused onto a secondary target at the final focal plane of the FRagment Separator (FRS), where two key types of reactions can be performed: relativistic Coulomb excitation and secondary fragmentation. The heavy ions travel at relativistic velocities, introducing large Doppler shift and Doppler broadening effects, and also initiate a variety of atomic background processes, making γ-ray spectroscopy in these conditions extremely challenging. A schematic drawing of the facilities at GSI is displayed in figure 3.1. The reaction mechanisms (see section 3.1), the use of MOCADI (see section 3.6), and the RISING (see section 3.4) and LYCCA (see section 3.5) detector configurations discussed in the current chapter are key components of the simulation process detailed in chapter 4.

3.1 Reaction Mechanisms

The main nuclear reactions performed at the secondary target of the FRS are projectile fragmentation and relativistic Coulomb excitation.

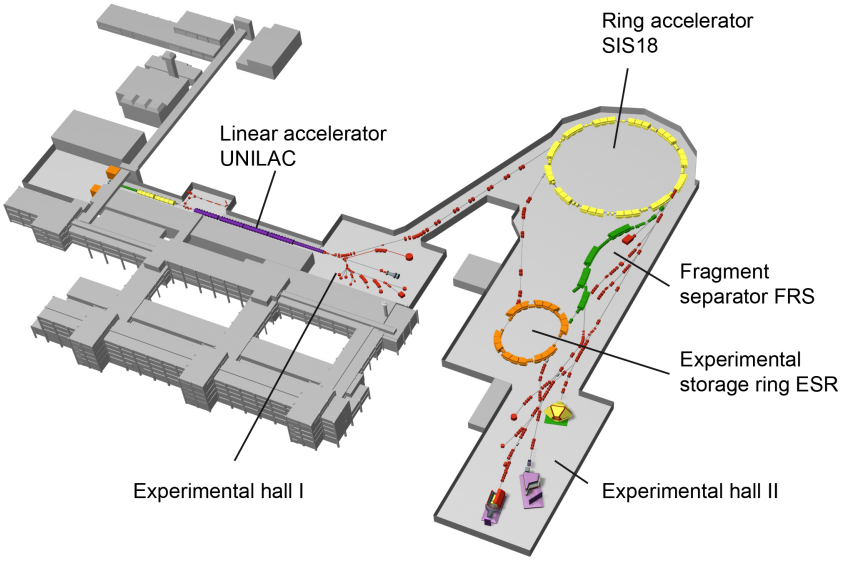

Figure 3.1: A schematic drawing of the accelerator facility at GSI. The acceleration of the heavy ions begins with the UNIversal Linear ACcelerator (UNILAC). Following the initial acceleration, the heavy ions are injected into the SchwerIonen-Synchrotron (SIS-18) for further acceleration. The accelerated ions are then either delivered to the Experimental Storage Ring (ESR), or to the primary target at the entrance to the FRS. The FRS separates ions of interest from the secondary beam, and following the FRS is the experimental area where the various detector systems such as LYCCA and RISING/AGATA are located. Figure taken from reference [32].

3.1.1 Projectile Fragmentation

The projectile fragmentation process is well described by the Abrasion-Ablation (ABRABLA) model [33] and can be split into two distinct phases. The process occurs at the primary target and similarly at the secondary target for a secondary fragmentation reaction. During the first stage (abrasion), based on the impact parameter, the interacting nucleons in the geometric overlap between the the projectile and target (known as 'participators') abrades nucleons from either nucleus. The non-overlapping areas (known as 'spectators') form prefragments that gain excitation energy and continue their trajectory at a similar velocity as prior to the interaction. The typical timescale of the first stage is of the order 10^{-23} s.

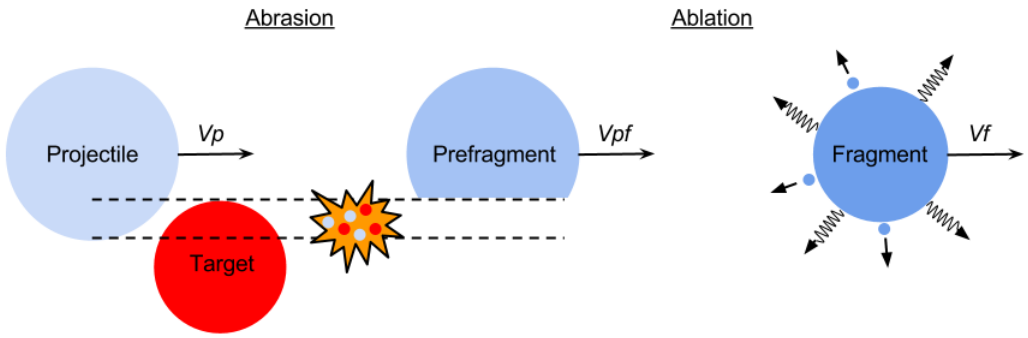

Figure 3.2: A schematic diagram of the projectile fragmentation reaction process. See text for details.

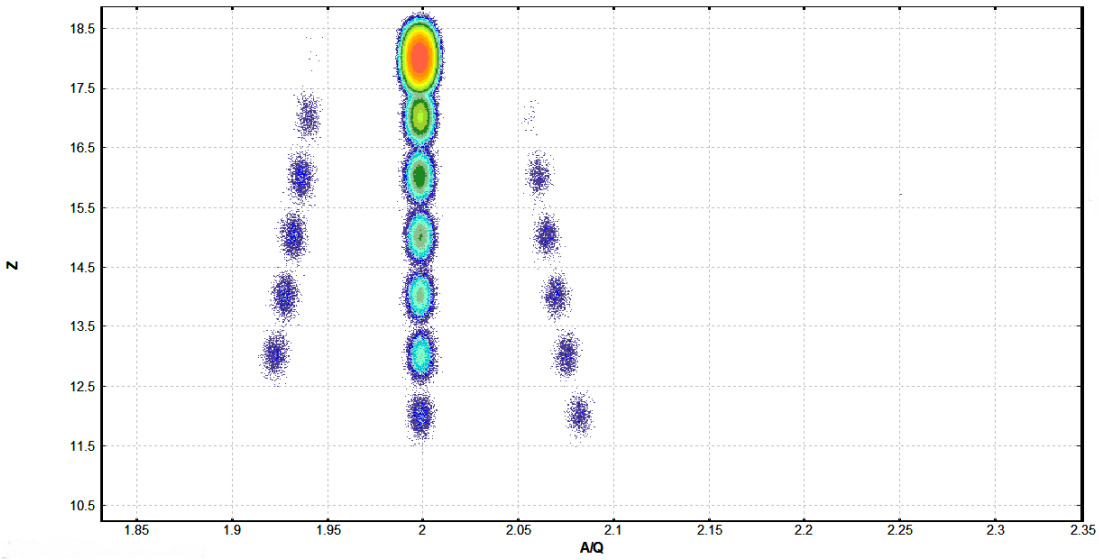

Figure 3.3: A simulated LISE++ Z vs. A/Q identification plot showing the range of isotopes created during a fragmentation reaction. The data represents the primary beam setting for experiment S377 where an ^{36}Ar beam (energy of 450 MeV/u and intensity of 2×10^{10} pps) is impinged onto a 4000 mg/cm^2 thick ^{9}Be target. The ^{36}Ar ions are represented by the intense region in the plot (Z=18, A/Q=2). The LISE++ file used to create the plots was taken from reference [34].

Following the abrasion stage, the projectile spectators (prefragments) de-excite by statistical evaporation of light particles and the emission of γ-rays. The typical time-scale of the evaporation process is of the order $10^{-16} - 10^{-21}$ s dependent on the excitation energy. Figure 3.2 illustrates the projectile fragmentation process.

Following a fragmentation reaction, a cocktail of fragments is typically created with different yields of each, as illustrated in figure 3.3. By identifying the outgoing

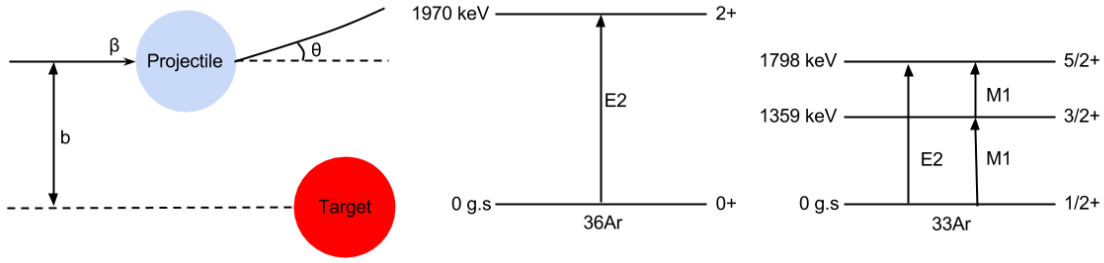

Figure 3.4: A schematic diagram of the Coulomb excitation process. The projectile with velocity, β, inelastically scatters off the target resulting in the population of a low-lying state in the projectile (or target). The notation, b, represents the impact parameter and θ is the scattering angle. The right-hand side shows the nuclear level diagrams for the peripheral ^{36}Ar and ^{33}Ar nuclei, which would be selected at extremely forward scattering angles for relativistic Coulex, corresponding to a large impact parameter, b.

fragments from the secondary target using LYCCA, it is possible to select, or 'gate', on fragments of interest which suppresses other reaction channels and reduces the corresponding atomic and high energy background.

3.1.2 Relativistic Coulomb Excitation

Coulomb excitation (Coulex) is an inelastic scattering process in which a nucleus excites another nucleus via the electromagnetic interaction. A simple schematic diagram of the process can be seen in figure 3.4. The technique has been widely used to investigate the excitation energies of low-lying states in exotic nuclei and the corresponding electromagnetic transition matrix elements B($\pi\lambda$) [35]. In low energy Coulex, stable targets are bombarded with heavy ions at energies well below the Coulomb barrier ('safe' energies) which prevents any excitation processes resulting from the nuclear force. At intermediate and relativistic energies, such as that of the secondary beams used at GSI, the energy of the projectiles are much greater than the repulsive Coulomb barrier, and for small impact parameters, the projectile and target nuclei will interact via the nuclear force. Unwanted nuclear reactions occur and the projectile is scattered at large angles. In order to suppress unwanted nuclear reactions, the peripheral reaction products following the secondary target (recorded in coincidence with γ-rays) are selected at extreme forward scattering angles ($\leq 3°$ at GSI [12]), corresponding to a larger impact parameter.

The Coulex cross section is proportional to Z^2 of the target and therefore heavy targets are desirable. To compensate for the low secondary beam intensities generated through fragmentation of the primary beam, thick targets can be utilised. For Coulex experiments performed at GSI, ^{197}Au targets are typically used with a thickness ranging between 1-4 g/cm^2. One disadvantage of using thick targets is that the energy straggling effect results in an energy distribution that is further enlarged by angular straggling [12], which in turn affects the measurement of the impact parameter for the peripheral collisions. Target excitations are also possible; for ^{197}Au, the highest energy γ-ray observed from target excitations is the 547 keV ($\frac{7}{2}^+ \rightarrow \frac{3}{2}^+$) transition [35].

For small scattering angles, the scattering angle, θ, in the laboratory frame can be approximated by [12]:

$$\theta \simeq \frac{2Z_pZ_te^2}{m_0c^2\gamma\beta^2b}, \tag{3.1}$$

where Z_p and Z_t are the atomic numbers of the projectile and target nuclei, e is the charge of an electron, m_0 is the rest mass of the projectile, γ is the Lorentz factor, β is the velocity of the projectile, and b is the impact parameter. The largest possible scattering angle in a Coulex experiment, referred to as the grazing angle, θ_{gr}, is roughly 3° for the typical experimental conditions at GSI [12]. For a detailed description of relativistic Coulex theory, see reference [36].

3.2 Primary Beam Production

The acceleration of the heavy ions supplied from the ion sources begins with UNILAC [37] which can accelerate ions ranging from Hydrogen to Uranium up to an energy of 11.4 MeV/u [37]. The ions are then injected into SIS-18 [38] and are further accelerated to the order of 1-4.5 GeV/u with intensities typically of the order $\sim$10^9-10^{10} particles per second [39]. The heavy ions are then delivered by fast extraction to the Experimental Storage Ring (ESR) [40], or by slow extraction with spill times ranging between $\sim$10-4000 ms to the target hall, which is referred to as the primary beam. The starting point of the simulation process discussed in this thesis is the primary beam entering the FRS which is defined in MOCADI.

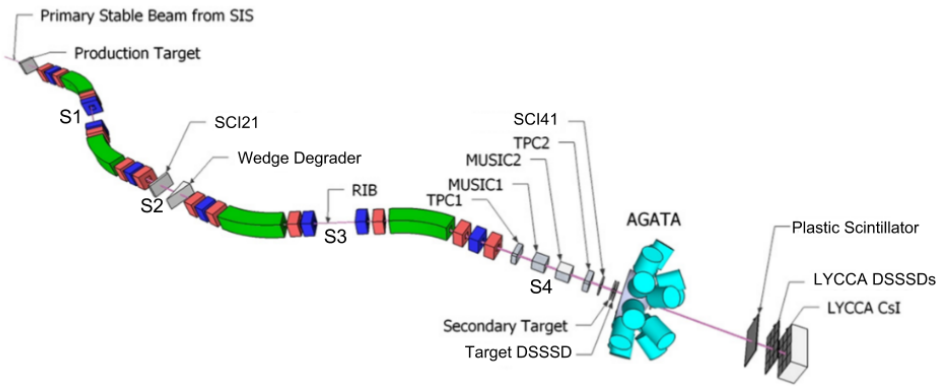

Figure 3.5: A schematic drawing of the FRS including some of the ion optics and detectors at each focal plane (S1, S2, S3, S4), as used during the PreSPEC setup. The detector setup following the FRS is also shown (AGATA/LYCCA). Until spring 2012, the RISING array was located 700 mm behind the secondary target, however, this is now replaced by the AGATA detectors, as pictured above. Figure adapted from reference [41].

3.3 Heavy Ion Selection with the FRagment Separator (FRS)

The FRS, as illustrated in figure 3.5, is a magnetic spectrometer used to separate reaction products from secondary radioactive beams following an initial fragmentation reaction. The spectrometer is symmetric and has four independent stages, each consisting of a 30° dipole magnet which is surrounded by quadrupoles that determine the ion optical conditions at each focal plane (S1, S2, S3, S4) [39]. The FRS is capable of analysing secondary beams up to a maximum magnetic rigidity of 18 Tm.

3.3.1 $B\rho$-ΔE-$B\rho$ Method

The $B\rho$-ΔE-$B\rho$ method is the technique used to separate the various ion species from the secondary beam for focusing at the secondary target at the exit of the FRS. The technique can be summarised into three stages. Prior to the S2 focal plane, the heavy ions are separated based on their magnetic rigidity, $B\rho$. The relativistic velocities of the fragments leaving the primary target are approximately equal, and since the bending radius, ρ, of the first two dipole magnets is fixed at 11.25 m, the ions obtain a similar $\frac{A}{Z}$ value within the acceptance of the dipole magnets which is

governed by the B-field. Therefore, the first stage of the selection is sensitive to the $\frac{A}{Z}$ ratio determined from:

$$B\rho = \frac{p}{q} = \beta\,\gamma\,\frac{m\,c}{q} = \left(\frac{A}{Z}\right)\beta\,\gamma\,c\,\left(\frac{u}{e}\right), \tag{3.2}$$

where β is the velocity of the heavy ion (v/c), γ is the Lorentz factor, u is the atomic mass unit and Z is the charge of the fully stripped ion ($q = Ze$ for fully stripped ions). Equation 3.2 is used experimentally to create identification plots from the FRS data which can be used as gating conditions during analysis, as seen in chapter 6.

The second selection stage is based on the energy loss of the ions through the degrader system located at the S2 focal plane. For experiment S377, a wedge shaped aluminium degrader was used which was set in achromatic mode. In the achromatic mode of operation, the fragment of interest is focused back to a small area at the final focal plane such that the momentum dispersion introduced during the first half of the spectrometer is reversed in the second half. As the ions pass through the varying thickness of the wedge degrader, they will undergo energy loss proportional to Z^2, as given by the Bethe-Bloch theory [15]:

$$-\frac{dE}{dx} = \frac{4\pi e^4 z^2}{m_0 v^2} NK \tag{3.3}$$

where

$$K \equiv Z[ln\frac{2m_0v^2}{I} - ln\left(1-\beta^2\right) - \beta^2]. \tag{3.4}$$

In the above equations, v is the velocity of the projectile, ze is the charge of the projectile, N is the number density of the target atoms, Z is the atomic number of the target, m_0 is the electron rest mass, and e is the charge of an electron. The parameter, I, can be determined experimentally for a given element and represents the average excitation and ionising potential of the target [15]. Ions with different Z will have different velocities following the degrader, allowing for separation of ions with a similar $\frac{A}{Z}$ ratio.

The third stage involves setting the $B\rho$ values of the second pair of dipoles corresponding to the fragment of interest which then focuses the desired fragment onto the secondary target. Thick copper slits can be utilised at each focal plane to further reduce the acceptance of ion species.

3.3.2 FRS Particle Identification Detectors

In order to track the positions and energy of the fragments through the FRS and to identify the various fragments that reach the S4 focal plane by their mass, A, and charge, Z, a variety of detectors are located throughout the spectrometer. The following subsection provides a brief summary of the most relevant detectors used during experiment S377.

- *MU*lti *S*ampling *I*onisation *C*hamber (MUSIC) detectors are located at the S4 (MUSIC41 and MUSIC42) focal plane and are used to determine the Z of the fragments in the second half of the FRS. Each chamber has an active area of 200 mm × 80 mm, an active length of 400 mm and is filled with methane (CH_4) at room temperature and atmospheric pressure which is used as a counting gas [42]. The chamber consists of a cathode, a Frisch grid and 8 independent anode strips. The energy loss of the fragments penetrating the chamber, as described by the Bethe-Bloch theory, can then be utilised to extract the nuclear charge, Z. For a detailed account on the extraction of the nuclear charge, Z, from the MUSIC detector data, see reference [43].

- Fast plastic position sensitive scintillator detectors constructed from the BC420 material are located at the S2 (SCI21) and S4 (SCI41) focal planes and are used to provide time-of-flight (TOF) measurements which are used to extract β on an event-by-event basis. As the flight path between SCI21 and SCI41 has a fixed distance of ∼35 m, the time difference between the arrival of the ions between each scintillator is used to calculate the TOF. The trajectory of the ion is also taken into consideration from the position measurements obtained from the scintillators and surrounding position sensitive detectors. The FRS-standard scintillators are ∼3 mm thick and each scintillator has a photomultiplier tube (PMT) mounted on the horizontal edges of the detector.

For detailed information on the algorithms used to convert the raw data measured with the FRS detectors into physical quantities, see reference [44].

3.4 RISING Cluster Array

The RISING (*R*are *IS*otope *IN*vestigations at *G*SI) germanium array consists of 105 crystals from the former Euroball array [45] arranged into 15 clusters; each

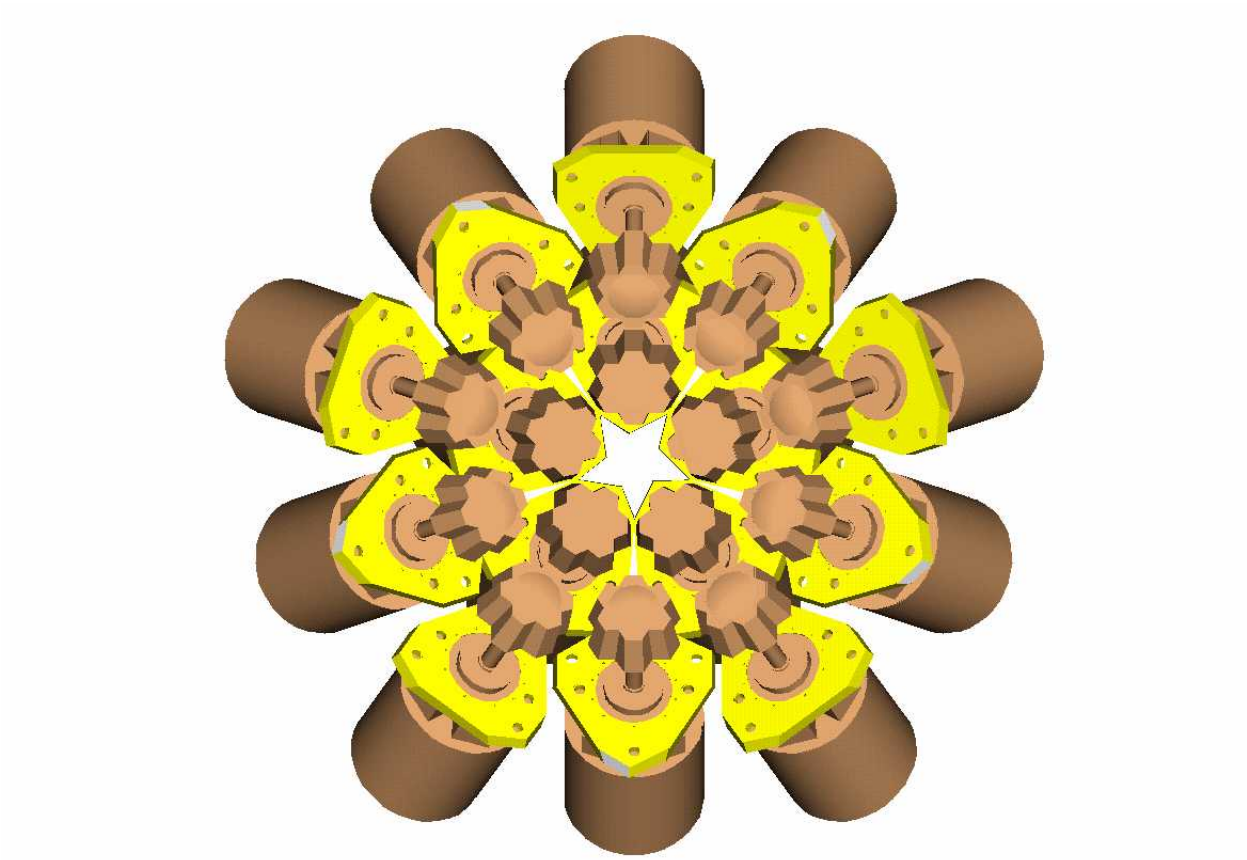

Figure 3.6: A schematic drawing of the RISING detector array. The array was arranged into 15 clusters, each containing 7 crystals. Each cluster was encapsulated in aluminium and was mounted in a common cryostat. Figure taken from reference [46].

containing seven tapered hexagonal germanium crystals. Each individual crystal has a 70 mm diameter and is encapsulated in aluminium. The seven crystals that form a cluster are mounted in a common cryostat. The array was arranged into three rings surrounding the beam pipe, and the central axis of the central detectors in each cluster form three rings at 15°, 33° and 36°. A schematic drawing of the RISING array can be seen in figure 3.6.

The array was designed to achieve an overall energy resolution of ∼1% at β=0.43. Due to the presence of the Lorentz boost and Doppler shift effects at beam energies of around 100 MeV/u, the ideal position for the array is at extreme forward angles. As a result, the energy resolution and efficiency in the second and third rings are notably worse than the first ring, and therefore their distance from the secondary target can be adjusted between 700 mm and 1400 mm in order to maximize the efficiency or energy resolution. In order to help reduce the atomic background and

Ring	Distance (mm)	Angle (°)	Energy Resolution (%)	Efficiency (%)
1	700	15.9	1.00	1.00
2	700	33.0	1.82	0.91
3	700	36.0	1.93	0.89
Total Cluster	-	-	1.56	2.81

Table 3.1: A summary of the ring positions and estimated performance of the RISING array based on the emission of 1.3 MeV γ-rays from nuclei with velocity β=0.43. The energy resolution and efficiency is based on estimations from the previous Euroball setup, and the angles correspond to the central axis of the centre crystal of a ring to the beam direction at a distance of 700 mm from the target. The data are taken from reference [12].

the background associated with heavy ion collisions, each cluster is surrounded by 2 mm of lead shielding with a 5 mm absorber at the front face which is a combination of lead and tin. A summary of the positions and performance parameters of the RISING array can be seen in table 3.1.

An 'addback' procedure is commonly applied to the γ-ray data recorded with the RISING array which increases the overall efficiency of the array. The technique has shown that with cluster detectors, it is possible to gain an increase in efficiency of one order of magnitude compared to standard germanium detectors for γ-ray energies of up to 10 MeV [47]. Following the interaction of a γ-ray within a crystal, the γ-ray may Compton scatter into a neighbouring crystal. The addback procedure sums the energies in neighbouring crystals within a cluster within a time window to reproduce the full photopeak energy; the Doppler correction is then applied to the crystal containing the highest energy. Different conditions can be applied based on the crystal multiplicity (or 'fold'). For example, if two crystals in a cluster detected a γ-ray in coincidence (crystal multiplicity=2), the energies would be summed and Doppler corrected to the crystal containing the highest energy. Implementing this condition on the data would result in a 2-fold γ-ray spectrum. The angle, θ, in the relativistic Doppler shift equation (equation 2.37) is taken as the angle between the beam axis (z-axis) and the central axis of the crystal containing the highest energy. Since the central axis of the crystal is used and the true γ-ray interaction point may deviate from the central axis, this introduces a Doppler broadening effect (see

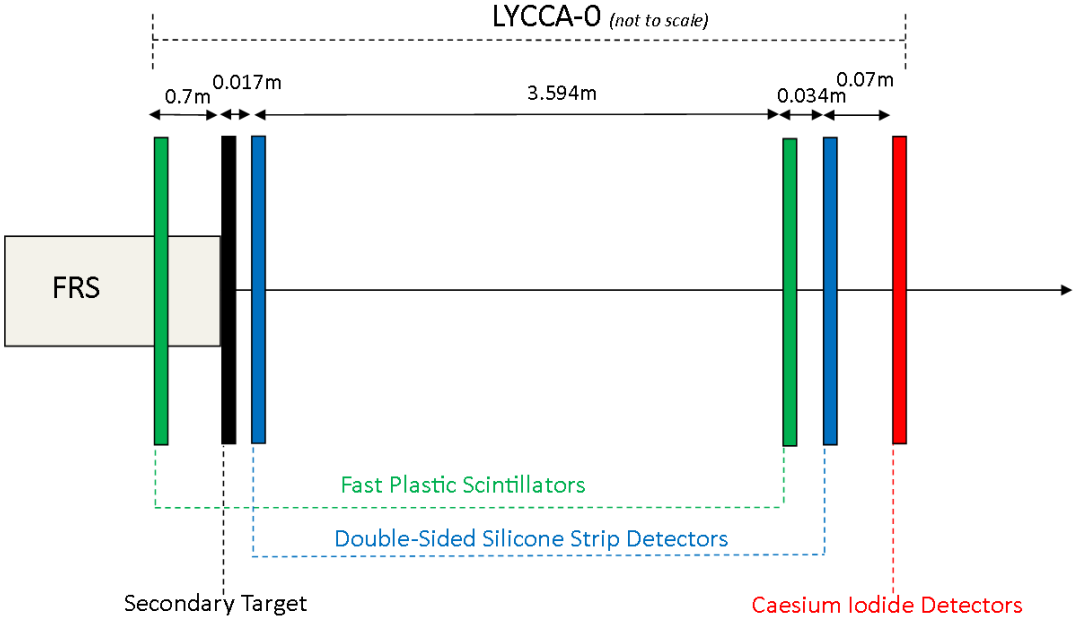

Figure 3.7: A schematic diagram of the LYCCA-0 detector array and the distances between the detectors as used in the simulations detailed in chapter 4.

section 2.5 for further details).

3.5 LYCCA Detector Array

The LYCCA (*L*und-*Y*ork-*C*ologne *CA*lorimeter) device is a highly modular detector array that has replaced the previous *CA*lorimeter *TE*lescope (CATE) [48] system. The detector array is used for reaction channel identification following relativistic Coulomb excitation and secondary fragmentation reactions performed at the secondary target at the final focal plane (S4) of the FRS. The array is part of the High-Resolution In-Flight SPECtroscopy (HISPEC)-DEcay SPECtroscopy (DESPEC) program, which is part of the NUclear STructure, Astrophysics and Reactions (NuSTAR) collaboration within Facility for Antiproton and Ion Research (FAIR) [8]. As the boundaries of nuclear physics are expanded through the use of Radioactive Ion Beams (RIBs), exotic nuclei of interest are produced with small cross sections meaning that the clean identification of these nuclei is vital in order to comprehend the origin of the detected γ-rays. The goal of the LYCCA array is to identify these exotic nuclei by their mass, A, and charge, Z. The initial test phase

of the LYCCA detector (known as LYCCA-0) is part of the PreSPEC program and consists of the following detectors:

- Double-sided Si-strip detectors (DSSSD) at the secondary target position and further downstream (LYCCA wall) for tracking and energy loss measurements
- Fast plastic scintillators located before the secondary target and further downstream towards the LYCCA wall for TOF measurements
- Caesium Iodide (CsI) detectors located at the LYCCA wall position for total kinetic energy measurements.

A schematic diagram of the LYCCA-0 detector layout used during experiment S377 is displayed in figure 3.7. The following subsections provide an overview of the LYCCA-0 detectors.

3.5.1 Double-sided Silicon-Strip Detectors

The DSSSD wafers used at both the secondary target and LYCCA wall positions consist of the same specifications and can be arranged into various configurations within the detector chamber mainframe, as seen in figure 3.8. The chip dimensions are $(60.0 \pm 0.2)\,\mathrm{x}\,(60.0 \pm 0.2)\,\mathrm{mm}^2$, however, when mounted on the printed circuit board (PCB), the overall outer dimensions are $62.5 \times 62.5\,\mathrm{mm}^2$. The active area of the wafers are $58.0 \times 58.0\,\mathrm{mm}^2$ and are $(303 \pm 3)\mu$m thick. A wafer contains $32\,\mathrm{x}\,32$ strips and has a physical pixel size of $1.8\,\mathrm{x}\,1.8\,\mathrm{mm}^2$, allowing for excellent position resolution. An image and drawing of the wafer and Printed Circuit Board (PCB) is illustrated in figure 3.9.

3.5.2 Large-area Fast Plastic Scintillator

The large-area fast plastic scintillator is 1 mm thick and has a 27 cm circular diameter which is housed in an octagonal acrylic glass frame surrounded by 32 PMTs. An image of the detector can be seen in figure 3.10. The detector is constructed from BC-420 scintillator material and is used as the TOF stop signal as part of the LYCCA-0 array. During the LYCCA-0 phase, the scintillator is required to be capable of handling a particle rate of $\sim$100 kHz and to achieve a timing resolution of $\sim$50 ps FWHM [49]. Recent experiments performed at GSI have indicated that

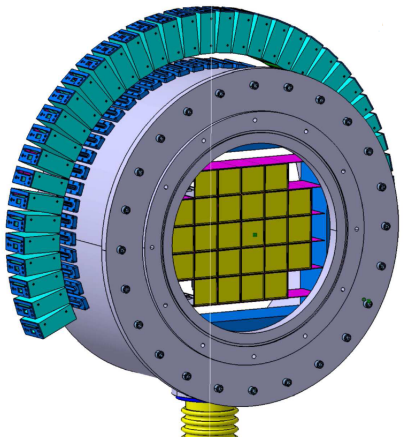

Figure 3.8: A schematic drawing of the LYCCA detector chamber mainframe (light blue) where the individual DSSSD and CsI modules can be arranged into different configurations (yellow). The PMTs (teal) from the fast plastic scintillator detector system can be seen surrounding the chamber. Figure taken from reference [8].

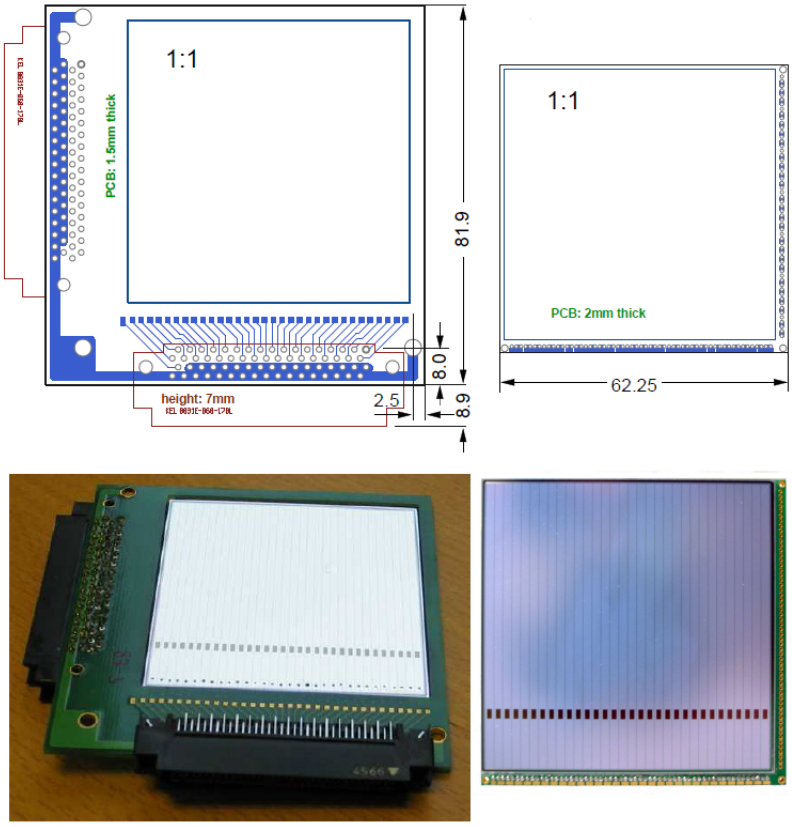

Figure 3.9: The upper panel displays a schematic drawing of the PCB layout for the secondary target position (left) and the LYCCA wall position (right) and the lower panel shows an image of the PCBs including the Si wafer for each position respectively. Figure taken from reference [8].

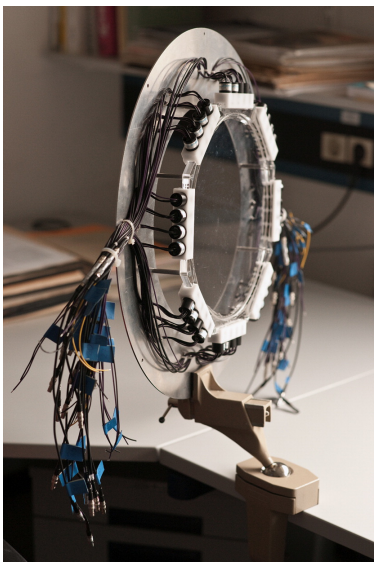

Figure 3.10: A photograph of the scintillator mounted on the octagonal acrylic glass frame surrounded by 32 PMTs. Figure taken from reference [49].

a timing resolution of ∼6 ps is achievable, although this value largely depends on experimental conditions [49].

3.5.3 Caesium Iodide Detectors

The Caesium Iodide (CsI) detectors are a type of non-hygroscopic inorganic scintillator that provides excellent charged particle energy resolution and are therefore utilised for total energy measurements. The CsI modules can also be arranged into various configurations within the detector chamber mainframe. Each individual CsI(Tl) crystal has a 19.0 x 19.0 mm^2 front-face and a 10.0 x 10.0 mm^2 back-end with a depth of 13 mm. Each crystal is wrapped in layers of foil which sums to approximately 0.25 mm, meaning that the effective size of one module is 19.5 x 19.5 mm^2. Photodiodes with the dimensions 10.5 x 11.5 mm^2 are glued directly onto the back-end of the individual crystals and the crystals are arranged into a configuration of 3x3 which is then backed by a PCB, as seen in figure 3.11.

3.6 Existing Simulation Tools

A variety of simulation tools are available to model different aspects of the setup at GSI. In the simulation work discussed in this thesis, the LYCCA-0 geometries from the LYCCA simulation package (see subsection 3.6.3) have been imported

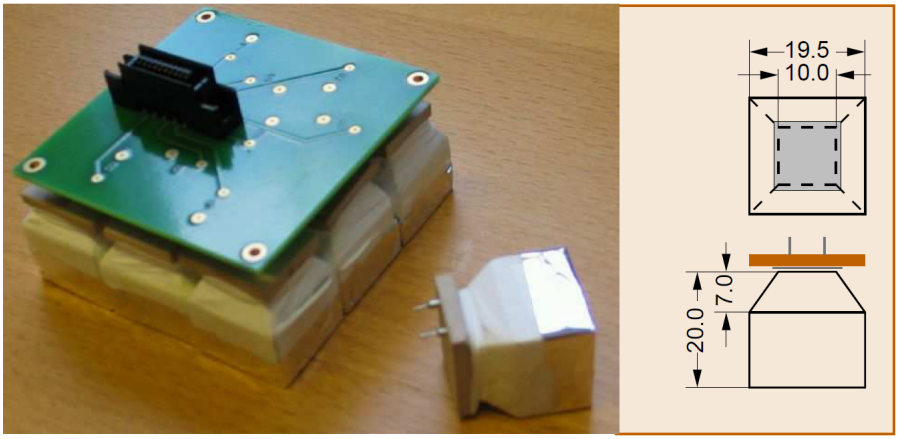

Figure 3.11: Left: The detector module containing 3 x 3 CsI crystals attached to a PCB and one single CsI element. Right: A schematic drawing of one CsI element and the gray area indicates the photodiode. The dimensions are in mm. Figure taken from reference [8].

into the AGATA code and adjusted corresponding to the setup of experiment S377 (see chapter 4). Similarly to the LYCCA simulation package, the MOCADI (see subsection 3.6.1) program is used to simulate the properties of the heavy ions leaving the secondary target of the FRS. The following subsections provides an overview of the programs.

3.6.1 MOCADI

MOCADI [50] is a Monte Carlo based code written in C that was designed in the late 1980s to aid with the development of the FRS [51]. The main objective of MOCADI is to calculate the transport of heavy ions through layers of matter and ion-optical systems, and is regularly used for preparation and analysis of experiments utilising the FRS at GSI to investigate the secondary beam properties.

MOCADI has been developed to account for nuclear and atomic interactions resulting from the penetration of heavy ions through matter. The nuclear interaction is modelled in terms of cross sections and nuclear kinematics, and the atomic interaction is modelled in terms of energy loss, energy-loss straggling, charge-state population and multiple angular scattering [51]. By default, MOCADI utilises the EPAX2 [52] formula for projectile fragmentation production cross sections. The higher order treatment of the heavy ions traversing the ion optics allows for detailed knowledge on the transport properties, which combined with the nuclear and

Property	Description
Save point	Save point number/id.
Fragment	Fragment index/id.
x	x-position in cm.
x′	Tan of the x-angle (x-angle in mrad).
y	y-position in cm.
y′	Tan of the y-angle (y-angle in mrad).
Energy	Energy in AMeV.
Time	Time in μs.
Mass	Mass in amu.
Z	Nuclear charge.
Electrons	Number of electrons.
nf/nsf	Ratio: number of fragments/number of surviving fragments.
Range	Range of the ion in mg/cm^2.
ToF	Time-of-Flight in μs.
dE	Energy loss in MeV.

Table 3.2: A summary of the ion properties output event-by-event from a MOCADI simulation.

atomic interactions allows for accurate simulations of relativistic beams in complex ion-optical systems with many layers of matter.

In order to perform a MOCADI simulation, an input text file with the extension *.in* is required containing 'keywords' or 'cards' that describe the setup of the matter and ion-optics used in the FRS for a particular experiment. The MOCADI manual contains explanations of the keywords and can be viewed, in addition to example input files, at reference [50]. After the input file has been passed to the MOCADI executable and the simulation performed, various formats can be output such as ROOT trees and text files containing properties of the ions at different user-defined 'Save points' of the FRS (such as particle rates and ion distributions). Table 3.2 highlights the available ion properties that can be extracted event-by-event. For a detailed guide on the use of MOCADI, see references [53] and [54].

3.6.2 LISE++

LISE++ [55] is a code written in C++ that has a similar purpose to MOCADI but utilises a user-friendly graphical interface. The user can construct a spectrometer through the use of different 'blocks' which define optics and matter, or use a preset configuration file defining the setup at a particular facility such as: the FRS/SuperFRS at GSI, A1900 and S800 at NSCL, LISE3 at GANIL or RIPS/BigRIPS at RIKEN. A LISE++ calculation can be performed much quicker than a MOCADI simulation and LISE++ has proven to be a very useful tool for beam identification and beam tuning during experiments.

Following the completion of a LISE++ simulation, the yield and transmission efficiency of the ion species resulting from projectile and fission fragmentation that lie within the acceptance of the FRS, are overlaid on the corresponding isotopes on the graphical nuclear chart. By changing various parameters in the simulation, such as the beam energy, slit acceptance, target thickness and wedge angles, the yield and transmission efficiency of the fragment of interest can be examined, making it possible to quickly optimise the setting for a particular fragment.

3.6.3 LYCCA Simulation Package

The simulation work discussed in this thesis stems from the LYCCA simulation package [10] and the concept of using MOCADI as a heavy ion event generator. The LYCCA detector geometries from reference [10] have been imported into the AGATA code allowing for the performance of AGATA coupled to LYCCA to be evaluated in response to an event file defining relativistic reaction processes (discussed further in chapter 4). The LYCCA simulation package was developed to validate and test the performance of the LYCCA-0 detector system in conjunction with the FRS, and utilises the Geant4 [21] framework, MOCADI, and ROOT [56]. The LYCCA simulation package was developed to compare simulations of secondary fragmentation reactions for A≈50 reaction products with experimental data. An investigation was performed to test the identification of A≈100 reaction products utilising the diamond detectors for the TOF measurements in order to find an optimum setup for the identification of the recoiling fragments. The simulation process for the LYCCA simulation package can be summarised into three stages:

1. MOCADI is used to simulate the ions travelling through the FRS and to generate the secondary fragmentation products leaving the secondary target.

2. Geant4 is used to model the LYCCA-0 detector setup and the tracking and detection of the secondary fragmentation reaction products produced using MOCADI.

3. ROOT is used to store, produce histograms and to analyse the response of the various detectors implemented in Geant4.

The package contains two very useful Perl scripts which can be used to set up a simulation input events file based on a secondary fragmentation reaction. As discussed previously, following a fragmentation reaction, a range of ions are produced (see figure 3.3). MOCADI produces output for one ion species at a time and therefore MOCADI must be executed multiple times for each required ion type. The first Perl script, *mocadi_replace.pl*, is used to replace the A and Z values in the MOCADI input file from a user specified list which allows MOCADI to be executed multiple times for a range of ion types. The package also contains a C++ program used to apply cross sections to the output from MOCADI after it has been run for each fragment. The second Perl script, *mocadi_mergeS2.pl*, is used to correlate ions between the S2 and S4 focal planes and separates the fragments incident onto the secondary target with fragments produced after the secondary target - the latter which is then used as an input file to the Geant4 stage of the simulation.

Chapter 4

Development of Simulation Tools for Relativistic Reaction Processes at GSI

The simulation tools discussed in the current chapter are based around the AGATA simulation code [11], which is a Geant4 application used to test the response of AGATA and ancillary detectors to an input events file detailing a nuclear reaction. For this work, which expands on reference [10], the concept of using MOCADI as a heavy ion event generator has been utilised and the LYCCA geometries have been imported into the AGATA code[1] and adjusted for the setup of experiment S377.

The simulation tools have been developed to investigate the response of AGATA in conjunction with LYCCA-0 in preparation for the AGATA campaign at GSI, and to investigate the performance of the γ-ray tracking algorithms in a relativistic environment. The simulations are based from an experimental point of view, meaning that LYCCA-0 is used as an ancillary detector in the simulations to track the recoiling nuclei, thus allowing calculation of θ (the angle between the detected γ-ray and the recoiling nucleus), in addition to β (the velocity of the recoiling nucleus), on an event-by-event basis. The simulated LYCCA-0 quantities are used to correct for Doppler effects, in addition to providing simulated quantities (such as the energy loss in the DSSSDs and the measured β etc.), for the application of particle gating conditions on the data. A flow chart summarising the simulation process can be seen in figure 4.1.

[1]Performed by Pankaj Joshi. e-mail: pankaj.joshi@york.ac.uk

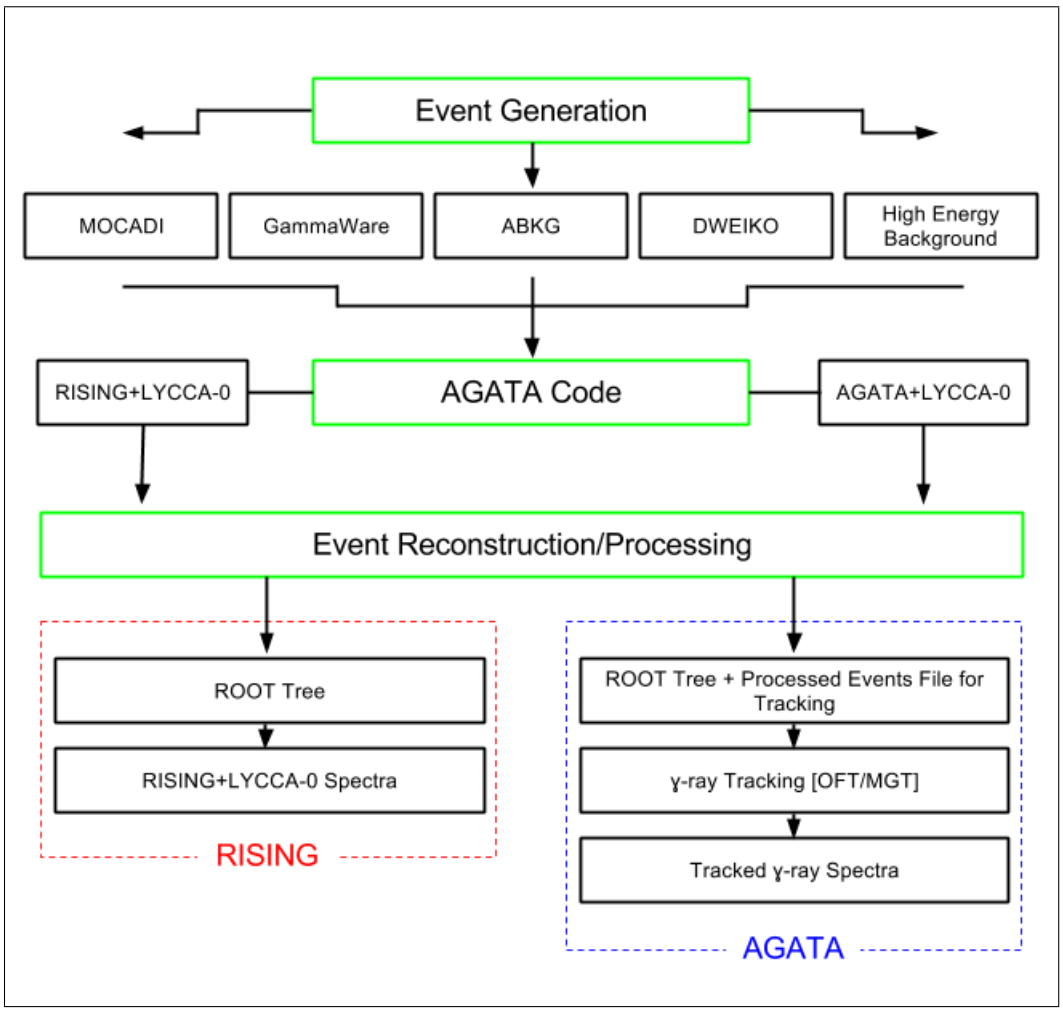

Figure 4.1: A flow chart of the complete simulation process used in this work. The three main stages of the simulation process are highlighted in green boxes. See sections 4.2, 4.3 and 4.4 for further details.

4.1 Detector Geometries

The following subsections detail the various detector geometries used for the simulations of experiment S377.

4.1.1 Simulated LYCCA-0 Geometry

For the simulation work discussed in this thesis, the LYCCA geometries have been imported into the AGATA code from reference [10] and adjusted corresponding to the setup of experiment S377. This involved removing the diamond detectors utilised in reference [10], corresponding to the setup of the initial test phase of the LYCCA array (LYCCA-0). The source code for the inclusion of the target DSSSD module was added, and additionally the LYCCA wall modules (which included removing

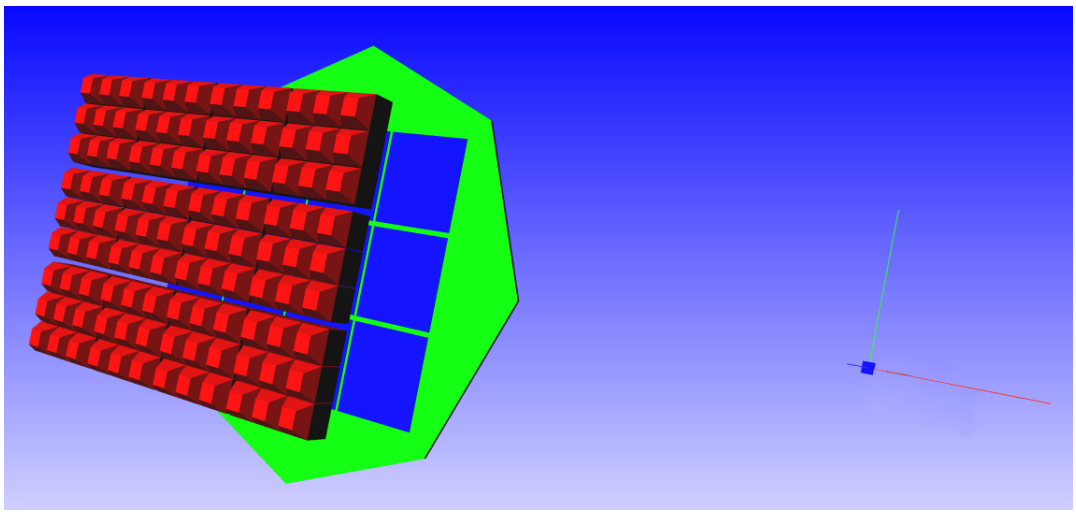

Figure 4.2: A virtual reality modelling language (VRML) image of the LYCCA-0 detector array. The target Double-Sided Silicone Strip Detector (DSSSD) is shown in the far distance (blue), followed by the Fast Plastic Scintillator (green), another layer of DSSSD modules (blue) followed by the CsI detector modules (red). The detector geometries correspond to the setup of experiment S377. The distances between the various detectors can be seen in figure 3.7.

the CATE CsI modules) was modified to correspond to the setup of experiment S377. A simulated VRML image of the LYCCA-0 geometry, as used in the current simulation work, can be seen in figure 4.2.

4.1.2 Simulated RISING Geometry

For the work discussed in this thesis, the RISING array geometry has been implemented in the AGATA code using the individual crystal angles (θ,ϕ) specified at reference [46]. The placement of the array was calculated by converting from spherical (r,θ,ϕ) to Cartesian (x,y,z) coordinates using the following transformations:

$$x = r\,cos\,\phi\,sin\,\theta,\;\; y = r\,sin\,\phi\,sin\,\theta,\;\; z = r\,cos\,\theta, \tag{4.1}$$

where r is the distance from the secondary target to the front face of the RISING detectors (700 mm). The aluminium encapsulation and the lead and tin absorbers have additionally been implemented. VRML images of the simulated RISING array are displayed in figure 4.3. For a detailed description of the format of the source code required to define a detector geometry in the AGATA code, see reference [57].

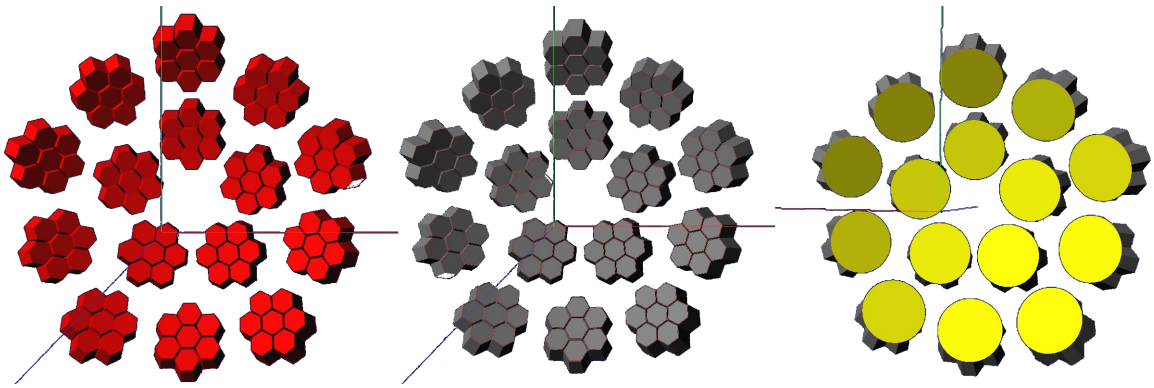

Figure 4.3: VRML images of the simulated RISING array: (left) without encapsulation, (middle) with encapsulation and (right) with encapsulation and the absorbers.

4.1.3 Simulated AGATA Geometries

Due to the size of the aluminium beam pipe at GSI (120 mm diameter and 4 mm thick), the geometry of the AGATA array must be adjusted from the previous setup at LNL in order to accommodate the larger beam pipe. Additionally, the experimental conditions at GSI are vastly different to those at LNL. The larger beam velocity ($\beta \sim 0.43$) and spatial distribution of the beam at the secondary target (FWHM$_x$ $\sim$ 6 cm) at GSI, in comparison with a beam velocity $\beta < 0.1$ and FWHM$_x$ $\sim$ 2 mm at LNL, requires the configuration of the AGATA detectors to be adapted in order to optimise the γ-ray efficiency and energy resolution [41]. The proposed solution was to develop AGATA double clusters (ADCs) using AGATA crystals of type B and C that share the same cryostat [41]. Extensive research has been performed [41] to investigate the performance of different possible geometries with a focus on the detection sensitivity in terms of photopeak efficiencies, angular range, energy resolutions and the P/T as a function of the target-to-array distance. The first milestone at GSI is geared towards constructing a 5ATC+5ADC geometry, and eventually a 10ATC+5ADC geometry [58]

Both of the above AGATA geometries (see figures 4.7 and 4.11) are used in the discussed simulation work to evaluate the improvements of each over the previous RISING array. The simulated performance of each AGATA sub-array, taken from a recent report at GSI [9], can be seen in the figures 4.4, 4.5 and 4.6 (5ATC+5ADC), and figures 4.8, 4.9 and 4.10 (10ATC+5ADC).

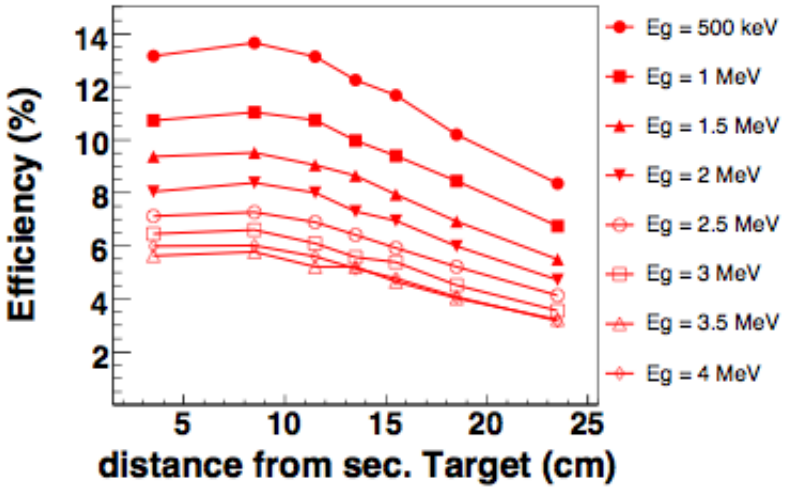

Figure 4.4: The simulated photopeak efficiency as a function of the target-to-array distance for a range of γ-ray energies, E_g. The simulations are for the 5ATC+5ADC geometry and include the spatial profile of the beam with velocity β=0.43. Figure taken from reference [41].

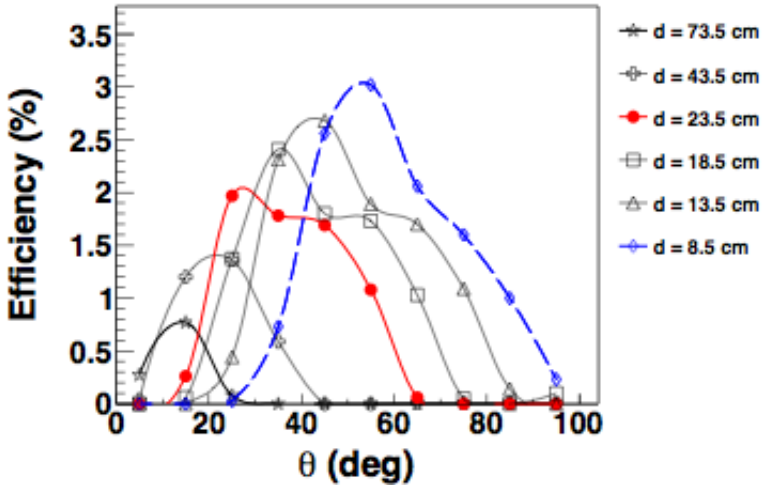

Figure 4.5: The simulated photopeak efficiency as a function of the γ-ray detection angle, θ, for a range of target-to-array distances, d. The simulations are for the 5ATC+5ADC geometry and include the spatial profile of the beam with velocity β=0.43. Figure taken from reference [41].

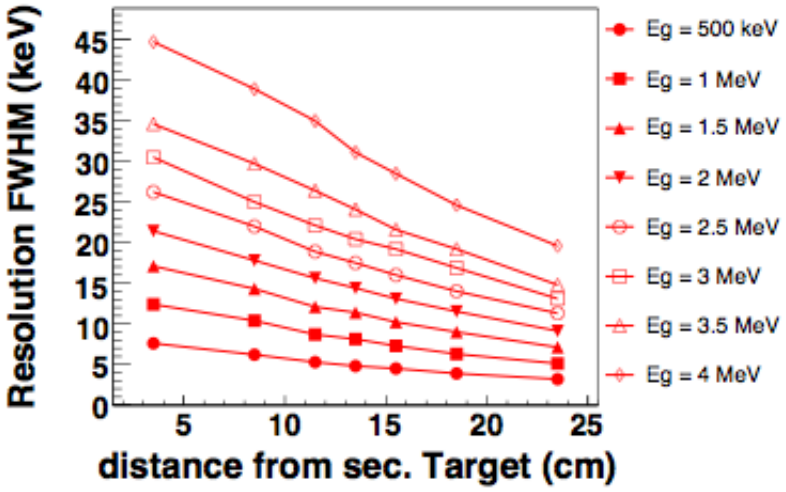

Figure 4.6: The simulated energy resolution (FWHM) as a function of target-to-array distance for a range of γ-ray energies, E_g. The simulations are for the 5ATC+5ADC geometry and include the spatial profile of the beam with velocity β=0.43. Figure taken from reference [41].

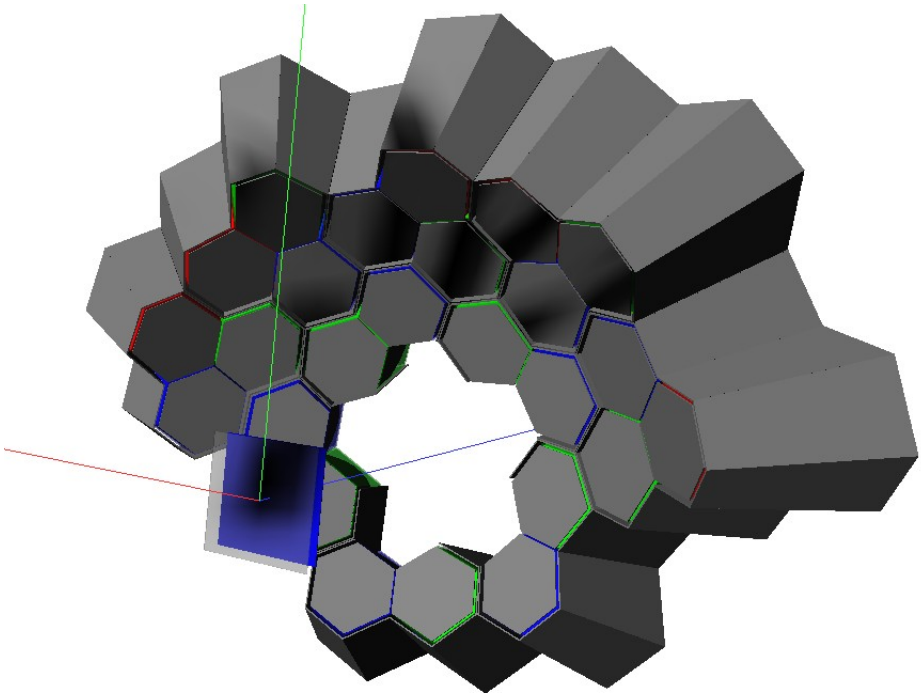

Figure 4.7: A VRML image of the simulated 5ATC+5ADC geometry including the target (transparent grey) and target DSSSD (blue). The figure was generated using a Geant4 macro file used for the simulations discussed in this thesis.

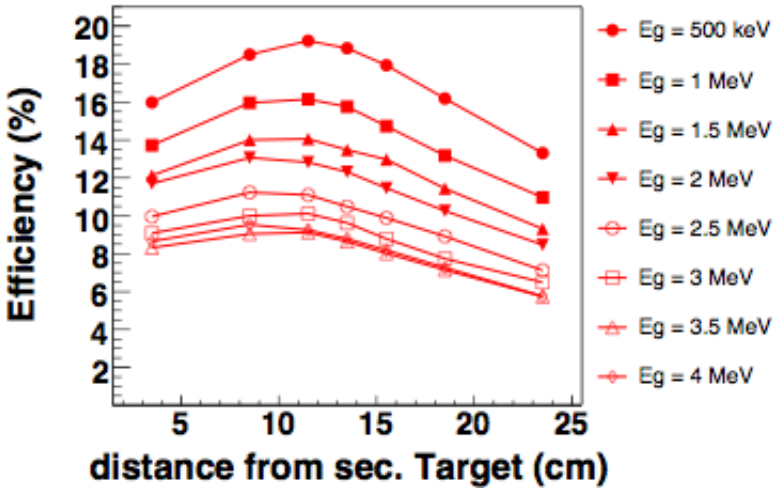

Figure 4.8: The simulated photopeak efficiency as a function of the target-to-array distance for a range of γ-ray energies, E_g. The simulations are for the 10ATC+5ADC geometry and include the spatial profile of the beam with velocity β=0.43. Figure taken from reference [41].

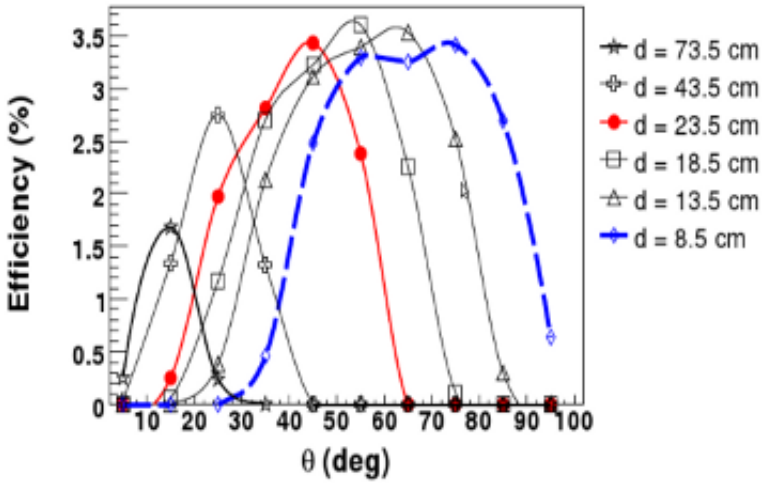

Figure 4.9: The simulated photopeak efficiency as a function of the γ-ray detection angle, θ, for a range of target-to-array distances, d. The simulations are for the 10ATC+5ADC geometry and include the spatial profile of the beam with velocity β=0.43. Figure taken from reference [41].

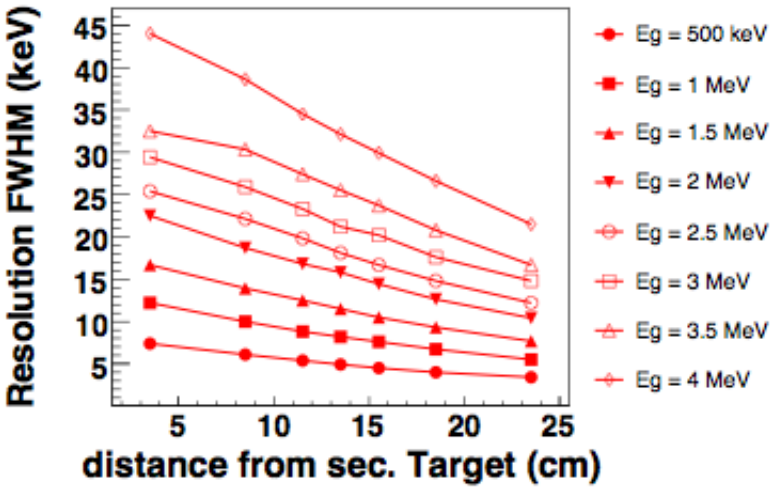

Figure 4.10: The simulated energy resolution (FWHM) as a function of target-to-array distance for a range of γ-ray energies, E_g. The simulations are for the 10ATC+5ADC geometry and include the spatial profile of the beam with velocity β=0.43. Figure taken from reference [41].

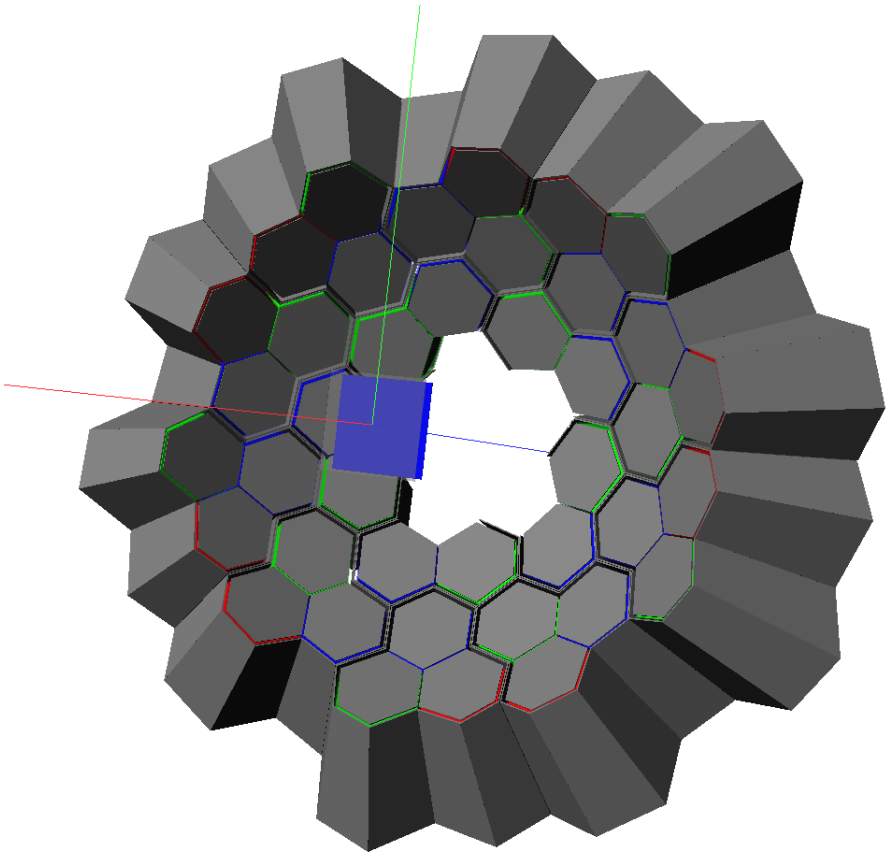

Figure 4.11: A VRML image of the simulated 10ATC+5ADC geometry including the target (transparent grey) and target DSSSD (blue). The figure was generated using a Geant4 macro file used for the simulations discussed in this thesis.

4.2 Event Generation

The event generation stage is the first step of the simulation process (see figure 4.1) and the resulting output is used as an input file to the AGATA code. A variety of codes are used which are subsequently merged together in the format required by the AGATA code.

4.2.1 MOCADI

A MOCADI input file was composed, defining the beam line components for experiment S377. The input file was based on an example file from the MOCADI website [50] which was primarily used for the setup of the FRS magnets. The target area, S1 and S3 focal planes were based on drawings from reference [59], and the S2 and S4 focal planes were setup according to the technical drawings taken from the experiment e-log [34]. The drawings of the S2 and S4 focal planes can be seen in figures 4.12 and 4.13. A C++ program was written that reads the output ASCII file from MOCADI and stores the ion information following the final save point (secondary target) event-by-event into a separate ASCII file. Alternatively, one of the Perl scripts from reference [10] can be used to extract the outgoing fragment information from the secondary target.

4.2.2 GammaWare

The GammaWare [60] package contains a ROOT script, *ToGeant.C*, which generates a cascade of γ-rays from a level scheme defined in the RadWare [61] format (*.ags or .gls* extension). The output file following execution of the script contains a list of γ-rays formatted for use with the AGATA code. In order to create the level scheme file, the *xmgls* program was used, which is part of the RadWare package. The level schemes used for the simulations of the Coulomb excitation of ^{36}Ar and ^{33}Ar can be seen in figure 4.14.

4.2.3 DWEIKO

The Distorted Wave EIKOnal Approximation (DWEIKO) code [62] is a relativistic Coulomb excitation code which produces an angular distribution for the γ-ray tran-

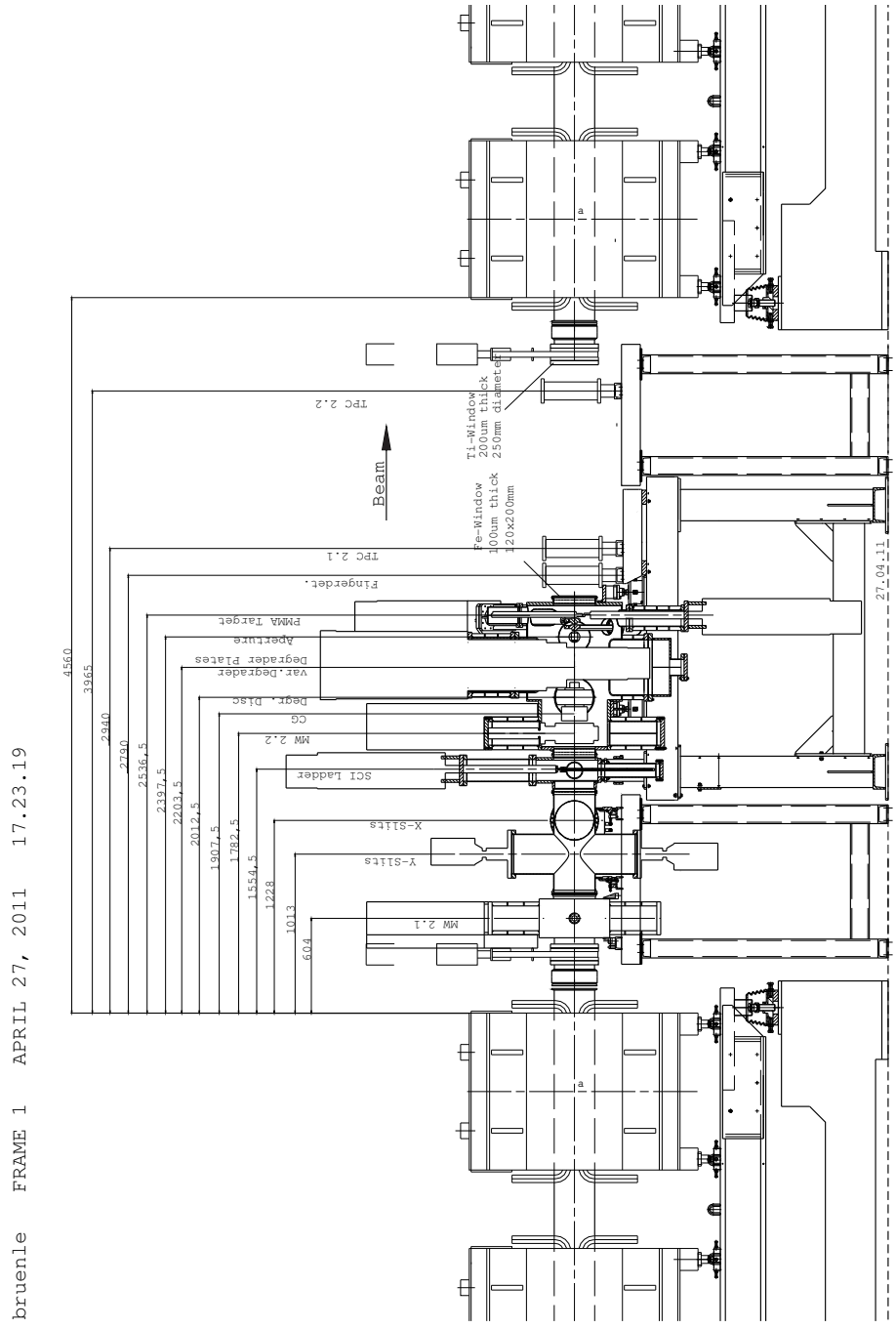

Figure 4.12: A technical drawing of the S2 focal plane from April 2011, taken from the experiment e-log [34]. The distances defined in the drawing were used for the setup of the S2 focal plane in the MOCADI input file and the dimensions are in mm.

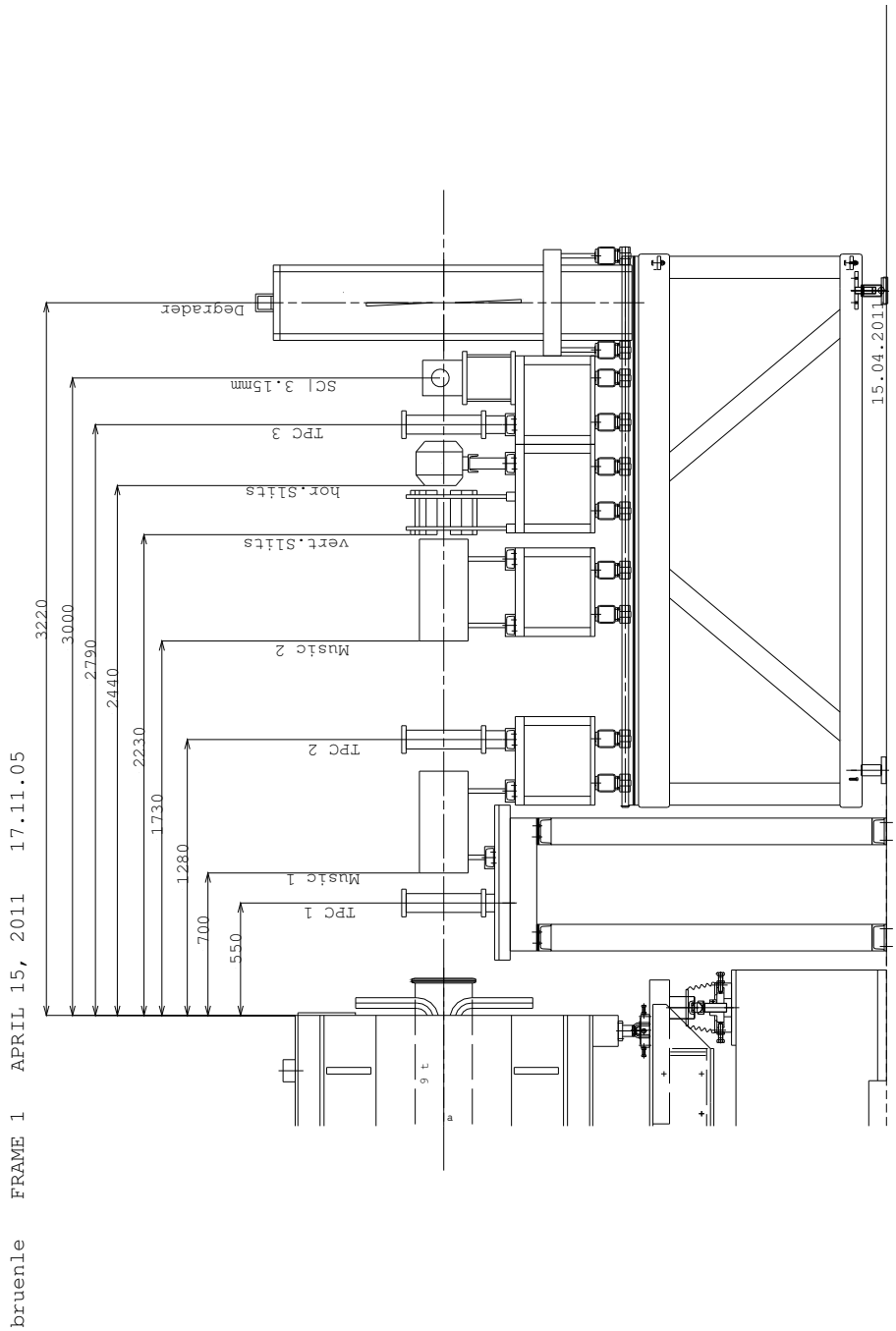

Figure 4.13: A technical drawing of the S4 focal plane from April 2011, taken from the experiment e-log [34]. The distances defined in the drawing were used for the setup of the S4 focal plane in the MOCADI input file and the dimensions are in mm.

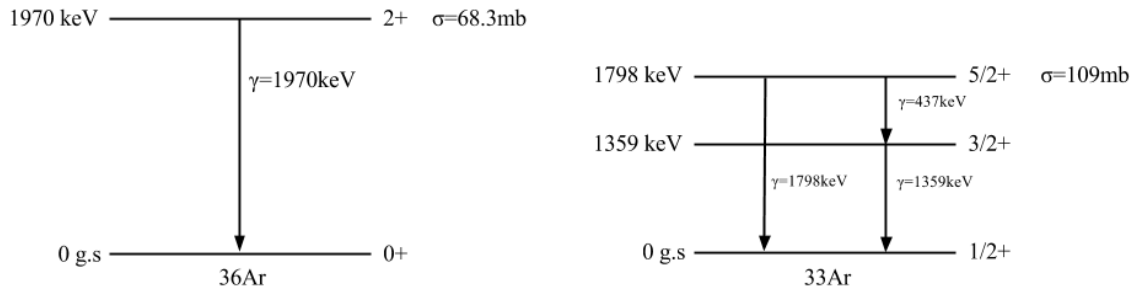

Figure 4.14: The level schemes of the ^{36}Ar and ^{33}Ar nuclei showing the states populated during the Coulomb excitation experiment. The cross section values displayed were calculated using DWEIKO [62].

sition of interest. A modified version was used[2] due to a bug in the original version. The purpose of using DWEIKO was to assign an emission direction to the γ-rays generated using GammaWare. It was not possible to extract the M1 angular distribution for the $\frac{5}{2}^+ \rightarrow \frac{3}{2}^+$ or $\frac{3}{2}^+ \rightarrow \frac{1}{2}^+$ transitions in ^{33}Ar from DWEIKO, therefore the E2 angular distribution belonging to the $\frac{5}{2}^+ \rightarrow \frac{1}{2}^+$ transition was used.

The general form of an E2 γ-ray angular distribution function in the centre of mass frame is given as [62]:

$$W(\theta_{cm}) = 1 + a_2 P_2\, cos(\theta_{cm}) + a_4 P_4\, cos(\theta_{cm}), \tag{4.2}$$

where a_2 and a_4 are coefficients and P_2 and P_4 are Legendre polynomials:

$$P_2(x) = \frac{1}{2}(3x^2 - 1),\ P_4(x) = \frac{1}{8}(35x^4 - 30x^2 + 3). \tag{4.3}$$

The laboratory frame distribution is expressed:

$$W(\theta_{lab}) = W(\theta_{cm}) \frac{1 - \beta^2}{(\beta\, cos(\theta_{lab}) - 1)^2}, \tag{4.4}$$

where $cos(\theta_{cm})$ and $cos(\theta_{lab})$ are related through the transformation:

$$cos(\theta_{cm}) = \frac{cos(\theta_{lab}) - \beta}{1 - \beta\, cos(\theta_{lab})}. \tag{4.5}$$

The modified version of DWEIKO prints the a_2 and a_4 coefficients to the terminal following execution. In order to plot and sample values of θ from the laboratory frame distribution (required by the format of the AGATA input events file - see section 4.2.6), a ROOT code was written to utilise equations 4.2, 4.3, 4.4 and 4.5. The sampled θ values were then output to an ASCII file. A plot of $W(\theta_{lab})$ which was used to sample values of θ for the $2^+ \rightarrow 0^+$ transition in ^{36}Ar can be seen in

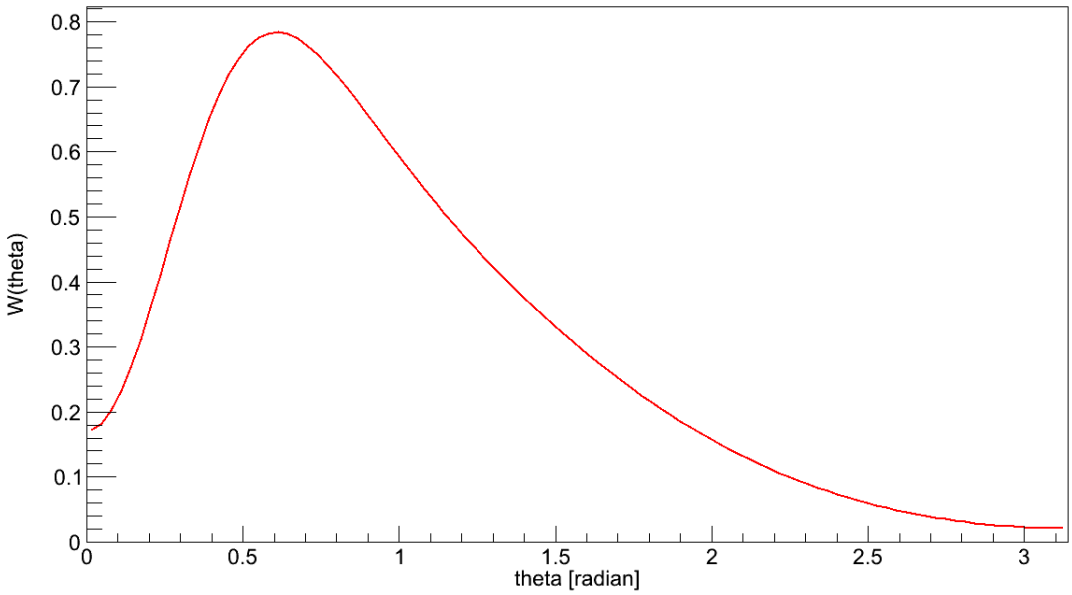

Figure 4.15: A plot of $W(\theta_{lab})$ used to sample values of θ that are used to assign an emission direction to the simulated ^{36}Ar γ-rays.

figure 4.15. Figure 4.16 shows the simulated average interaction positions (x,y) in the RISING crystals weighted by the energy of the γ-ray interactions for an input events file containing only ^{36}Ar γ-rays (no high energy or atomic background components), which highlights the forward focussed angular distribution of the γ-rays.

4.2.4 ABKG

The ABKG code [63] is used to simulate the key atomic background radiation processes associated with heavy ions interacting with matter, as discussed in subsection 2.5.1. The output of ABKG is a *.hst* file which can then be converted into ROOT format using the program *h2root*. The generated ROOT file contains 4 histograms; the first displaying an energy vs. θ distribution in the laboratory frame for the atomic background processes, as displayed in figure 4.17. A ROOT code was written which uses the *TH2::GetRandom2* method in ROOT to sample two random numbers (E,θ) multiple times from the distribution displayed in 4.17, which were then output to an ASCII file. The sampled values are then used to define the energy and emission direction of the x-rays included in the simulations. Simulations containing only atomic background events can be seen in subsection 6.3.1.

[2]Obtained from Piotr Bednarczyk. e-mail: piotr.bednarczyk@ifj.edu.pl

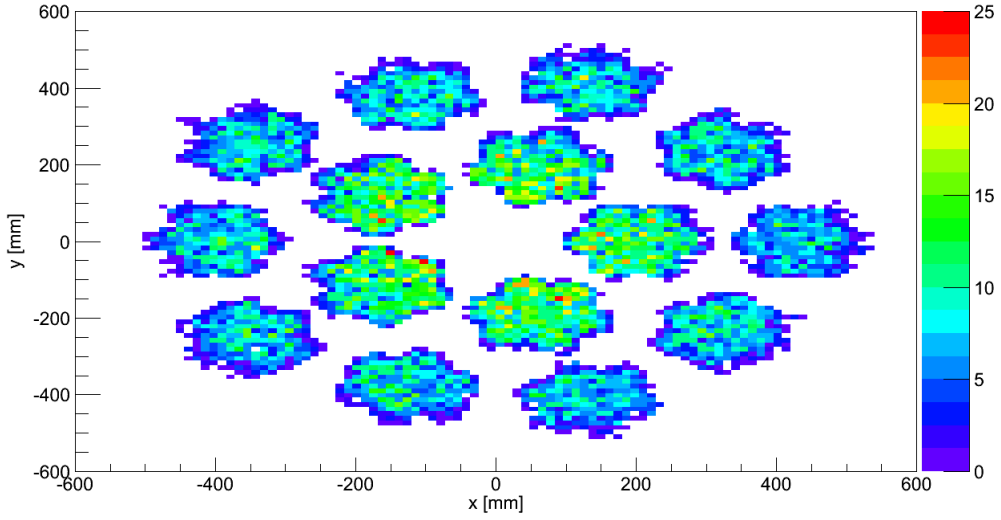

Figure 4.16: The average interaction positions (x,y) in the RISING crystals weighted by the energy of the γ-ray interaction points in a RISING simulation containing only ^{36}Ar γ-rays and no background components.

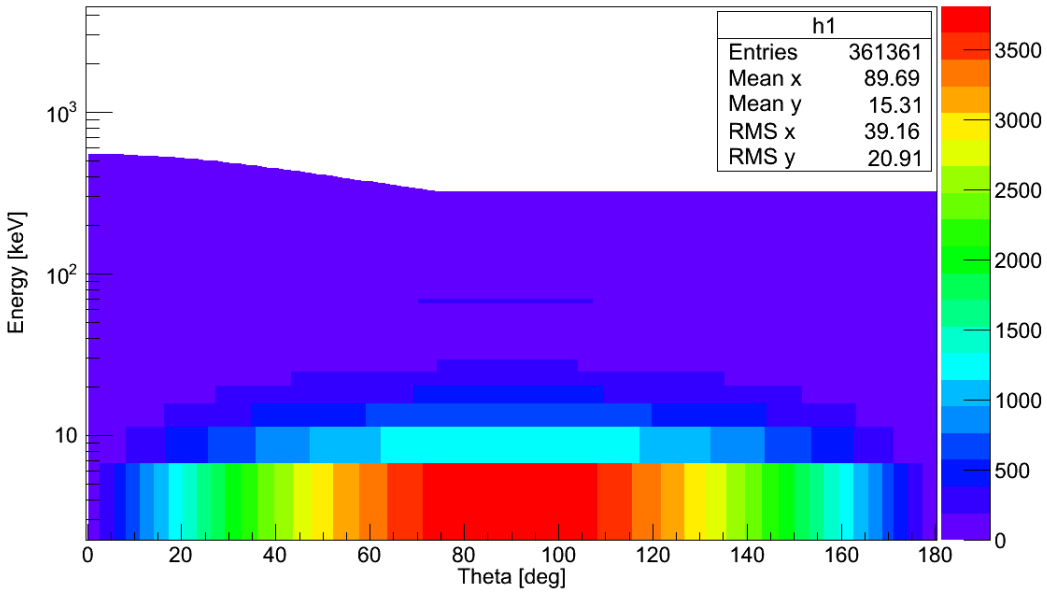

Figure 4.17: A spectrum showing the energy vs. θ distribution produced using ABKG for ^{36}Ar ions at an energy of 137 MeV/u impinging on a ^{197}Au target.

Array Index [i]	**Gaus(μ,σ) [keV]**
0	$\mu = 1000$, $\sigma = 212.77$
1	$\mu = 1250$, $\sigma = 265.96$
2	$\mu = 1500$, $\sigma = 319.15$
3	$\mu = 1750$, $\sigma = 372.34$
...	...
20	$\mu = 6000$, $\sigma = 1276.59$

Table 4.1: An example of the array elements used to generate the high energy background.

4.2.5 High Energy Background

The high energy background is a key feature of the γ-spectra seen at GSI. This is believed to result from highly energetic light particles interacting with a variety of elements along the beam line causing a significant γ-ray background, however, the precise origin is unknown. It is essential to include the background in the simulations as it largely contributes to the shape of the spectra, and ultimately the performance of the tracking codes under these conditions, which to date remains untested. The background in the simulations is assumed to be from high energy γ-rays, and a method of artificially creating the background has been developed which is based on the sampling of Gaussian distributions defined over a similar energy range to that observed in the experimental spectrum. The method has no physical meaning, however, it produces a similar shaped background to that seen in the experimental spectra, as well as the interaction information in the output of the AGATA code which allows the performance of the tracking codes to be evaluated under these conditions. The high energy background is generated during the merging process, as described in subsection 4.2.6. An investigation into the determination of the high energy background multiplicity is discussed in section 6.3.3.

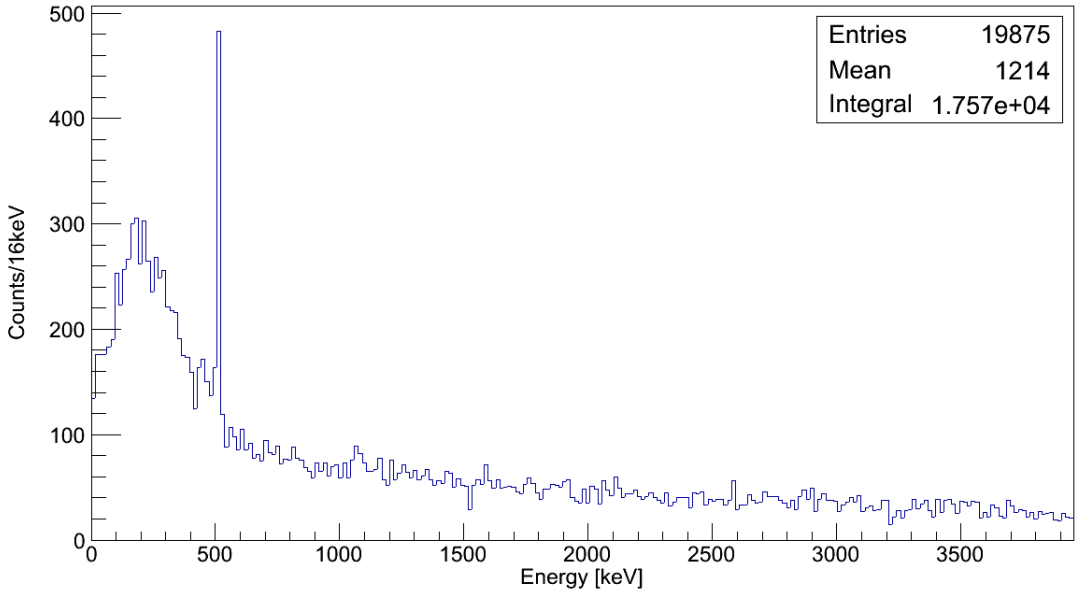

Figure 4.18: The resulting spectrum for an input events file containing only high energy background. Due to the high multiplicity of γ-rays of varying energies, the background is completely smeared with no visible transitions, apart from the 511 keV peak resulting from the pair production mechanism (see section 2.2.3).

Firstly, a loop is created based on the defined multiplicity. For each iteration through the loop, an array is filled with random numbers generated with the *TRandom3::Gaus(μ,σ)* method in ROOT, where μ is incremented from 1 MeV to 6 MeV in steps of 250 keV. The random number generated is selected from a Gaussian distribution with a defined μ and σ. An investigation showed that the most similar shaped background to the experimental background was achieved when the FWHM was set to $0.5\,\mu$. Table 4.1 illustrates an example of the contents of the array. A random number, i, is generated between the index limits of the array and the energy value stored in the array element is then taken as the energy of the high energy γ-ray. The simulated spectral response of RISING to an input events file containing only high energy background can be seen in figure 4.18.

4.2.6 Creation of the Input Events File

The format of the input events file (defined in the AGATA code documentation) used in the discussed simulations is summarised in table 4.2. A ROOT code has been written to read the output created by the various programs during the event

FORMAT *emitterType emittedType*	In the simulation work discussed, *emitterType=0* and *emittedType=2*. In this configuration, the emitter line (which describes the emitting nucleus) is written (*-101 zEmi aEmi eEmi Dx Dy Dz Sz Sy Sz*) where *zEmi* and *aEmi* are the atomic and mass number of the emitting nucleus, *eEmi* is the energy of the emitting nucleus in the laboratory frame, (*Dx, Dy, Dz*) is the direction of the emitting nucleus in the laboratory frame, and (*Sx, Sy, Sz*) is the position of emission of the emitting nucleus in the laboratory frame. The emitted line (which describes the emitted particle) is written (*type Elab Dx Dy Dz*) where type is the species of the emitted particle (*1=*γ), *Elab* is the energy in the laboratory frame, and (*Dx, Dy, Dz*) is the direction in the laboratory frame. Multiple emitted lines are used dependent on the defined multiplicity of the γ-rays per event.
EMITTED *nEmitted emi_0 . . . emi_N*	*nEmitted* represents the number of types of emitted particles in the simulation and *emi* represents the types of emitted particles (in the current work: *1=*γ*, 8=generic ion*).

The input events file therefore has the following format:
FORMAT *0 2*
EMITTED *2 1 8*
$
-101 zEmi aEmi eEmi Dx Dy Dz Sz Sy Sz
-1 Elab Dx Dy Dz
$
-101 zEmi aEmi eEmi Dx Dy Dz Sz Sy Sz
-1 Elab Dx Dy Dz
repeated for n events

Table 4.2: A table summarising the format of the key features of the input events file for the AGATA code, as specified in the AGATA code manual [11].

generation stage, and processes the values into the format described in table 4.2. The various variables read in by the program are stored in a ROOT tree event-by-event, which is useful for monitoring the merged events. A flag in the source code can be set to define the components to be included in the merged input file. The possible options are:

- atomic background only
- high energy background only
- atomic background + high energy background + γ-rays of interest
- γ-rays of interest only
- γ-rays of interest + atomic background
- γ-rays of interest + high energy background.

Firstly, the program loops through the stored output from MOCADI and processes the properties of the ions into the format described in table 4.2 (line beginning '-101' in table 4.2). For each iteration through the loop, the program reads in γ-ray(s) of interest from the output of GammaWare in addition to a sampled value of θ from the output of DWEIKO. The γ-ray(s) of interest can then be assigned an emission direction. The energy of the γ-ray read in from GammaWare is defined in the centre-of-mass frame, and therefore the energy is converted to the laboratory frame using equation 2.37 and 2.38. The γ-ray(s) of interest are then written to the merged input events file as described in table 4.2 (line beginning '-1' in table 4.2).

The next step implements the atomic background. A loop is created based on the defined multiplicity, and for each iteration through the loop, the program reads in a sampled energy and θ value from the stored output of ABKG. The x-ray is then assigned an emission direction and written to the merged input events file (line beginning '-1' in table 4.2). Following the completion of the atomic background loop, the high energy background is implemented using the method described in subsection 4.2.5 and is written to the merged input events file (line beginning '-1' in table 4.2). The ROOT tree is then filled and the program moves onto the next event. The process is then repeated for the remainder of the simulated heavy ions in the stored output file from MOCADI.

$	Beginning of the events section in the list-mode output.
-100	Beginning of an event.
-101 beta Dx Dy Dz	Recoil velocity and direction.
-102 Px Py Pz	Position of the emitting nucleus.
-type energy Dx Dy Dz evNum	Type represents the particle species (type 1 = γ, type 8 = generic ion) and the energy and direction of the particle are specified. evNum represents the particle emission number.
-ndet edep Px Py Pz nseg time	If an interaction occurred, the detector ID, deposited energy, position of the interaction, the segment ID for a segmented detector, and the time of the interaction from the start of the event are output.
repeated for n events	

Table 4.3: A summary of the format of the list-mode output file produced by the AGATA code.

4.3 AGATA Simulation Code

Following the event generation stage, the merged input events file is passed to the AGATA code for the response of the RISING+LYCCA-0 or AGATA+LYCCA-0 geometries to be evaluated. The list-mode output from the AGATA code is written to an ASCII file (*GammaEvents.0000*). The file contains a large header describing various properties of the simulation such as geometry descriptions and event generation information. The AGATA code manual contains detailed information of the list-mode output file [11]. Following the header is the interaction information measured with the detector setup on an event-by-event basis. The format of an event in the list-mode output of the AGATA code, as used in the discussed simulations, is given in table 4.3.

From the AGATA code, the visualisation drivers within Geant4 can be used to display the simulated detector setup and the trajectories of the emitted particles. Figure 4.19 displays an image created with the OpenGLImmediateX (OGLIX) visu-

alisation driver, showing the detector setup and trajectories of the various particles present in the simulations discussed in this thesis.

4.4 Event Reconstruction and Processing

The final part of the simulation process is the processing/event reconstruction which is performed on the output from the AGATA code. The primary goals of the event reconstruction are to determine the recoil direction and velocity using the LYCCA-0 interactions, provide simulated LYCCA-0 quantities for gating conditions, and to histogram the LYCCA-0 and AGATA/RISING spectra. The event processing varies slightly for each detector setup; for the RISING simulations, a ROOT tree is created containing the simulated quantities used to plot the RISING and LYCCA-0 spectra with gating conditions, however, the AGATA simulations result in a modified version of the *GammaEvents.0000* file with gating conditions applied. The modified *GammaEvents.0000* file can then be passed to the OFT/MGT tracking codes. The event processing is performed with a ROOT code which loops over each event in the *GammaEvents.0000* file and performs a variety of operations which are highlighted below.

4.4.1 Detector Resolutions

The detector resolutions are implemented during the event processing stage. The detector resolution for the AGATA detector setup, however, is defined in the tracking codes. Table 4.4 summarises the detector resolutions included in the simulations.

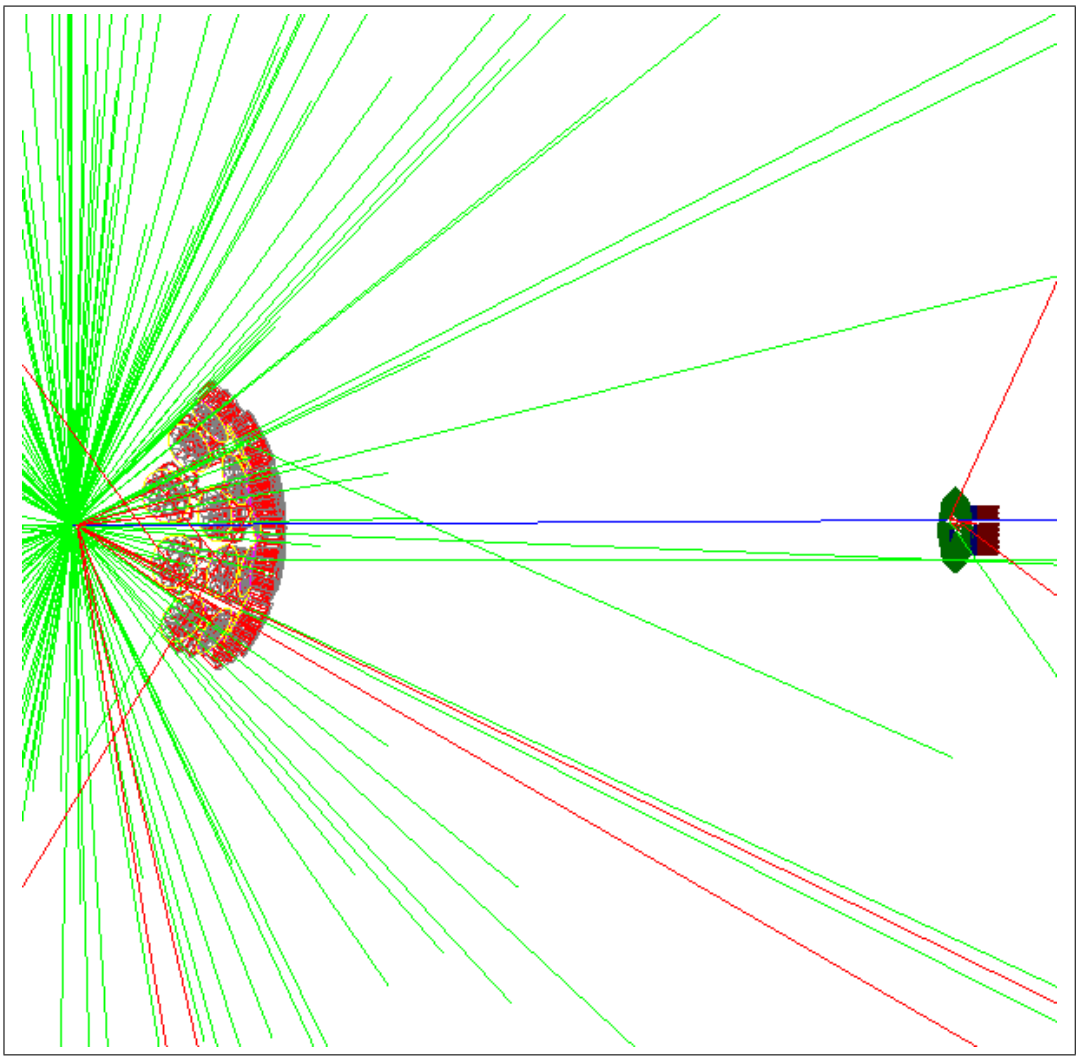

Figure 4.19: An image of the RISING+LYCCA-0 detector setup and particle trajectories created with the OGLIX visualisation driver within Geant4. One simulated event is displayed which includes a ^{36}Ar γ-ray, 20 high energy γ-rays and a tiny fraction of the total amount of atomic background (200 x-rays). The blue trajectory represents the ^{36}Ar ion, the green trajectories represent photons, and the red trajectories represent electrons. The image illustrates the 'prompt flash' at the secondary target and highlights the difficulty of performing γ-spectroscopy in the GSI environment.

Detector	Resolution
AGATA	MGT: 1.9 keV (FWHM) at 1332 keV
AGATA	OFT: 2.4 keV (FWHM) at 1332 keV
RISING	3%
LYCCA-0: Target & Wall DSSSDs	Position(x,y): 1.8 mm FWHM
LYCCA-0: Fast Plastic Scintillator	Timing: 50 ps FWHM
LYCCA-0: CsI	Energy: 0.81%

Table 4.4: A summary of the detector resolutions included in the simulations. The energy resolution for AGATA is given in each tracking code and the overall RISING energy resolution was determined from the experimental spectra displayed in chapter 6. The LYCCA-0 DSSSD resolution was obtained from reference [8], and the LYCCA-0 scintillator and CsI detector resolutions were obtained from reference [64].

4.4.2 Recoil Direction

The recoil direction represents the direction of the heavy ion following scattering at the secondary target. In order to calculate the recoil direction, the coordinates of the interactions in each LYCCA-0 detector are firstly averaged and weighted by the energy of the interaction point, as given by:

$$\bar{c} = \frac{\sum_{i=1}^{n} E_i c_i}{\sum_{i=1}^{n} E_i}, \tag{4.6}$$

where $\bar{c}$ is the weighted mean (which represents either the x, y or z coordinates), c is the interaction coordinate and E is the interaction point energy.

The recoil direction of the heavy ion is calculated using position information provided by the target DSSSD and the wall DSSSDs. The weighted means of the interaction points in each detector are used to construct two vectors:

$$\boldsymbol{v1} = (\bar{x}_{wall}, \bar{y}_{wall}, \bar{z}_{wall}), \boldsymbol{v2} = (\bar{x}_{target}, \bar{y}_{target}, \bar{z}_{target}), \tag{4.7}$$

and the magnitude between the two vectors is given by:

$$\mid \boldsymbol{v1} - \boldsymbol{v2} \mid = \sqrt{(\bar{x}_{wall} - \bar{x}_{target})^2 + (\bar{y}_{wall} - \bar{y}_{target})^2 + (\bar{z}_{wall} - \bar{z}_{target})^2}. \tag{4.8}$$

The recoil direction is then expressed by the unit vectors given by:

$$\hat{\boldsymbol{u}}_{\boldsymbol{x}} = \frac{\bar{x}_{wall} - \bar{x}_{target}}{\mid \boldsymbol{v1} - \boldsymbol{v2} \mid}, \hat{\boldsymbol{u}}_{\boldsymbol{y}} = \frac{\bar{y}_{wall} - \bar{y}_{target}}{\mid \boldsymbol{v1} - \boldsymbol{v2} \mid}, \hat{\boldsymbol{u}}_{\boldsymbol{z}} = \frac{\bar{z}_{wall} - \bar{z}_{target}}{\mid \boldsymbol{v1} - \boldsymbol{v2} \mid}. \tag{4.9}$$

The calculated recoil direction and knowledge of the first/highest energy γ-ray interaction in the RISING array can then be used to calculate the angle θ, which is the angle between the detected γ-ray interaction and the heavy ion. In the AGATA simulations, the calculated recoil direction replaces the corresponding values in the emitter line and is written to the modified *GammaEvents.0000* file; θ is then calculated by the OFT or MGT codes. In the RISING simulations, the crystal with the highest detected energy is selected and the centre-axis coordinates of the crystal are converted to Cartesian coordinates (see equation 4.1) and the unit vectors are calculated similar to above. The unit vectors representing the recoil direction and the crystal axis are then used to determine $cos\,\theta$:

$$cos\,\theta = \hat{\boldsymbol{u}}_{\boldsymbol{ion}} \cdot \hat{\boldsymbol{u}}_{\boldsymbol{crystal}}. \tag{4.10}$$

4.4.3 Recoil Velocity

The recoil velocity, β, is extracted from the TOF measurements between the scintillator located before the secondary target and the LYCCA-0 wall scintillator. The energy loss of the ions through the target and the target DSSSD before the TOF stop signal is acquired results in a lower measured β. Therefore, the velocity extracted directly from the TOF measurement is not an accurate representation of the velocity of the ion where the γ-ray was emitted, i.e. directly after the target, and a correction is required. In the simulations, the γ-decays are considered prompt and are emitted from the target position. However, experimentally, the γ-rays may be emitted from within the target or further along the z-direction.

The correction is implemented as follows and utilises the ratios of the measured energies to extract the velocities. Firstly, a value for the rest mass, m_0, of the heavy ion is determined. The distance between the TOF start and stop scintillators in the simulations is fixed at precisely 4.311 m, and therefore using the measured value of the TOF, a velocity can be calculated (v=d/t). The TOF measurement is the mean value weighted by the energy, calculated similarly to equation 4.6. With the velocity, the Lorentz factor can be calculated where $\gamma = 1/\sqrt{1-\beta^2}$ and $\beta = v/c$. The rest mass can then be expressed as:

$$m_0 = \frac{E}{c^2(\gamma - 1)}, \tag{4.11}$$

where E is the total kinetic energy, which in the initial step is the sum of the

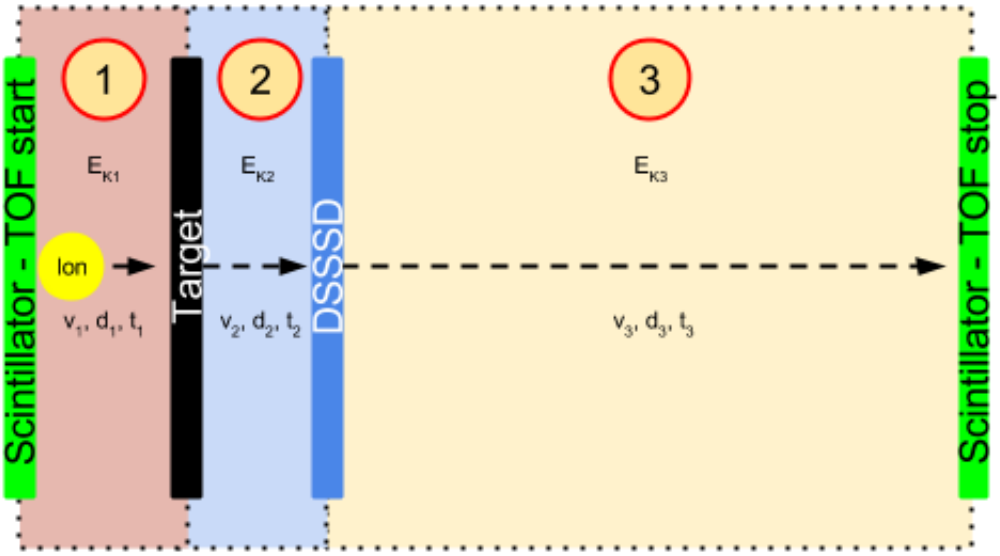

Figure 4.20: A schematic diagram of the LYCCA-0 TOF setup. The diagram is split into three regions (1, 2 and 3) separated by a distance, d, and the properties (velocity, v and time, t) of the ion (shown in yellow) varies between each region.

energy deposited in the target DSSSD, fast plastic scintillator, wall DSSSDs and CsI detectors.

As can be seen in figure 4.20, the kinetic energy of the ion will differ between region 1, 2 and 3 in the diagram as the ions pass through layers of matter. The kinetic energy in each region can be expressed as follows:

$$\begin{aligned} E_{K1} &= E_{target} + E_{DSSSD\_target} + E_{Scint} + E_{DSSSD\_wall} + E_{CsI}, \\ E_{K2} &= E_{DSSSD\_target} + E_{Scint} + E_{DSSSD\_wall} + E_{CsI}, \\ E_{K3} &= E_{Scint} + E_{DSSSD\_wall} + E_{CsI}. \end{aligned} \tag{4.12}$$

The next step is to define ratios between the velocities between each region:

$$\begin{aligned} k_1 &= v_2/v_1, \\ k_2 &= v_3/v_2, \end{aligned} \tag{4.13}$$

where v is extracted from equation 4.11. The ratios of the time of the ion between each region can be expressed as:

$$\begin{aligned} \frac{t_1}{t_2} &= \frac{d_1/v_1}{d_2/v_2} = k_1\frac{d_1}{d_2} = K_1, \\ \frac{t_2}{t_3} &= \frac{d_2/v_2}{d_3/v_3} = k_2\frac{d_2}{d_3} = K_2, \end{aligned} \tag{4.14}$$

where the distances d_1, d_2 and d_3 are determined by the magnitude of the vectors between the corresponding detectors. The corrected recoil velocity can then be

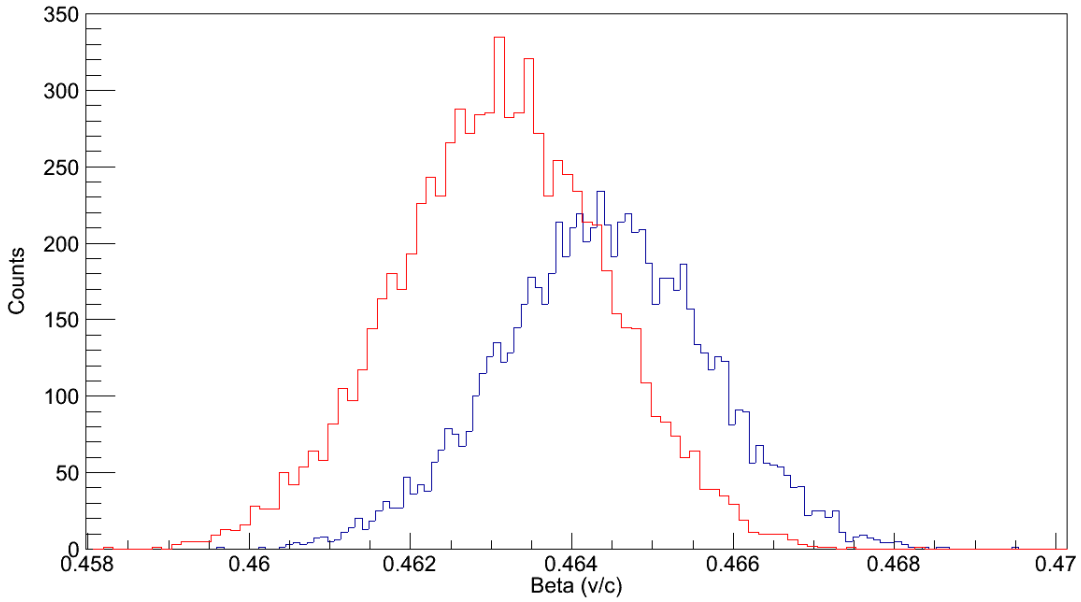

Figure 4.21: A comparison between the β distribution extracted directly from the TOF measurement (red) and the corrected β distribution (blue) which takes into account the energy loss through the secondary target and target DSSSD. The data are for a simulated ^{36}Ar setting.

calculated as follows:

$$\beta = \frac{v_2}{c} = \frac{d_2/(t_3 K_2)}{c}, \tag{4.15}$$

where $t_3 = TOF/(K_2\,K_1 + K_2 + 1)$ and $TOF = t_1 + t_2 + t_3$.

In the RISING simulations, the recoil velocity is used to apply the Doppler correction and the γ-spectra information are then stored in a ROOT tree for further analysis. In the AGATA simulations, the recoil velocity is written to the corresponding part of the emitter line in the modified *GammaEvents.0000* file, and the modified file is then used by the MGT or OFT codes. A comparison between the $\beta_{measured}$ and $\beta_{corrected}$ distributions for an ^{36}Ar simulation can be seen in figure 4.21.

4.4.4 Rest Mass

Using the corrected value of β (equation 4.15) and the total kinetic energy measurements from the LYCCA-0 detectors, the rest mass of the ion emitting the detected γ-ray can be calculated using equation 4.11 on an event-by-event basis. The mass distribution can be used as a gating condition during analysis which is particularly

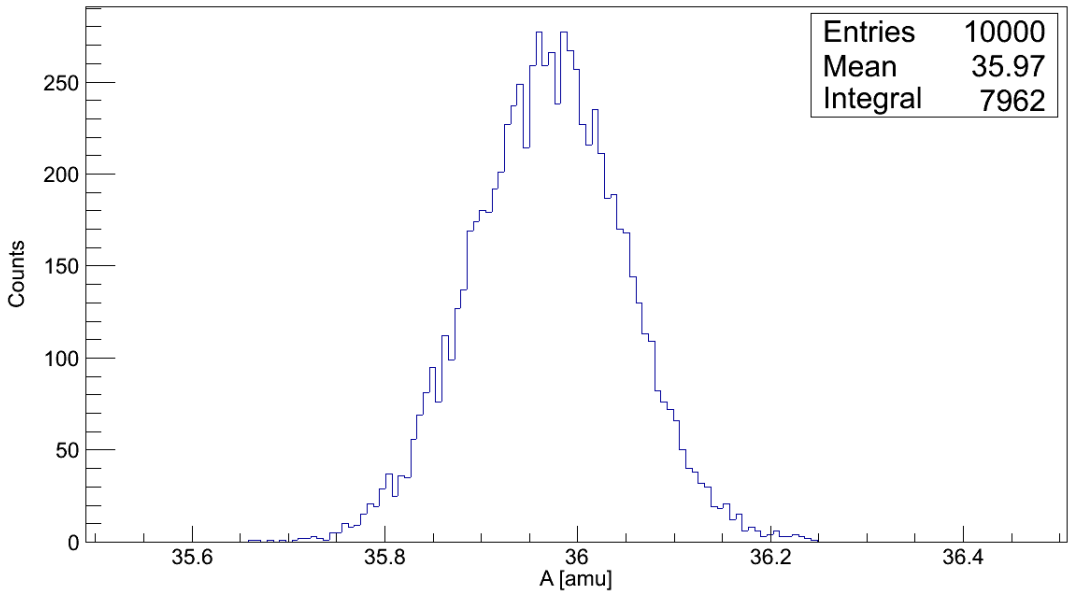

Figure 4.22: A simulated mass distribution created from β and K.E measurements for the ^{36}Ar setting.

useful during a secondary fragmentation reaction where many reaction channels may be present. A mass distribution for the simulated ^{36}Ar setting can be seen in figure 4.22.

4.4.5 Simulated LYCCA-0 Spectra

The interaction information from the LYCCA-0 detectors can be used to create a variety of different spectra. Referring to table 4.3, the interaction energy and (x,y,z) coordinates are available from the output of the simulation, in addition to other quantities such as β; all of which are stored in a ROOT tree event-by-event.

The following subsection illustrates some of the LYCCA-0 spectra that are useful for monitoring, tracking and identification of the reaction products. Figure 4.23 displays a simulated energy loss vs. energy spectrum created from the interaction information in the wall DSSSDs and CsI detectors. Figure 4.24 displays a simulated TOF vs. energy spectrum. The TOF is taken from the scintillator located behind the secondary target and the scintillator located in the LYCCA detector chamber mainframe. The energy measurement is taken as the energy loss in the wall DSSSDs and the energy deposited in the CsI detectors. Figures 4.25 and 4.26 display the hit pattern (x,y coordinates) of the beam at the target and wall DSSSDs respectively.

All four spectra displayed are for the ^{36}Ar setting.

The simulated LYCCA-0 quantities are used as gating conditions during later analysis (see chapter 6); the interaction information from the target and wall DSSSDs are used to determine the recoil direction, and the TOF and energy measurements are used to determine the rest mass of the outgoing ions.

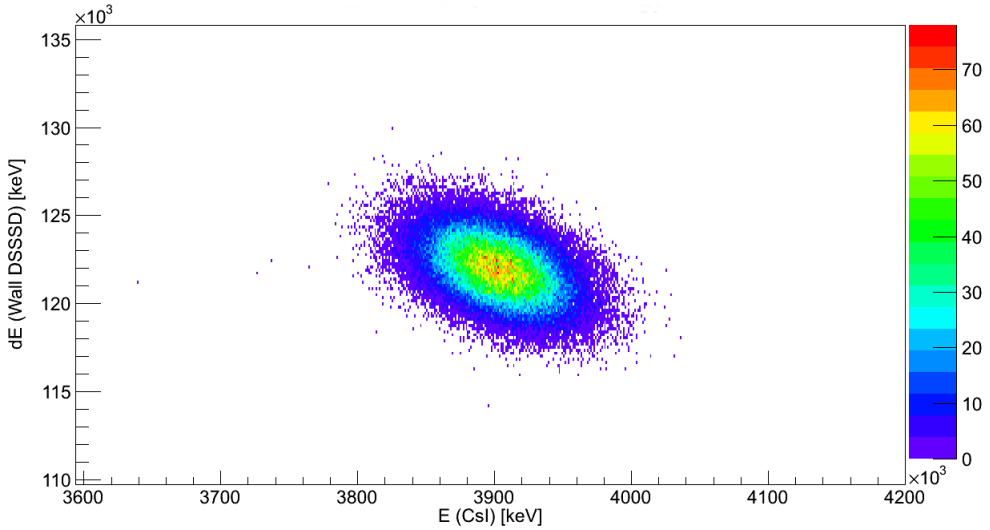

Figure 4.23: A simulated spectrum showing the energy loss vs. energy distribution for the ^{36}Ar setting. The energy loss is taken from the wall DSSSDs and the energy measurement is taken from the CsI detectors. The fragments can be identified by their charge, Z ($Q = Z$ in the GSI environment).

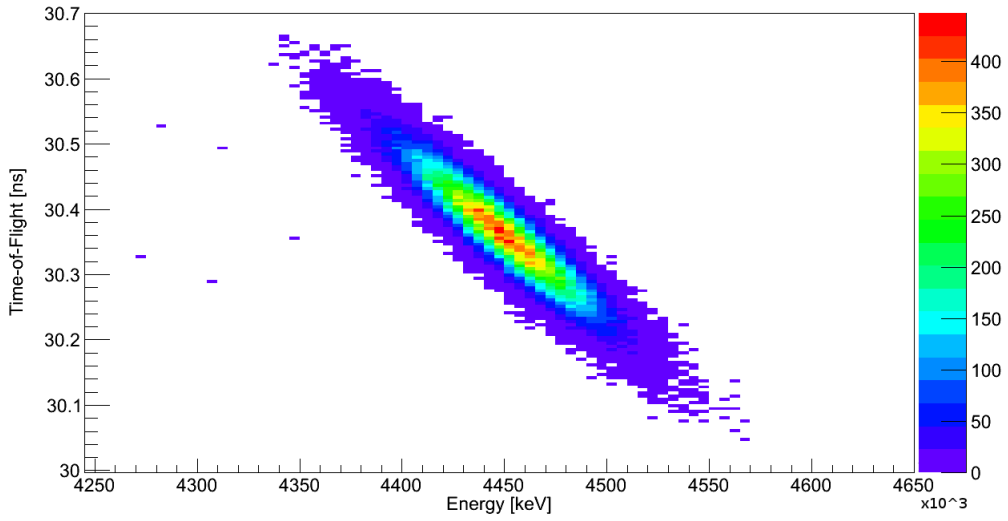

Figure 4.24: A simulated spectrum showing the TOF vs. the total K.E distribution for the ^{36}Ar setting. The TOF is the corrected quantity taken from the TOF start (FRS) and stop (LYCCA-0) scintillators, and the total K.E is taken from the wall DSSSDs and CsI detectors. The fragments can be identified by their mass, A.

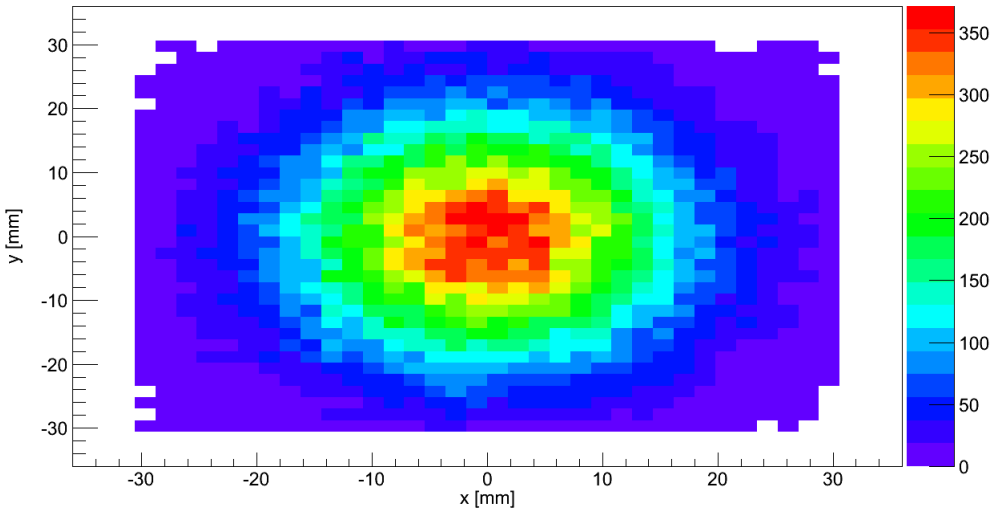

Figure 4.25: A simulated spectrum showing the hit pattern of the beam at the target DSSSD for the ^{36}Ar setting.

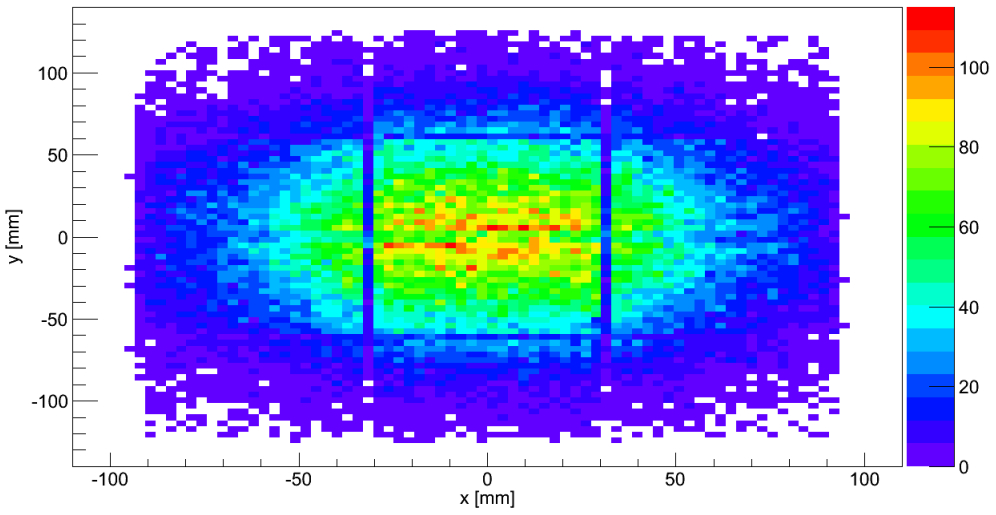

Figure 4.26: A simulated spectrum showing the hit pattern of the beam at the wall DSSSDs for the ^{36}Ar setting. The dead space between each individual DSSSD module is visible which results from the aluminium fixings within the detector chamber mainframe.

Chapter 5

Simulations for AGATA at INFN

The work discussed in the current chapter highlights how the performance of the γ-ray tracking depends on the accuracy of the PSA, which is one of the main concepts of the AGATA project. During the AGATA campaign at Legnaro National Laboratory (LNL), the UK AGATA project was split into eight different work packages which formed part of the UK STFC AGATA project grant. These packages were distributed between institutions in the UK. The simulation work was covered by Work Package 3 (WP3) which was led by R. Wadsworth at the University of York. The primary goals of WP3 were to implement experimental facilities into Geant4, simulate key experiments and the reaction mechanisms involved, and to verify and test the performance of the tracking algorithms. After the initial setup of the detectors at LNL, the project was run through a commissioning phase with the main goal of testing the response and performance of the demonstrator in various experimental situations. The demonstrator (5ATCs), was funded to enable proof of concept before further funds could be committed to enable the construction of the full array. Following the commissioning phase, the demonstrator entered the physics campaign where experiment proposals approved by the Legnaro PAC were performed with a view to exploring new physics.

5.1 The Effect of Position Smearing on the γ-ray Tracking

Using the data from the ^{60}Co source test measurement of August 2009, where 2ATCs were used, it was possible to compare an AGATA code [11] simulation to experimen-

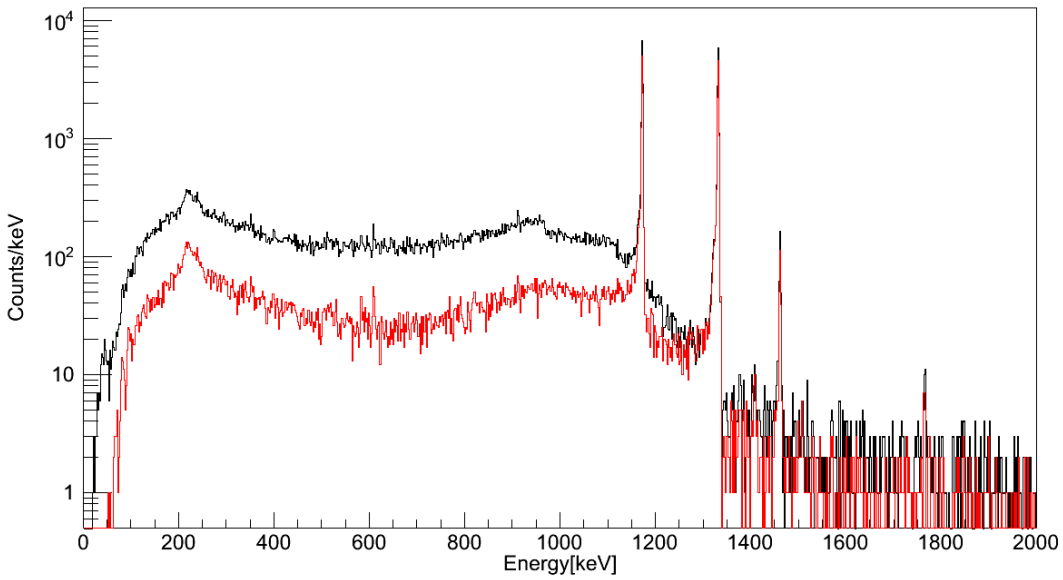

Figure 5.1: The core (black) and tracked (red) experimental ^{60}Co γ-spectra measured with 2ATCs. The core spectrum corresponds to the sum of the energy depositions in each individual crystal. The comparison of the core spectrum against the tracked can determine how efficiently the tracking is performing; for example there is a clear reduction in Compton background when the tracking algorithm is applied. The P/T of the core spectrum is ∼20% and the P/T of the tracked spectrum is ∼40%; the P/T was taken as the sum of both photopeak areas to the background between 150 keV and 1340 keV. The transitions of interest from the ^{60}Co source can be seen at 1173.2 keV and 1332.5 keV. Also present in the spectrum is a photopeak at 1460 keV due to the decay of ^{40}K and at 1765 keV due to the decay of ^{214}Bi resulting from background radiation.

tal data and investigate the effect of the smearing parameter (see section 2.6.2) in the OFT tracking code. Figure 5.1 shows the 2ATCs core and tracked experimental spectra [65]).

A comparison of the tracked experimental spectrum with the tracked simulation spectrum results in a large difference between the P/T values (see figure 5.2), which led to an investigation of the effect of position smearing of the interaction points. This was done by scaling the position smearing function in the OFT code (see equation 5.1). By smearing the interaction points in the simulation, the position of the interaction points are less accurately known and can be used to account for any discrepancy in the interaction positions provided by PSA. In the 'smearpoints'

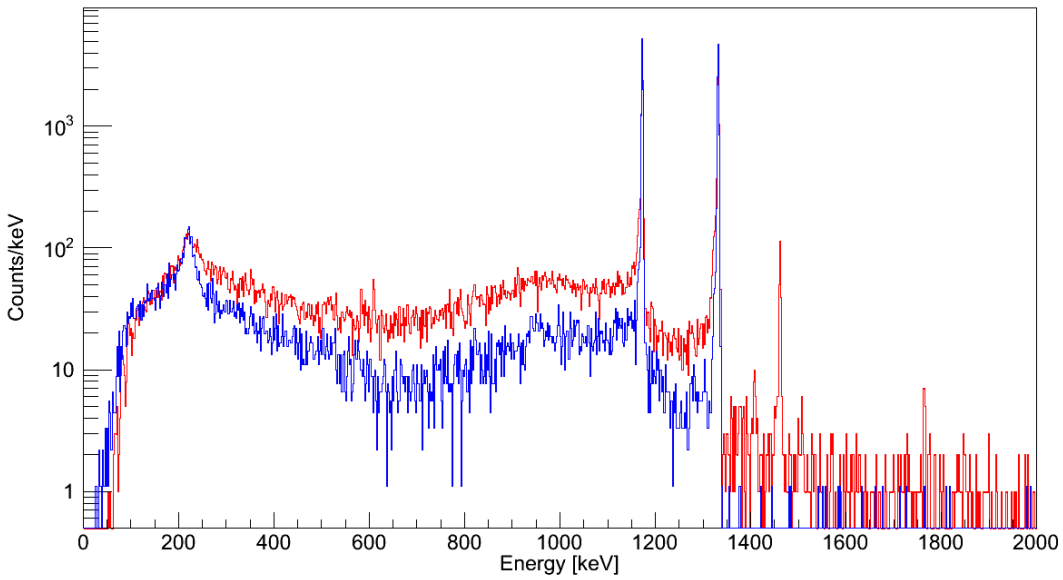

Figure 5.2: A comparison between the tracked experimental (red) and simulated (blue) spectra, using the default position smearing function in the OFT code (FWHM of 0.5 cm at 100 keV). A calculation of the P/T values shows there is a large difference; P/T(expt.)∼40% and P/T(sim.)∼58%. The P/T values were calculated between the energy range of 150 keV and 1340 keV to avoid the inclusion of additional transitions due to natural background radiation in the experimental spectrum which are not present in the simulations.

routine in the OFT code, the position of the interaction points can be set to be smeared with a Gaussian of width:

$$\sigma_p = \frac{FWHM_{x,y,z}}{2.35} = \frac{\frac{1}{2}\sqrt{\frac{0.1}{E}}}{2.35}, \tag{5.1}$$

such that for an interaction point energy of E=0.1 MeV, the FWHM of a position coordinate is 0.5 cm. The energies are smeared by a sigma given as:

$$\sigma_u = \frac{FWHM_E}{2.35} = \frac{\sqrt{1+3.7E}}{2.35}, \tag{5.2}$$

where E is the interaction point energy in MeV, giving the $FWHM_E$ in keV. For an interaction point energy of E=1 MeV, the $FWHM_E$ is ∼2.17 keV.

To simulate the experiment, the ^{60}Co source was placed at (x,y,z) = (0,0,-11)cm with the inclusion of a 2 mm thick aluminium target chamber with a radius of 150 mm. Two ATCs were used and ancillary detector number 6 was selected in the AGATA code, which is a block of steel used to simulate the effects of PRISMA, which

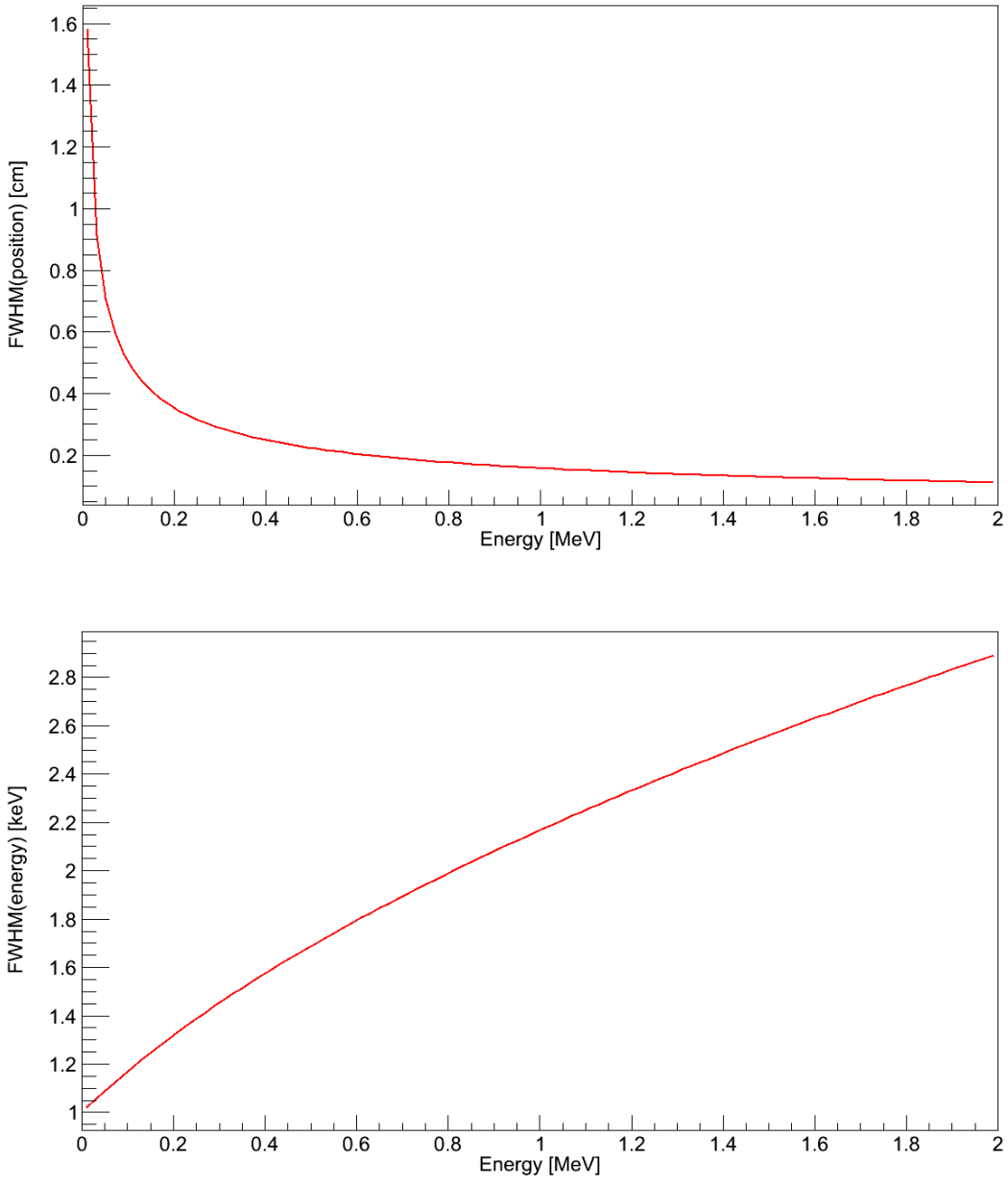

Figure 5.3: The position (top) and energy (bottom) smearing functions used by the OFT code. The position uncertainty has a FWHM of 0.5 cm at 100 keV and 0.16 cm at 1 MeV.

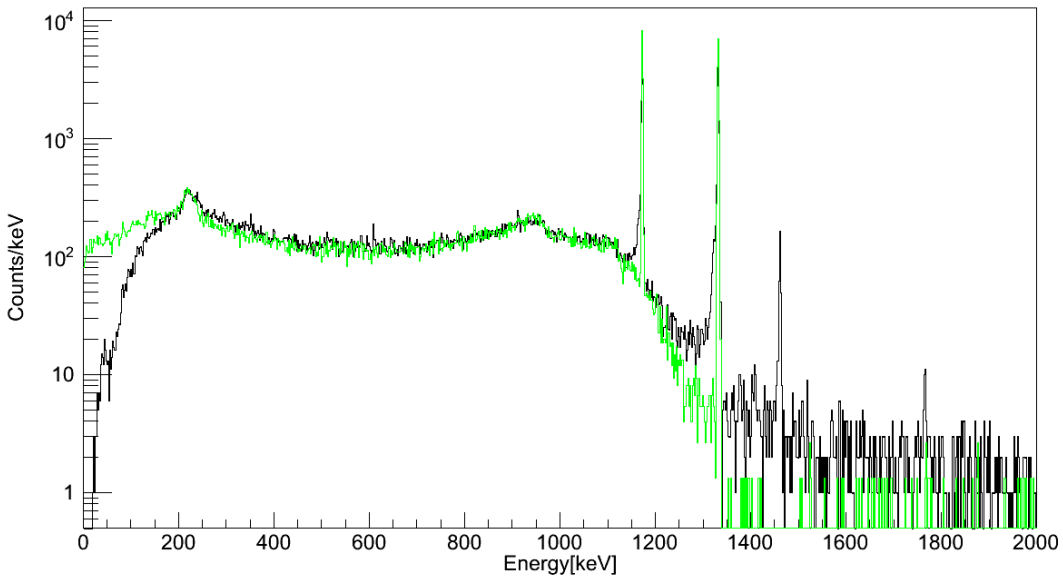

Figure 5.4: The normalised experimental (black) and simulated (green) core spectra. The inclusion of PRISMA in the simulation results in a better comparison between the backscatter peaks and the main differences between the simulation and experiment is the mismatch in the lower region of the spectra resulting from differences in energy thresholds, and also the low energy tails of the photopeaks present in the experimental spectrum.

is a spectrometer used to detect light particle fragments from deep inelastic nuclear reactions. The AGATA crystals at LNL were mounted at the PRISMA spectrometer target position. The inclusion of PRISMA in the simulation reproduces the large backscatter peak seen in the core detector response of the experiment (see figure 5.4) [65]. Figure 5.5 shows a VRML image of the setup.

The simulated and experimental core spectra were normalised to each other using the areas of the photopeaks, as displayed in figure 5.4. Typically, the source activity would be used to normalise data sets, however, the source activity was unknown for the experiment and therefore an assumption was made that the efficiency of the detectors in the simulation is the same as in the experiment, henceforth using the photopeaks to normalise the data sets.

With the data sets normalised, it was possible to investigate the scaling of the position smearing function and the effect on the P/T. Figure 5.2 shows the spectra for both the tracked experimental and simulated data, using the default position smearing function that is active by default within the code. By expressing equation

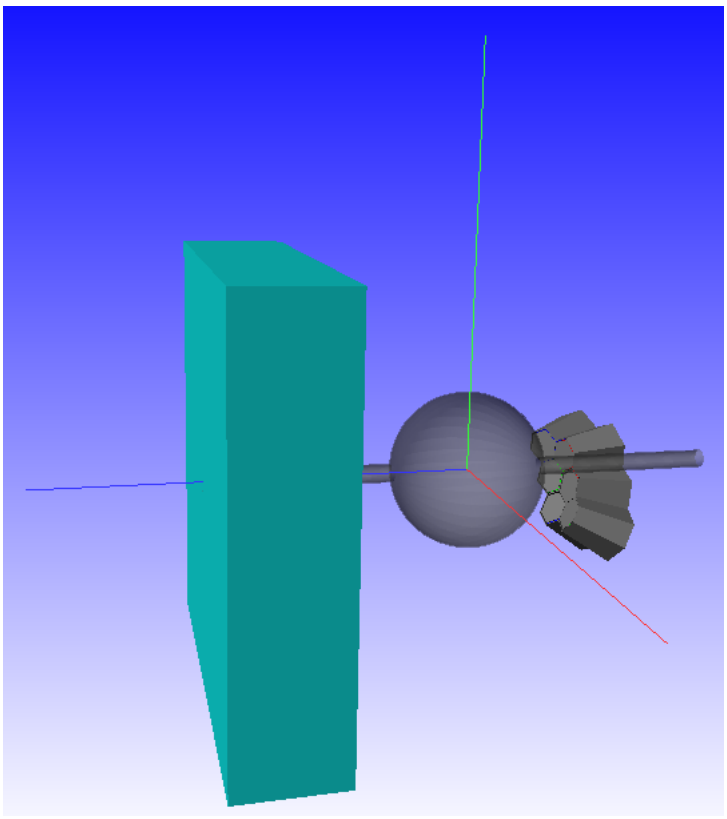

Figure 5.5: A VRML image of the simulation setup showing the 2ATCs, the aluminium target chamber and the block of steel representing the PRISMA spectrometer. The beam direction (z) goes from right to left along the blue trajectory and the source position was located at (x,y,z)=(0,0,-11)cm from the centre of the target chamber.

5.1 as follows:

$$\sigma_p = \frac{P\sqrt{\frac{0.1}{E}}}{2.35}, \tag{5.3}$$

it was possible to scale σ_p by varying the value of the parameter P. Using the default position smearing function of the OFT code, it was shown that the position error has a FWHM of 0.5 cm at 100 keV and 0.16 cm at 1 MeV. By varying the scaling factor, P, in equation 5.3 and measuring the simulated P/T, it was possible to calculate a value of P that results in a similar P/T for both simulation and experiment. This is illustrated in figure 5.6.

With the determined value of P, the position uncertainty has a FWHM of 3.7 cm at 100 keV and 1.17 cm at 1 MeV. Using the value of P=3.7, the P/T of the simulation yields a similar P/T to that of the experiment, as shown in figure 5.7. Equation 5.1 has a dependence on the energy of an interaction point, however, from Work Package 2 (part of the UK STFC AGATA project grant) which focusses on the

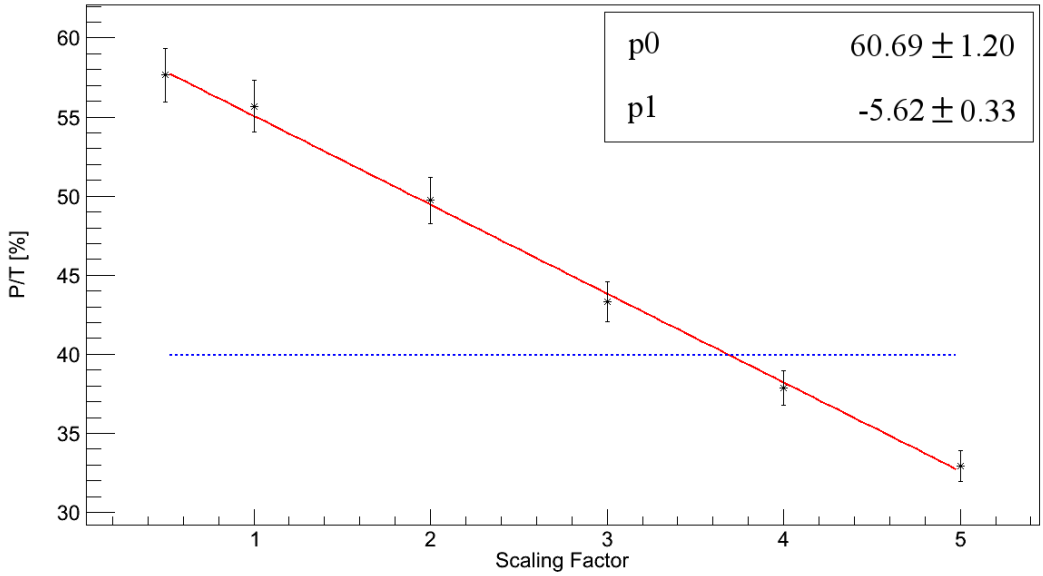

Figure 5.6: A plot of the P/T against the scaling factor, P. Using the intercept between the P/T value from the experiment (blue dashed line) and the fit to the simulated data, it was possible to determine a value of the scaling factor, P, that resulted in a similar P/T value between the experiment and simulation. This resulted in a scaling factor of P=3.7.

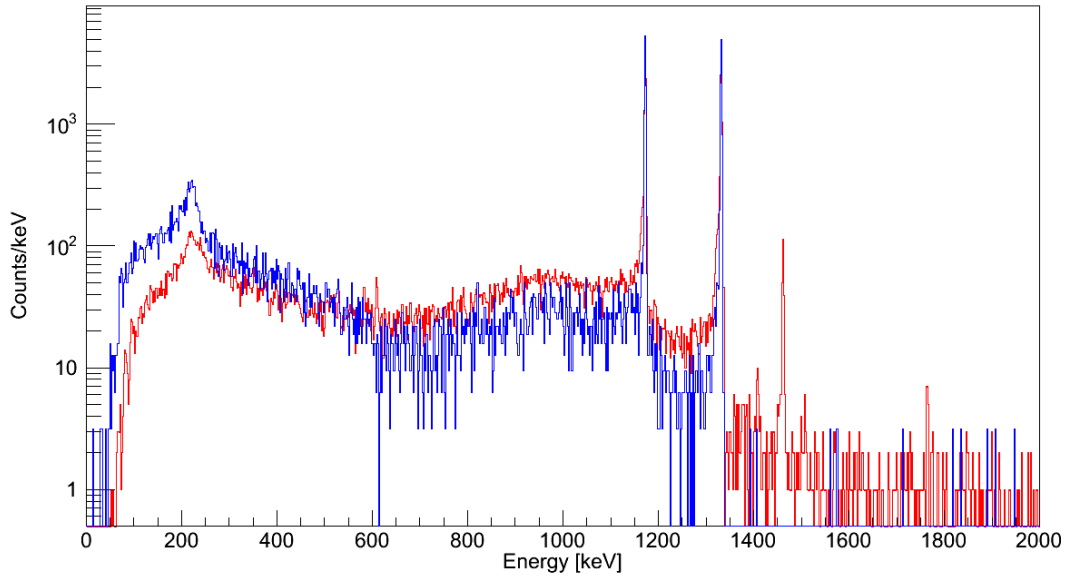

Figure 5.7: A comparison of the experimental (red) and simulated (blue) tracked spectra using a value of P=3.7 in equation 5.3. The P/T (between 150 keV and 1340 keV) for both spectra are ∼40%. The spectra were renormalised using the sum of the peak areas.

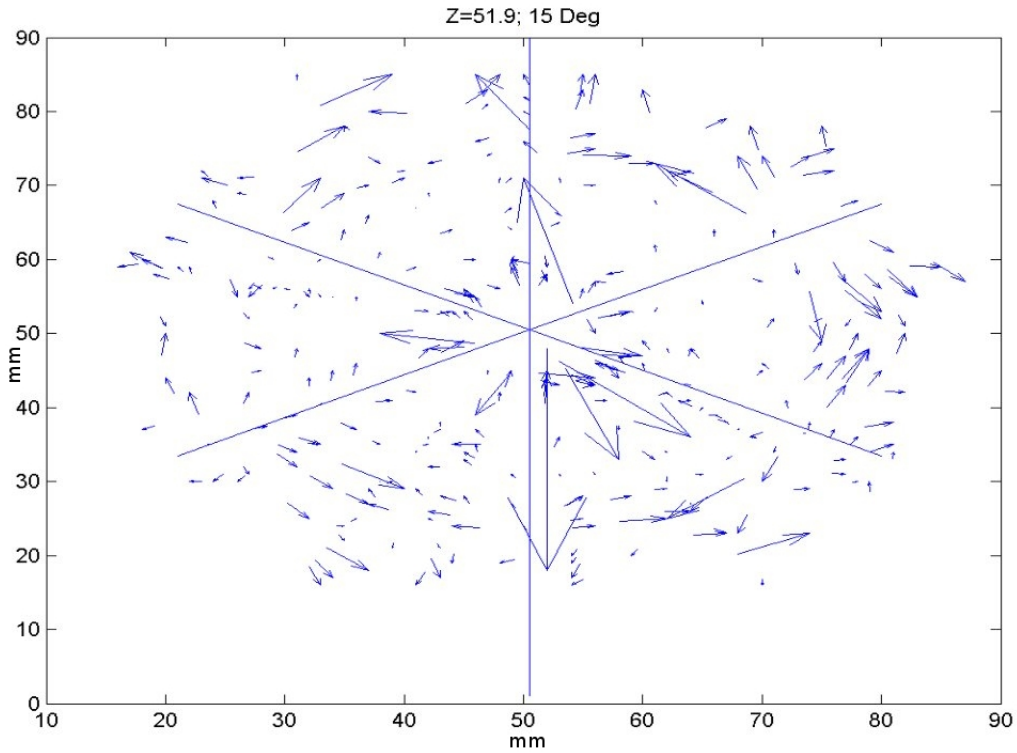

Figure 5.8: A Quiver plot showing the direction and magnitude of the difference in position between the simulated pulse shapes determined from the JASS code, and the nearest experimental pulse shape. The magnitude is represented by the size of the arrows, and the directions point to the nearest similar pulse shape. Figure taken from reference [66].

PSA, it is known that the electric field is not well simulated at the boundaries of the crystals. If an interaction occurs in this region, the interaction position uncertainty will be dependent on not only the energy of the interaction point, but also on the position of the interaction point. In order to include a higher order correction to the position smearing function, Quiver plots (see figure 5.8) should be used, which show the difference in interaction positions between the experimental PSA data, and the PSA basis which is a set of simulated signals obtained from the MGS or JASS codes. The information represented in a Quiver plot could be used to implement a position dependence in the position smearing function.

However, following a suggestion from the collaboration, it was discovered that a similar spectral response can be achieved between the tracked experimental and simulated spectra if an assumption is made that the interaction points in the simulation are packed at the centre of the segments, as displayed in figure 5.9. This suggests that the positions given by the PSA for the experimental data are very approxi-

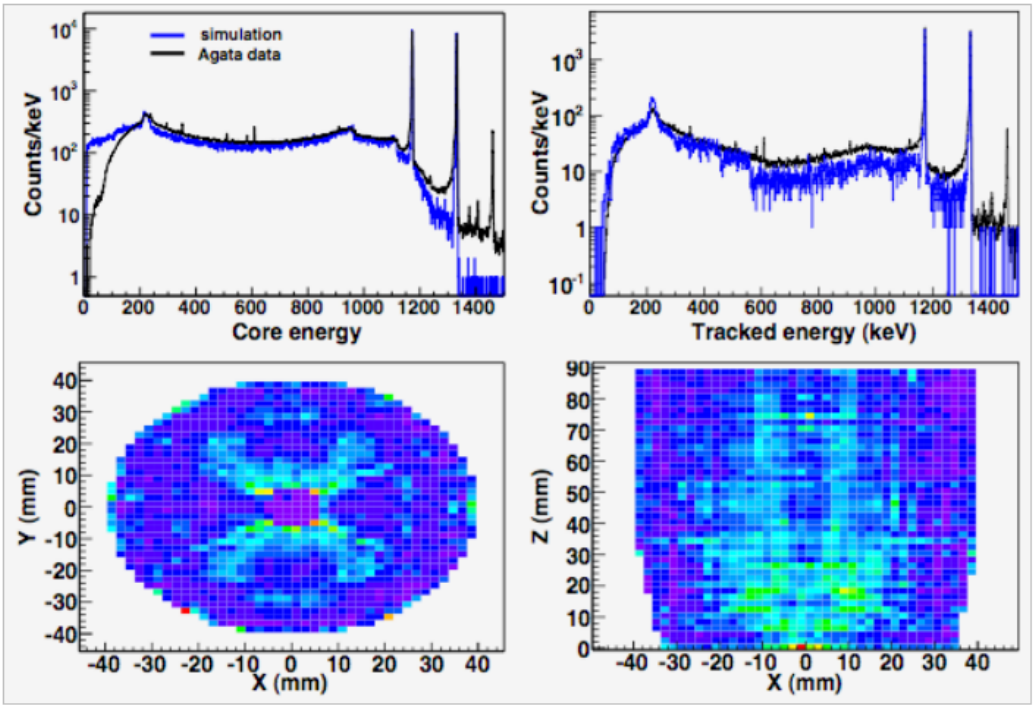

Figure 5.9: The top left panel displays the simulated (blue) and experimental (black) core spectra and the top right displays the simulated (blue) and experimental (black) tracked spectra; the simulated tracked spectrum (blue) in the top right is the result of packing the interaction points in the centre of each segment. The bottom two plots shows the distribution of hits provided by the PSA, where Z is the crystal depth. Figure courtesy of [65].

mate and so including an additional position dependence in the position smearing function would be unnecessary until better PSA data becomes available. Through investigation of position smearing, it was determined that in order to produce more accurate simulations, equation 5.1 should be scaled as follows:

$$\sigma_p = \frac{3.7\sqrt{\frac{0.1}{E}}}{2.35}. \tag{5.4}$$

However, by packing the interaction points in the simulation at the centre of each segment, this works equally as well as scaling the position smearing function. This highlights how the performance of the tracking codes largely depends on the accuracy of the PSA algorithms in determining the interaction positions, and in this instance, better PSA data are clearly required. It was not possible to obtain the required PSA data by the end of this thesis due to the early termination of the AGATA project grant.

Chapter 6

Simulations for AGATA at GSI (Expt. S377)

6.1 Experiment S377 Setup

The motivation behind experiment S377 was to measure the B(E2) values of the first two excited states in ^{33}Ar. This thesis, however, concerns the experimental spectral response of the RISING array for comparison with the simulated response of the AGATA geometries. The experimental setup was as follows: a primary beam of ^{36}Ar at an energy of 450 MeV/u and intensity of 2×10^{10} pps was impinged onto a 4 g/cm^2 thick ^{9}Be production target at the entrance to the FRS, where an initial fragmentation reaction occurred. The FRS was used to select the ^{33}Ar ions, which were then focussed onto a 388 mg/cm^2 thick ^{197}Au secondary target located at the final focal plane of the FRS, where Coulomb excitation took place. A 2 g/cm^2 thick ^{27}Al homogeneous degrader was used at the S1 focal plane, and a 2 g/cm^2 thick ^{27}Al wedge degrader was used at the S2 focal plane. Data were taken for two different settings; the stable primary ^{36}Ar beam and the radioactive ^{33}Ar beam. The experiment was run for $\sim$4 days, however, due to problems with the buncher component of UNILAC, it was not possible to achieve the desired beam intensity of 2×10^{10} pps at all times. Initially, data was also to be taken for the ^{29}S FRS setting, however, this was hindered due to the problems with the beam intensity. The LYCCA-0 detectors and the RISING array were located after the secondary target to track and identify the outgoing heavy ions and to detect γ-rays emitted from the ions.

6.2 Experimental Spectra

The experimental data and gating conditions discussed in the following section are taken from the analysis of experiment S377 (see reference [67]).

6.2.1 Experiment Particle Gate Conditions

In order to select the heavy ion of interest (^{36}Ar or ^{33}Ar) both before and after the secondary target, numerous particle gates were applied to the quantities recorded with the FRS particle identification detectors and the LYCCA-0 detectors in order to separate reaction products from other contaminants.

The primary cut on the secondary beam is based on the A/Q and Z measurements determined from the calculated A and Z values of the incoming ions. Due to pile-up effects in the MUSIC detector, a gate on the Z of the incoming secondary beam was taken from the Z identification of LYCCA-0 following the secondary target. Figure 6.1 shows the A/Q vs. Z plot both before and after the chosen gate for the ^{36}Ar setting.

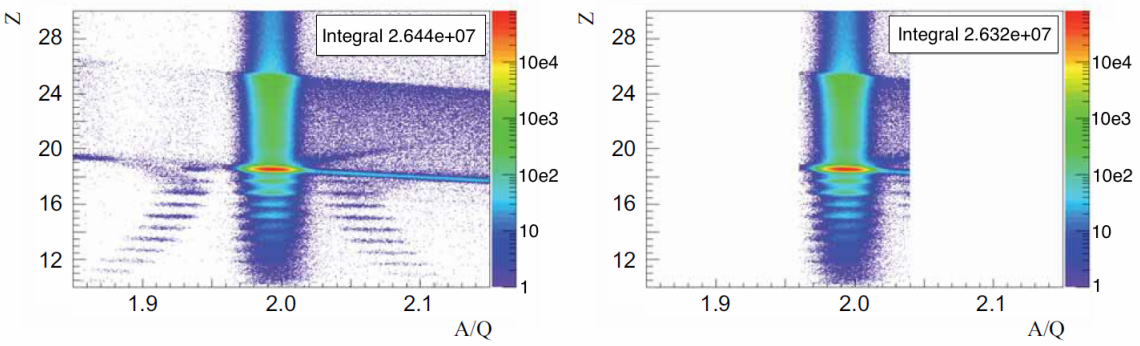

Figure 6.1: The Z vs. A/Q identification plot of the incoming ions both before and after the application of the chosen gate for the ^{36}Ar setting. Figure courtesy of Andreas Wendt, University of Cologne [67].

The LYCCA-0 Z gate is based on the ΔE_{DSSSD} vs. $E_{DSSSD+CsI}$ correlation, where ΔE_{DSSSD} is the energy loss recorded by the wall DSSSDs and $E_{DSSSD+CsI}$ is the total kinetic energy deposited in both the wall DSSSDs and the CsI detectors. Figure 6.2 shows the ΔE_{DSSSD} vs. $E_{DSSSD+CsI}$ plot both before and after the chosen gate for the ^{36}Ar setting.

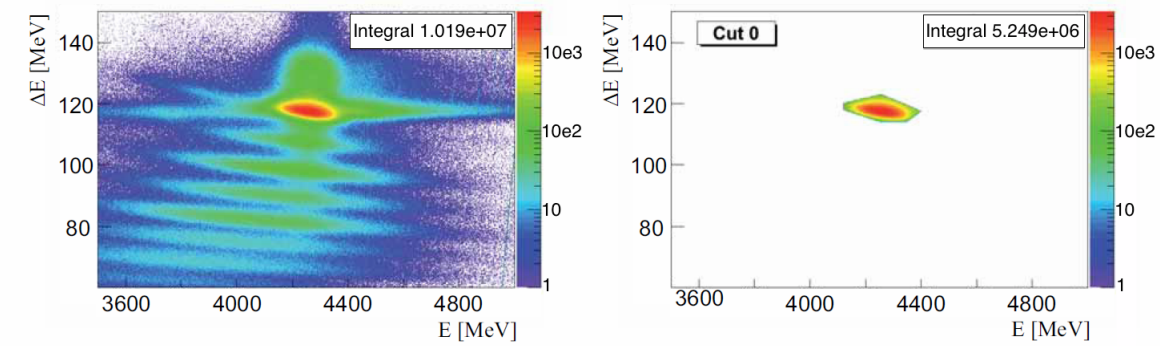

Figure 6.2: The ΔE_{DSSSD} vs. $E_{DSSSD+CsI}$ plot both before and after the chosen gate which is used for Z identification following the secondary target. The data are for the ^{36}Ar setting. Figure courtesy of Andreas Wendt, University of Cologne [67].

The Z determination was further improved by applying gating conditions on correlations between other recorded LYCCA-0 quantities such as the energy loss in the wall DSSSDs, the measured value of β, and the total energy measurement from the CsI detectors. A gate was applied on the ΔE_{wall} vs. ΔE_{target} correlation, where ΔE_{wall} and ΔE_{target} are the energy loss in the wall and target DSSSDs respectively. Figure 6.3 shows the ΔE_{wall} vs. ΔE_{target} plot both before and after the chosen gate for the ^{36}Ar setting.

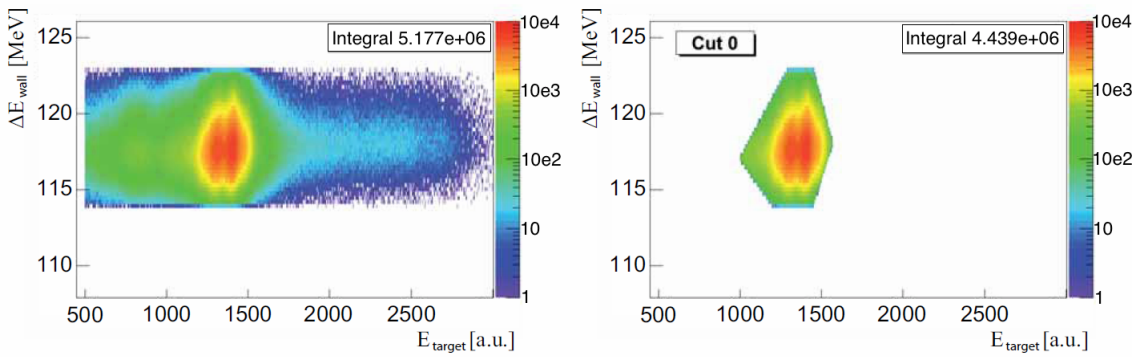

Figure 6.3: The ΔE_{wall} vs. ΔE_{target} plot both before and after the chosen gate for the ^{36}Ar setting. Figure courtesy of Andreas Wendt, University of Cologne [67].

A gate was applied to the $\beta_{LYCCA-0}$ vs. β_{FRS} correlation, where $\beta_{LYCCA-0}$ is the velocity of the ion determined from the LYCCA-0 detectors (S4 scintillator to the LYCCA-0 plastic scintillator) and β_{FRS} is the velocity of the heavy ion determined from the FRS detectors (S2 finger detector to the S4 scintillator). Figure 6.4 shows the $\beta_{LYCCA-0}$ vs. β_{FRS} plot both before and after the chosen gate for the ^{36}Ar setting.

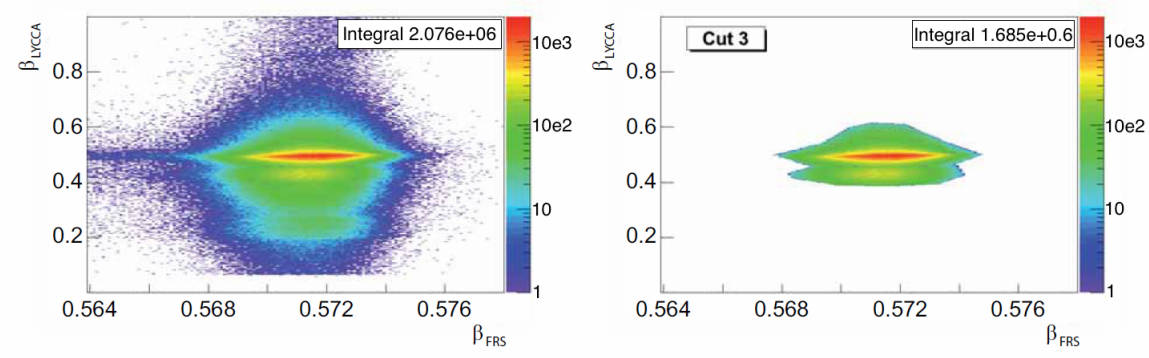

Figure 6.4: The $\beta_{LYCCA-0}$ vs. β_{FRS} plot both before and after the chosen gate for the ^{36}Ar setting. Figure courtesy of Andreas Wendt, University of Cologne [67].

Additionally, a gate was applied to the $\beta_{LYCCA-0}$ vs. E_{CsI} correlation, where E_{CsI} is the energy deposited in the CsI detectors. Figure 6.5 shows the $\beta_{LYCCA-0}$ vs. E_{CsI} plot both before and after the chosen gate for the ^{36}Ar setting.

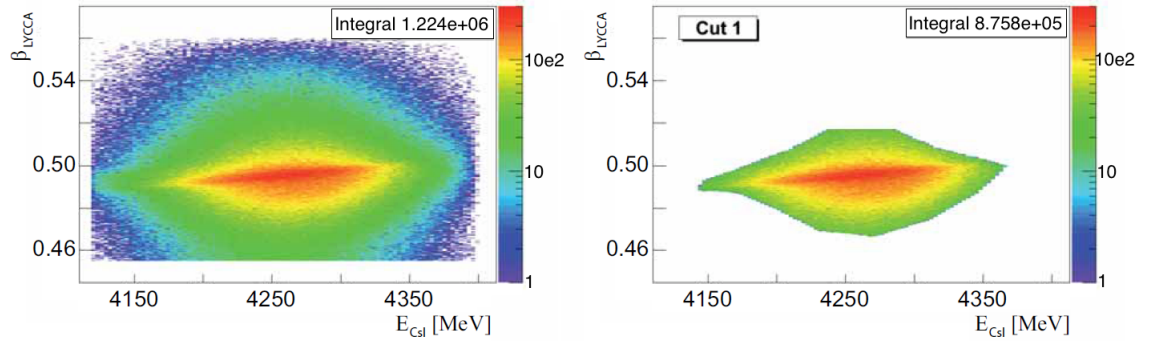

Figure 6.5: The $\beta_{LYCCA-0}$ vs. E_{CsI} plot both before and after the chosen gate for the ^{36}Ar setting. Figure courtesy of Andreas Wendt, University of Cologne [67].

Finally, a gate was applied to the time difference (SC41 to target DSSSD) vs. energy correlation of the target DSSSD. Figure 6.6 shows the time vs. energy plot for both before and after the chosen gate for the ^{36}Ar setting.

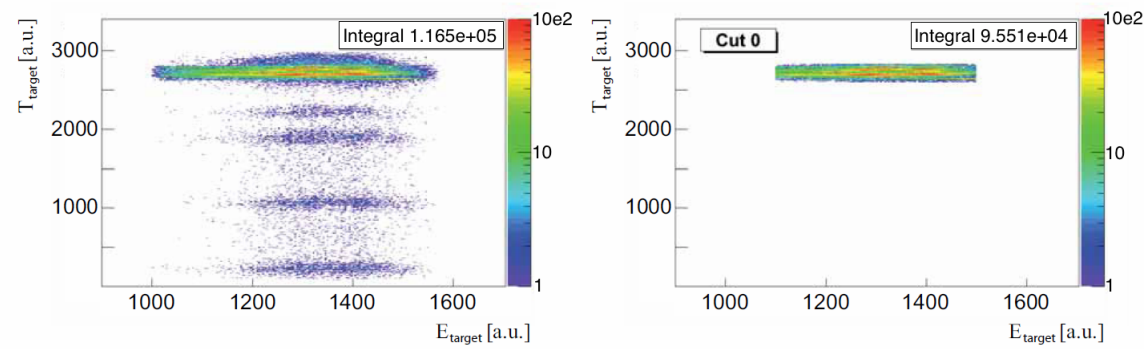

Figure 6.6: The time vs. energy plot of the target DSSSD both before and after the chosen gate for the ^{36}Ar setting. Figure courtesy of Andreas Wendt, University of Cologne [67].

Following the application of the various particle gates, a timing gate was applied to the time information recorded with the RISING detectors. Figure 6.7 shows the Doppler corrected time vs. energy matrix following the application of the particle gates discussed above. The spectrum contains events for a germanium crystal multiplicity of 1 ('singles') and a crystal multiplicity of 2 where an addback method was applied.

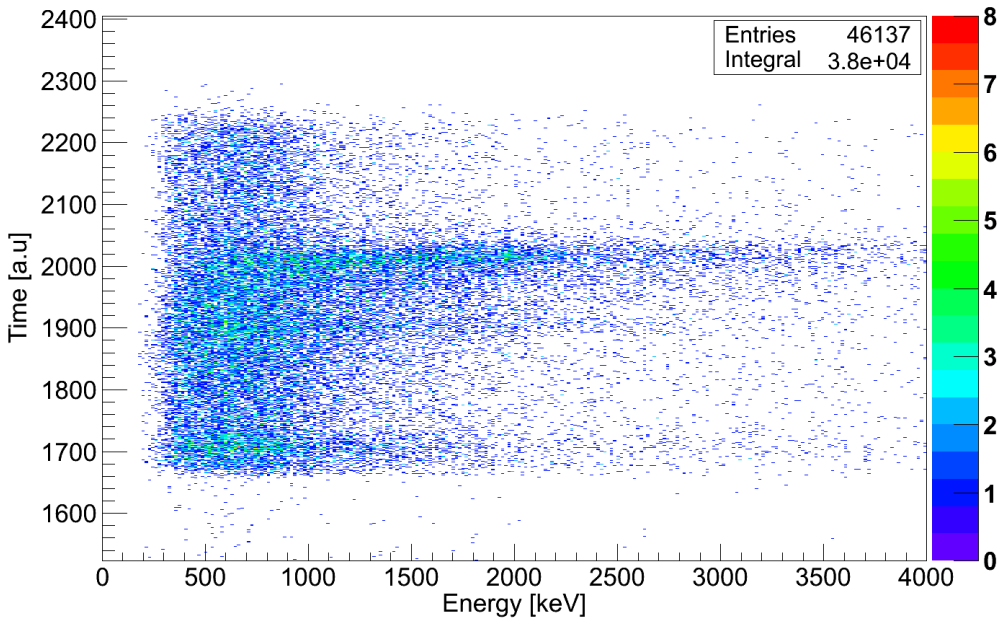

Figure 6.7: The time vs. energy matrix of the RISING array following the application of the particle gates discussed in subsection 6.2.1 for the ^{36}Ar setting. The matrix contains singles and addback (crystal multiplicity=2) events. Data courtesy of Andreas Wendt, University of Cologne.

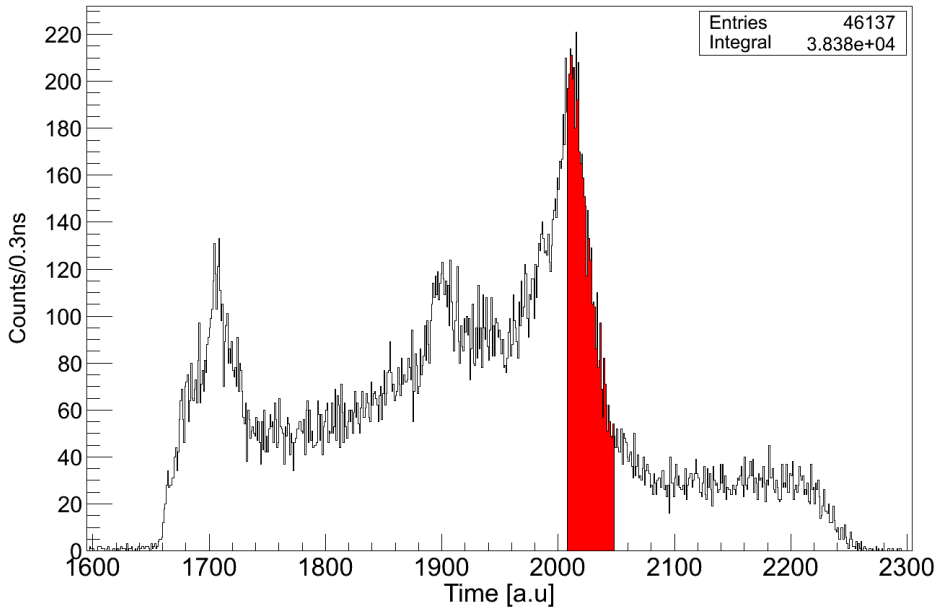

Figure 6.8: The time spectrum of the RISING array for the ^{36}Ar setting. The chosen time gate is highlighted in red (see text for details). Data courtesy of Andreas Wendt, University of Cologne.

Projecting the y-axis of the matrix seen in figure 6.7 results in the time spectrum seen in figure 6.8. An energy threshold was also applied to the data which has the effect of removing x-rays associated with the atomic background from the low energy regions of the spectra. A hardware threshold of ∼500 keV was applied using the constant fraction discriminators (CFDs) and a software threshold of 300 keV was applied.

The peak structure at channel ∼2000 in figure 6.8 corresponds to the 'prompt' peak. The prompt peak contains events where γ-rays were emitted from the secondary target location (γ-rays that reach the RISING crystals first) which includes the γ-rays of interest emitted by the ^{36}Ar and ^{33}Ar ions. The other regions in the spectrum correspond to other sources of radiation leaving a trace in the germanium crystals such as ions and other particles (α-particles and protons) leaving the FRS, and interacting with matter along the beam line causing the emission of high energy γ-rays. The typical energy of a heavy ion leaving the secondary target is of the order ∼150 MeV/u, meaning that further fragmentation will occur as the ions penetrate through the LYCCA-0 detectors.

In order to discard events contributing to the background, a time gate was applied

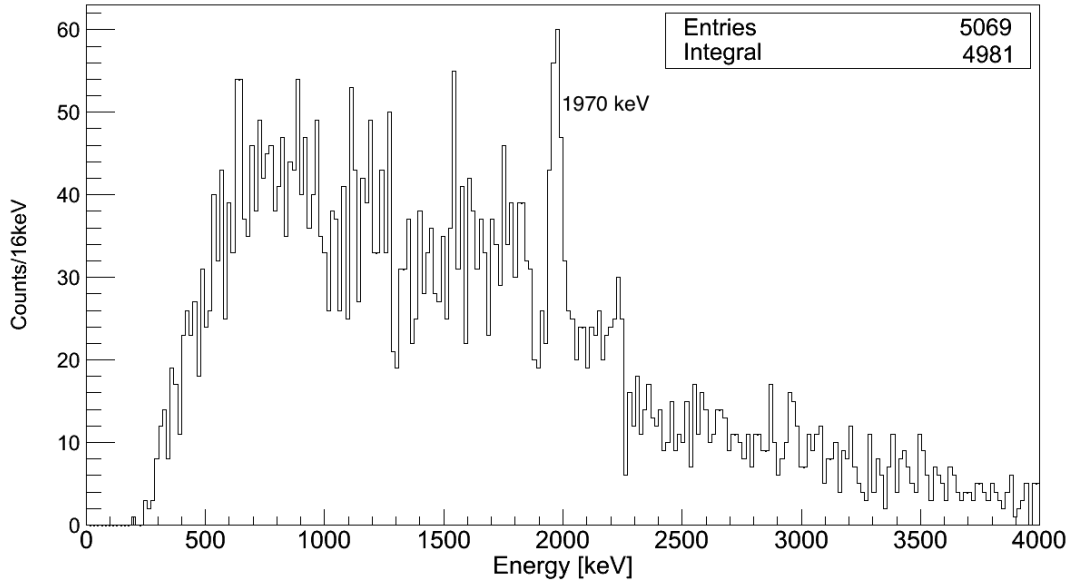

Figure 6.9: The energy spectrum showing the relativistic Coulomb excitation of ^{36}Ar. The spectrum contains singles and addback (crystal multiplicity=2) events. Data courtesy of Andreas Wendt, University of Cologne.

to the right-hand side of the prompt peak (see reference [67] for further details). The right-hand side of the peak was chosen since photons emitted from the ^{36}Ar ions will reach the germanium detectors first as opposed to the other particles mentioned previously that travel at lower velocities.

6.2.2 ^{36}Ar: Experimental Spectra

Projecting the x-axis of the matrix displayed in figure 6.7 between the channels corresponding to the chosen time gate results in the energy spectrum displayed in figure 6.9. Figures 6.10 and 6.11 show the same data as figure 6.9, but for singles and addback (crystal multiplicity=2) events individually. The transition from the $2^+ \rightarrow 0^+_{g.s}$ resulting from the Coulomb excitation can be seen at 1970 keV and sits above an exponentially decaying background extending to more than 4 MeV.

6.2.3 ^{33}Ar: Experimental Spectra

Projecting the x-axis of the time vs. energy matrix for the ^{33}Ar data between the channels corresponding to the chosen time gate results in the energy spectrum displayed in figure 6.12. Figure 6.13 and 6.14 shows the same data as figure 6.12

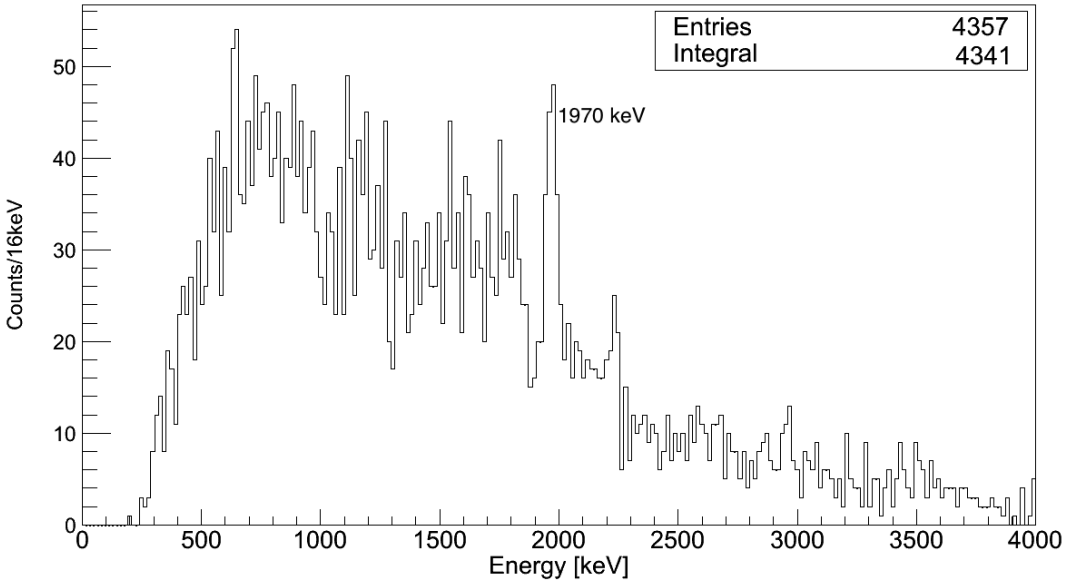

Figure 6.10: The singles energy spectrum showing the relativistic Coulomb excitation of ^{36}Ar. Data courtesy of Andreas Wendt, University of Cologne.

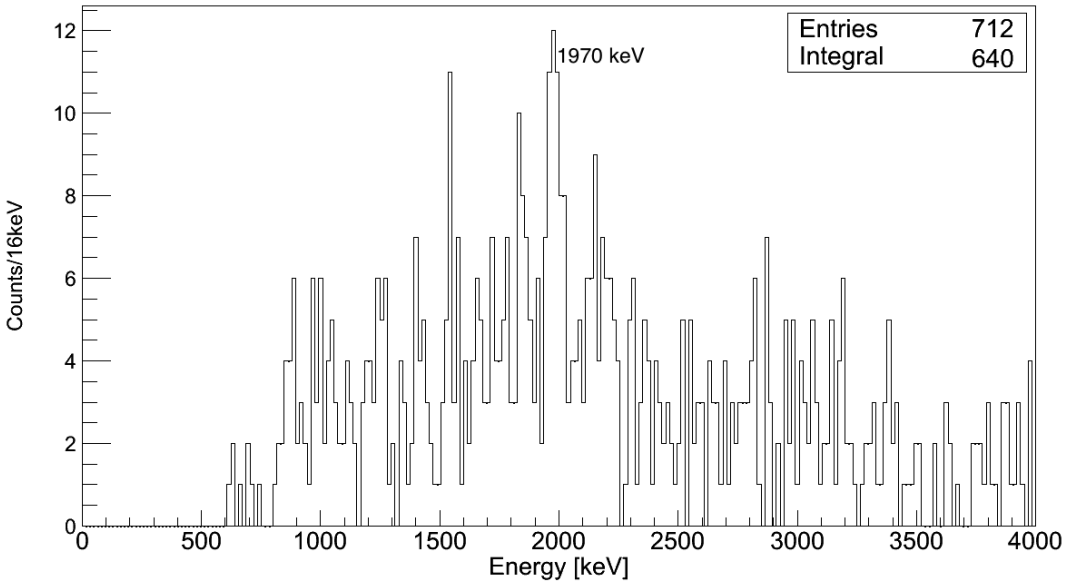

Figure 6.11: The addback (crystal multiplicity=2) energy spectrum showing the relativistic Coulomb excitation of ^{36}Ar. Data courtesy of Andreas Wendt, University of Cologne.

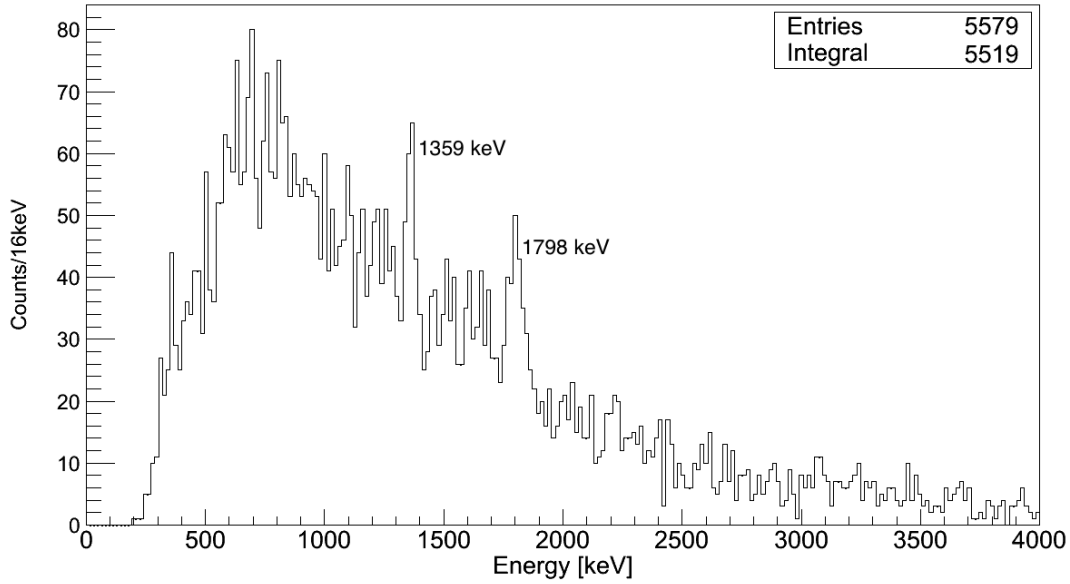

Figure 6.12: The experimental energy spectrum showing the relativistic Coulomb excitation of ^{33}Ar. The spectrum contains singles and addback (crystal multiplicity=2) events. Data courtesy of Andreas Wendt, University of Cologne.

but for singles and addback (crystal multiplicity=2) events individually.

The transition between the $\frac{3}{2}^+ \rightarrow \frac{1}{2}^+$ states can be seen at 1359 keV, and the transition between the $\frac{5}{2}^+ \rightarrow \frac{1}{2}^+$ states can be seen at 1798 keV. Both peaks are situated on an exponentially decaying background extending over 4 MeV. The 437 keV peak from the $\frac{5}{2}^+ \rightarrow \frac{3}{2}^+$ transition lies beneath the energy threshold and is therefore not visible.

6.3 RISING Simulations

The goal of the RISING simulations was to achieve simulated spectra that provide a similar spectral response to the experimental spectra, in order to determine the simulation settings to be used for the AGATA simulations discussed later in the current chapter.

6.3.1 Atomic Background Considerations

In order to save simulation run-time, an assumption was made that each event in the input event file contains an excited nucleus at the target position, whereas experimentally there will be many events containing unreacted secondary beam from

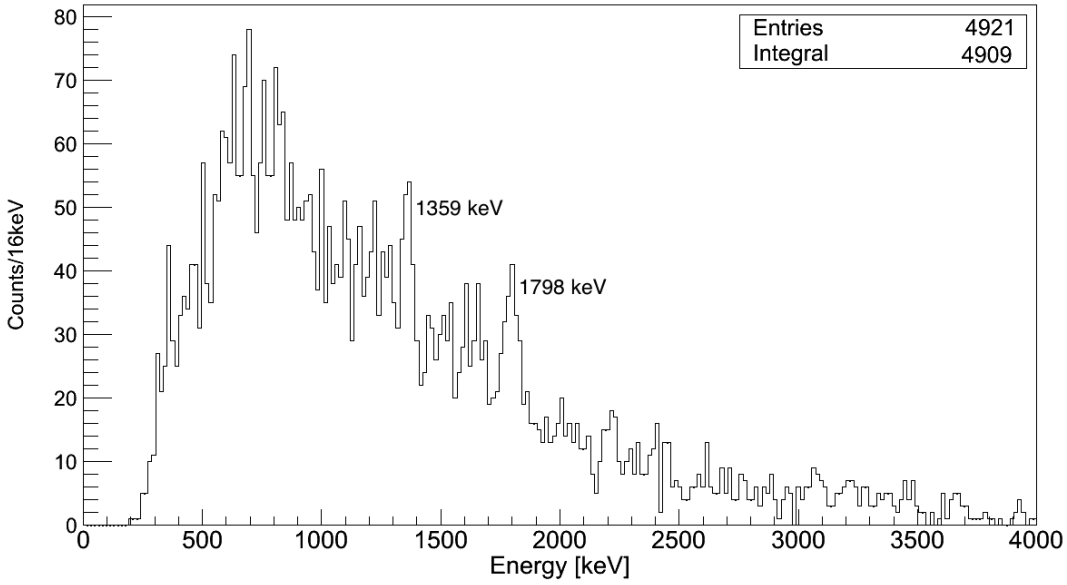

Figure 6.13: The singles energy spectrum showing the relativistic Coulomb excitation of ^{33}Ar. Data courtesy of Andreas Wendt, University of Cologne.

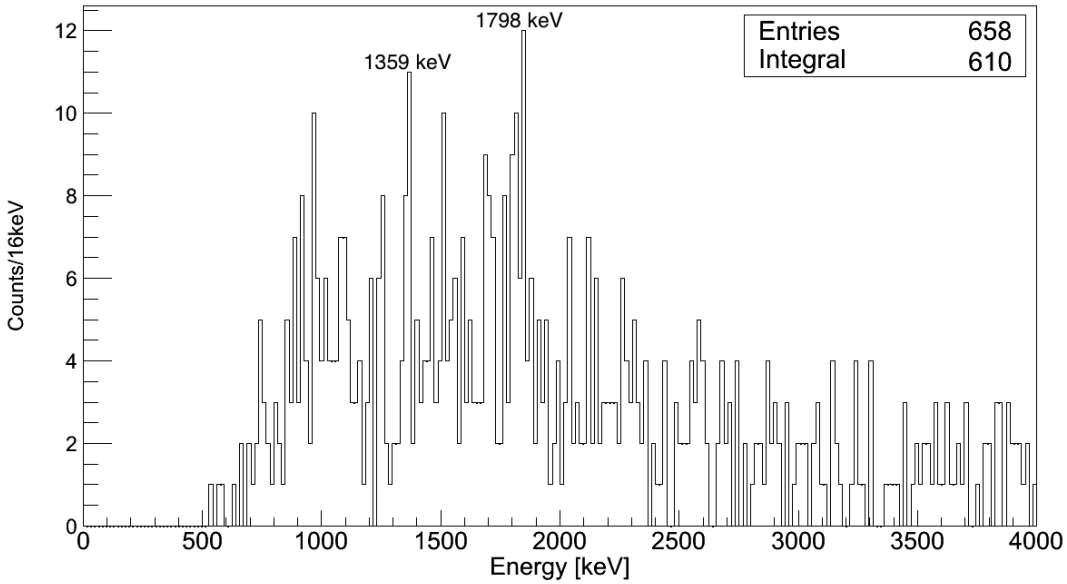

Figure 6.14: The addback (crystal multiplicity=2) energy spectrum showing the relativistic Coulomb excitation of ^{33}Ar. Data courtesy of Andreas Wendt, University of Cologne.

anywhere in the beam line. Since each event contains an excited nucleus, the cross section value for the Coulomb excitation given by DWEIKO can be compared with the cross section for the production of the atomic background processes given by ABKG, in order to give a physical value for the multiplicity of the atomic background per event to include in the simulations.

For the ^{36}Ar setting, the cross section determined by ABKG is 6.895×10^4 b and the Coulomb excitation cross section determined by DWEIKO is 0.683×10^2 mb. Therefore, the ratio between either cross section implies that $\sim 10^6$ x-rays are required to be included per event in the simulations. For an events file containing 10,000 events, $\sim 10^{10}$ x-rays would be included in the simulation. Similarly for the ^{33}Ar setting, the ratio between the cross section implies that $\sim 10^9$ x-rays would need to be included for an events file containing 10,000 events. Merging an input events file with these levels of atomic background takes a considerable amount of time and results in a file size of $\sim$370 GB. Running such an events file through the AGATA code additionally takes a considerable amount of time, and the output files are split into 2GB chunks by default, of which there would be $\sim$ 70 files in total.

The AGATA code terminates at 1×10^9 emitted particles and therefore the final output file would be incomplete before the end of the input events file is reached. Since each output file from the AGATA code contains a header detailing the simulation, an additional step would be required to merge all the output files into a single file whilst removing the headers, in order for the file to be in the format required for the event processing/reconstruction stage. This step also increases the simulation time significantly.

In order to reduce simulation run-time, the atomic background was therefore removed from the RISING simulations. To validate this, a simulation was run containing only atomic background, without and with the absorbers placed in front of the RISING array (see figures 6.15 and 6.16). In order to determine the shape of the spectrum and to stay within the allowed number of particle emissions governed by the AGATA code, the simulations contained 5,000 events, with each event containing 100,000 x-ray emissions.

As can be seen in figure 6.15, the inclusion of the absorbers results in the highest point of the atomic background distribution being less than the energy threshold ($\sim$700 keV) which is later applied to the data. Therefore it was deemed acceptable to remove the atomic background from the RISING simulations to save simulation

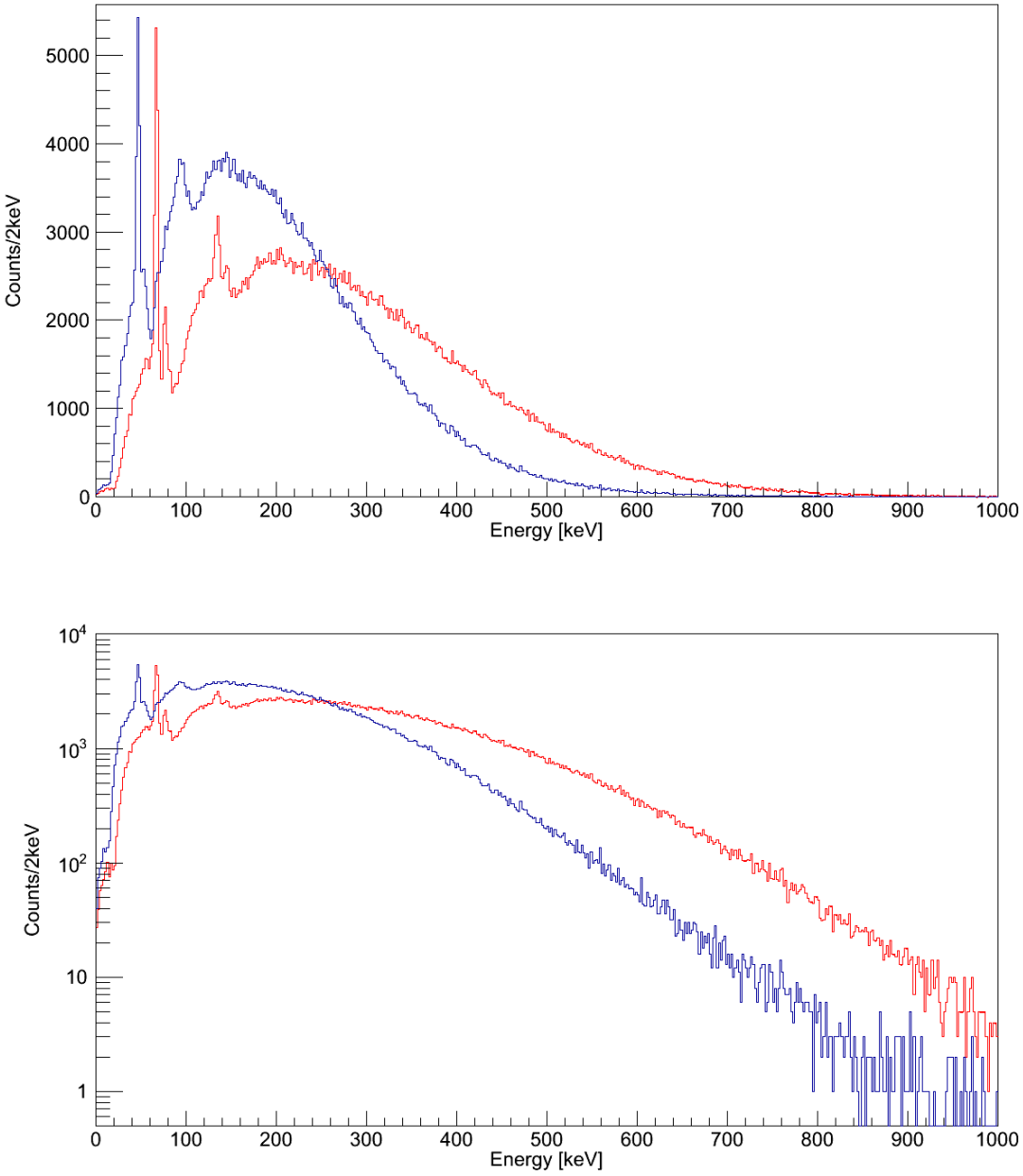

Figure 6.15: The top spectrum shows the spectrum containing only atomic background events in both the centre-of-mass frame (blue) and laboratory frame (red) ona linear scale, for a simulation without the absorbers placed in front of the RISING clusters for the ^{36}Ar setting. The bottom spectrum shows the same on a logarithmic scale. Neither spectra have any applied particle gates.

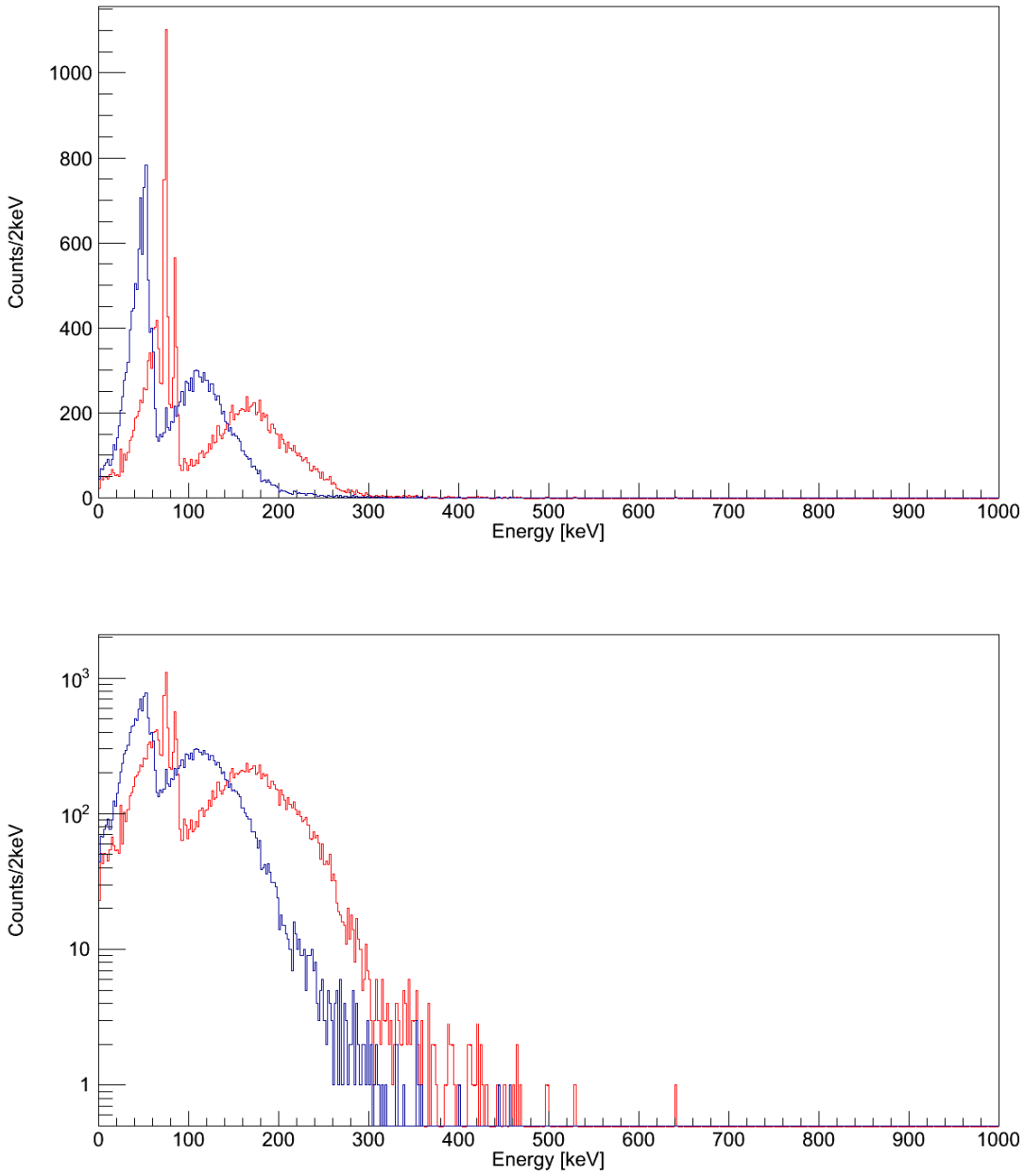

Figure 6.16: The top spectrum shows the spectrum containing only atomic background events in both the centre-of-mass frame (blue) and laboratory frame (red) on a linear scale, for a simulation with the absorbers placed in front of the RISING clusters for the ^{36}Ar setting. The bottom spectrum shows the same on a logarithmic scale. Neither spectra have any applied particle gates.

run-time. The atomic background will need to be reconsidered for the AGATA simulations as no absorbers are used with this array.

6.3.2 ^{33}Ar: Determination of the Branching Ratio

In order to determine the correct amount of each transition in ^{33}Ar to include in the simulations, the branching ratio of the decay from the $\frac{5}{2}^+$ state to either the $\frac{1}{2}^+$ (ground state) state or to the $\frac{3}{2}^+$ state must be determined. A DWEIKO calculation showed that the cross section for directly populating the $\frac{5}{2}^+$ state is $\sigma = 0.109 \times 10^3$ mb (see figure 4.14) and is $\sigma = 0.608 \times 10^{-3}$ mb for the $\frac{3}{2}^+$ state. As the cross section for populating the $\frac{5}{2}^+$ state is ∼179,000 times larger than that of the $\frac{3}{2}^+$ state, an assumption is made in the simulations that only the $\frac{5}{2}^+$ state is populated via Coulomb excitation. The $\frac{3}{2}^+$ state is therefore assumed to be 100% fed from the $\frac{5}{2}^+$ state. The branching ratio for the decay of the $\frac{5}{2}^+$ state can be determined from the peak areas in the experimental ^{33}Ar spectrum, however, a correction must be applied for the efficiency of the RISING array. Using the peak areas and the efficiency value of the RISING array for the 1359 keV and 1798 keV γ-rays, the true number of emitted γ-rays can be determined and the branching ratio calculated.

An experimental efficiency curve for the RISING array was unavailable, therefore a simulated efficiency curve was created in response to a stationary ^{56}Co source located at the target position, as can be seen in figure 6.17.

The efficiency curve shown in figure 6.17 is not a true reflection of an efficiency curve expected from typical experimental conditions at GSI. Due to the Lorentz boost, the efficiency of the inner ring would in fact be greater than the efficiency of the outer rings. The dependence of the efficiency on the incident γ-ray energies would however remain the same, and therefore it was deemed acceptable to determine the branching ratio from this efficiency curve.

The region in the experimental spectrum where the 1798 keV peak is situated is contaminated with a larger amount of background primarily from the outer detector rings (see figure 6.18), which results in the broadening of the peak. Therefore, the areas of each peak used to calculate the branching ratio was determined from the experimental inner ring spectrum, displayed in figure 6.19.

Using the fit function described in subsection 6.3.3, the inner ring spectrum was fit which allowed for the peak areas to be extracted, as displayed in figure 6.20. A

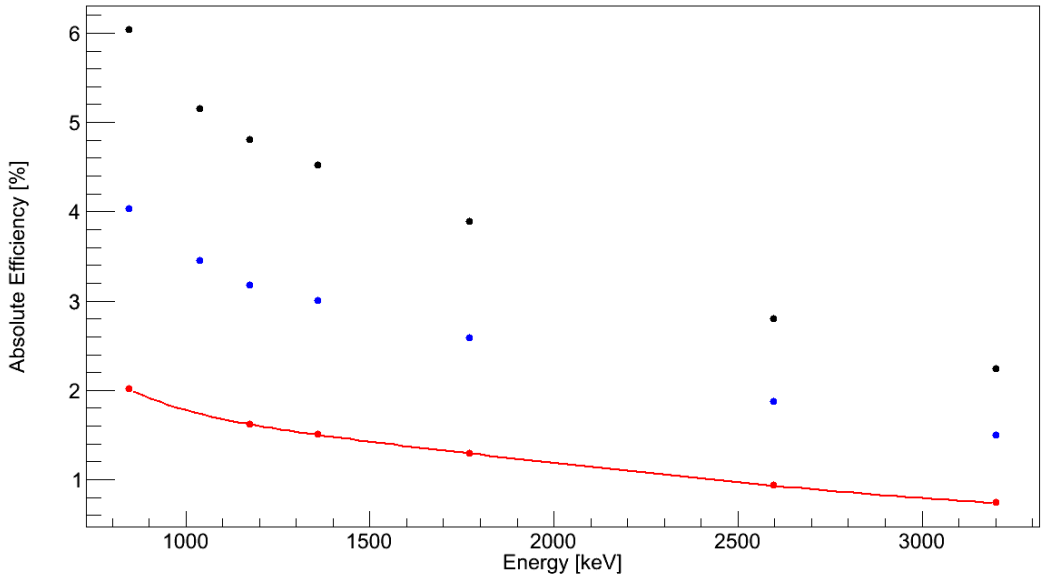

Figure 6.17: A simulated absolute efficiency curve of the RISING array in response to a stationary ^{56}Co source located at the target position. The bottom dataset (red) represents the inner ring which was used to determine the ^{33}Ar branching ratio, the middle dataset (blue) represents the outer rings, and the top dataset (black) represents the total array.

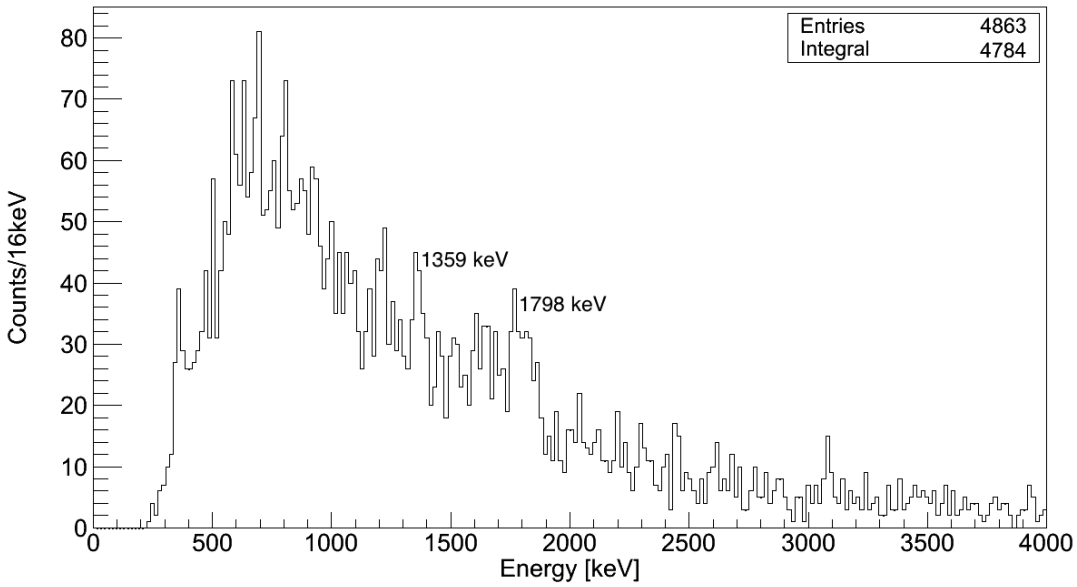

Figure 6.18: The ^{33}Ar RISING outer rings spectrum containing singles and addback (crystal multiplicity=2) events. The 1798 keV peak is broadened due to higher background in the region, only present in the outer rings spectrum.

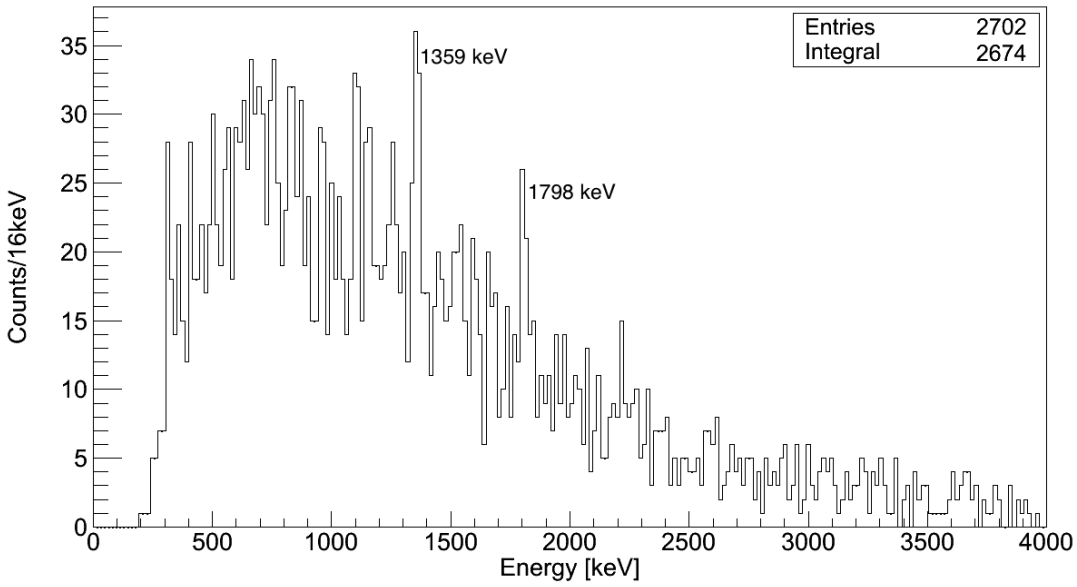

Figure 6.19: The ^{33}Ar RISING inner ring spectrum containing singles and addback (crystal multiplicity=2) events.

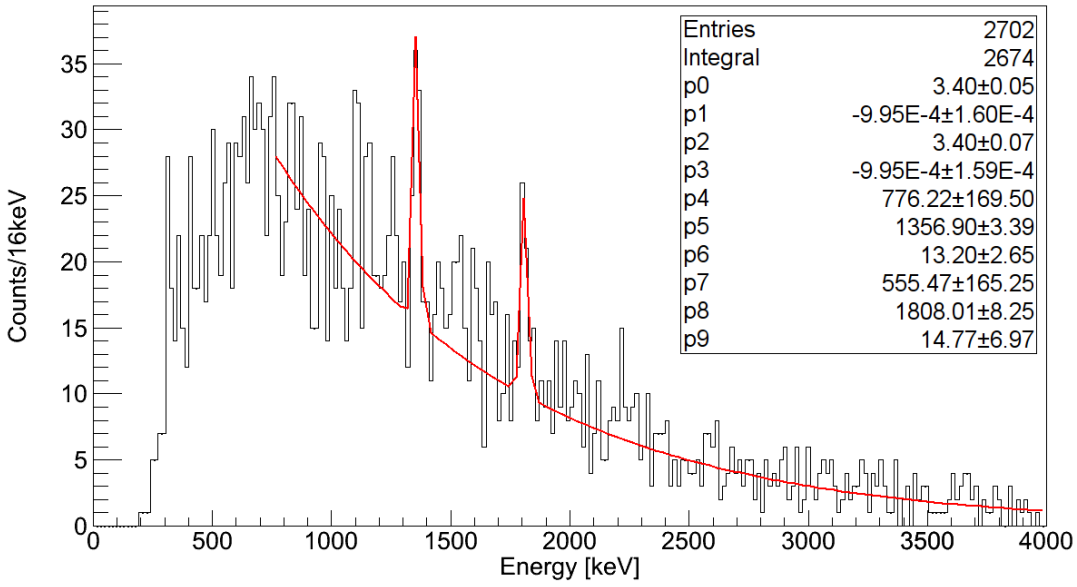

Figure 6.20: The ^{33}Ar RISING inner ring spectrum and the fit function.

function of the following form [68] was fit to the inner ring efficiency data (see figure 6.17) between 846 keV and 3201 keV, where E is the energy [MeV] and p_i are the fit parameters:

$$\epsilon(E,p) = \left[p_1 + p_2\, ln(E) + p_3\, ln^2(E) + p_4\, ln^3(E) + p_5\, ln^5(E) + p_6\, ln^7(E)\right]/E. \tag{6.1}$$

This allowed for the absolute efficiency to be determined at 1359 keV and 1798 keV, which was 1.50% and 1.28% respectively. Using the peak areas extracted from the inner ring spectrum, and correcting for the efficiencies, the branching ratio was determined to be $0.56 : 0.44$ ($\frac{5}{2}^+ \rightarrow \frac{3}{2}^+ \rightarrow \frac{1}{2}^+ : \frac{5}{2}^+ \rightarrow \frac{1}{2}^+$).

6.3.3 Determination of the High Energy Background Multiplicity

The high energy background multiplicity per simulated event must be determined in order to compare the simulated spectra with the experimental spectra. This was achieved by varying the multiplicity during the merging process (see subsection 4.2.6) and extracting the P/T from the simulated spectrum for comparison with the experimental P/T. For each setting, the total area of the spectra was taken between 700 keV-4000 keV due to dissimilarities in the lower region of the spectra between the experiment and simulation. This is possibly due to the global energy threshold applied to the simulated data. An energy threshold applied to each individual crystal may provide a better comparison in the lower energy region. The shape of the singles and singles+addback spectra (as seen in figures 6.9, 6.10, 6.12 and 6.13) can be described by Gaussian peaks on an exponentially decaying background. In order to gauge the correct level of background for the ^{36}Ar setting, exponential functions were individually fit between the regions 700-1450 keV and 2300-4000 keV. The purpose of this was to avoid the Compton edge structure at ∼1744 keV as it is not true background, and also to avoid the unknown structure at ∼2200 keV (see figure 6.21). The same method was also applied to the ^{33}Ar spectra for consistency. The exponential functions were then combined with a normalised Gaussian function to give the complete function:

$$f(x) = p_0\, exp(p_1\, x) + p_2\, exp(p_3\, x) + p_4\, exp\left(-0.5\left((x - p_5)/\, p_6\right)^2/\sqrt{2\,\pi}\, p_6\right), \tag{6.2}$$

where $p_0 - p_3$ are the fit parameters of the exponential components and $p_4 - p_6$ are the fit parameters for the Gaussian component.

For the ^{33}Ar setting, individual exponential functions were fit between 750 keV-1000 keV and 2300 keV-4000 keV, which were then combined with two normalised Gaussian functions:

$$f(x) = p_0\, exp(p_1\, x) + p_2\, exp(p_3\, x) + p_4\, exp\left(-0.5\left((x - p_5)/\, p_6\right)^2/\sqrt{2\,\pi}\, p_6\right) + p_7\, exp\left(-0.5\left((x - p_8)/\, p_9\right)^2/\sqrt{2\,\pi}\, p_9\right). \tag{6.3}$$

For both the ^{36}Ar and ^{33}Ar spectra, the values of the parameters determined from the exponential shoulders ($p_0 - p_3$) were not fixed, but set as initial guesses in equations 6.2 and 6.3. As a result, the exponential parameters in the final fit have similar values. Figures 6.21 and 6.22 shows the fits for the singles and singles+addback data for both ^{36}Ar and ^{33}Ar, and tables 6.1 and 6.2 summarises the P/T, FWHM and energy resolutions extracted from the fits.

The high energy background multiplicity was incremented per simulation, with the multiplicity ranging from 10 high energy γ-rays per event to 50 per event. The resulting spectra following the processing were fit with identical functions as described above, and the P/T values were extracted. The P/T values were then compared with the experimental P/T values to determine a multiplicity that produced the same P/T as the experimental spectra. The simulation P/T values as a function of the high energy background multiplicity are displayed in figure 6.23.

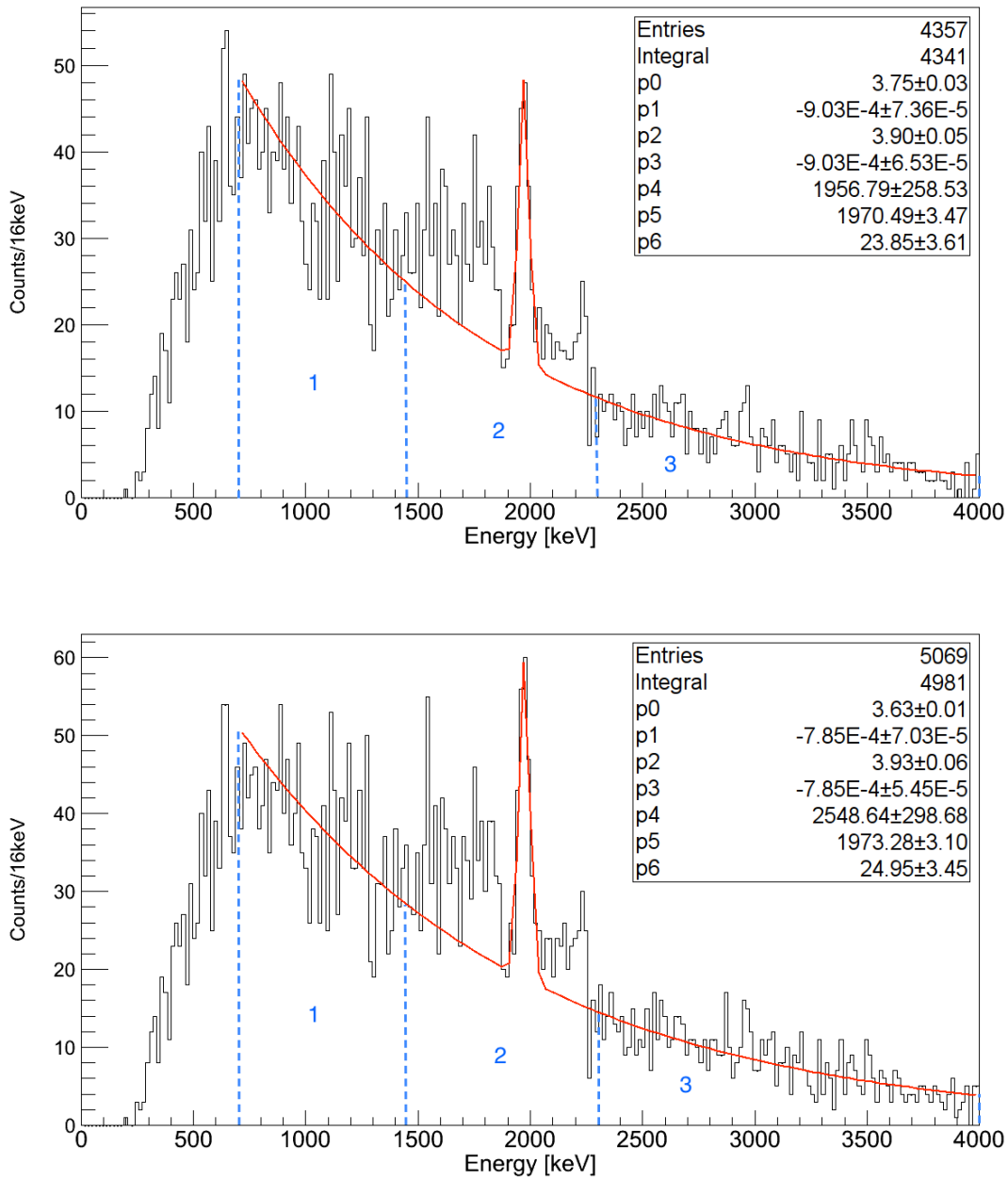

Figure 6.21: The fitted experimental spectra for ^{36}Ar for both singles (top) and singles+addback (bottom). Regions 1 and 3 represent the location of the exponential shoulders that were individually fit, and region 2 represents the location of the Gaussian fit.

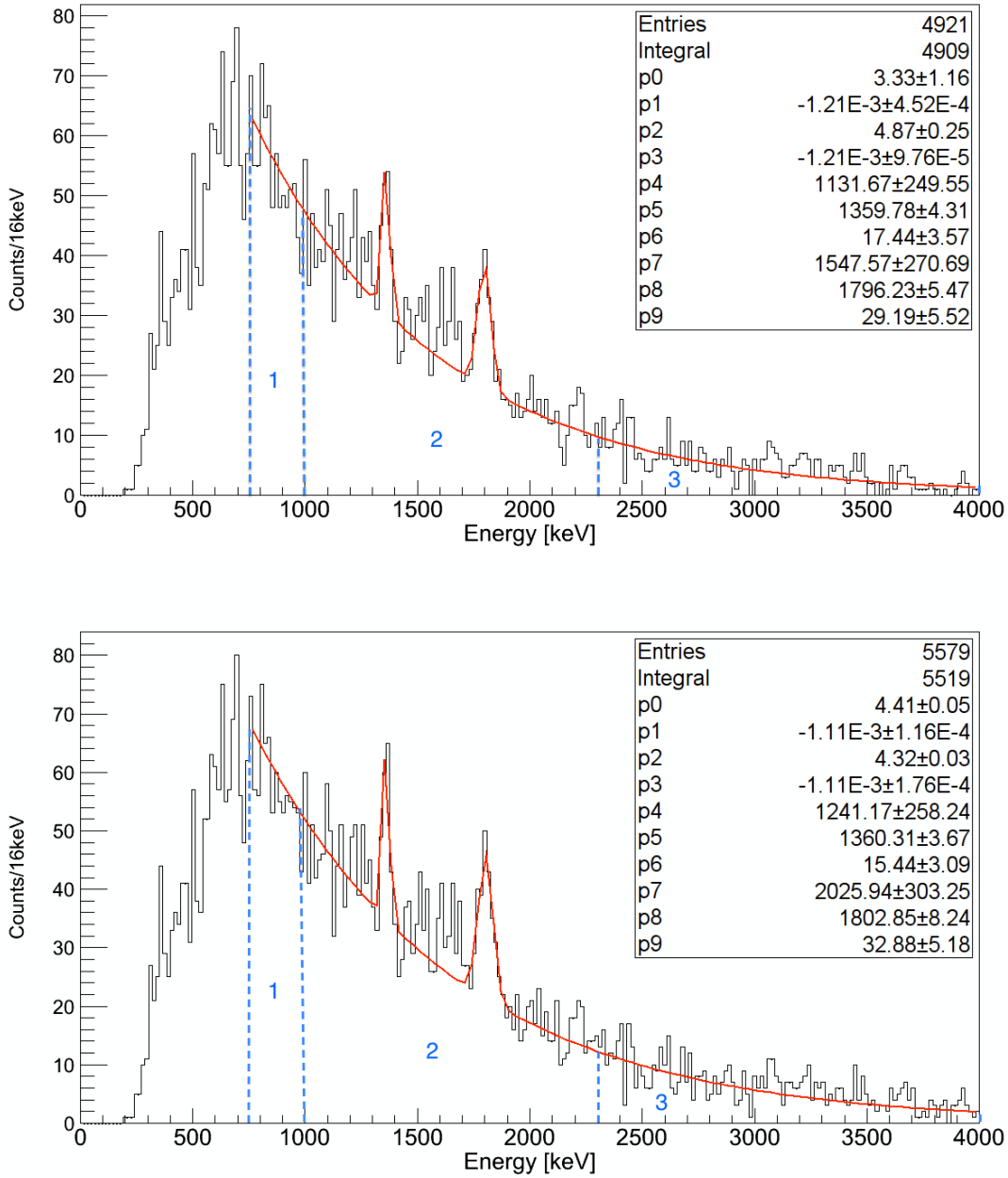

Figure 6.22: The fitted experimental spectra for ^{33}Ar for both singles (top) and singles+addback (bottom). Regions 1 and 3 represent the location of the exponential shoulders that were individually fit, and region 2 represents the location of the Gaussian fits.

	^{36}Ar: 1970 keV	
	singles	singles+addback
FWHM [keV]	56.05±8.48	58.63±8.10
P/T [%]	3.31±0.44	3.68±0.44
E_{res} [%]	2.84±0.43	2.97±0.41

Table 6.1: A summary of the FWHM, P/T and energy resolution values extracted from the experimental ^{36}Ar spectra.

	^{33}Ar			
	1359 keV		1798 keV	
	singles	singles+addback	singles	singles+addback
FWHM [keV]	40.99±8.39	36.28±7.27	68.59±12.98	77.26±12.18
P/T [%]	1.82±0.40	1.73±0.36	2.49±0.44	2.82±0.42
E_{res} [%]	3.01±0.62	2.67±0.53	3.82±0.72	4.29±0.68

Table 6.2: A summary of the FWHM, P/T and energy resolution values extracted from the experimental ^{33}Ar spectra.

Using the point of intersection between the experimental P/T values (blue dashed line) and the simulated functions (red) displayed in figure 6.23, it was possible to determine the high energy background multiplicity per simulated event that yields an identical P/T value between the simulated and experimental spectra. For the ^{36}Ar setting, the multiplicity of the high energy background per simulated event is 19, and for the ^{33}Ar setting, the multiplicity is 18.

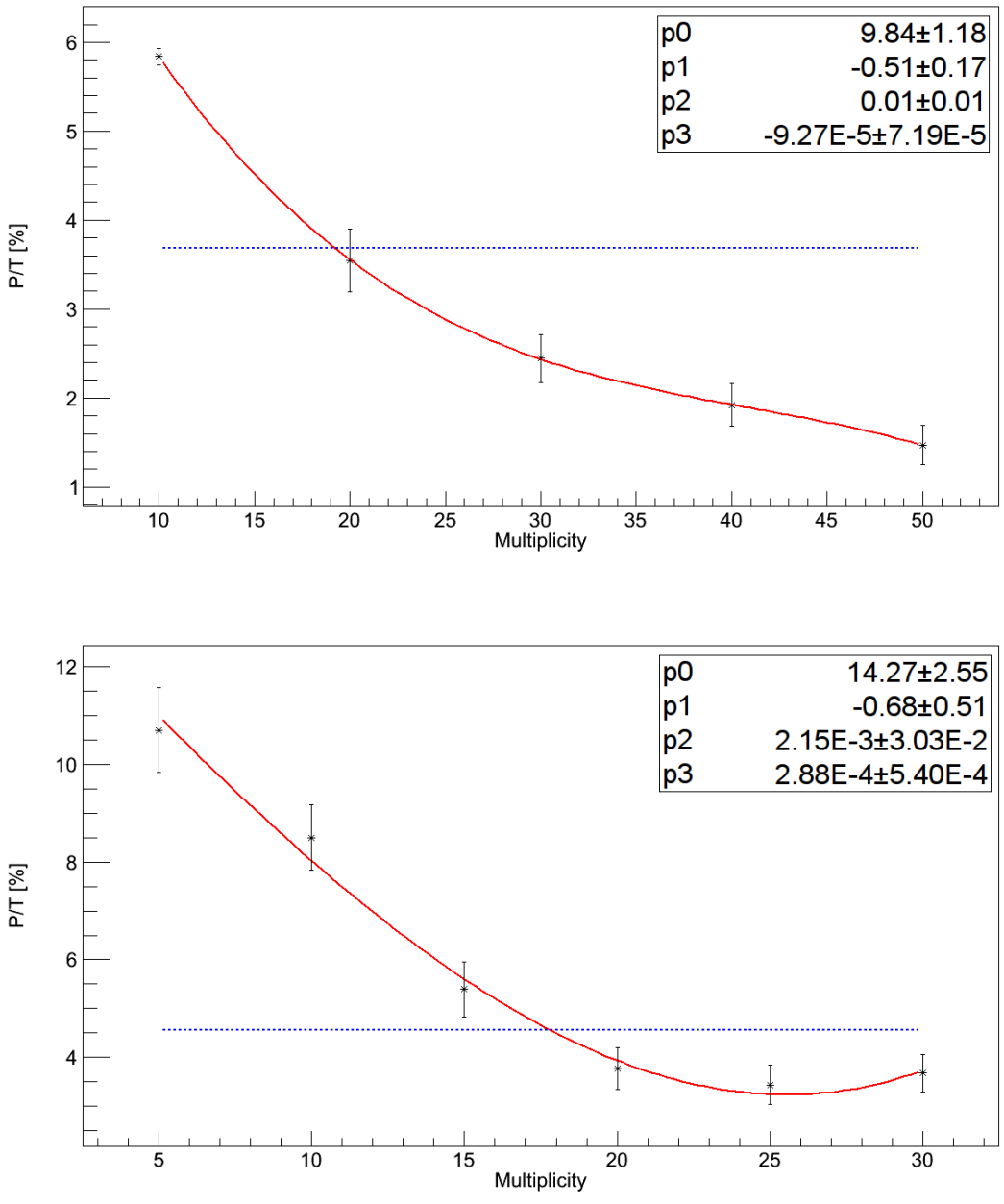

Figure 6.23: The P/T values as a function of the high energy background multiplicity per simulated event, for both the ^{36}Ar (top) and ^{33}Ar (bottom) setting. For the ^{33}Ar setting, the P/T value represents the sum of both the 1359 keV and 1798 keV peaks to the total number of counts between 700 keV and 4000 keV. The simulated P/T data was fit with 3rd order polynomials. The experimental P/T values are indicated by the blue dashed lines.

6.3.4 Simulation Particle Gate Conditions

For each simulated setting, only one heavy ion is simulated (i.e. ^{36}Ar or ^{33}Ar) without any additional contaminants. The gating conditions are therefore simpler than the experimental gating conditions discussed in subsection 6.2.1. The following conditions were applied to the simulated data:

1. An energy threshold of 700 keV was applied to the uncorrected RISING energies. The threshold is slightly higher than the threshold applied to the experimental data, however, a threshold of 700 keV gave the best results in terms of matching the lower portion of the background in the simulated spectra to the experimental spectra. A comparison between the simulated and experimental ^{36}Ar spectra with an energy threshold of 500 keV (as applied experimentally with the CFDs) is displayed in figure 6.24

2. A requirement for events in both the target DSSSD and wall DSSSDs, allowing selection of events where the recoil direction could be determined, resulting in properly Doppler corrected events.

3. A gating condition applied to the calculated mass distribution for each ion, allowing selection of events where the total kinetic energy and β of the heavy ions could be determined.

6.3.5 ^{36}Ar: Simulation and Experiment Comparison

The comparison between the simulated and experimental RISING spectra for the ^{36}Ar setting is displayed in figure 6.25. The spectra were normalised using the area of the 1970 keV peaks. Figure 6.24 displays the same comparison, however, an energy threshold of 500 keV has been applied to the simulated data (whereas an energy threshold of 700 keV has been applied to the simulated data in figure 6.25) to match the threshold applied experimentally with the CFDs.

6.3.6 ^{33}Ar: Simulation and Experiment Comparison

The final comparison between the simulated and experimental RISING spectra for the ^{33}Ar setting is displayed in figure 6.26. The sum of the peak areas were not suitable for normalisation due to the background contamination in the region of

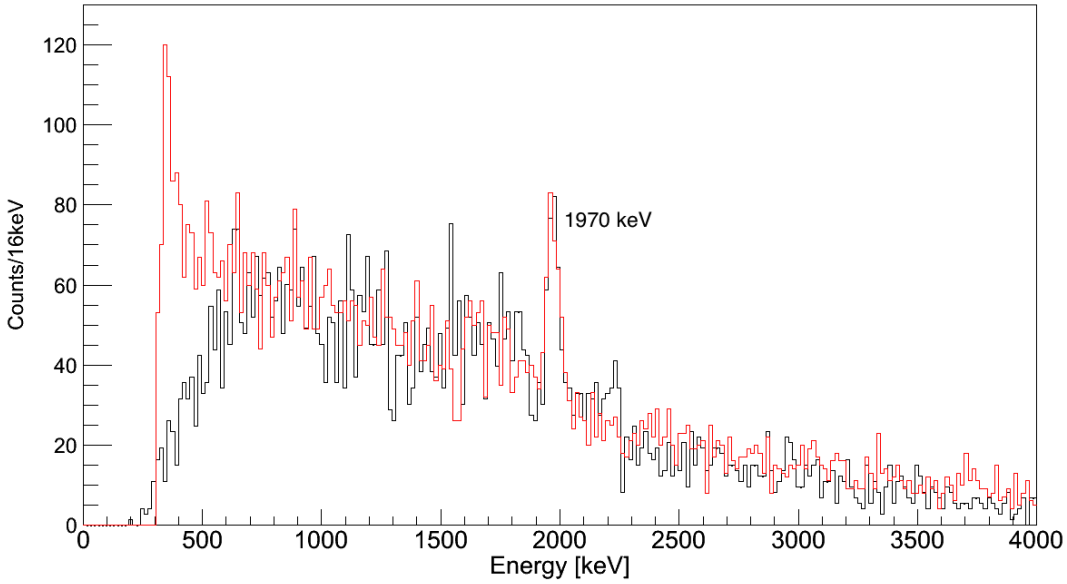

Figure 6.24: A comparison between the simulated (red) and experimental (black) RISING spectra for ^{36}Ar. An energy threshold of 500 keV has been applied to the simulated data matching the threshold applied experimentally with the CFDs. The lower energy region (<600 keV) of the spectra are not well matched at this energy threshold value. The spectra contain singles and addback (crystal multiplicity=2) events.

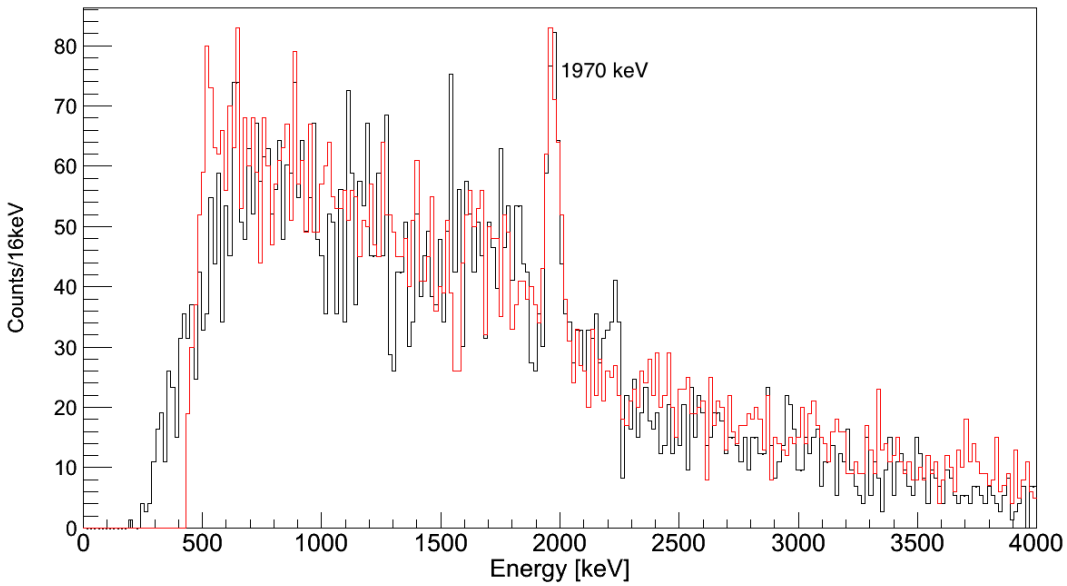

Figure 6.25: The final comparison between the simulated (red) and experimental (black) RISING spectra for ^{36}Ar. The spectra contain singles and addback (crystal multiplicity=2) events.

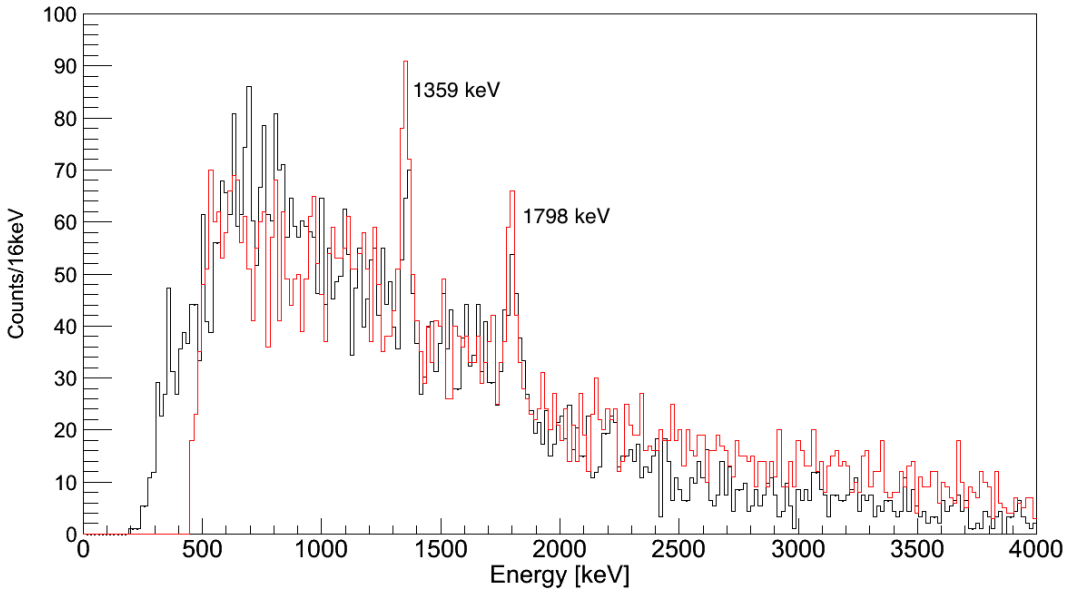

Figure 6.26: The final comparison between the simulated (red) and experimental (black) RISING spectra for ^{33}Ar. The spectra contain singles and addback (crystal multiplicity=2) events.

the 1798 keV peak in the experimental spectrum arising from the outer RISING rings (see subsection 6.3.2). The spectra were therefore normalised using the P/T values. As the simulated spectrum does not include the contamination present in the region of the higher energy peak, and since the P/T was taken as the sum of both peaks in the ^{33}Ar spectra, the quality of the comparison is not as good as the ^{36}Ar setting (see subsection 6.3.5). Additionally, the E2 angular distribution produced with DWEIKO was used to assign an emission direction to the 1359 keV γ-rays (see subsection 4.2.3), whereas the transition is an M1 transition. The intensity of the simulated 1359 keV peak may differ to that seen in the experimental spectra.

As discussed in subsection 6.3.2, the experimental RISING inner ring does not contribute to the background contamination in the 1798 keV peak region. Figure 6.27 displays the comparison between the simulated and experimental RISING inner ring spectra. Although the peaks are better matched than in figure 6.26, there is a mismatch in the background - particularly in the lower energy region. This suggests that further adjustments should be made to the high energy background component in the ^{33}Ar simulations (see subsection 4.2.5) in order to obtain a better comparison.

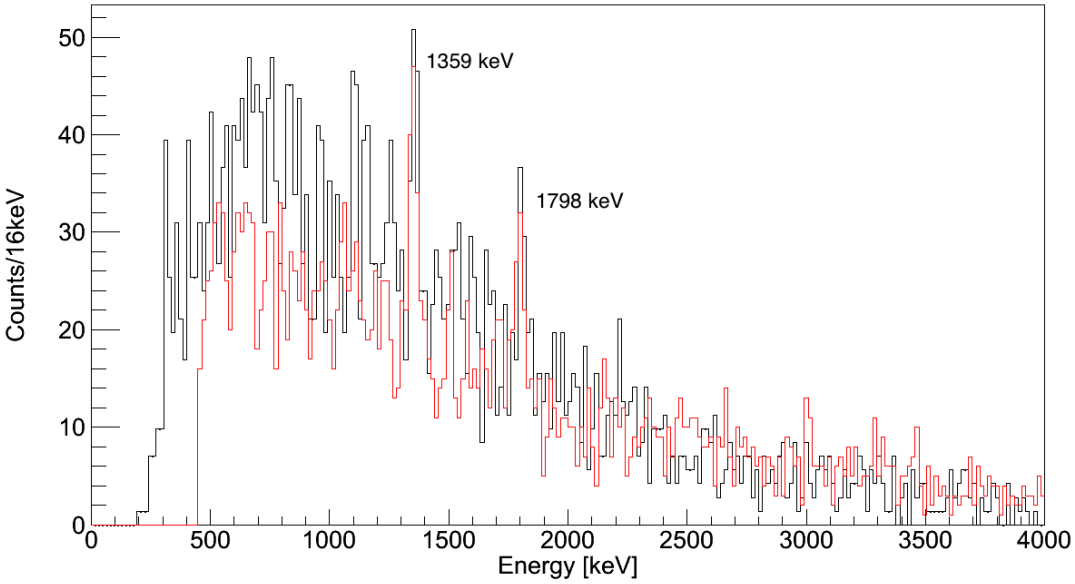

Figure 6.27: A comparison between the simulated (red) and experimental (black) RISING inner ring spectra for ^{33}Ar. The spectra contain singles and addback (crystal multiplicity=2) events.

6.4 AGATA Simulations

It can be seen in the comparisons between the simulated and experimental RISING spectra (figures 6.25 and 6.26) that a satisfactory comparison can be obtained by including the various simulation components discussed in chapter 4. As discussed in subsection 6.3.1, the atomic background component was removed from the RISING simulations, however, this component must be considered for the AGATA simulations since no absorbers are used experimentally. The performance of the γ-ray tracking algorithms have previously been untested to such levels of background and is to be investigated in the current section. The simulations presented below consider the 5ATC+5ADC and 10ATC+5ADC AGATA configurations, for both the ^{36}Ar and ^{33}Ar FRS settings.

6.4.1 Effect of the Background on the $\gamma-$ray Tracking

In order to investigate the performance of the tracking codes to the high level of background experienced at the GSI facility, the tracking codes were used in a variety of simulated conditions:

- without any atomic or high energy background

- without atomic background and the inclusion of high energy background (the same events file used for the final comparison between the simulated and experimental RISING spectra)

- inclusion of the high energy background with the atomic background increased in stages until the maximum amount is reached, as defined in section 6.4.

The processing stage in the AGATA simulations, as discussed in chapter 4, is used to calculate the recoil direction and velocity from the LYCCA-0 interactions and to apply particle gates to the original *GammaEvents.0000* file, resulting in a modified output file which is then passed to the tracking codes. The version of the OFT used (for externally generated input event files for use within the AGATA code) was modified to read in the source positions and velocity event-by-event, as calculated from the simulated LYCCA-0 interactions. For each simulation, a ROOT file is generated during the processing stage that contains the 'raw' spectrum corresponding to the sum of all interaction energies per crystal. The raw spectra, which corresponds to a typical γ-ray detector response, can be compared to the tracked spectra to determine how well the tracking is performing.

6.4.1.1 γ-rays of Interest (No Background)

The raw (defined in subsection 6.4.1) and tracked spectra for each fragment setting for an input events file containing only γ-rays of interest is displayed in figures 6.28 and 6.29. The spectra were tracked with the default tracking settings. The tracking codes were successfully able to track the simulated data with no background components and the improvement in the P/T and energy resolution can be seen in each case following the application of the tracking codes. The P/T and photopeak efficiency values extracted from the spectra are displayed in table 6.3.

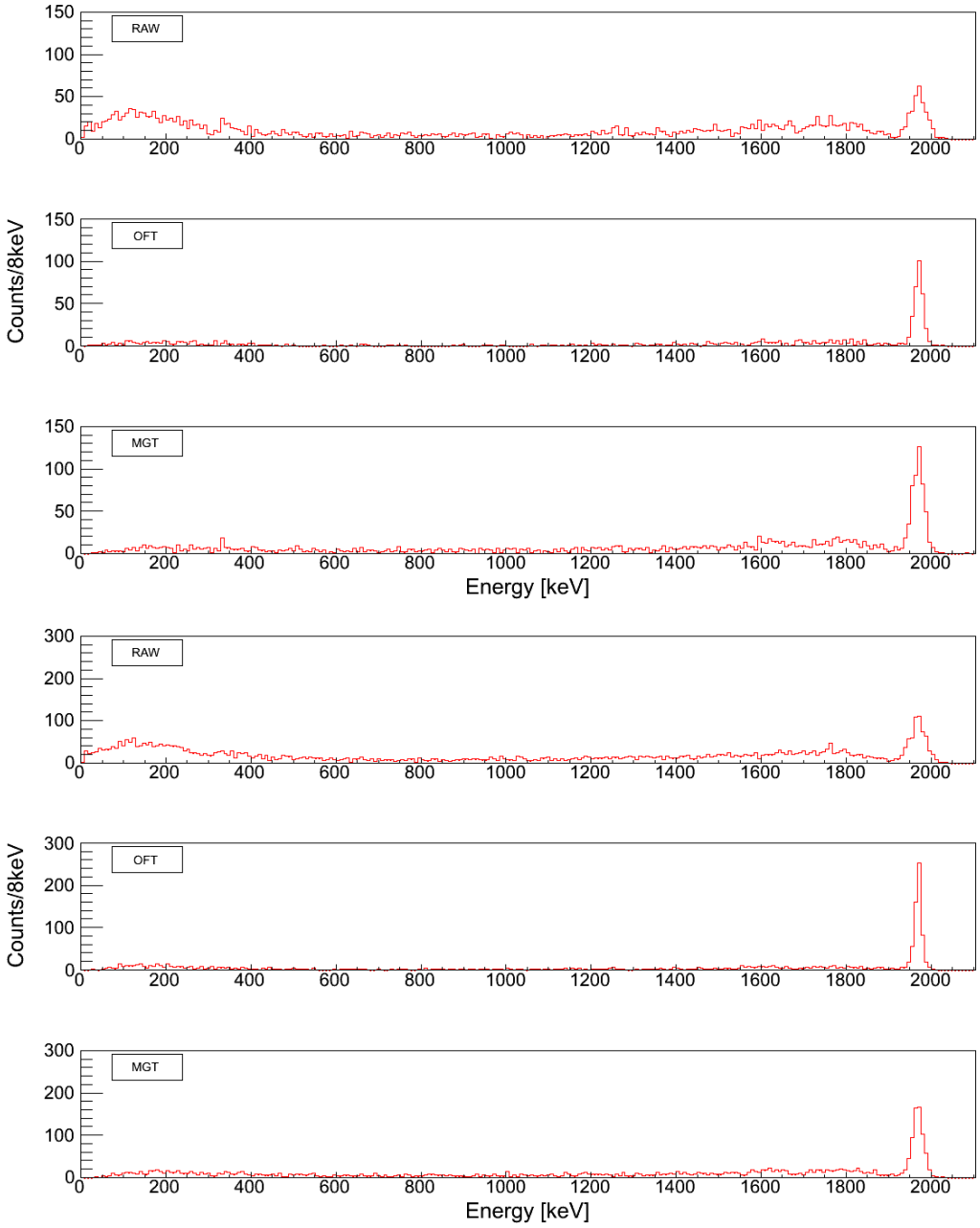

Figure 6.28: The raw and tracked ^{36}Ar spectra (top 3 panels: 5ATC+5ADC, bottom 3 panels: 10ATC+5ADC) resulting from an input events file containing only γ-rays of interest and no sources of background.

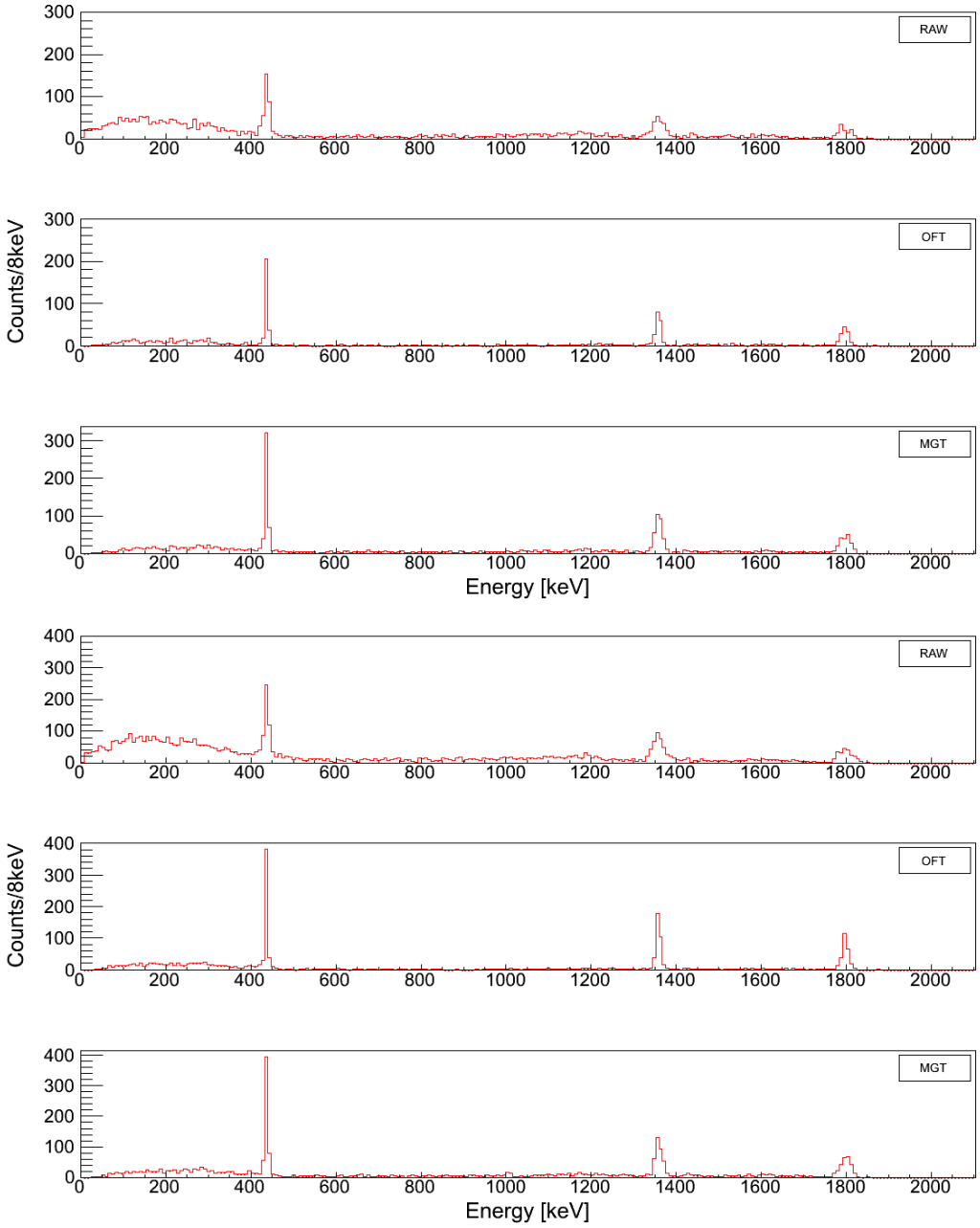

Figure 6.29: The raw and tracked ^{33}Ar spectra (top 3 panels: 5ATC+5ADC, bottom 3 panels: 10ATC+5ADC) resulting from an input events file containing only γ-rays of interest and no sources of background.

Tracking	Setting	Geometry	P/T [%]	$\epsilon_{photopeak}$ [%]
RAW	^{36}Ar	5ATC+5ADC	19.75±1.22	3.14±0.18
RAW	^{36}Ar	10ATC+5ADC	22.04±1.00	5.92±0.24
RAW	^{33}Ar	5ATC+5ADC	30.35±2.56	3.42±0.18
RAW	^{33}Ar	10ATC+5ADC	32.23±1.84	6.38±0.25
OFT	^{36}Ar	5ATC+5ADC	53.71±3.83	3.03±0.17
OFT	^{36}Ar	10ATC+5ADC	57.74±3.03	5.72±0.24
OFT	^{33}Ar	5ATC+5ADC	65.46±5.11	3.01±0.18
OFT	^{33}Ar	10ATC+5ADC	67.73±3.83	5.76±0.24
MGT	^{36}Ar	5ATC+5ADC	33.07±1.71	5.03±0.22
MGT	^{36}Ar	10ATC+5ADC	34.79±1.56	6.72±0.26
MGT	^{33}Ar	5ATC+5ADC	47.00±2.89	5.20±0.23
MGT	^{33}Ar	10ATC+5ADC	43.48±2.26	6.08±0.25

Table 6.3: The P/T and photopeak efficiency values extracted from the spectra displayed in figures 6.28 and 6.29.

6.4.1.2 Atomic Background+High Energy Background+γ-rays of Interest

The method of estimating the atomic background multiplicity per simulated event, as discussed in subsection 6.3.1, is valid in the case of a high intensity beam where multiple ions are incident on the target. This estimation resulted in an atomic background multiplicity of $\sim 1\times10^{6}$/event, which can be considered as an extreme upper limit. Another method of estimating the atomic background multiplicity can be achieved by considering the background induced by a single incident beam particle. This is a reasonable approximation for low intensity beams where the beam rate is much lower than the maximum DAQ event rate.

In the low intensity limit, the x-ray yield per beam particle for the ^{33}Ar setting has been calculated to be ∼82. The yield was calculated using a cross section of 69×10^{3} b as determined with ABKG (see subsection 6.3.1) and a target areal number density of $1.2\times10^{21}\,\mathrm{cm}^{-2}$ (gold target of thickness $0.388\,\mathrm{g/cm}^{2}$). As can be seen in figure 4.17, the average energy of an x-ray is ∼15 keV. For a yield of 82 x-rays resulting from a single incident beam particle, this contributes to a total

energy yield of ∼1.3 MeV. This corresponds to ∼0.3% of the average energy loss of 436 MeV in the secondary target (determined with MOCADI). Having the total energy loss emitted as x-rays would give $\sim 28.5 \times 10^3$ x-rays per beam particle, which can be considered as an upper limit for a low intensity beam.

As highlighted in subsection 6.3.1, the use of the absorbers with the RISING array greatly suppresses the atomic background which justified the removal of the atomic background from the simulations. As the target-to-array distance in the AGATA simulations is 23.5 cm, whereas the RISING array is 70 cm, the solid angle coverage of the array is different, and therefore a different level of background will be detected. In order to investigate the response of AGATA to the atomic background, simulations containing only atomic background have been performed for the ^{33}Ar setting with the 5ATC+5ADC geometry (see figure 6.30). The multiplicity of atomic background per simulated event was increased from 10, 100, 1000, 10000 to 100000 to cover the range determined by the low and high intensity limits. Each simulation contained 9000 events to ensure there were less than 1×10^9 particle emissions when an atomic background multiplicity of 100000/event was included in the simulations (see subsection 6.3.1). Simulations were also performed for the optimum ^{33}Ar setting (see sub-subsection 6.4.1.3) with the multiplicity of atomic background per simulated event set in the same range (see figure 6.31).

As can be seen in figure 6.31, tracking is possible for an atomic background multiplicity of 10000/event or less, however, it is not possible for a multiplicity of 100000/event. The simulations suggest that when unshielded detectors are utilised, providing the atomic background multiplicity remains below 10000/event, it will be possible to apply the tracking. The tracking deteriorates between an atomic background multiplicity of 10000/event and 100000/event. Table 6.4 displays the P/T and photopeak efficiency values extracted from the spectra display in figures 6.31.

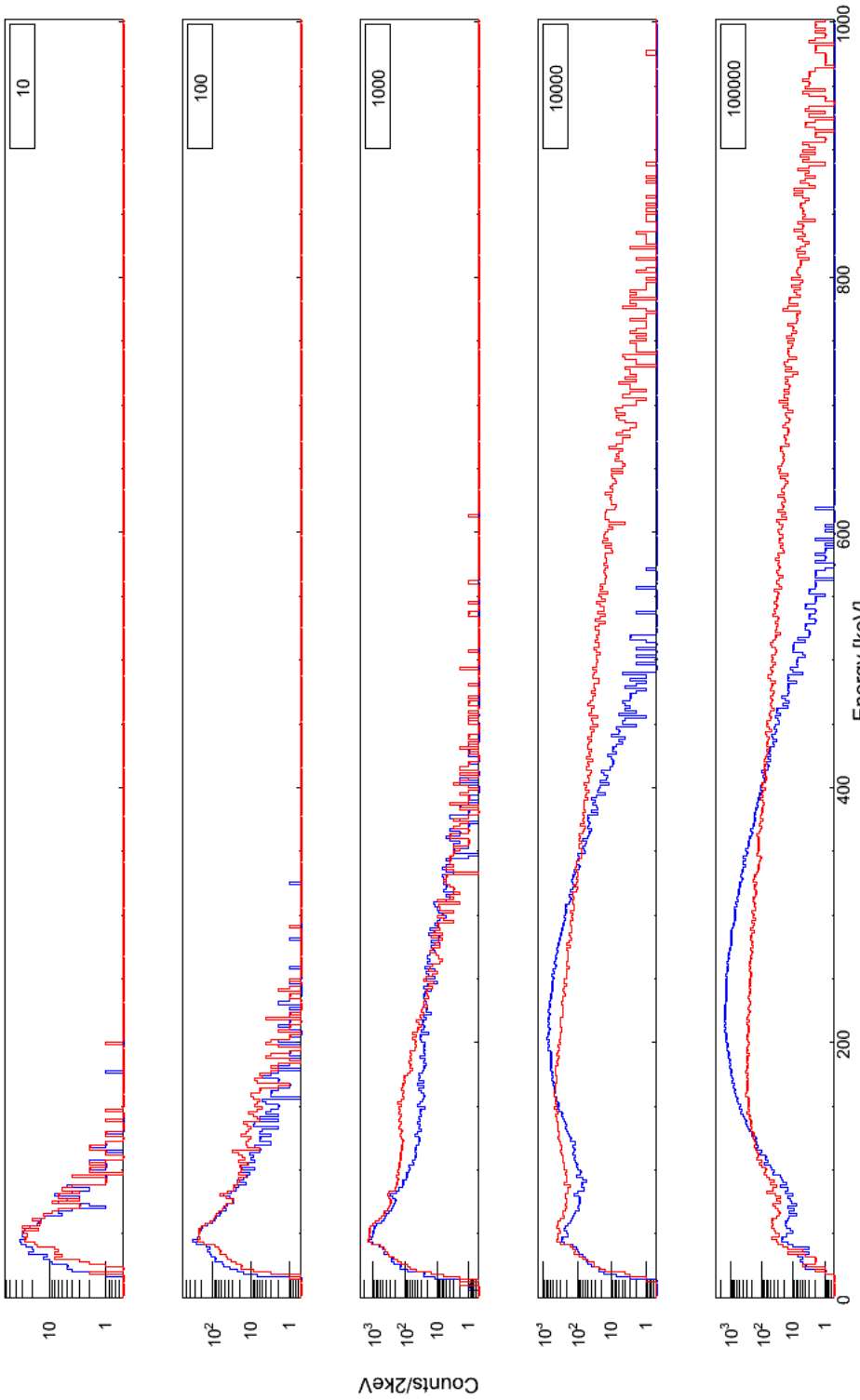

Figure 6.30: The tracked OFT (red) and MGT (blue) spectra for simulations containing only atomic background for the ^{33}Ar setting with the 5ATC+5ADC geometry. The atomic background multiplicity has been increased from 10/event (top) to 100000/event (bottom).

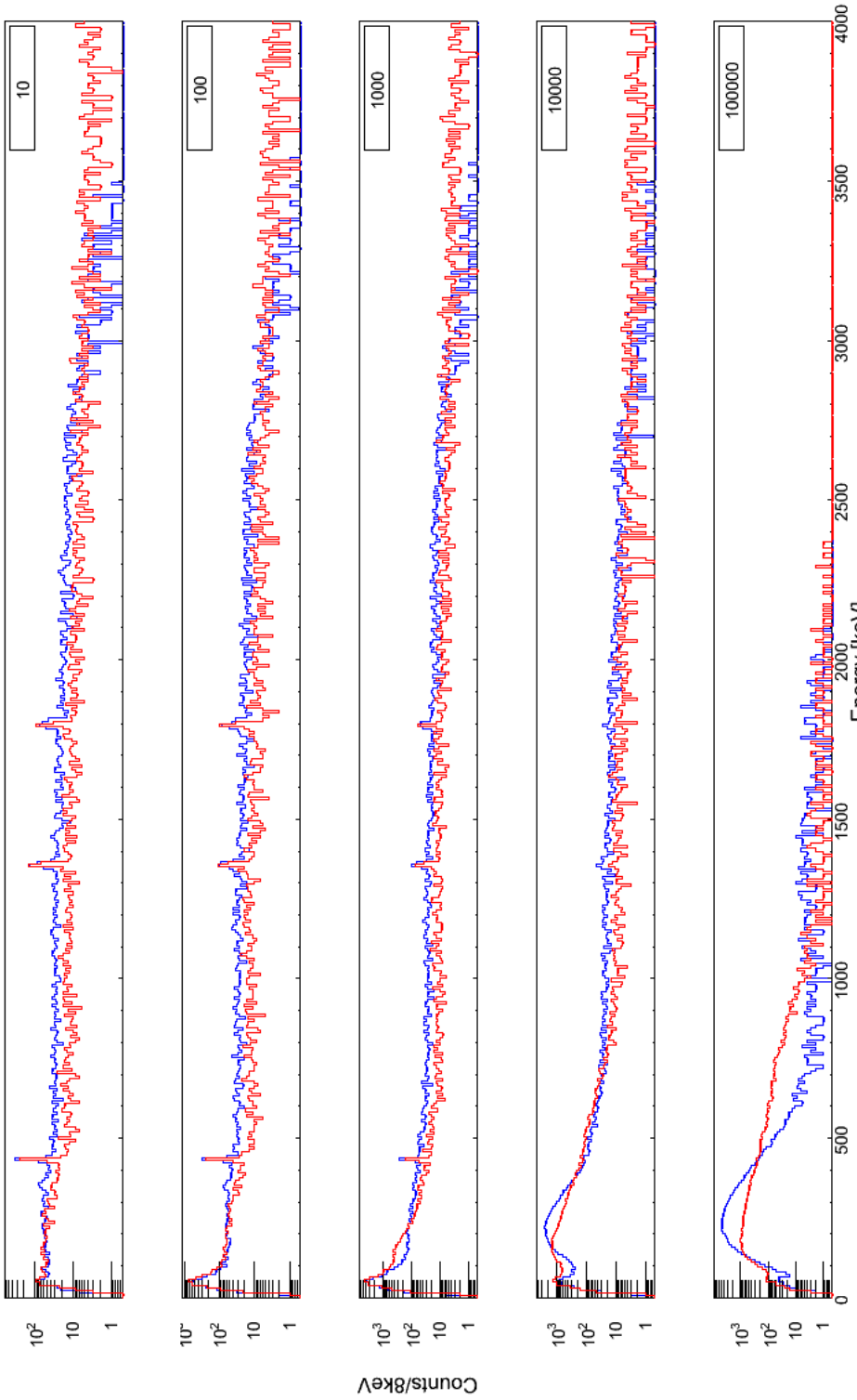

Figure 6.31: The tracked OFT (red) and MGT (blue) spectra for simulations containing atomic background, γ-rays of interest and high energy background for the ^{33}Ar setting with the 5ATC+5ADC geometry. The atomic background multiplicity has been increased from 10/event (top) to 100000/event (bottom).

Tracking	ABKG Multiplicity/event	P/T [%]	$\epsilon_{photopeak}$ [%]
OFT	10	8.45±0.53	3.49±0.22
MGT	10	5.90±0.39	4.21±0.28
OFT	100	7.85±0.50	3.11±0.20
MGT	100	5.31±0.40	3.65±0.28
OFT	1000	4.81±0.46	1.73±0.17
MGT	1000	3.98±0.36	2.53±0.24
OFT	10000	1.11±0.30	0.29±0.08
MGT	10000	1.88±0.35	0.86±0.16
OFT	100000	-	-
MGT	100000	-	-

Table 6.4: The P/T and photopeak efficiency values extracted from the spectra displayed in figure 6.31.

6.4.1.3 High Energy Background+γ-rays of Interest

Figures 6.32 and 6.33 display the raw and tracked spectra for the simulations containing high energy background and γ-rays of interest, i.e. the same input events file used for the final RISING simulations. The P/T and photopeak efficiency values extracted from the spectra are displayed in table 6.5.

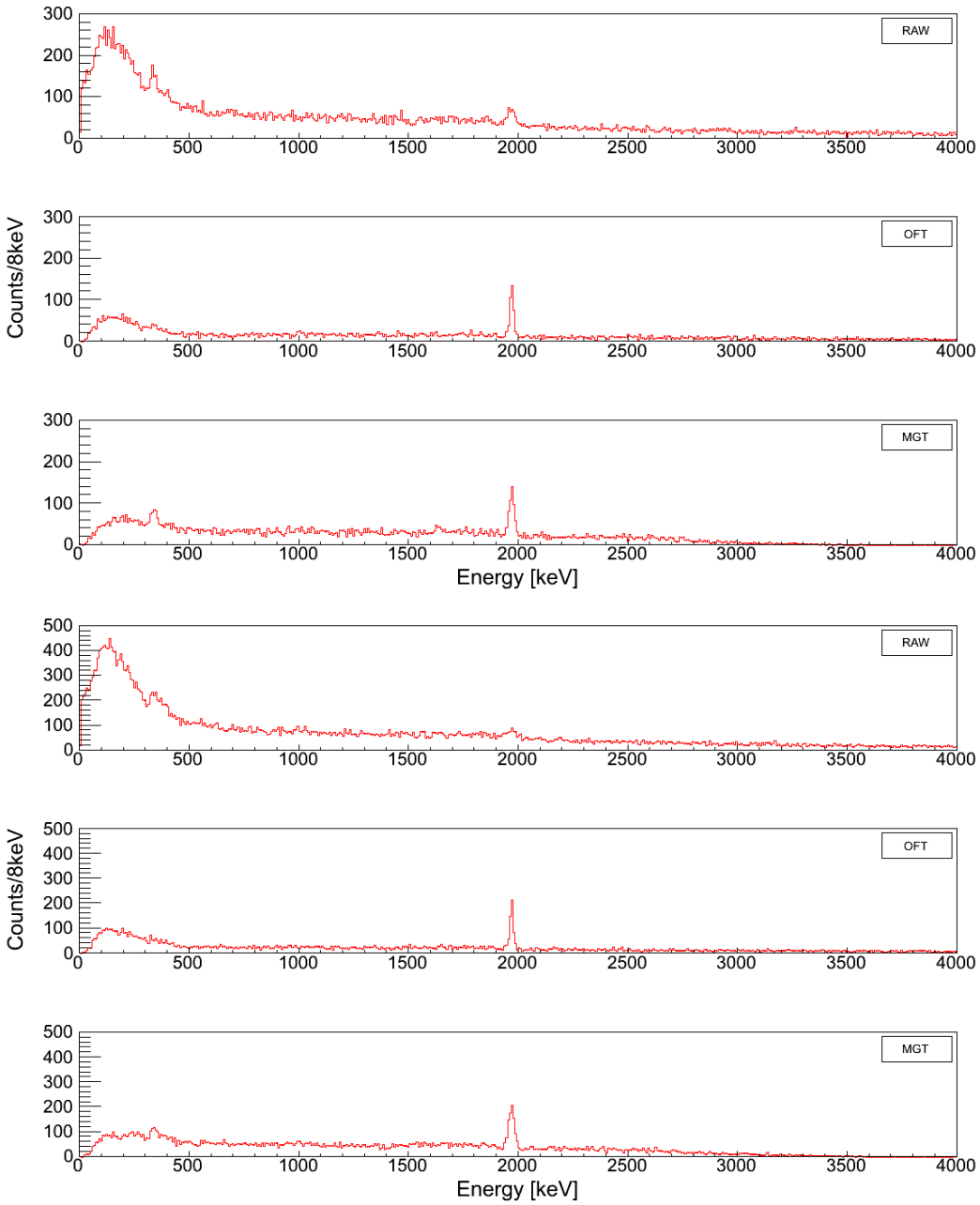

Figure 6.32: The raw and tracked ^{36}Ar spectra (top 3 panels: 5ATC+5ADC, bottom 3 panels: 10ATC+5ADC) resulting from an input events file containing high energy background and γ-rays of interest. The input events file used corresponds to the input events file used to create the final RISING array spectra, as displayed in subsection 6.3.5.

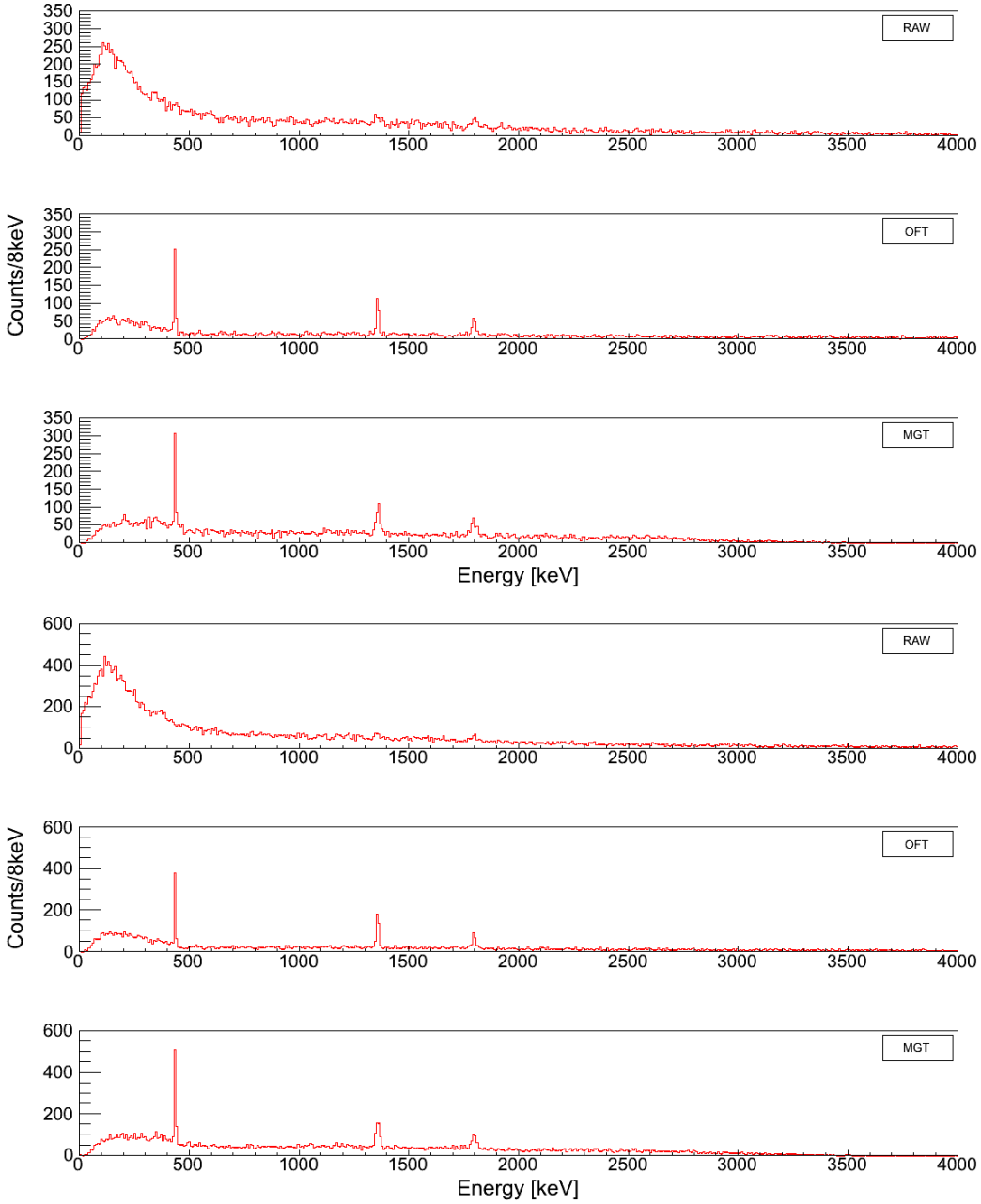

Figure 6.33: The raw and tracked ^{33}Ar spectra (top 3 panels: 5ATC+5ADC, bottom 3 panels: 10ATC+5ADC) resulting from an input events file containing high energy background and γ-rays of interest. The input events file used corresponds to the input events file used to create the final RISING array spectra, as displayed in subsection 6.3.6.

Tracking	Setting	Geometry	P/T [%]	$\epsilon_{photopeak}$ [%]
RAW	^{36}Ar	5ATC+5ADC	1.88±0.23	2.29±0.28
RAW	^{36}Ar	10ATC+5ADC	1.36±0.22	2.39±0.39
RAW	^{33}Ar	5ATC+5ADC	1.45±0.30	1.48±0.31
RAW	^{33}Ar	10ATC+5ADC	1.19±0.27	1.81±0.41
OFT	^{36}Ar	5ATC+5ADC	7.98±0.48	3.37±0.20
OFT	^{36}Ar	10ATC+5ADC	7.46±0.38	4.64±0.23
OFT	^{33}Ar	5ATC+5ADC	9.18±0.60	3.17±0.21
OFT	^{33}Ar	10ATC+5ADC	9.00±0.49	4.66±0.26
MGT	^{36}Ar	5ATC+5ADC	5.38±0.34	3.91±0.24
MGT	^{36}Ar	10ATC+5ADC	6.21±0.29	7.07±0.32
MGT	^{33}Ar	5ATC+5ADC	6.34±0.43	3.83±0.26
MGT	^{33}Ar	10ATC+5ADC	6.13±0.34	5.87±0.33

Table 6.5: The P/T and photopeak efficiency values extracted from the spectra displayed in figures 6.32 and 6.33.

The remainder of the work discussed in subsections 6.4.2 and 6.4.3 assumes that experimental methods are to be utilised to reduce the background and therefore the atomic background has been removed from the simulations, i.e. the same input event files used for the final RISING simulations is used containing high energy background and γ-rays of interest.

6.4.2 Effect of the Timing Resolution on the Peak Shape

For the RISING array, the Doppler broadening of the photopeak(s) is dominated by the large opening angles of the RISING crystals. For the AGATA crystals, where the opening angle is smaller than 1°, it is expected that the peak shape will be sensitive to the timing resolution of the scintillators used to provide the TOF start and stop signal. A larger spread in β will affect the Doppler correction which subsequently contributes to the broadening of the peak(s). For a 'perfect' timing resolution, the only contribution to the β spread is from the momentum spread of the beam following fragmentation at the primary and secondary targets. In this case, no matter how large the β spread, the γ-ray photopeak will appear at the correct energy and the peak shape will be unaffected as β is determined event-by-event.

In the case of an imperfect timing resolution, the β spread has two contributions resulting from the momentum spread of the beam and from the measurement itself; the latter of which affects the peak shape. In order to investigate whether this effect has any significance on the AGATA spectra, the timing resolution was increased from 25 ps to 150 ps in steps of 25 ps during the processing stage. The current obtainable experimental timing resolution is $\sim$50 ps with the plastic scintillators used at GSI [69].

The investigation was performed with the ^{33}Ar fragment setting as the energy spread of the heavy ions leaving the secondary target is larger than that of the primary beam, which results in a broader β distribution. The MOCADI output files used during the event generation stage give the energy spread for the ^{33}Ar setting as ΔE=26.37 MeV/u, whereas the energy spread for the ^{36}Ar setting is ΔE=7.43 MeV/u. Figures 6.34 and 6.35 display the tracked ^{33}Ar spectra and the β distributions as the timing resolution is incremented. For the γ-ray spectra displayed on the left-hand side of figures 6.34 and 6.35, the dashed lines represent the photopeaks corresponding to a perfect timing resolution. Similarly, the dashed lines on the right-hand sides of figures 6.34 and 6.35 represents the β distributions corresponding to a perfect timing resolution. As the timing resolution progresses from 25 ps to 150 ps, the width of the photopeaks and β distributions can be compared to the reference perfect case, which illustrates the contribution of an imperfect timing resolution on the β spread and the resulting peak shape.

A Gaussian function was fit to the β distribution from each simulation, and functions identical to that described in subsection 6.3.3 were fit to the tracked OFT and MGT spectra. The FWHM of the photopeaks extracted from the spectra, in addition to the FWHM of the β distributions as a function of the timing resolution are displayed in table 6.6. For each case, the FWHM values of the photopeaks and the β distributions from the imperfect timing resolutions are compared to the perfect case, which highlights the increase in FWHM resulting from an imperfect timing resolution.

The simulated data suggests that AGATA will be sensitive to the timing resolution of the scintillators. For imperfect timing resolutions, the increase in FWHM increases linearly, resulting in a degradation in energy resolution (see subsection 7.1.2 for further discussion).

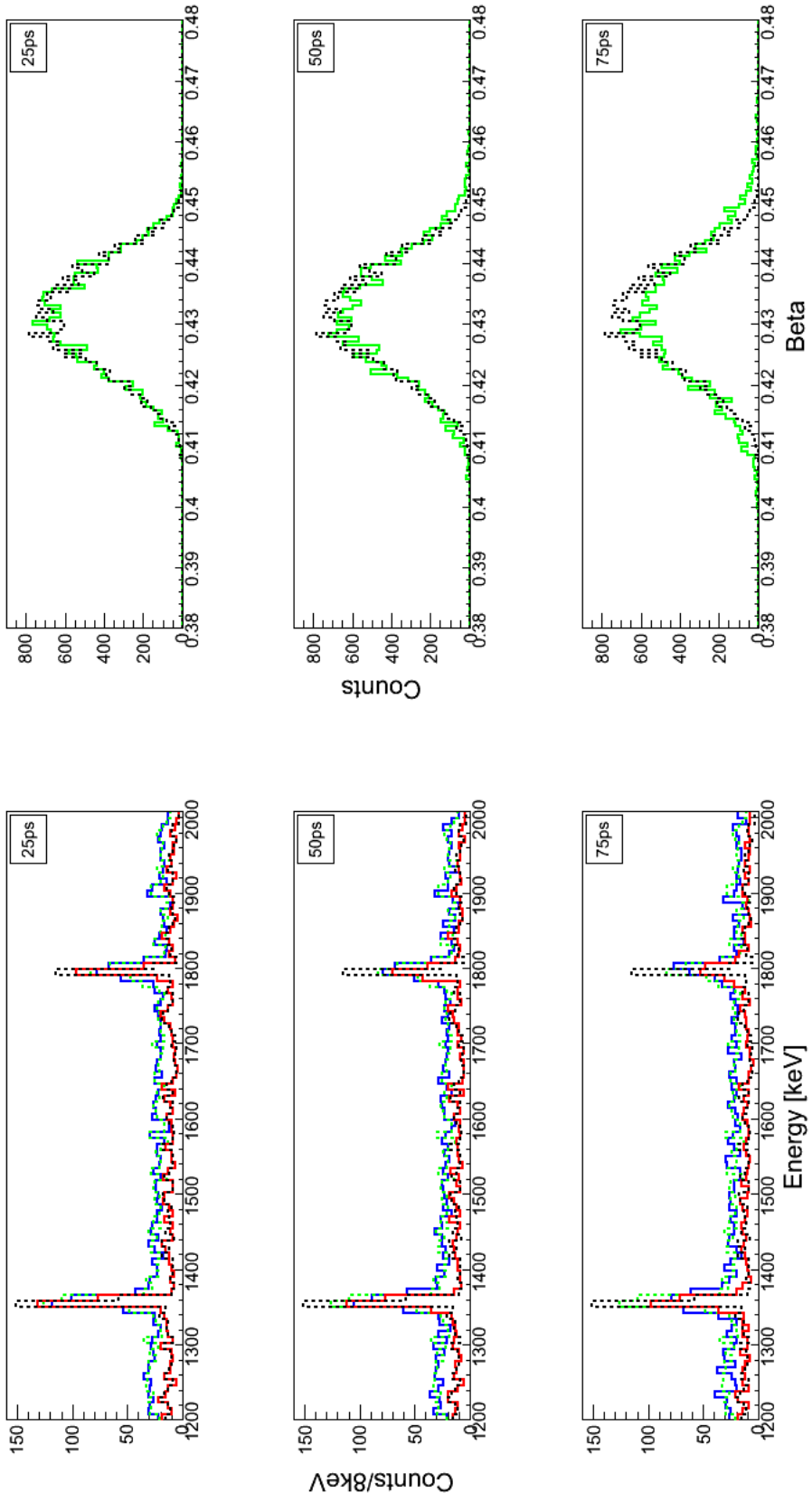

Figure 6.34: The left-hand panels display the tracked ^{33}Ar spectra (MGT:blue, OFT:red) and the right-hand panels display the β distributions as the timing resolution is incremented from 25 ps to 75 ps. The dashed lines in the left-hand side spectra correspond to photopeaks resulting from a perfect timing resolution (MGT:green, OFT:black), and similarly, the black dashed lines in the right-hand side spectra represent the β distributions resulting from a perfect timing resolution. See text for further details.

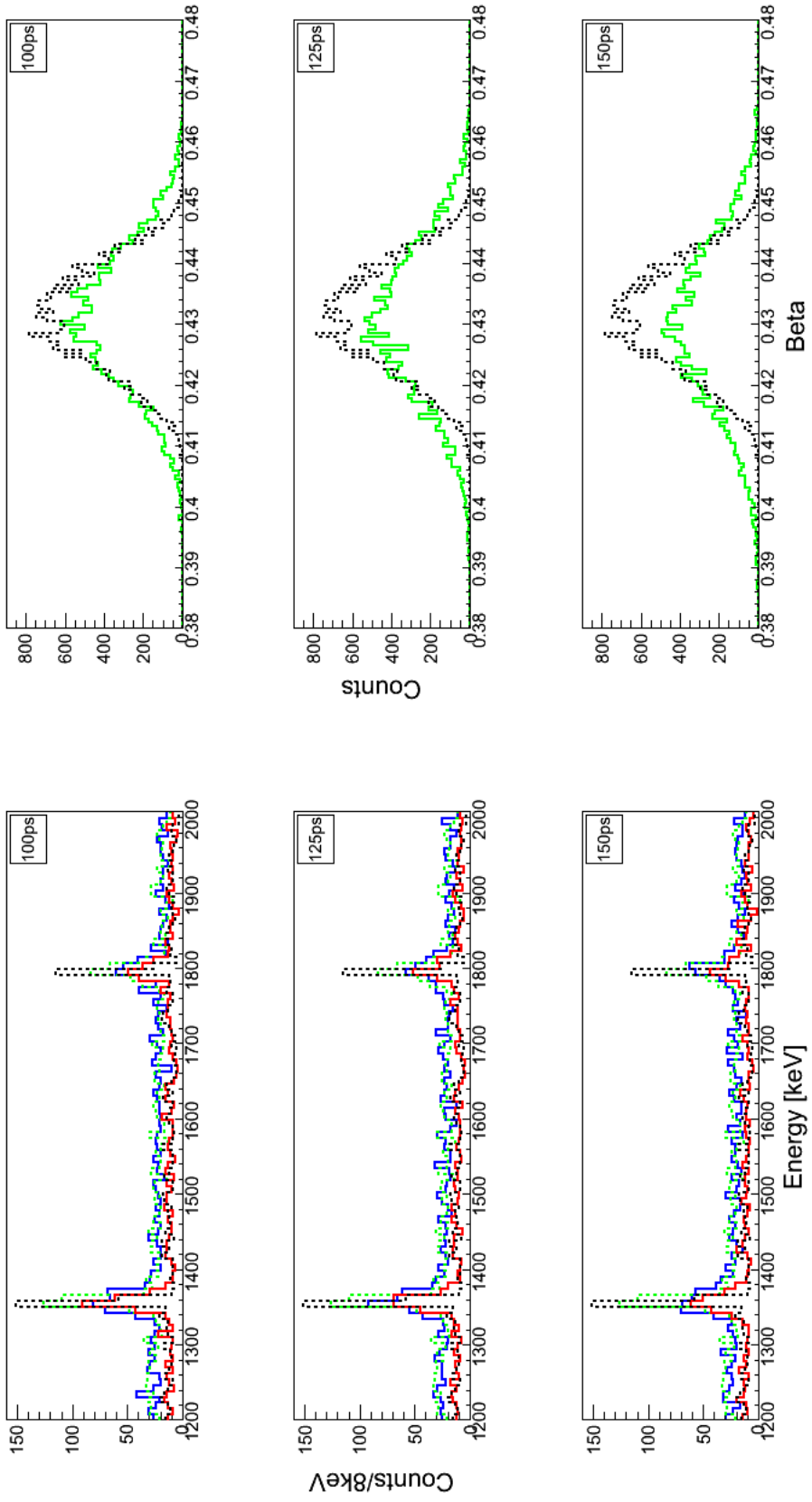

Figure 6.35: The left-hand panels display the tracked ^{33}Ar spectra (MGT:blue, OFT:red) and the right-hand panels display the β distributions as the timing resolution is incremented from 100 ps to 150 ps. The dashed lines in the left-hand side spectra correspond to photopeaks resulting from a perfect timing resolution (MGT:green, OFT:black), and similarly, the black dashed lines in the right-hand side spectra represent the β distributions resulting from a perfect timing resolution. See text for further details.

R_{time} [ps]	FWHM$_\beta$	$\uparrow FWHM_\beta$	$\overline{FWHM}_{OFT}$ [keV]	$\uparrow$FWHM$_{OFT}$ [keV]	$\overline{FWHM}_{MGT}$ [keV]	$\uparrow$FWHM$_{MGT}$ [keV]
25	$1.81\times10^{-2} \pm 7.75 \times 10^{-5}$	$3.39\times10^{-4} \pm 1.09 \times 10^{-4}$	10.60±0.58	2.11±0.85	18.39±1.17	0.94±1.46
50	$1.98\times10^{-2} \pm 8.64 \times 10^{-5}$	$2.10\times10^{-3} \pm 1.16 \times 10^{-4}$	14.26±0.83	5.77±1.03	20.61±0.50	3.15±1.01
75	$2.24\times10^{-2} \pm 1.06 \times 10^{-4}$	$4.67\times10^{-3} \pm 1.31 \times 10^{-4}$	20.32±1.78	11.83±1.88	22.59±2.45	5.13±2.60
100	$2.48\times10^{-2} \pm 1.20 \times 10^{-4}$	$7.10\times10^{-3} \pm 1.42 \times 10^{-4}$	21.68±1.86	13.19±1.96	25.57±1.98	8.11±2.17
125	$2.68\times10^{-2} \pm 1.25 \times 10^{-4}$	$9.06\times10^{-3} \pm 1.47 \times 10^{-4}$	25.18±2.16	16.68±2.25	30.97±2.87	13.51±3.00
150	$2.87\times10^{-2} \pm 1.38 \times 10^{-4}$	$1.09\times10^{-2} \pm 1.58 \times 10^{-4}$	27.52±2.09	19.03±2.18	31.97±2.49	14.08±2.64

Table 6.6: The average FWHM values of the tracked peaks ($\overline{FWHM}_{OFT}$ and $\overline{FWHM}_{MGT}$) and β distributions (FWHM$_\beta$) as the timing resolution (R_{time}) is incremented between 25-150 ps. For each timing resolution, the increase in FWHM is displayed ($\uparrow$) compared to the perfect timing resolution case, which highlights the effect of an imperfect timing resolution on the β spread and peak shape.

6.4.3 Tracking Settings Considerations

Various parameters within the tracking codes can be adjusted which affect the P/T and photopeak efficiency of the output spectra. The goal of the tracking is to increase the P/T by reconstructing the full energy of the incident γ-ray from the scattered interaction points. The energy threshold applied to the packed interaction points and the packing and smearing of interaction points were varied in order to study the effects on the P/T and photopeak efficiency.

6.4.3.1 Energy Threshold

At GSI, a hardware energy threshold is set just above the noise on the digital electronics (typically in the 20-60 keV region), and an additional energy threshold is applied to the trigger for the particle-γ coincidence (coincidence trigger requires heavy ion+γ-rays detected). The trigger threshold is typically set between 100 and 400 keV, dependant on: the amount of atomic background present, the effect on the data acquisition, the coincidence rate, and the energy of the γ-rays of interest. The threshold for the coincidence determines the atomic background rate for each passing ion. Typical values are $\sim$400 keV for a relativistic Coulex reaction and $\sim$200 keV for a secondary fragmentation reaction[1].

The energy threshold of the packed interaction points (set in the tracking codes) was varied between 100 keV and 300 keV in steps of 100 keV, in order to investigate the effect on the P/T and photopeak efficiency, and to determine an optimum value for the discussed simulations. The tracked spectra and extracted P/T and photopeak efficiency values for each energy threshold are displayed in figures 6.36, 6.37 and 6.38, and tables 6.7, 6.8 and 6.9. The P/T in each case was calculated between 0-4000 keV.

[1]Private communication with Stephane Pietri. e-mail: s.pietri@gsi.de

Energy Threshold = 100 keV

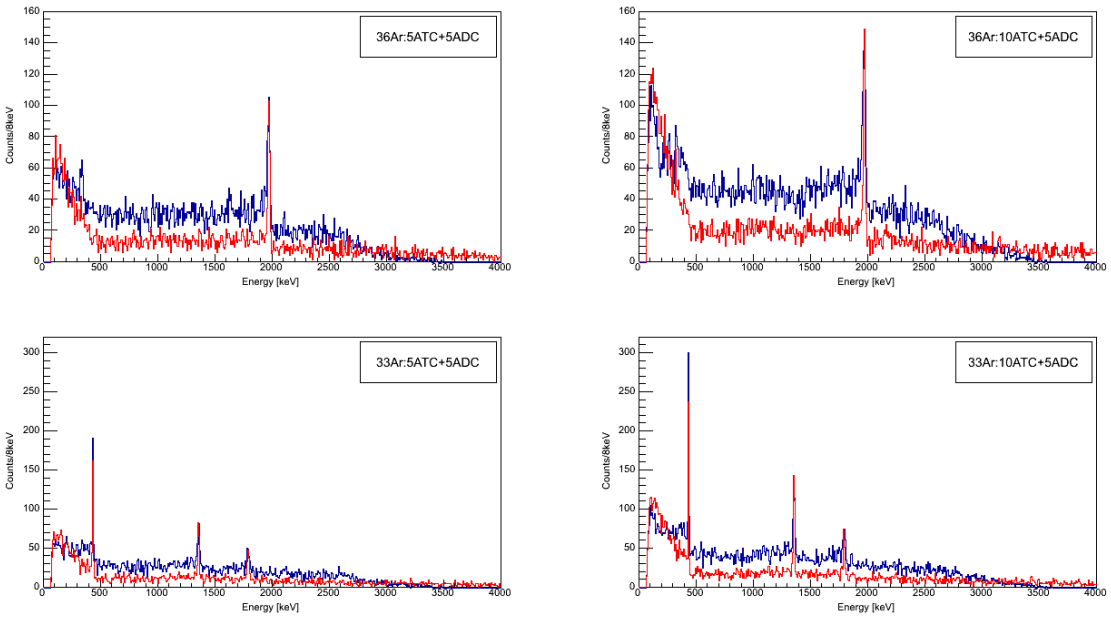

Figure 6.36: The tracked OFT (red) and MGT (blue) spectra with an energy threshold of 100 keV applied to the packed interaction points for: the ^{36}Ar setting and 5ATC+5ADC geometry (top left), the ^{36}Ar setting and 10ATC+5ADC geometry (top right), the ^{33}Ar setting and 5ATC+5ADC geometry (bottom left), and the ^{33}Ar setting and 10ATC+5ADC geometry (bottom right).

			E_{thresh}=100 keV		E_{thresh}=5 keV	
Tracking	Setting	Geometry	P/T [%]	ϵ [%]	P/T [%]	ϵ [%]
OFT	^{36}Ar	5ATC+5ADC	4.30±0.29	2.70±0.18	5.07±0.30	3.37±0.20
OFT	^{36}Ar	10ATC+5ADC	3.53±0.22	3.44±0.21	4.59±0.23	4.64±0.23
OFT	^{33}Ar	5ATC+5ADC	4.42±0.33	2.57±0.20	5.30±0.33	3.22±0.20
OFT	^{33}Ar	10ATC+5ADC	4.12±0.25	3.60±0.23	5.12±0.27	4.74±0.25
MGT	^{36}Ar	5ATC+5ADC	2.96±0.24	3.08±0.25	3.69±0.24	4.02±0.25
MGT	^{36}Ar	10ATC+5ADC	3.11±0.19	4.99±0.30	4.03±0.19	6.84±0.33
MGT	^{33}Ar	5ATC+5ADC	2.84±0.27	2.64±0.26	3.83±0.27	3.74±0.27
MGT	^{33}Ar	10ATC+5ADC	2.77±0.20	4.03±0.30	3.80±0.21	5.85±0.33

Table 6.7: The P/T and photopeak efficiency values extracted from the spectra displayed in figure 6.36. The P/T and photopeak efficiency values for an energy threshold of 5 keV (default value) are also displayed as a reference.

Energy Threshold = 200 keV

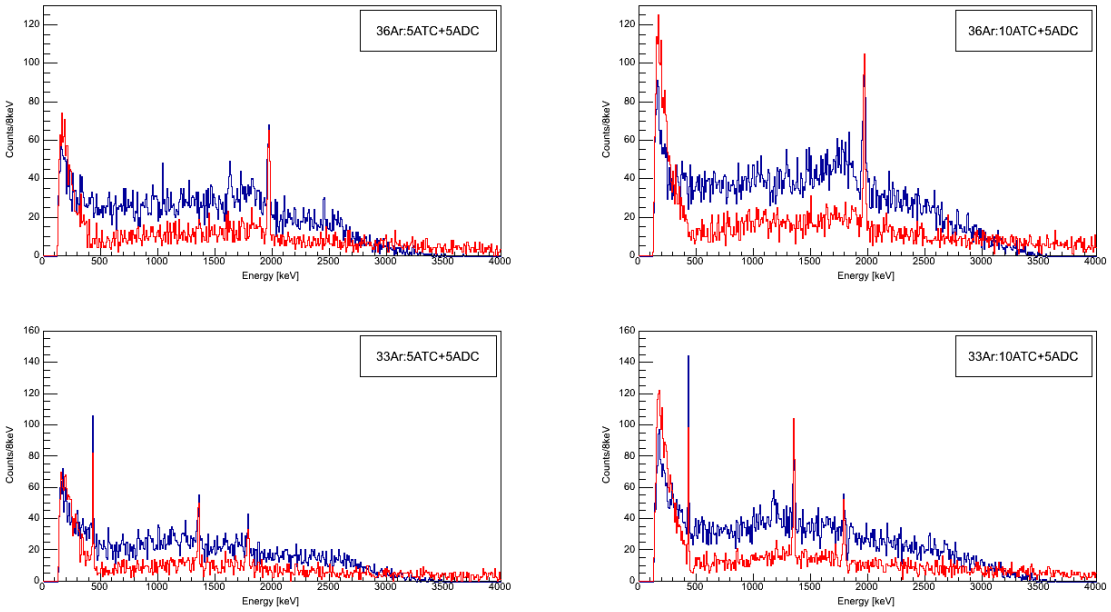

Figure 6.37: The tracked OFT (red) and MGT (blue) spectra with an energy threshold of 200 keV applied to the packed interaction points for: the ^{36}Ar setting and 5ATC+5ADC geometry (top left), the ^{36}Ar setting and 10ATC+5ADC geometry (top right), the ^{33}Ar setting and 5ATC+5ADC geometry (bottom left), and the ^{33}Ar setting and 10ATC+5ADC geometry (bottom right).

			E_{thresh}=200 keV		E_{thresh}=5 keV	
Tracking	Setting	Geometry	P/T [%]	ϵ [%]	P/T [%]	ϵ [%]
OFT	^{36}Ar	5ATC+5ADC	3.43±0.31	1.71±0.15	5.07±0.30	3.37±0.20
OFT	^{36}Ar	10ATC+5ADC	3.17±0.24	2.40±0.18	4.59±0.23	4.64±0.23
OFT	^{33}Ar	5ATC+5ADC	3.77±0.37	1.75±0.17	5.30±0.33	3.22±0.20
OFT	^{33}Ar	10ATC+5ADC	3.89±0.29	2.67±0.20	5.12±0.27	4.74±0.25
MGT	^{36}Ar	5ATC+5ADC	1.89±0.21	1.66±0.19	3.69±0.24	4.02±0.25
MGT	^{36}Ar	10ATC+5ADC	2.18±0.19	2.86±0.25	4.03±0.19	6.84±0.33
MGT	^{33}Ar	5ATC+5ADC	1.66±0.26	1.28±0.20	3.83±0.27	3.74±0.27
MGT	^{33}Ar	10ATC+5ADC	1.52±0.20	1.75±0.24	3.80±0.21	5.85±0.33

Table 6.8: The P/T and photopeak efficiency values extracted from the spectra displayed in figure 6.37. The P/T and photopeak efficiency values for an energy threshold of 5 keV (default value) are also displayed as a reference.

Energy Threshold = 300 keV

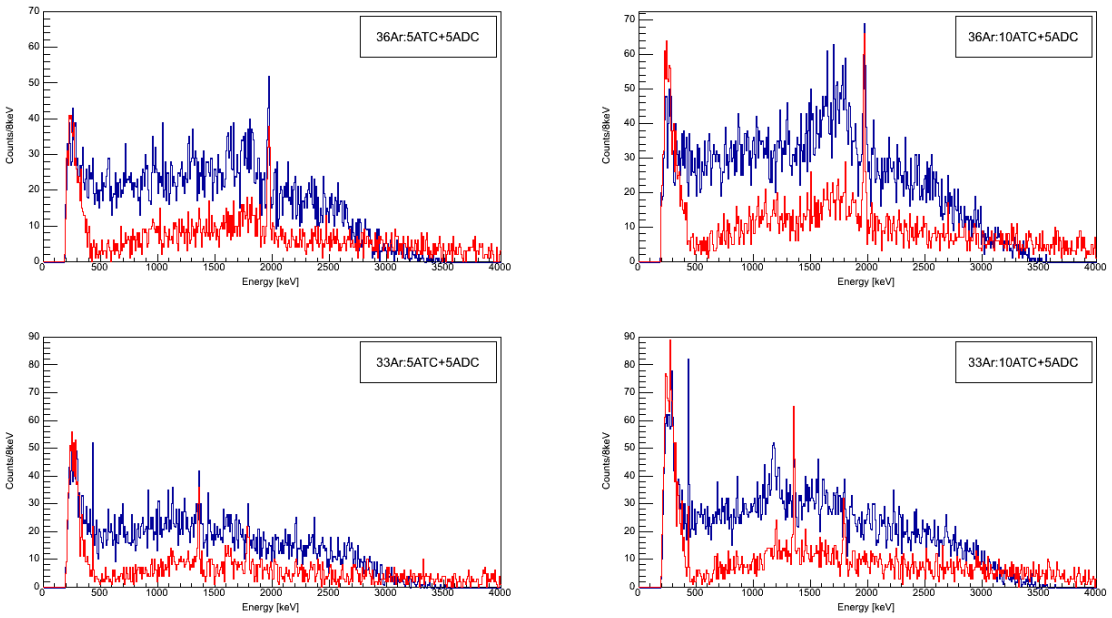

Figure 6.38: The tracked OFT (red) and MGT (blue) spectra with an energy threshold of 300 keV applied to the packed interaction points for the: ^{36}Ar setting and 5ATC+5ADC geometry (top left), ^{36}Ar setting and 10ATC+5ADC geometry (top right), ^{33}Ar setting and 5ATC+5ADC geometry (bottom left), and ^{33}Ar setting and 10ATC+5ADC geometry (bottom right).

			E_{thresh}=300 keV		E_{thresh}=5 keV	
Tracking	Setting	Geometry	P/T [%]	ϵ [%]	P/T [%]	ϵ [%]
OFT	^{36}Ar	5ATC+5ADC	3.11±0.37	1.06±0.12	5.07±0.30	3.37±0.20
OFT	^{36}Ar	10ATC+5ADC	2.78±0.30	1.41±0.15	4.59±0.23	4.64±0.23
OFT	^{33}Ar	5ATC+5ADC	3.67±0.45	1.14±0.14	5.30±0.33	3.22±0.20
OFT	^{33}Ar	10ATC+5ADC	3.33±0.34	1.52±0.16	5.12±0.27	4.70±0.25
MGT	^{36}Ar	5ATC+5ADC	1.13±0.19	0.84±0.14	3.69±0.24	4.02±0.25
MGT	^{36}Ar	10ATC+5ADC	1.24±0.18	1.32±0.19	4.03±0.19	6.84±0.33
MGT	^{33}Ar	5ATC+5ADC	0.71±0.21	0.47±0.14	3.83±0.27	3.74±0.27
MGT	^{33}Ar	10ATC+5ADC	0.74±0.17	0.72±0.17	3.80±0.21	5.85±0.33

Table 6.9: The P/T and photopeak efficiency values extracted from the spectra displayed in figure 6.38. The P/T and photopeak efficiency values for an energy threshold of 5 keV (default value) are also displayed as a reference.

The results show that the P/T and photopeak efficiency worsen as the energy threshold is increased from 5 keV to 300 keV. Using the ^{36}Ar simulation with the 5ATC+5ADC geometry as an example, the P/T reduces from 5.1% (OFT) and 3.7% (MGT) to 3.1% (OFT) and 1.1% (MGT) when the energy threshold is increased from 5 keV to 300 keV. Similarly, the photopeak efficiency reduces from 3.4% (OFT) and 4.0% (MGT) to 1.1% (OFT) and 0.8% (MGT). Therefore, there is no benefit in increasing the energy threshold above the default threshold of 5 keV in the discussed simulations.

6.4.3.2 Packing & Smearing

As discussed in subsection 2.6.2, the packing and smearing parameters are used to account for any discrepancies with the PSA in identifying close lying interaction points, and to account for the uncertainty in the determined interaction positions. Figure 6.39 displays the simulated tracked spectra when packing and smearing has been disabled. For experimental data, the packing and smearing parameters would be disabled as the data would already include the uncertainties from the PSA. Table 6.10 displays the P/T and photopeak efficiency values extracted from the spectra displayed in figure 6.39. The P/T in each case was determined between 700-4000 keV. As it was not possible to obtain any experimental AGATA data and information regarding the performance of the PSA in the GSI environment, the packing and smearing values were left at the default values.

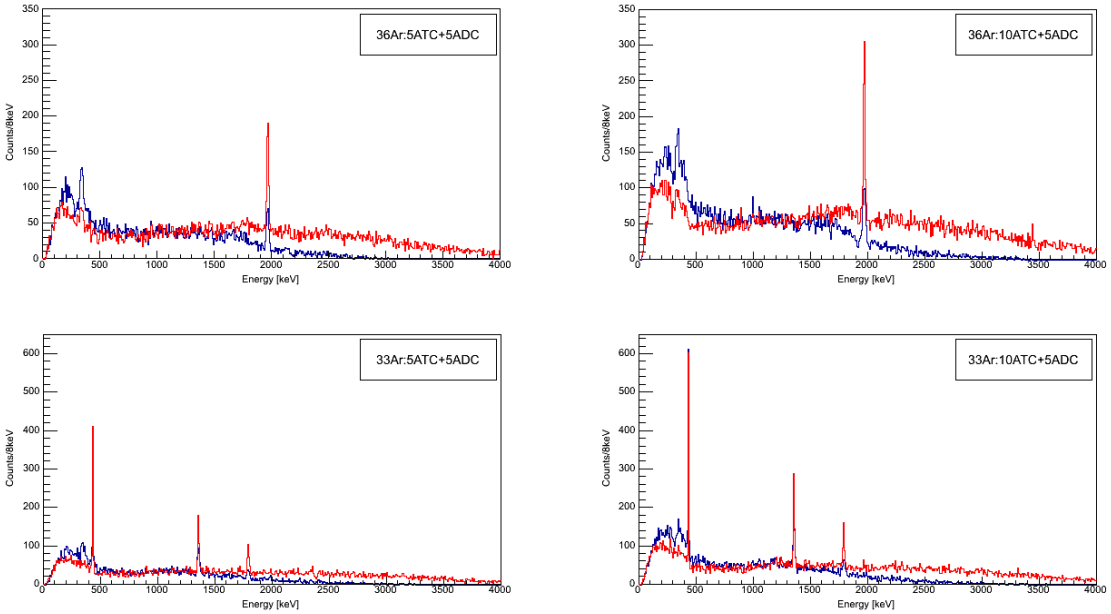

Figure 6.39: The tracked OFT (red) and MGT (blue) spectra with packing and smearing disabled.

			Pack & Smear ×		Pack & Smear ✓	
Tracking	Setting	Geometry	P/T [%]	ϵ [%]	P/T [%]	ϵ [%]
OFT	^{36}Ar	5ATC+5ADC	3.25±0.20	4.17±0.25	7.98±0.48	3.37±0.20
OFT	^{36}Ar	10ATC+5ADC	3.02±0.16	5.66±0.29	7.46±0.38	4.64±0.23
OFT	^{33}Ar	5ATC+5ADC	3.97±0.25	4.17±0.27	9.18±0.60	3.17±0.21
OFT	^{33}Ar	10ATC+5ADC	3.73±0.20	5.75±0.32	9.00±0.49	4.66±0.26
MGT	^{36}Ar	5ATC+5ADC	2.87±0.27	1.78±0.17	5.38±0.34	3.91±0.24
MGT	^{36}Ar	10ATC+5ADC	3.02±0.24	2.93±0.23	6.21±0.29	7.07±0.32
MGT	^{33}Ar	5ATC+5ADC	5.30±0.47	2.63±0.24	6.34±0.43	3.83±0.26
MGT	^{33}Ar	10ATC+5ADC	5.07±0.38	4.13±0.31	6.13±0.34	5.87±0.52

Table 6.10: The P/T and photopeak efficiency values extracted from the tracked AGATA spectra with packing and smearing disabled (×). The P/T and photopeak efficiency values for the simulations where packing and smearing is enabled (✓) are also displayed for reference.

6.4.4 Comparison Between the RISING and AGATA Simulations

The final RISING simulations, as displayed in subsections 6.3.5 and 6.3.6, determined the setup of the input events file that provided the best comparison between the simulated and experimental spectra. Using the same input event files and replacing the RISING array geometry in the simulations with the AGATA 5ATC+5ADC and 10ATC+5ADC geometries, it was possible to compare each detector response to the same simulated conditions, and to evaluate the performance of the tracking codes with the simulated AGATA data.

Figures 6.40 and 6.41 display the RISING and tracked AGATA spectra for each fragment setting, for each AGATA geometry. The tracking codes were used with default settings which includes an energy threshold of 5 keV applied to the packed energy points. The RISING data has an energy threshold of 5 keV applied to each crystal for comparison with the tracked spectra.

The results presented in chapter 6 highlight that the atomic and high energy background included in the simulations has a large effect on the performance of the tracking in comparison with simulations containing no background, and additionally, further investigations including the possible use of shielding needs to be performed in order to further evaluate the effect of the atomic background on the tracking. The comparisons between the AGATA simulations and the RISING simulations displayed in subsection 6.4.4 indicate that for each setting and each AGATA geometry, the tracked spectra offer a higher P/T than the RISING array. Further discussion of the results displayed in this are presented in chapter 7.

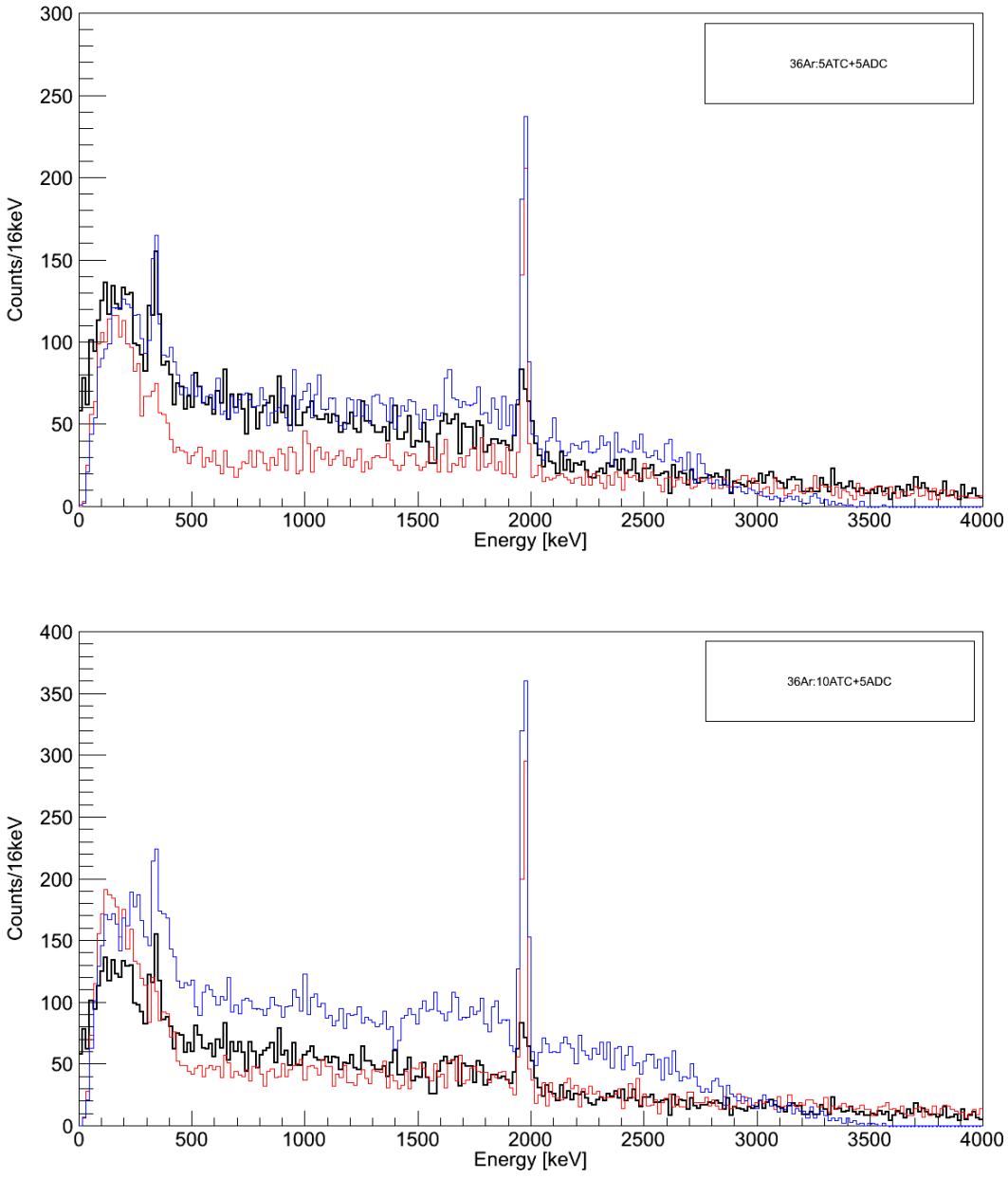

Figure 6.40: The comparison between the RISING (black) spectrum and the tracked OFT (red) and MGT (blue) spectra (top: 5ATC+5ADC, bottom: 10ATC+5ADC). The spectra are for the ^{36}Ar setting. The P/T values (calculated between 700-4000 keV) for the 5ATC+5ADC simulation are: OFT=7.98%, MGT=5.38% and RISING=3.68%, and the P/T values for the 10ATC+5ADC simulation are: OFT=7.46% and MGT=6.21%.

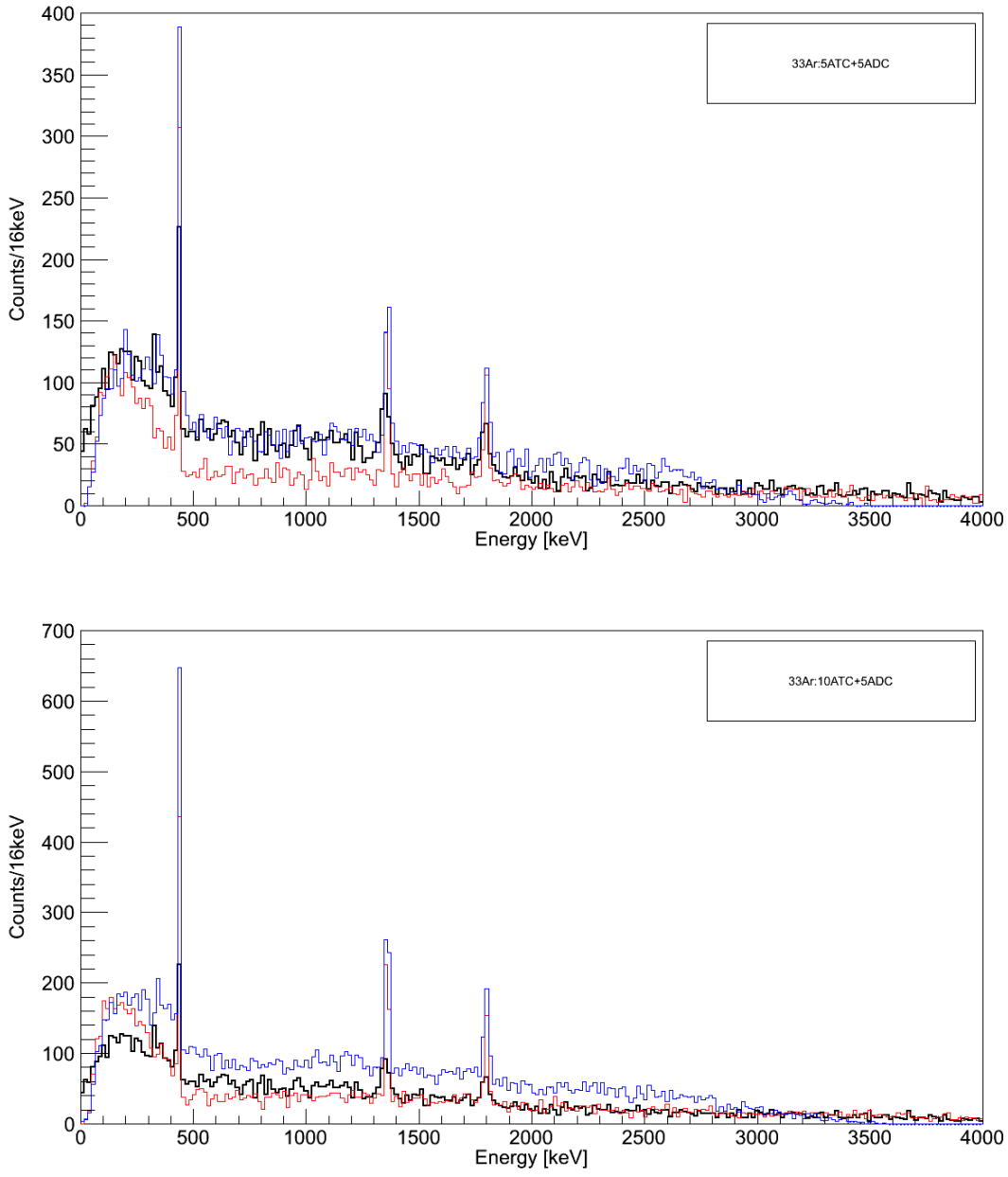

Figure 6.41: The comparison between the RISING (black) spectrum and the tracked OFT (red) and MGT (blue) spectra (top: 5ATC+5ADC, bottom: 10ATC+5ADC). The spectra are for the ^{33}Ar setting. The P/T values for the 5ATC+5ADC simulation (calculated between 700-4000 keV) are: OFT=9.18%, MGT=6.34% and RISING 4.56%, and the P/T values for the 10ATC+5ADC simulation are: OFT=9.00% and MGT=6.13%.

Chapter 7

Discussion and Conclusions

In order to determine the performance of the proposed AGATA geometries for use at GSI, and the tracking codes to a relativistic Coulex experiment, a PreSPEC experiment was simulated which utilised the RISING array and the LYCCA-0 calorimeter. Upon determining the simulation input parameters which resulted in a similar spectral response between the simulation and experiment, the same input parameters were used with the AGATA geometries replacing the RISING array in the simulations, and the spectral response of the AGATA geometries in the same simulated conditions evaluated.

The LYCCA-0 geometries have been implemented in the AGATA code, and the processing of the simulated output file allowed for the recoil velocity and direction of the heavy ions leaving the secondary target to be determined event-by-event, as performed experimentally. The simulated LYCCA-0 quantities were then used to apply particle gating conditions on the simulation output files, resulting in a modified output file to be passed to the tracking codes.

The tracking codes were used in a variety of simulated conditions in order to investigate the performance of the tracking: without any background components (γ-rays of interest only), high energy background and γ-rays of interest, and atomic background + high energy background + γ-rays of interest. The sensitivity of the timing resolution of the plastic scintillators on the peak shape has been investigated, and finally the simulated tracked AGATA spectra were compared to the experimental RISING spectra in order to provide an interpretation on the spectral response if AGATA were to have been used instead of RISING during experiment S377.

7.1 Evaluation of the AGATA Simulations

7.1.1 Tracking Performance

Two AGATA geometries have been considered during the work presented in this thesis; the 5ATC+5ADC and 10ATC+5ADC geometries. Previous work [9] has reported that for simulations containing no background or LYCCA tracking, at a target-to-array distance of 23.5 cm, the photopeak efficiency of the 5ATC+5ADC array is 7% for 1 MeV γ-rays, ranging to 5% for 2 MeV γ-rays. The maximum angular efficiency of the array is 2% at a detection angle of $\sim$25°. Similarly, for the 10ATC+5ADC array, at a target-to-array distance of 23.5 cm, the efficiency is 11% for 1 MeV γ-rays, ranging to 9% for 2 MeV γ-rays. The array has a maximum angular efficiency of 3.4% at a detection angle of $\sim$45°, as displayed in subsection 4.1.3. As can be seen in figure 4.15, the angular distribution of the γ-rays of interest emitted from the ^{36}Ar ions peaks at $\sim$30-35° and therefore the 10ATC+5ADC array is the most efficient in this angular range and for γ-rays between 1 and 2 MeV.

A comparison between the P/T and photopeak efficiency values for the simulations presented in chapter 6 are displayed in figure 7.1. When no background is included in the simulations, the P/T calculated from the OFT spectra is greater than the P/T from the MGT spectra, and the photopeak efficiency calculated from the MGT spectra is greater than the OFT spectra for both settings. This is due to the way single interaction points are treated within the tracking codes (see subsection 2.6.2). Comparing the P/T values extracted from the raw spectra to the tracked spectra highlights the benefit of using γ-ray tracking, i.e. a large portion of the scattered γ-rays contributing to the Compton background are reconstructed into the full incident γ-ray energy when the tracking is applied. With background included in the simulations, the high multiplicity of unwanted x-rays and γ-rays affects the ability of the tracking codes to disentangle the scattered interactions belonging to the γ-rays of interest.

As discussed in subsection 6.3.1 and sub-subsection 6.4.1.2, two methods were discussed to estimate the atomic background multiplicity per simulated event. Assuming a low beam intensity, the x-ray yield per incident beam particle was determined as a lower limit, and the total energy loss in the secondary target emitted as x-rays was taken as an upper limit. This resulted in an x-ray multiplicity per simu-

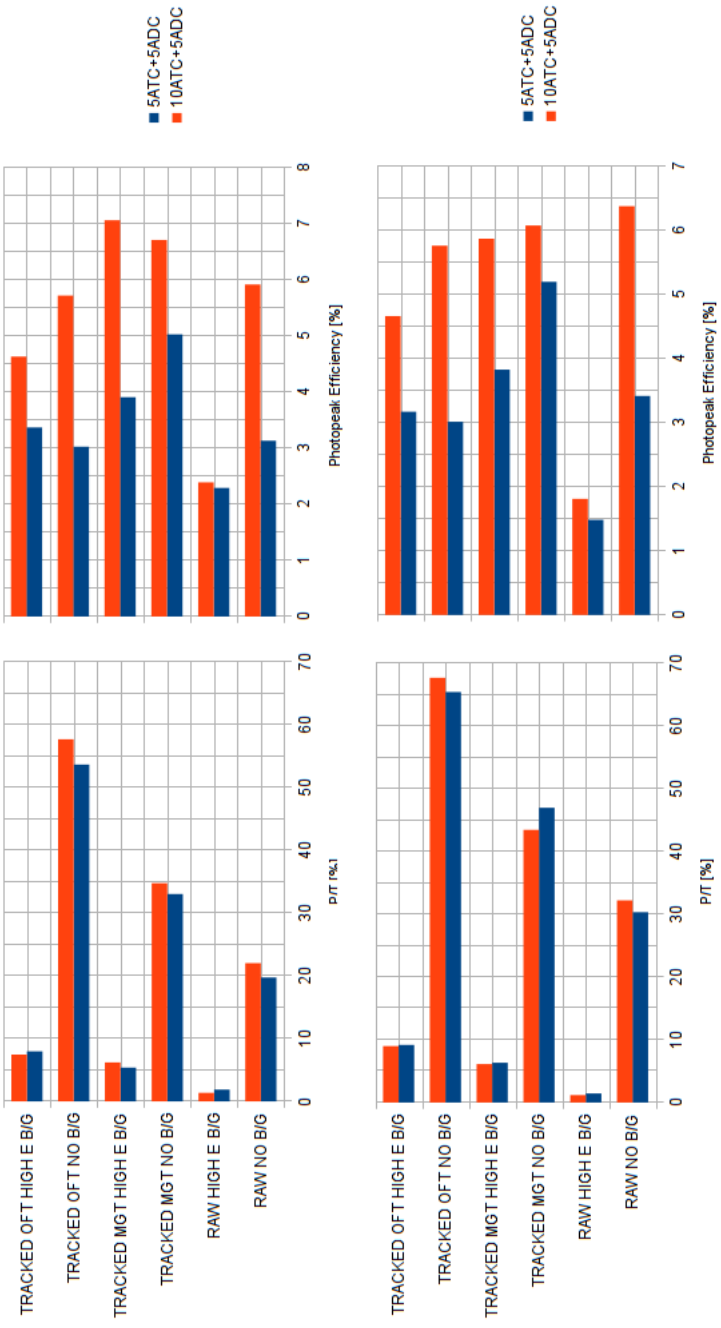

Figure 7.1: The extracted P/T and photopeak efficiency values for the different simulated conditions for both fragment settings (top: ^{36}Ar and bottom: ^{33}Ar). Two cases are displayed: (i) γ-rays of interest (no background) and (ii) high energy background+γ-rays of interest. For each case, the P/T and photopeak efficiency has been calculated for the raw spectrum and the tracked spectra, for both the 5ATC+5ADC and 10ATC+5ADC simulations.

lated event in the range of ∼80-25000. For a high intensity beam, the ratio between the atomic background cross section (output by ABKG) and the Coulex cross section (output by DWEIKO) was taken as an extreme upper limit, resulting in a multiplicity of $\sim 1 \times 10^6$ x-rays per simulated event. Simulations have been performed over the range of atomic background multiplicities determined above in order to evaluate the performance of the tracking. Figure 7.2 displays plots of the P/T and photopeak efficiency values as a function of the atomic background multiplicity extracted from the simulations. The tracking breaks down between an atomic background multiplicity of 10000/event and 100000/event, although due to time and computing complications, it was not possible to identify the exact point of failure. Providing the atomic background multiplicity is kept below 10000/event through the use of shielding, the simulations suggest that tracking is possible. The high x-ray flux has a large effect on the photopeak efficiency and reduces by an average factor of ∼8.5 at an x-ray multiplicity of 10000/event. The reduction in photopeak efficiency may make certain experiments impossible and special consideration should be taken as to whether the reduction in photopeak efficiency, in cases where the x-ray multiplicity is in the range 1000-10000/event, is acceptable.

In order to directly compare the AGATA spectra with the RISING spectra, the atomic background component was removed from the AGATA simulations leaving only the high energy background and γ-rays of interest, i.e. the exact same input events file as used for the final RISING spectra. An assumption was made that lead shielding or analysis techniques are to be used experimentally to reduce the background, hence the decision to remove the atomic background from the simulations. The tracking codes were successfully able to process the modified *GammaEvents.0000* files with high energy background and γ-rays of interest included, which allowed for a comparison of the simulated tracked AGATA spectra in the exact same simulated conditions as the RISING simulations.

Using the ^{33}Ar setting with the 5ATC+5ADC simulation as an example, by including the high energy background component in the simulations, the P/T reduces to 9.2% (OFT) and 6.3% (MGT) from 65.5% (OFT) and 47.0% (MGT) compared to the background free simulations. This shows that the high energy background component alone has a massive effect on the P/T, however, the photopeak efficiency remains fairly consistent with the background free simulations. Based on the simulations containing the high energy background component, the results suggest that

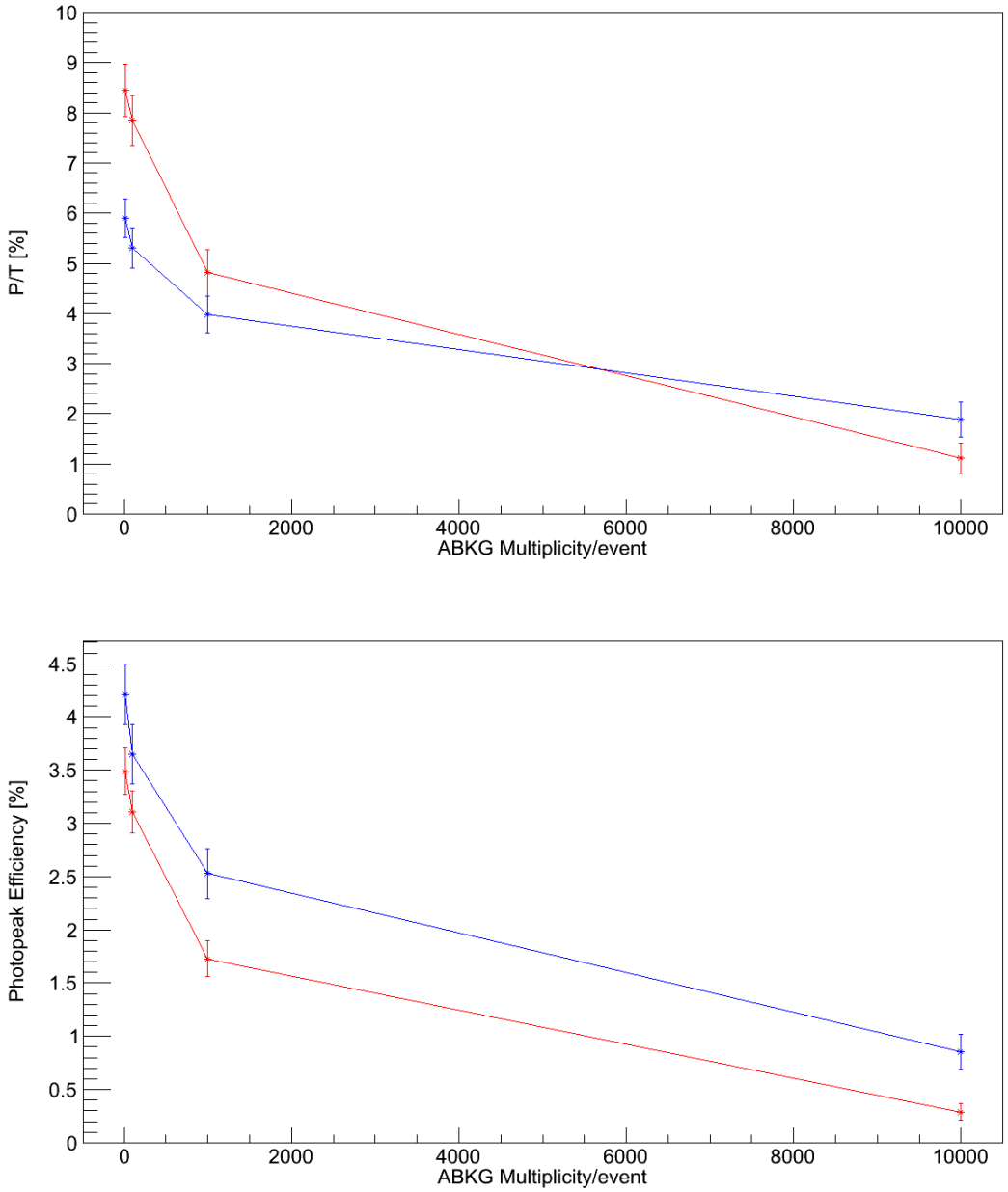

Figure 7.2: The P/T and photopeak efficiency values (OFT: red, MGT: blue) as a function of the atomic background multiplicity extracted from the simulations displayed in sub-subsection 6.4.1.2. The data represents the ^{33}Ar setting with the 5ATC+5ADC geometry.

the OFT provides better performance than the MGT in the GSI environment in terms of the P/T. In the GSI environment, due to the high multiplicities of background x-rays and γ-rays, it is unlikely for a single interaction event to occur or to be successfully disentangled by the tracking codes. Therefore, the OFT is more suitable for the conditions at GSI due to the treatment of single interactions. As discussed in section 2.6.2, when no single interactions are found, this results in a higher P/T at intermediate to high energy γ-rays and a large efficiency loss at low energies, which is where the background x-rays are dominant.

Within the tracking codes, the energy threshold applied to the packed interaction points has been investigated, and additionally, the effect of disabling the packing and smearing parameters (see sub-subsections 6.4.3.1 and 6.4.3.2). Using the ^{33}Ar simulation with the 5ATC+5ADC geometry as an example, increasing the energy threshold of the packed interaction points from 5 keV (default) to 300 keV resulted in the P/T reducing from 5.3% (OFT) and 3.8% (MGT) to 3.7% (OFT) and 0.7% (MGT). Additionally, the photopeak efficiency reduced from 3.2% (OFT) and 3.7% (MGT) to 1.1% (OFT) and 0.5% (MGT). Therefore, increasing the energy threshold of the packed interaction points did not benefit the spectral response. As it was not possible to obtain any experimental AGATA data or information regarding the performance of the PSA at GSI, the packing and smearing values were left at the default values.

7.1.2 Effect of the Timing Resolution on the Peak Shape

Due to the small angular resolution of AGATA, simulations have highlighted that the peak shape has a sensitivity to the timing resolution of the plastic scintillators used to provide the TOF start (FRS) and stop (LYCCA-0) signals (see subsection 6.4.2). The timing resolution was incremented between 25 ps and 150 ps during the processing stage, and the modified *GammaEvents.0000* files were passed through both the OFT and MGT tracking codes. Figure 7.3 displays the average increase in resolution (FWHM) of the 1359 keV and 1798 keV peaks as a function of the timing resolution of the plastic scintillators, for both the OFT and MGT codes.

As can be seen in figure 7.3, the increase in FWHM compared to the perfect timing resolution case increases linearly as the timing resolution is incremented, resulting in a degradation in energy resolution. At 150 ps, the MGT gives a FWHM

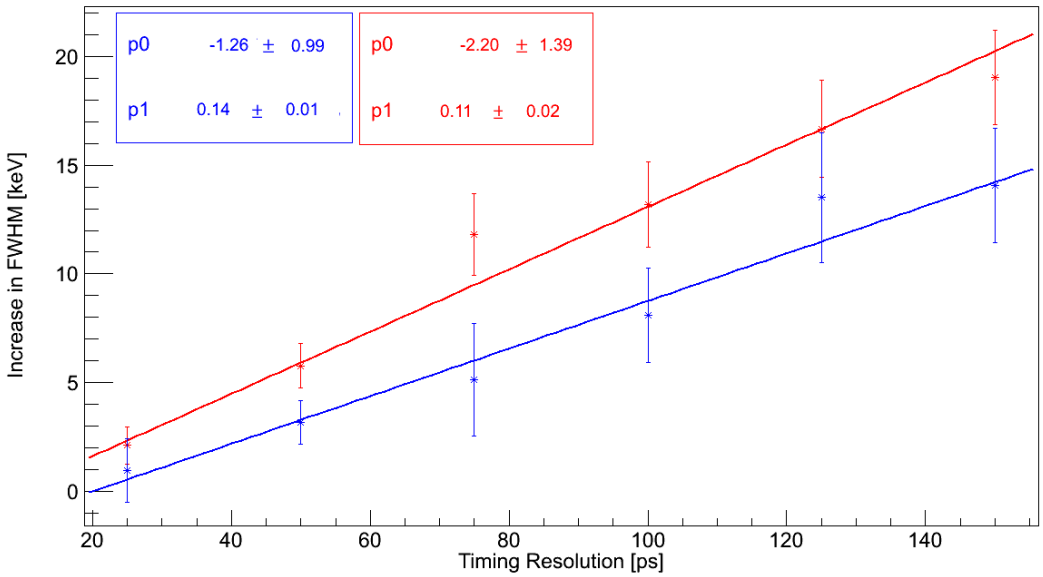

Figure 7.3: The increase in the average FWHM of the 1359 keV and 1798 keV peaks as the timing resolution of the plastic scintillators is increased. Each data point represents the difference between the FWHM resulting from a perfect timing resolution and the given timing resolution. The OFT data is displayed in red and the MGT in blue. The plot represents the ^{33}Ar setting with the 5ATC+5ADC geometry. The data were taken from table 6.6.

of 31.53 keV and the OFT gives 27.52 keV. Currently, a timing resolution of 50 ps is typically obtained experimentally [69] in each of the individual plastic scintillators, corresponding to a simulated FWHM at 50 ps of 14.3 keV for the OFT, and 20.6 keV for the MGT. The experimental inner ring (see figure 6.19) and total rings (see figure 6.12) ^{33}Ar RISING spectra give an average FWHM of 32.9 keV and 56.8 keV respectively (the outer rings are contaminated with background in the energy region of the 1798 keV peak, hence the larger FWHM for the total rings spectrum). Comparing the experimental RISING inner ring FWHM with the tracked simulated AGATA spectra offers a 56% improvement for the OFT and 37% for the MGT in terms of the FWHM at a timing resolution of 50 ps. At a timing resolution of 50 ps, 5.8 keV of the 14.3 keV FWHM value determined with the OFT results from the timing resolution. Similarly, for the MGT, the timing resolution contributes to 3.2 keV of the calculated FWHM value of 20.61 keV.

7.1.3 Improvements of AGATA over RISING

The final comparisons between the simulated RISING and AGATA spectra are displayed in subsection 6.4.4. For each comparison, the simulated RISING spectrum has been compared with the tracked OFT and MGT AGATA spectra. Four comparisons have been made:

1. the ^{36}Ar setting with the 5ATC+5ADC geometry
2. the ^{36}Ar setting with the 10ATC+5ADC geometry
3. the ^{33}Ar setting with the 5ATC+5ADC geometry
4. the ^{33}Ar setting with the 10ATC+5ADC geometry.

Table 7.1 displays the ratio between the P/T of the AGATA 5ATC+5ADC and the 10ATC+5ADC spectra to the P/T of the RISING spectra for both the ^{36}Ar and ^{33}Ar settings. Each case highlights the factor of improvement in terms of the P/T compared to the RISING spectra.

Tracking	Setting	Geometry	$\frac{P/T(AGATA)}{P/T(RISING)}$
OFT	^{36}Ar	5ATC+5ADC	2.17
OFT	^{36}Ar	10ATC+5ADC	2.03
MGT	^{36}Ar	5ATC+5ADC	1.46
MGT	^{36}Ar	10ATC+5ADC	1.69
OFT	^{33}Ar	5ATC+5ADC	2.01
OFT	^{33}Ar	10ATC+5ADC	1.97
MGT	^{33}Ar	5ATC+5ADC	1.39
MGT	^{33}Ar	10ATC+5ADC	1.34

Table 7.1: A table displaying the ratios between the P/T of the tracked AGATA spectra and the RISING spectra.

Figure 7.4 displays the comparisons between the simulated AGATA spectra (MGT and OFT) and the experimental RISING spectra, to give a view on the improvement in spectral response if AGATA were to have been used in experiment S377. The spectra have been normalised using the same normalisation factors used

to compare the simulated RISING spectrum with the experiment (for the ^{36}Ar setting - the peak area of the 1970 keV transition, and for the ^{33}Ar setting - the P/T values).

7.2 Future Work

7.2.1 AGATA and Pb Shielding

Previous simulations have explored the possibility of using lead shielding, however, no background components were considered [41]. As discussed in chapter 6, the simulated RISING spectra were compared to the experimental spectra for experiment S377, which allowed for the simulation input to be determined that produced a similar spectral response in terms of background. With the possibility of including a realistic background in the simulations, the effect of lead shielding should be fully investigated.

The atomic background was removed from the RISING simulations due to the use of the absorbers, however, it was reintroduced in the AGATA simulations. Including extremely high levels of atomic background in the simulations without the use of absorbers resulted in output spectra completely saturated by background with no visible transitions of interest; the tracking, however, was able to identify the peaks of interest below an x-ray multiplicity of ∼10000/event. With no lead shielding included and with the atomic background removed from the AGATA simulations (leaving only the high energy background component), the tracking codes were able to track the interactions of interest, however, the background has a big effect on the P/T compared to simulations without any background components. With the high energy background component included, the P/T values determined from the 5ATC+5ADC and 10ATC+5ADC simulations are identical with the 10ATC+5ADC array showing no major improvement over the 5ATC+5ADC array. Simulations without any background components has highlighted that the 10ATC+5ADC geometry has a higher efficiency than the 5ATC+5ADC geometry, and although it is more efficient at detecting γ-rays of interest, it is also more efficient at detecting unwanted background; this is why the simulation P/T values between either geometry are similar. If lead shielding had been used in the simulations discussed in this thesis, it is expected that the 10ATC+5ADC would give more of a noticeable

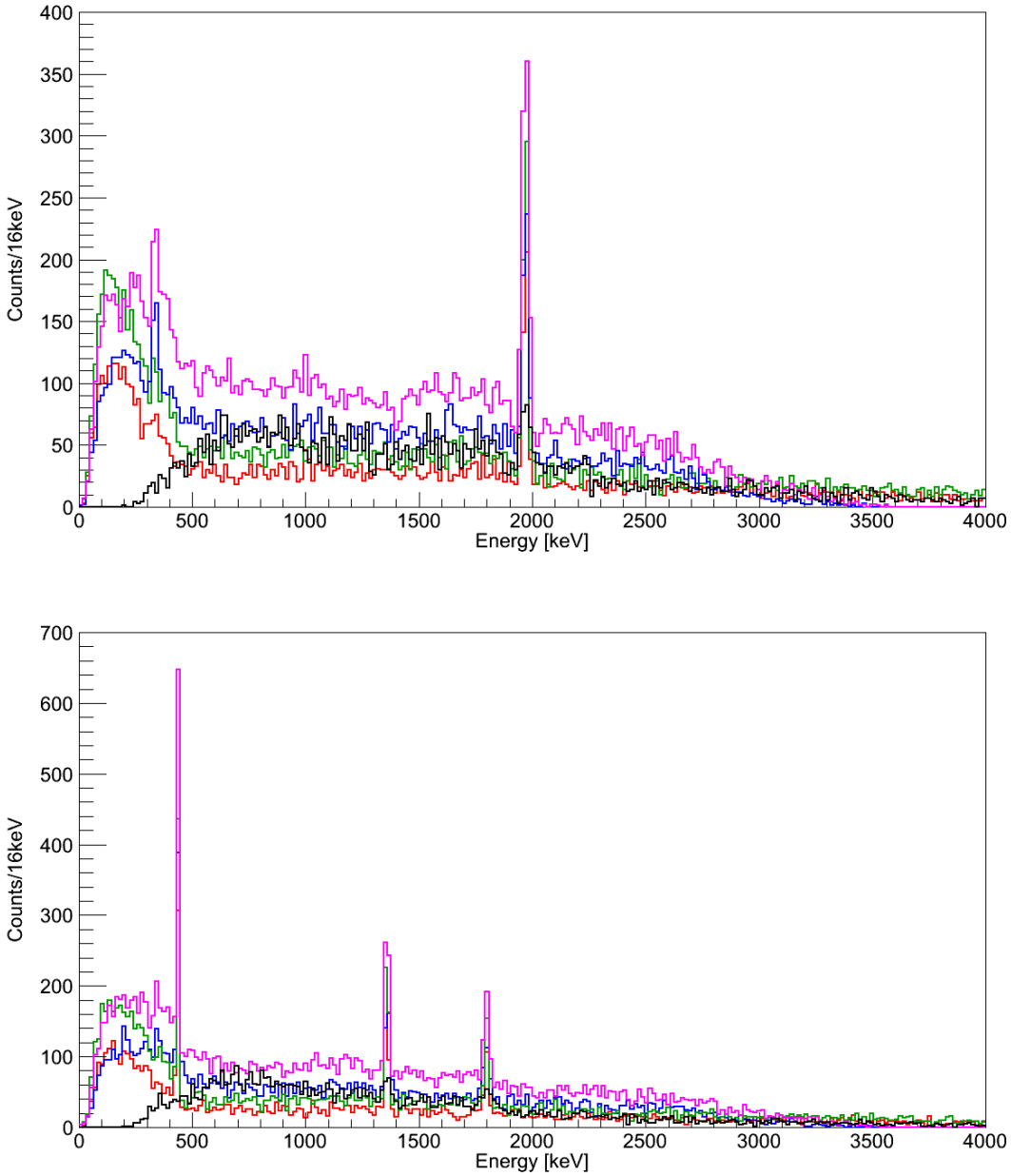

Figure 7.4: Comparison between the experimental ^{36}Ar (top) and ^{33}Ar (bottom) RISING spectra (black) and the simulated tracked AGATA spectra for both the 5ATC+5ADC (OFT: red, MGT: blue) and 10ATC+5ADC (OFT: green, MGT: purple) geometries.

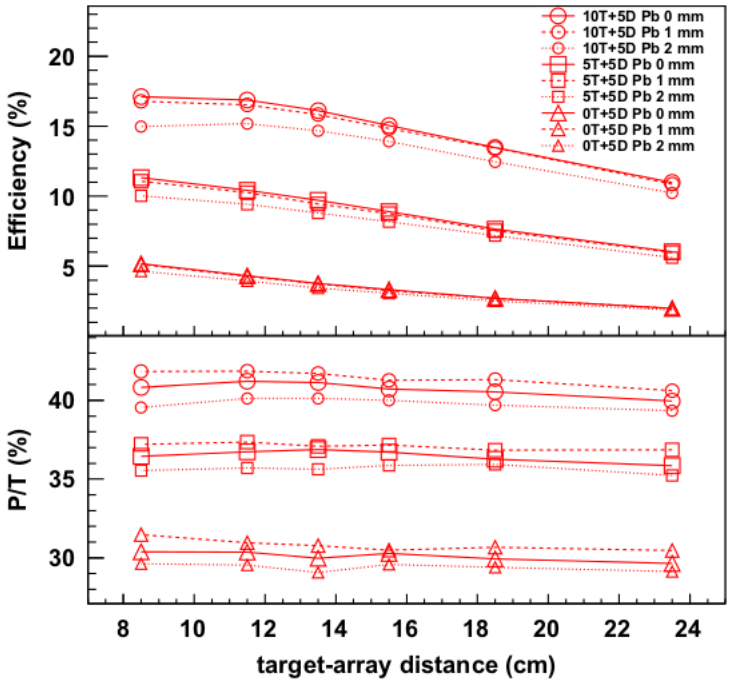

Figure 7.5: The efficiency and P/T of the 10ATC+5ADC, 5ATC+5ADC and 5ADC AGATA geometries as a function of the distance from the secondary target with the inclusion of lead shielding. The simulations contained 1 MeV γ-rays emitted at β=0.43. Figure taken from reference [41].

improvement compared to the 5ATC+5ADC setup.

The efficiency and P/T values with lead shielding surrounding the target chamber, as reported in reference [41], are displayed in figure 7.5. The plot shows how the efficiency and P/T decrease as the thickness of the Pb shielding surrounding the target chamber is increased from 0 to 2 mm. The use of lead shielding should be investigated in the simulation conditions discussed in this thesis, so as to determine the effect of large levels of background on the spectral response and the performance of the tracking. Lead shielding can be implemented during the simulation setup for the AGATA code, and the thickness of the shielding should be varied whilst using the same input events files used for the results displayed in chapter 6.

7.2.2 AGATA and Miniball

It has been proposed that AGATA is to be used in conjunction with the Miniball detectors at GSI. The Miniball detectors are six-fold segmented and a PSA technique is used to identify the position of the first γ-ray interaction within a detector.

Investigations [70] have involved using a reference 5ATC+5ADC AGATA geom-

etry combined with seven different Miniball geometries. The Miniball clusters are implemented as triple clusters (MTCs) and are constructed from simulated Euroball detector geometries. The simulations contained 1 MeV γ-rays emitted at β=0.43 and a typical beam profile of that at GSI. The following seven configurations have been investigated:

1. Inner ring of 5ADCs and an outer ring consisting of packed 5ATCs on the upper half and 5MTCs on the lower half of the array. The ATCs and ADCs have a target-to-detector distance of 235 mm and the MTCs have a target-to-detector distance of 300 mm.

2. Inner ring of 5ADCs and an outer ring consisting of semi-consecutive ATCs and MTCs. The ATCs and ADCs have a target-to-detector distance of 235 mm and the MTCs have a target-to-array distance of 300 mm.

3. 5 MTCs placed at 90° with a target-to-detector distance of 170 mm.

4. 5 MTCs placed at 90° with a target-to-detector distance of 235 mm.

5. 4 MTCs placed at 95° and 4 MTCs placed at 129° with a target-to-detector distance of 206 mm.

6. 4 MTCs placed at 95° and 4 MTCs placed at 129° with a target-to-detector distance of 250 mm.

7. 4 MTCs placed at 95° and 4 MTCs placed at 129° with a target-to-detector distance of 400 mm.

The results of the simulations suggested it is possible to gain an improvement of more than 30% in photopeak efficiency with the 5ATC + 5ADC + 4MTCs at 95° + 4MTCs at 130° geometry, at a target-to-detector (MTCs) distance of 250 mm, in comparison with the 5ATC+5ADC geometry alone. It was also discovered that the lower position resolution of Miniball compared to the AGATA detectors does not have a major effect on the γ-ray detection sensitivity. The energy resolutions for both AGATA and Miniball are dominated by $\Delta\beta$ at the secondary target, and the uncertainty in the position of the γ-ray emissions along the z-direction resulting from states with longer half lives. The simulations discussed in reference [70] contain no background components or LYCCA tracking and should be investigated with the

simulation process discussed in the work of this thesis, in order to evaluate the performance of the various configurations in a high background environment.

7.2.3 Simulation Upgrades

In the simulations presented in this thesis, the γ-rays are emitted promptly following the secondary target position, whereas in reality, dependent on the lifetime of the state, the γ-ray(s) may be emitted from within the target, or further along the z-direction, for example, following the target DSSSD. Heavy ions that penetrate through the DSSSD before emitting a γ-ray will have a slightly reduced β due to the lower velocity following the energy loss in the DSSSD. This will result in a larger β spread which further contributes to the broadening of the peaks.

In order to include this effect in the simulations, the time of particle emission should be included during the event generation stage, i.e. the input events file to the AGATA code. Additionally, a time of emission for the background components present in the simulation could be included in order to recreate a more realistic germanium timing structure similar to the experimental timing structure, as displayed in figure 6.8. This will allow for additional simulated gating conditions which could be used to further reduce the amount of background in the final spectra.

7.3 Concluding Remarks

The use of the tracking codes in a relativistic environment has shown to be beneficial in terms of the spectral response and the increase in P/T, however, an assumption was made during the simulations that shielding is to be used experimentally which justified the removal of the atomic background from the simulations. Simulations have shown that tracking is possible providing the atomic background can be kept below a multiplicity of $\sim$10000/event, which is $\sim$10% of the extreme upper limit. Therefore, it needs to be decided if shielding will be used experimentally and for the corresponding shielding to be implemented during the simulations, in order to determine the effect on the tracking performance for very high multiplicities of x-rays.

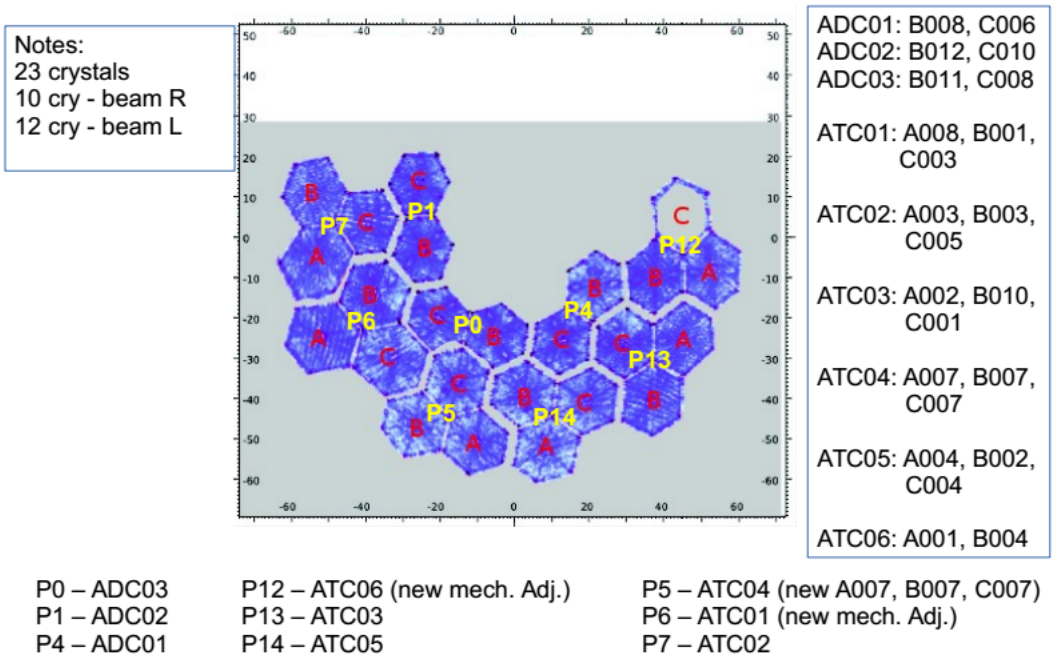

Figure 7.6: An (x,y) image of the current AGATA geometry at GSI consisting of 23 crystals. The axis dimensions are in cm and the crystal labelling is displayed. Figure taken from reference [58].

At the time of writing, the AGATA geometry is approaching the 5ATC+5ADC setup and consists of 23 crystals (see figure 7.6). The current 23 crystals geometry is available in the AGATA code [58].

References

[1] Euroball Homepage. http://eballwww.in2p3.fr/EB/. Accessed August 2010.

[2] Miniball Homepage. http://www.miniball.york.ac.uk/. Accessed August 2010.

[3] Gammasphere Homepage. http://www.phy.anl.gov/gammasphere/index.html. Accessed August 2010.

[4] G. J. Schmid *et al.* A gamma-ray tracking algorithm for the GRETA spectrometer. *Nuclear Instruments and Methods in Physics Research A*, 430:69–83, 1999.

[5] I. Y. Lee *et al.* GRETINA: A gamma ray energy tracking array. *Nuclear Instruments and Methods in Physics Research A*, 746:255–259, 2004.

[6] S. Akkoyun *et al.* AGATA-Advanced GAmma Tracking Array. *Nuclear Instrumentation and Methods in Physics Research A*, 668, 2012.

[7] J. Simpson *et al.* AGATA Technical Design Report. December 2008.

[8] D. Rudolph *et al.* LYCCA Technical Report. June 2008.

[9] C. Domingo-Pardo *et al.* AGATA at GSI-FRS MC-Simulations. Technical report, February 2011.

[10] M.J. Taylor *et al.* A new simulation package to model detector systems with fragmentation reactions and ion separators: Application to the LYCCA-0 system. *Nuclear Instruments and Methods in Physics Research A*, 606:589–597, 2009.

[11] AGATA Code Homepage. http://agata.pd.infn.it/documents/simulations/agataCode.html. Accessed October 2009.

[12] H.J. Wollersheim *et al.* Rare ISotopes INvestigation at GSI (RISING) using gamma-ray spectroscopy at relativistic energies. *Nuclear Instruments and Methods in Physics Research A*, 537:637–657, 2005.

[13] K. S. Krane. *Introductory Nuclear Physics.* John Wiley & Sons, Inc., 1988.

[14] M. Bentley. Nuclear Physics II Module, University of York, 2010.

[15] G. F. Knoll. *Radiation Detection and Measurement.* John Wiley & Sons, Inc., 2000.

[16] W. R. Leo. *Techniques for Nuclear and Particle Physics Experiments.* Springer-Verlag Berlin Heidelberg, 1987.

[17] Gammasphere Online Booklet Homepage. `http://nucalf.physics.fsu.edu/~riley/gamma/`. Accessed May 2013.

[18] R. Anholt *et al.* Observation of Radiative Capture in Relativistic Heavy-Ion-Atom Collisions. *Physical Review Letters*, 53(3), 1984.

[19] R. Anholt *et al.* Atomic collisions with relativistic heavy ions. VI. Radiative processes. *Physical Review A*, 33(4), 1986.

[20] R. Anholt *et al.* Atomic collisions with relativistic heavy ions. Target inner-shell ionization. *Physical Review A*, 30(5), 1984.

[21] GEANT4 Homepage. `http://geant4.cern.ch/`. Accessed October 2009.

[22] E. Farnea *et al.* Conceptual design and Monte Carlo simulations of the AGATA array. *Nuclear Instruments and Methods in Physics Research A*, 621:331–343, 2010.

[23] M. A. Deleplanque *et al.* GRETA: utilizing new concepts in gamma-ray detection. *Nuclear Instruments and Methods in Physics Research A*, 430:292–310, 1999.

[24] J. Eberth *et al.* From Ge(Li) detectors to gamma-ray tracking arrays - 50 years of gamma spectroscopy with germanium detectors. *Progress in Particle and Nuclear Physics*, 60:283–337, 2008.

[25] P. Medina *et al.* Proceedings of the Twenty-first IEEE Instrumentation and Measurement Technology Conference. 3:1828–1832, 2004.

[26] M. Schlarb *et al.* Pulse shape analysis for gamma-ray tracking (Part I): Pulse shape simulation with JASS. *European Physical Journal A*, 47:132, 2011.

[27] A. Lopez-Martens *et al.* gamma-ray tracking algorithms: a comparison. *Nuclear Instruments and Methods in Physics Research A*, 533:454–466, 2004.

[28] A. Lopez-Martens. Author of the OFT tracking code. `Araceli.Lopez-Martens@csnsm.in2p3.fr`.

[29] D. Bazzacco. Author of the MGT tracking code. `dino.bazzacco@pd.infn.it`.

[30] D. Bucurescu *et al.* Fuzzy clustering algorithm for gamma ray tracking in segmented detectors . *Romanian Reports in Physics*, 62(1):27–36, 2010.

[31] F. Didierjean *et al.* The Deterministic Annealing Filter: A new clustering method for gamma-ray tracking algorithms. *Nuclear Instruments and Methods in Research A*, 615:188–200, 2010.

[32] GSI Homepage. `http://www.gsi.de`. Accessed September 2010.

[33] J. J. Gaimard and K. H. Schmidt. A Reexamination of the Abrasion-Ablation model for the description of the nuclear fragmentation reaction. *Nuclear Physics A*, 531:709–745, 1991.

[34] Experiment S377 ELOG. `https://elog.gsi.de/s377`. Accessed May 2011.

[35] T. Glasmacher. Coulomb Excitation at Intermediate Energies. *Annual Review of Nuclear and Particle Science*, 48:1–31, 1998.

[36] C. Bertulani. Theory and Application of Coulomb Excitation. *8th CNS-EFES Summer School Lecture Notes*, 2009.

[37] UNILAC website. `http://www-inj.gsi.de/index.php?section=3`. Accessed October 2011.

[38] SIS-18 website. `http://www.gsi.de/en/gsiwork/accelerator/sis18.htm`. Accessed October 2011.

[39] H. Geissel *et al.* The GSI projectile fragment separator (FRS): a versatile magnetic system for relativistic heavy ions. *Nuclear Instruments and Methods in Physics Research B*, 70:286–297, 1992.

[40] ESR website. `http://www.gsi.de/en/gsiwork/accelerator/esr.htm`. Accessed October 2011.

[41] C. Domingo-Pardo *et al.* Conceptual design and performance study for the first implementation of AGATA at the in-flight RIB facility of GSI. *Nuclear Instruments and Methods in Physics Research A*, 694:297–312, 2012.

[42] MUSIC detector manual. `http://www-w2k.gsi.de/frs/technical/FRSsetup/detectors/music80/music80\_manual.pdf`. Accessed October 2011.

[43] P. Doornenbal. *In-beam gamma-ray spectroscopy of two-step fragmentation reactions at relativistic energies - The case of* ^{36}Ca. PhD thesis, 2007.

[44] FRS algorithms. `http://www-w2k.gsi.de/frs/technical/daq/frs-algorithms.asp`. Accessed October 2011.

[45] J. Simpson. The Euroball Spectrometer. *Zeitschrift Fur Physik A Hadrons and Nuclei*, 358(2):139–143, 1997.

[46] RISING Homepage. `http://www-linux.gsi.de/~wolle/EB\_at\_GSI/FRS-WORKING/index.html`. Accessed September 2010.

[47] M. Wilhelm *et al.* The response of the Euroball Cluster detector to γ-radiation up to 10 MeV. *Nuclear Instruments and Methods in Physics Research A*, 381:462–465, 1996.

[48] R. Lozeva *et al.* A novel Calorimeter Telescope for indentification of relativistic heavy-ion reaction channels. *Nuclear Instruments and Methods in Physics Research A*, 562:298–305, 2006.

[49] R. Hoischen *et al.* Fast timing with plastic scintillators for in-beam heavy-ion spectroscopy. *Nuclear Instruments and Methods in Physics Research A*, 654:354–360, 2011.

[50] MOCADI Homepage. http://www-linux.gsi.de/~weick/mocadi/. Accessed September 2010.

[51] N. Iwasa *et al.* MOCADI, a universal Monte Carlo code for the transport of heavy ions through matter within ion-optical systems. *Nuclear Instruments and Methods in Physics Research B*, 126:284–289, 1997.

[52] K Summerer *et al.* Modified empirical parametrization of fragmentation cross sections. *Physical Review C*, 61(034607), 2000.

[53] FRS Training Homepage. http://www-linux.gsi.de/~frsgast/. Accessed November 2010.

[54] R. Hoischen. An Isomer Study of the Nucleus ^{54}Ni Preparations, Simulations and First Results. Masters Thesis, Lund University, 2006.

[55] LISE++ Homepage. http://groups.nscl.msu.edu/lise/lise.html. Accessed November 2010.

[56] ROOT Homepage. http://root.cern.ch. Accessed October 2009.

[57] AGATA Code Detector Geometry. http://agata.pd.infn.it/documents/simulations/docs/GeometryDescription.html. Accessed March 2012.

[58] C. Domingo-Pardo. Private Communication. cesar.domingo@ific.uv.es.

[59] FRS-Setup Homepage. http://www-w2k.gsi.de/frs-setup/. Accessed November 2010.

[60] Gammaware Homepage. http://www.ipnl.in2p3.fr/gammaware/. Accessed September 2010.

[61] RadWare Tools. http://radware.phy.ornl.gov/. Accessed October 2009.

[62] C. A. Bertulani *et al.* A computer program for nuclear scattering at intermediate and high energies. *Computer Physics Communications*, 152:317–340, 2003.

[63] ABKG code - originating from GSI. R. Holzmann (1998) & H. Scheit (2001) .

[64] L. Scruton. *Polycrystalline Diamond Detectors for Fast Timing Applications at FAIR.* PhD thesis, 2013.

[65] A. Lopez-Martens. Private Communication. Araceli.Lopez-Martens@csnsm.in2p3.fr.

[66] M. Schlarb. Private Communication. Michael.Schlarb@ph.tum.de.

[67] A. Wendt. *Isospin symmetry in the sd shell: Coulomb excitation of ^{33}Ar at relativistic energyes and the new 'Lund-York-Cologne-Calorimeter'*. PhD thesis, 2013.

[68] P. W. Gray *et al.* Linear Classes of Ge(Li) Detector Efficiency Functions. *Nuclear Instruments and Methods in Physics Research A*, 237:577–589, 1985.

[69] P. Golubev *et al.* The Lund–York–Cologne Calorimeter (LYCCA): Concept, design and prototype developments for a FAIR-NUSTAR detector system to discriminate relativistic heavy-ion reaction products. *Nuclear Instrumentation and Methods in Physics Research A*, 723:55–66, 2013.

[70] C. Domingo-Pardo *et al.* Complementing AGATA with MINIBALL. Technical report, December 2012.